SANDIA REPORT
SAND2019-11174
Printed Click to enter a date

Monitoring and Repair of Cement-Geomaterial Interfaces in Borehole and Repository Scenarios

Team Members:
Edward N. Matteo (PI - Sandia National Laboratories)
Kevin McMahon (PM - Sandia National Laboratories)
R. Chris Camphouse (PM - Sandia National Laboratories)
Thomas Dewers (Sandia National Laboratories)
Carlos Jové-Colon (Sandia National Laboratories)
Timothy Fuller (Sandia National Laboratories)
Joseph Mohagheghi (Sandia National Laboratories)

John. C. Stormont (University of New Mexico)
Mahmoud R. Taha (University of New Mexico)

Additional Contributors:
Laura Pyrak-Nolte (Purdue University)
Chaoyi Wang (Purdue University)
A. Douba (University of New Mexico)
Moneeb Genedy (University of New Mexico)
Serafin G. Fernandez (University of New Mexico)
U. F. Kandil (Egyptian Petroleum Research Institute)
E. E. Soliman (University of New Mexico)
J. Starr (University of New Mexico)
Mike Stenko (Transpo Industries, Inc.)

Issued by Sandia National Laboratories, operated for the United States Department of Energy by National Technology & Engineering Solutions of Sandia, LLC.

Available to DOE and DOE contractors from
U.S. Department of Energy
Office of Scientific and Technical Information
P.O. Box 62
Oak Ridge, TN 37831

Telephone: (865) 576-8401
Facsimile: (865) 576-5728
E-Mail: reports@osti.gov
Online ordering: http://www.osti.gov/scitech

Available to the public from
U.S. Department of Commerce
National Technical Information Service
5301 Shawnee Rd
Alexandria, VA 22312

Telephone: (800) 553-6847
Facsimile: (703) 605-6900
E-Mail: orders@ntis.gov
Online order: https://classic.ntis.gov/help/order-methods/

ABSTRACT

The failure of subsurface seals (i.e., wellbores, shaft and drift seals in a deep geologic nuclear waste repository) has important implications for US Energy Security. The performance of these cementitious seals is controlled by a combination of chemical and mechanical forces, which are coupled processes that occur over multiple length scales. The goal of this work is to improve fundamental understanding of cement-geomaterial interfaces and develop tools and methodologies to characterize and predict performance of subsurface seals. This project utilized a combined experimental and modeling approach to better understand failure at cement-geomaterial interfaces. Cutting-edge experimental methods and characterization methods were used to understand evolution of the material properties during chemo-mechanical alteration of cement-geomaterial interfaces. Software tools were developed to model chemo-mechanical coupling and predict the complex interplay between reactive transport and solid mechanics. Novel, fit-for-purpose materials were developed and tested using fundamental understanding of failure processes at cement-geomaterial interfaces.

ACKNOWLEDGEMENTS

The authors wish to acknowledge the Earth Sciences Research Foundation for their generous support over the last three years. In particular, we thank Erik Webb for his numerous suggestions, comments, feedback, and encouragement over the course of the project. There many who helped bring this project to fruition, including: Dave Borns, Steve Bauer, Pania Newell, Heeho Park, and Doug Blankenship. There are many support personnel who we thank for their valuable contributions to the logistics and business of management side of the project, including: Tracy Woolever, Libby Sanzero, and Nancy Vermillion.

CONTENTS

LIST OF FIGURES

LIST OF TABLES

This page left blank

ACRONYMS AND DEFINITIONS

Acronym	Definition
ANP	aluminum nanoparticle
API	American Petroleum Institute
ASTM	American Society for Testing and Materials
C/S ratio	CaO/SiO_2 weight ratio
CEP	capillary entry pressure
CNT	carbon nanotube
COOH	carboxyl group
DETA	diethylenetriamine
DMA	dynamic mechanical analysis
DOE	Department of Energy
FE	finite element
FTIR	Fourier transform infrared
LCL	lower control limit
LDRD	Laboratory Directed Research & Development
MAS	magic angle spinning
MMA	methyl methacrylate
MWCNT	multiwalled carbon nanotube
NETL	National Energy Technology Laboratory
NM-MMA	nanomodified methyl methacrylate
NMR	nuclear magnetic resonance
OWC	oil well cement
PC	polymer concrete
PCN	polymer cement nanocomposite
PCNA	PCN mixed with ANPs
PCNC	PCN mixed with MWCNTs
PCNS	PCN mixed with SNPs
PVC	polyvinyl chloride
SBR	styrene-butadiene rubber
SEM	scanning electron microscope
SNP	silica nanoparticle
TEM	transmission electron microscope
TGA	thermogravimetric analysis

Acronym	Definition
UATR	universal attenuated total reflectance
USB	universal serial bus
w/c ratio	water-to-cement ratio
XRD	X-ray diffraction

1. INTRODUCTION

Subsurface engineering applications place heavy reliance on reliability of cementitious materials as both structural components and for containment: geothermal, carbon storage, unconventional resources, deep borehole disposal, and geologic repositories. The interface between cementitious materials and host media represents vulnerability for ensuring structural and containment integrity. Failure behavior of such interfaces is poorly understood, owing to coupled chemical and mechanical time-dependent processes. Complexity of cement-geomaterial interfaces necessitates a multi-scale approach to gain fundamental understanding of the evolution of interfacial bond. *The main premise of this project was that a fundamental understanding of failure mechanisms and detectability could be developed and subsequently used to design more robust seal materials to minimize interfacial failure and/or self-healing materials to repair failed interfaces.* Our team engaged in experimental and modeling tasks focused on gaining fundamental understanding of cement-geomaterial interfaces under a range of high-temperature, high-pressure conditions, and then used this knowledge to develop purpose-built seal materials. Stakeholders in this research area, which includes oil and gas/geothermal operators and repository designers, are focused on utilization of established technologies for seal materials. Our approach aimed to fill a critical knowledge-gap of failure behavior at cement-geomaterial interfaces, enhance predictive capabilities for subsurface engineering scenarios, and enable development of novel, fit-for-purpose seal materials with unprecedented robustness for harsh subsurface environments.

The work contained in this report fills a knowledge gap in the area of coupled chemo-mechanical processes at cement-geomaterial interfaces. Chemical processes for cement-geomaterial interfaces have been studied extensively focusing on cement degradation mechanisms in nuclear waste repositories (Berner 1992, Pabalan et al., 2009), geologic storage of CO_2 (Kutchko et al. 2007, Matteo and Scherer 2012), as well as studies focused on the mechanical response in wellbores(Carey et al. 2013) and thermal-hydrologic-mechanical (THM) modeling of shaft seal systems(Hansen and Knowles 2000, Blanco-Martín et al. 2016). Work has also been completed that couples field-scale deformation during a CO_2 injection operation to a 3D geomechanical wellbore model (Sobolik et al. 2015), but this, too, was a purely mechanical representation of the cement-geomaterial interfaces along the length of a wellbore. Studies that address chemo-mechanical coupling of geomaterials focus solely on micro-scale phenomenon(Gajo et al. 2015, Hu and Hueckel 2007), and fail to capture multi-scale processes that are needed to address realistic applications. Coupled chemo-mechanical modeling, as well as understanding of the relevant fundamental processes, of such systems is lacking. Failure of cement-geomaterial interfaces in the Gulf of Mexico and in Aliso Canyon, CA demonstrated a pressing need to not only understand these phenomenon, but also a need for robust, purpose-built remediation solutions (i.e. seal repair materials).

The objectives of this project were as follows:

(1) ***Characterize the chemistry and physics of a cement-geomaterial interfaces*** under relevant *in situ* chemical and geomechanical conditions to develop a conceptual understanding of failure modes, as well as to create a basis for validation, parameter input, and constitutive model development for chemo-mechanical simulation; (

2) ***Develop a modeling capability*** that includes coupling between solid mechanics (Albany)and reactive transport/flow(PFLOTRAN) that enables simulation of cement-geomaterial interfaces with predicative capability, and

(3) ***Develop and evaluate next-generation seal repair materials suitable for the expected shaft/wellbore environments*** that have the ability of the seal material to penetrate and effectively repair degraded cement-geomaterial interfaces at representative subsurface high-temperature, high-pressure conditions.

This project combined experimental and modeling tasks focused on cement-geomaterial interfaces under a range of high-temperature, high-pressure conditions including: recognition and interpretation of guided acoustic waves and attenuation for use in detection of interfacial changes; long-term "creep" experiments to examine corrodibility and elastic moduli (or velocity) degradation; and scale-dependent nucleation and propagation of flaws at interfaces. We used a multi-scale testing and analytical approach, including a battery of core scale mechanical testing to characterize interfacial mechanics, continuum scale and system scale modeling, and microscale characterization of failure surfaces (microCT, SEM-EDS, nano/micro-indentation, optical/Laser Confocal profilometry). We developed capabilities at Sandia for triaxial testing with chemical alteration and utilized x-Ray tomographic imaging and acoustics/ultrasonics to track interfacial characteristics over time and at elevated temperature, pressure, stress, and chemically corrosive environments. With this capability, baseline physico-chemical properties of interfaces were measured, and were then evolved the interface during experiments while measuring the interface response to coupled chemical and mechanical stresses. Two Sandia codes with coupled multiphysics capability: Albany and PFLOTRAN were fully coupled to examine chemical-mechanical phenomena and this "new" code was used to model simultaneous chemical-mechanical evolution. Novel repair materials, including polymer nanocomposites with self-repair capabilities, which have been investigated in lower-T applications, will be developed and applied to interfacial repair and tested for flow properties, bond strength with both cement and host media, and material robustness.

The report organization is a s follows: Ch. 2 through Ch.5 covers chemical and mechanical testing related to understanding cementitious interfaces. Ch. 6 though Ch. 9 document the development of novel materials development for wellbore repair and/or other subsurface applications. Table 1-1 below documents the journal submissions directly funded by this project. Conclusions appear at the end of each section.

Table 1-1. Journal Articles Appearing as Sections in This Report

Title of Journal Article	Author	Organization	Journal	Year of Publication
Characterization of Chemo-mechanical Evolution of a Cement-Granite Interface	Joseph Mohagheghi	Materials Engineering Department, New Mexico Institute of Mining and Technology; Sandia	Still to be submitted	Not applicable
	Thomas Dewers	Sandia		
	Chaoyi Wang	Earth Atmospheric and Planetary Sciences, Purdue University		
	Laura Pyrak-Nolte	Earth Atmospheric and Planetary Sciences, Purdue University		
	Ed Matteo	Sandia		
Gas Flow through Cement-Casing Microannuli under Varying Stress Conditions	John C. Stormont	Department of Civil Engineering, University of New Mexico	*Journal of Geomechanics for Energy and the Environment*	2018
	Serafin Garcia Fernandez	Department of Civil Engineering, University of New Mexico		
	Mahmoud R. Taha	Department of Civil Engineering, University of New Mexico		
	Edward N. Matteo	Sandia		
Characterization of Wellbore Microannuli	Serafin Garcia Fernandez	Department of Civil Engineering, University of New Mexico	*Journal of Natural Gas Science and Engineering*	2019
	Edward N. Matteo	Sandia		
	Mahmoud Reda Taha	Department of Civil Engineering, University of New Mexico		
	John C. Stormont	Department of Civil Engineering, University of New Mexico		
Albany-PFLOTRAN Coupling	Timothy Fuller Carlos Jové-Colón Edward N. Matteo	Sandia	Still to be submitted	Not applicable
A New Polymer Nanocomposite Repair Material for	M. Genedy	Department of Civil Engineering, University of New Mexico	*International Journal of Greenhouse*	2017

Title of Journal Article	Author	Organization	Journal	Year of Publication
Restoring Wellbore Seal Integrity	U.F. Kandil	Egyptian Petroleum Research Institute	*Gas Control*	
	E. Matteo	Sandia		
	J Stormont	Department of Civil Engineering, University of New Mexico		
	M.M. Reda Taha	Department of Civil Engineering, University of New Mexico		
The Significance of Nanoparticles on Bond Strength of Polymer Concrete to Steel	A. Douba	Department of Civil Engineering, University of New Mexico	*International Journal of Adhesion and Adhesives*	2017
	M. Genedy	Department of Civil Engineering, University of New Mexico		
	E. Matteo	Sandia		
	U.F. Kandil	Polymer Nanocomposite Center, Egyptian Petroleum Research Institute		
	J Stormont	Department of Civil Engineering, University of New Mexico		
	M.M. Reda Taha	Department of Civil Engineering, University of New Mexico		
Nanomodified Methyl Methacrylate Polymer for Sealing of Microscale Defects in Wellbore Systems	Moneeb Genedy	Department of Civil Engineering, University of New Mexico	*ASCE Journal of Materials in Civil Engineering*	2019
	Edward Matteo	Sandia		
	Mike Stenko	Transpo Industries, Inc.		
	John Stormont	Department of Civil Engineering, University of New Mexico		
	Mahmoud Reda Taha	Department of Civil Engineering, University of New Mexico		
Engineering a Low Modulus Polymer-Modified Calcium-Silicate-Hydrate (C-S-H) Binder for Wellbore	J. Starr	Department of Civil, Construction & Environmental Engineering, University of New Mexico	Cement and Concrete Composites	In Review

Title of Journal Article	Author	Organization	Journal	Year of Publication
Applications	E.E. Soliman	Department of Civil, Construction & Environmental Engineering, University of New Mexico; Civil Engineering Department, Faculty of Engineering, Assiut University, Assiut, Egypt		
	E.N. Matteo	Sandia		
	T. Dewers	Sandia		
	J. Stormont	Department of Civil, Construction & Environmental Engineering, University of New Mexico, University of New Mexico		
	M.M. Reda Taha	Department of Civil, Construction & Environmental Engineering, University of New Mexico		

2. CHARACTERIZATION OF CHEMO-MECHANICAL EVOLUTION OF A CEMENT-GRANITE INTERFACE

2.1. Overview

A major leakage pathway in wellbore systems derives from interaction between cement and adjacent rock or well casing. These interactions arise from thermal, mechanical, hydrological, and chemical (THMC) processes during the lifetime of a wellbore, including cement emplacement, wellbore uses including injection and production, local deformation such associated with reservoir pressure changes, and post-closure aging. In this chapter we examine temporal and spatial modifications of a wellbore annulus following flow of acid solutions and show how ultrasonic methods can be used to detect such modifications. Controlled triaxial benchtop experiments, monitor real-time cement-granite interface degradation in situ by ultrasonic and chemical methods, and pre- and post-experiment using nanoindentation and microCT imaging. Full waveform analysis shows a decrease in microannuli interface wave speed indicating a reduction in specific stiffness following portlandite dissolution from the surrounding cement matrix, followed by an increase stiffness as the experiment progresses. The sensitivity of the interface wave to microannuli conditions make these modes a potential tool for the detection of interface alteration in wellbores. Tomographic images show detailed development of three-dimensional leaching patterns involving reaction fronts migrating from the interface as well as wormhole development within the interface. Results are being used to validate a THMC computational fluid dynamics/mechanics code using COMSOL Multiphysics^{TM}. Future plans call for using the validated coupled chemo-mechanical model specifically in analyzing the spatio-temporal evolution of other types of interface alteration including carbonation and sulfonation, and in general as a predictive tool for assessment of cement barrier integrity.

2.2. Introduction

Interest in wellbore integrity spans the oil and gas industries and includes recent concerns about geologic carbon storage (GCS; Carey et al. 2007; Crow et al. 2010; Jun et al. 2013; Kutchko et al. 2007). GCS involves injecting super critical carbon dioxide ($scCO_2$) into brine-bearing formations and depleted oil reservoirs, using wellbores as the injection pathway and as well as brine extraction for reservoir pressure management. A wellbore is constructed from first drilling a tubular hole in the ground, inserting the steel casing, flooding the casing with cement, and forcing the cement through the annulus of the casing in order to lock the casing in place. This process is repeated with depth with consecutively smaller and smaller drill bits, narrowing the size of the wellbore, until the desired depth for operation is achieved. We can simplify GCS scenarios to involve an overburden region, a caprock, and a reservoir, with all three possessing different requirements for wellbore integrity and different possibilities for wellbore leakage pathway development. The overburden region can include aquifers with drinking water resources that should be protected for future foreseeable use. The caprock seal layer (Matteo and Scherer 2012) prevents the buoyant $scCO_2$ and CO_2-acidified aqueous solutions from migrating to overlying aquifers and the earth's surface. The last region is the reservoir, which consists of porous rock materials where the CO_2 is stored. To interact with reservoirs, wellbores intersect the overlying two regions and as such create possibilities for leakage of CO_2 and any associated contaminants into overlying aquifers (Jun et al. 2013; Matteo and Scherer 2012; Shao et al. 2010; Kutchko et al. 2011; Shao et al. 2010; Allahverdi and Skvara 2000; Bullard et al. 2011; Duguid 2009; Scherer et al. 2005; Li et al. 2015).). This paper examines potential leakage pathway development associated with flow of acidified aqueous solutions in simulated cement-rock interfaces, or what is referred to as micro-annular regions, referring to the annular interfaces created by cement emplacement during wellbore engineering. Our purpose in this section is to examine in detail the evolution of a micro-annulus between Type G cement and Westerly granite subject to flow of acidic solutions. We limit our discussion to degradation or leaching of calcium that attends reaction with hydrochloric acid (HCl), and how this degradation could be monitored remotely via ultrasonic methods.

2.3. Background

2.3.1. Previous Studies of Cement Alteration Exposed to Acidic Conditions

Wellbore cement chemical alteration can be broadly placed into three classes including cement degradation or leaching, sulfonation (precipitation of gypsum and other sulfate minerals within the cement) and carbonation, or precipitation of calcite or other carbonate minerals within the cement (Jacques, 2009). Of these, both carbonation and degradation are relevant to GCS, and we review how $scCO_2$ and associated products affects Portland cement over time.

Degradation experiments involving cement interacting with CO_2, as both a supercritical phase and as a component dissolved in brine, generally involve small cores of cement with flow-through of a reactive fluid phase (Jun et al. 2013; Kutchko et al. 2007; Matteo and Scherer 2012; Kutchko et al. 2011; Shao et al. 2010; Allahverdi and Skvara 2000; Scherer et al. 2005). Overall, these studies show reaction is initially very fast and then quickly slows down as calcium is leached out, mainly from Portlandite ($Ca(OH)_2(s)$)dissolution, at advancing reacting fronts. This means that if the acid is contacting Portlandite, the reaction is very aggressive. However, after the initial quick and aggressive reaction, a layer of amorphous silica gel derived from calcium-silica hydrates (CSH) is residual that serves as a protective coating slowing overall reaction progress (Jun et al. 2013; Kutchko et al. 2007; Matteo and Scherer 2012; Kutchko et al. 2011; Shao et al. 2010; Allahverdi and Skvara 2000; Scherer et al. 2005).

Small-scale experimental studies can only reveal so much about the real-world cement acid reaction progression. There are two examples of large-scale and long term-exposure of acid to wellbore cement. The first is the study of a 55-year-old well at the SACROC field in west Texas, USA, that was exposed to carbon dioxide 22 years into its use (Carey et al. 2007) and the second is a study of a 30-year-old well exposed to carbon dioxide from the start of its life (Crow et al. 2010). In the Carey et al. study, CO2 migration along the cement-rock and cement-steel casing microannuli induced alteration in the cement that progressed inward into the cement as a reaction front, leaving behind reaction zones consistent with both degradation and carbonation of the cement. Both studies show that after initially corroding the cement at the microannulus interface, carbonation with calcium carbonate precipitation commences and spreads inward away from the locations of CO_2 ingress. Both authors agreed that as long as the wellbore was constructed carefully and up to code it would serve as an effective geological barrier against acidic brine migration (Carey et al. 2007; Crow et al. 2010; Jun et al. 2013; Kutchko et al. 2007; Matteo and Scherer 2012; Kutchko et al. 2011; Shao et al. 2010; Allahverdi and Skvara 2000; Scherer et al. 2005). The combination of both small- and large-scale studies have shown that cement does corrode, but with time the reaction front decreases with reaction products armoring or protecting unaltered cement from damage. Research has shown that corroding the entire mechanical barrier via acidification and calcium leaching by exposure to CO_2 could take geological time meaning several of thousands of years (Carey et al. 2007; Crow et al. 2010; Matteo and Scherer 2012).

To examine only effects associated with degradation or calcium leaching, in this study we examine the alteration of a cement-rock micro-annulus subject to hydrochloric acid attack. Figure 2-1 and chemical reactions listed in Equation 2-1, Equation 2-2, Equation 2-3, and Equation 2-4 show the proposed reaction progression between Portland cement and hydrochloric acid (Jun et al. 2013; Kutchko et al. 2007; Matteo and Scherer 2012; Shao et al. 2010; Allahverdi and Skvara 2000; Bullard et al. 2011; Li et al. 2015).

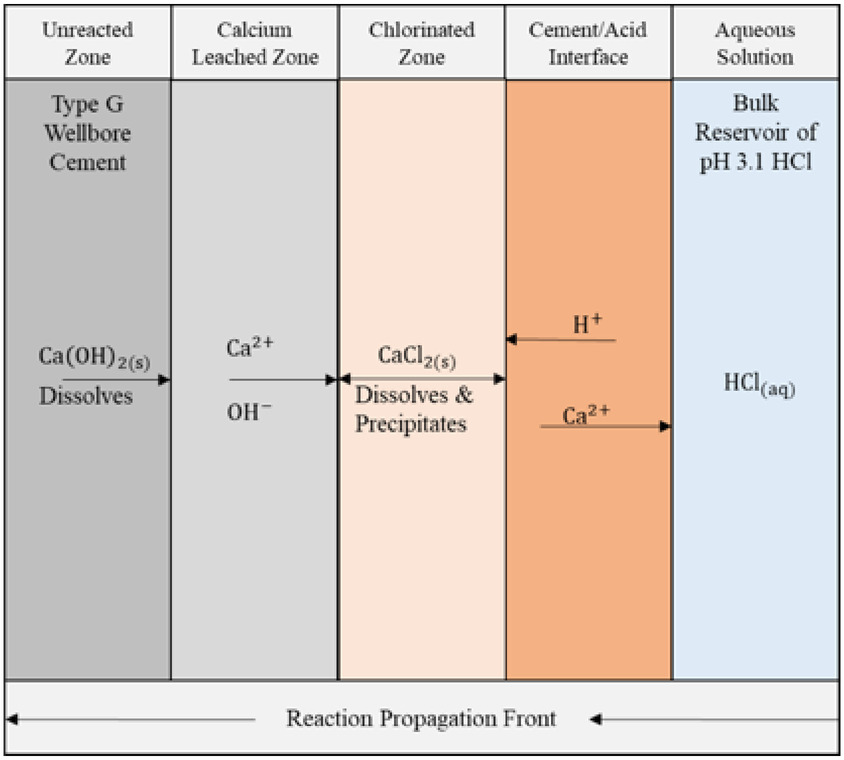

Figure 2-1. Proposed mechanism for the degradation of Portland cement in a HCl Environment

$$HCl \rightarrow H^+ + Cl^- \qquad \textit{Equation 2-1}$$

$$Ca^{2+} + HCl + OH^- \rightarrow CaCl_2 + H_2O \qquad \textit{Equation 2-2}$$

$$H^+ + CaCl_2 \rightarrow Ca^{2+} + HCl \qquad \textit{Equation 2-3}$$

$$CSH \rightarrow Ca^{2+} + OH^- + SiO_2 \qquad \textit{Equation 2-4}$$

In the presence of water, hydrochloric acid will self-dissociate into its hydrogen and chlorine atoms (Equation 2-1). Cement, largely being an alkaline material, is extremely susceptible to corrosive attacks from acidic solutions. At the cement-surface-reservoir interface, free hydrogen atoms will initiate a reaction propagation front with the calcium hydroxide within the Portland cement. This acidic attack will cause the calcium hydroxide in the Portland cement to dissociate into its calcium and hydroxide atoms (Equation 2-2). The free calcium then bonds with the free chlorine atoms forming the highly soluble compound, calcium chloride (Equation 2-2).

The solid precipitant of calcium chlorine reacts with free hydrogen atoms, further dissociating into free calcium and chlorine (Equation 2-3). This reaction causes an orange calcium leached layer to form cement surface. Eventually, Calcium Silica Hydrate in the Portland cement (CSH) will degrade leaving behind a residual silica gel layer (Equation 2-4). After the calcium is leached from the surface, the amorphous silica gel has been shown to act as a temporary barrier against further corrosion from the acid (Carey et al. 2007; Crow et al. 2010; Kutchko et al. 2007; Kutchko et al. 2011).

2.3.2. Ultrasonic Applications

Ultrasonic testing of materials uses high frequency elastic waves for imaging, detection of flaws, and to characterize properties of materials through which they propagate. For this study we are interested in monitoring changes in material properties at a micro-annuls existing between cement and other materials as the cement degrades. As such, this involves both changes in so-called body waves (waves that propagate through the material volume), and surface (or guided) waves, that propagate along interfaces or along surfaces. Material elastic properties such as the bulk modulus, shear modulus, and the hardness of the cement can all be monitored by how the ultrasonic p (primary) and s (shear) waves change over time. Monitoring the degradation of cement will provide initial estimates of how much structural integrity the cement loses and how fast the cement will corrode, making this technique an effective way of monitoring wellbore integrity. P and S waves are body waves, meaing they travel through the body of a medium. These waves can be used to determine shear and bulk moduli, or alternatively Young's modulus, and Poisson's ratio, of a material. The following equations are used to calculate the material properties by determining the wave speed , or velocity, of wave propagation.

- laboratory measurements
  - density of the cement (ρ in kg/m^3)
  - length of cement sample (L in m)
  - arrival time of the primary waves (p in seconds)
  - arrival time of the secondary waves (s in seconds)

- primary and secondary velocities

$$primary\ velocity\left(\frac{m}{sec}\right) = V_p = \frac{L\,(m)}{s(sec)} \qquad \text{Equation 2-5}$$

$$secondary\ velocity\left(\frac{m}{sec}\right) = V_s = \frac{L\,(m)}{s(sec)} \qquad \text{Equation 2-6}$$

- shear modulus

$$shear\ modulus\left(\frac{kg}{msec^2}\right) = \mu\ (\text{Pa}) = (\rho)(V_s)^2 \qquad \text{Equation 2-7}$$

- bulk modulus

$$bulk\ modulus\left(\frac{kg}{msec^2}\right) = \mathrm{K\ (Pa)} = (V_p)^2(\rho) - \mu\frac{4}{3} \qquad \textit{Equation 2-8}$$

- Young’s modulus

$$Young's\ modulus\left(\frac{kg}{msec^2}\right) = \mathrm{E\ (Pa)} = \frac{9K\mu}{3K + \mu} \qquad \textit{Equation 2-9}$$

- Poisson's ratio

$$Poisson's\ ratio\left(\frac{Pa}{Pa}\right) = \nu = \frac{3K - 2\mu}{2(3K + \mu)} \qquad \textit{Equation 2-10}$$

Ultrasonic monitoring is a common practice in non-destructive detection of corrosion in steel pipelines and monitoring fracture propagation in bridges and roads, for example. The ultrasonic testing process works by either a pulse-receiver or pulse-echo method, whereby ultrasonic waves traveling through a material are attenuated and/or reflected back by changes in material properties such as attend degradation or by the presence of flaws or are transmitted through the material and received by a separate transducer (Zhen et al. 2017).

2.4 METHODS

2.4.1 Sample Fabrication

Type G cement samples were prepared from cement powder provided by Professor Mahmoud Taha from the University of New Mexico. There were several steps taken to ensure that the cement cores used in these experiments were made with precision and integrity. The first step to this process was safety. Powdered cement was handled exclusively with in a Labconco Precise® HEPA-Filtered Glove Box to ensure operator safety. In order to make a homogenous batch of cement, the American Petroleum Institute Recommended Practice 10B was used as a guideline for making of Type G Wellbore Cement. This guideline defines Type G cement slurries as "100 parts dry cement by weight to 44 parts mixing water by weight" or 2.27 parts cement to every one-part water. Using the ratio defined by the API guidelines, the cement and water was added to the mixing device inside the glove box. After being taken out of the glove box, the slurry was mixed at a rate of four rotations per second for one minute using a KitchenAid™ mixer. The consistency of the slurry was checked and then mixed for another minute at eight rotations per second. A 3D printed mold held four PTFE tubes (three and a half inches long with an inner diameter of one inch) at a 90° angle. The slurry was then poured into the PTFE tubes and placed onto a vibration table and vibrated at 60 Hz for 15 minutes to get rid of any void spaces in the cement slurry. After vibration the cement molds were allowed to dry for 24 hours before being cut out of their PTFE molds. The cement cores were then placed into a room temperature water bath to cure for 28 days under 100% humidity conditions to reach 97% ultimate compression strength. After the cores cured, they were dried for 24 hours and cut down into 2-in.-long cores.

A core of 1" diameter Westerly Granite supplied by the Geomechanics Department at Sandia was sectioned into several 2" length cores. Both the two-inch cores of cement and westerly granite were sectioned in half horizontally to make half cylinders of both materials using a diamond saw. Once the cement and granite halves where cut, the two equal halves were matched and held together in place by Teflon tape. A small mismatch in the diameters of the two cores was ameliorated by applying a small dab of epoxy to the sides of the cement/granite sample. This was to prevent fluid flow from localizing along the mismatched surface. Once this was done, the sample was ready to be inserted into a cylindrical viton which served to separate the confining fluid (used to impose a confining pressure on the sample) from the solutions within the sample pore space.

2.4.2 Triaxial Core Holder Set Up

A CoreLabs Model HCHT 10,000 psi triaxial coreholder is used to place the vessel under stress, pressure, and temperature conditions and allows transmission of ultrasonic waves across a 1"diameter by 2" in length sample as well as pore pressure control and pore fluid metering (Figure 2-2). The rock/cement core sample is held within a viton rubber sleeve by confining and/or radial pressure, with the radial pressure simulating overburden pressures and the axial pressure simulating maximum principle compressive stress. All wetted parts exposed to rock core are composed of either Hastelloy C276 or titanium for corrosion resistance when exposed to chloride solutions. For this series of experiments, two Teledyne-ISCO™ 100DX high pressure pumps are used for pressure control of the axial and confining fluid lines. An ELDEX™ Optos pump (not shown in the schematic) is used to meter fluid into the sample at low flow rates via the upstream fluid port, whereas the downstream fluid port is connected to a nalgene reservoir for fluid collection. Two Omega™ pressure transducers are connected to the upstream fluid pressure ports and the confining pressure plumbing, used to monitor pressure via a data acquisition system. All components are rated to a maximum allowable working temperature of 150°C or higher. A port on the coreholder vessel is fitted with an Inconel sheathed thermocouple which is wired to the DAS. A separate thermocouple is attached to the surface, used along with an Omega heater controller to power two Omega silicon sheet heaters wrapped around the coreholder.

The aqueous HCl solution is pumped into the cement/granite microannulus at a rate of .4 mL per minute using the Optos pump and PEEK tubing (with Hastelloy fittings for attaching to the Coreholder upstream pore fluid port). Pore solutions are metered at a constant rate, and conductivity is determined from knowledge of the flow rate, upstream and downstream pressures, and fluid viscosity. On the way to the waste collection bin, the effluent solution passes through an inline pH probe measuring the pH of the solution as it reacts with the surface of the cement. Each of these individual components is electronically wired to a data collector where the outputs of each component are stored internally as a voltage. At the end of the experiment, all of the voltage data was collected and converted into meaningful measurements by using their respective calibration data. In this experiment, we use an axial pressure of 16.8 MPa, a confining pressure of 13.3 MPa, and a temperature of 65.6 degrees Celsius to replicate real world wellbore conditions.

In addition to the before and after comparison of the flow through experiment, a falling head permeability test is done by displacing an isopropyl alcohol solution through the cement. This composition was used so as not to react within the phases lining the microannulus. The following equation is used to calculate hydraulic conductivity from the falling head data (Fetter 2014):

$$K = \left(\frac{d^2}{D^2}\right)\left(\frac{L}{t}\right)\left(ln\left(\frac{h_o}{h}\right)\right) \qquad \textit{Equation 2-11}$$

where K is the hydraulic conductivity and L is the length of the cement sample. h_o is the initial head in the falling tube, h is the final head in the falling tube, t is the time it takes to go from h_o to h, d is the inside diameter of the falling head tube, and D is the diameter of the cement/granite sample.

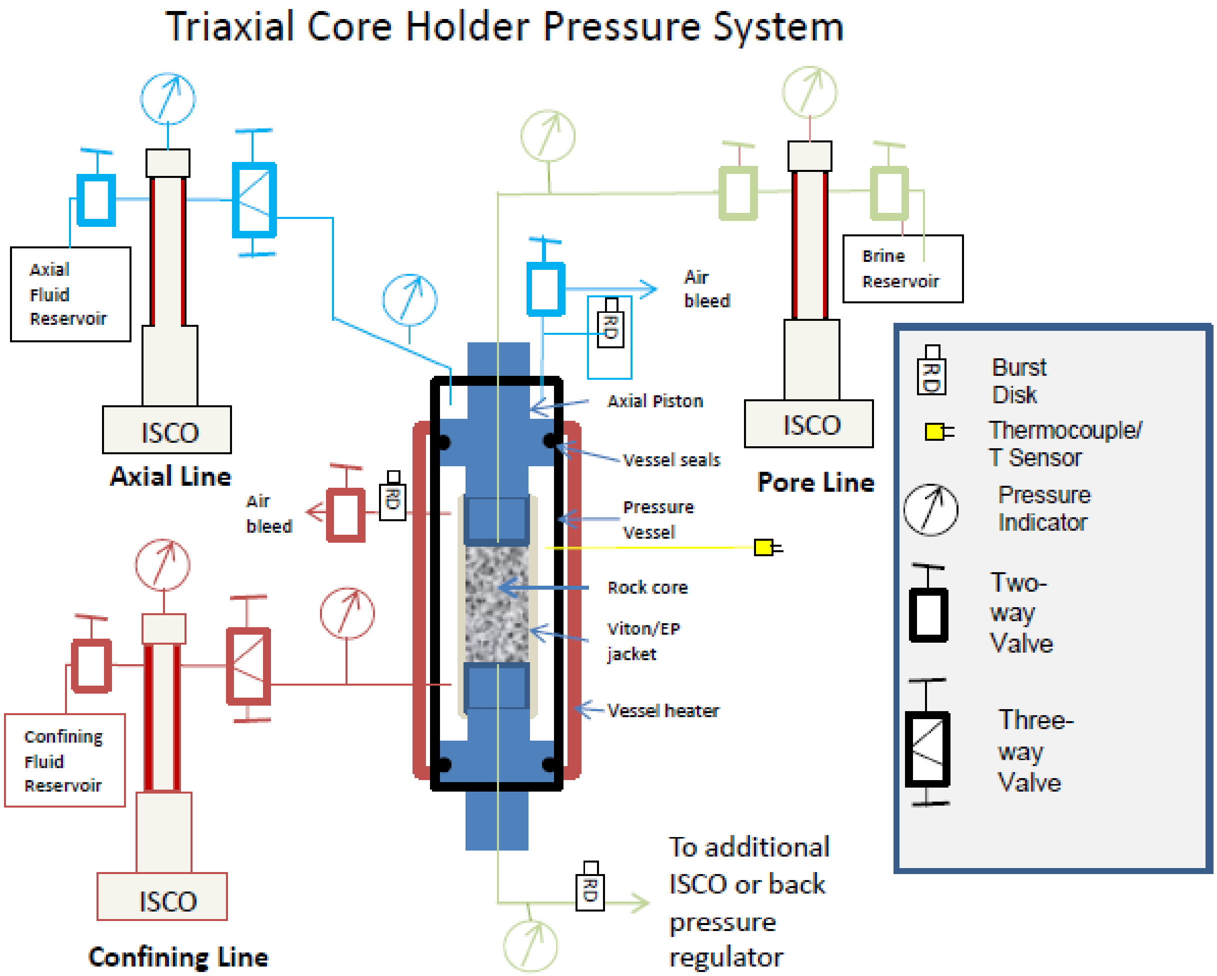

Figure 2-2. Schematic representation of the flow system piping and core holder used in the experimental design.

2.4.3 *Physical Measurements*

2.4.3.1 Acoustics

One goal of this section is to correlate the chemical-material degradation of cement micro-annulus to a measurable change in the response of a secondary surface waveform. We investigate this by using the pulsing and receiving acoustics transducers within the Corelabs core holder. The acoustic crystals sit on either end of the axial piston, which is composed of titanium. After confirming with CoreLabs^{TM} we established the crystal layout in Figure 2-3. Additionally, the acoustic crystals sit 1.63 inches from cement-granite interfaces, transmitting and receiving energy through the upstream titanium end piece, through the cement-granite sample both as body and surface waves, and then through the titanium downstream end-piece to the receiving transducer.

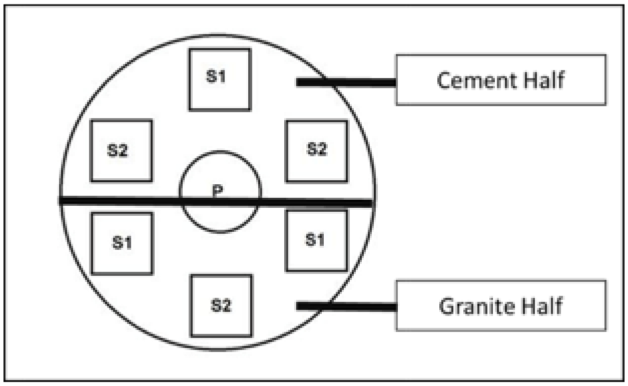

Figure 2-3. Location of the P, S1, and S2 Crystals and the location of the cement and granite

With the layout of the crystals, orientation of the cement-granite core, and distance between the interfaces known, we used a stand-along Olympus acoustic pulser-receiver to calibrating the acoustic signals against a known aluminum cylinder standard. Additionally, the acoustics of the westerly granite and the cement were taken independently to measure their primary and secondary velocities. After verifying the primary and secondary velocities of the system, the cement-granite sample was loaded into the Tri Axial Core Holder, raised to the desired experimental conditions, removed from the vessel for imaging (described below) and then reloaded into the vessel for the flow-through experiment. During the course of the experiment the compressional, shear, and polarized shear waveforms were be captured and recorded using a pulsing frequency of 1500KHz frequency.

2.4.4 Solution Chemistry

An HCl solution was prepared to pH 3 using reagent grade HCl supplied by Alpha-Aesar and Millipore deionized water. Once the solution is reacted with the sample, it is directed to an in line pH probe which was connected to the system DAS. Periodically samples were taken for Ca and Si analysis with inductively couple plasma-optical emission spectrophotometry.

2.4.5 Imaging and Modeling

2.4.5.1 X-ray μCT Imaging and Analysis

X-ray micro-computed tomography (X-ray μCT) imaging was performed on the cement-granite samples using a Zeiss Xradia 520 Versa 3D X-ray microscope. This microscope combines geometric and optical magnification to produce tomographic reconstructions of sample core. This method provided tomographic reconstructions in the form of stacks of registered tiff images with a voxel size of 65e3 μm^3 (40.3 μm × 40.3 μm × 40.3 μm). Image analysis of the reconstructed image sets utilized FIJI^{TM} software (Schindelin et al. 2012) to perform a cylindrical crop which provided clean right-circular cylindrical boundaries, and to equalize grey levels via a histogram-matching algorithm. The modified image stacks were then examined via the Thermo PERGEOS^{TM} v1.7 software. A median filter algorithm applied to the image stacks improved delineation of phase boundaries. A segmentation algorithm was then applied to determine, label, and extract STL surfaces for export to a computational fluid dynamics software.

2.4.5.2 Computational Fluid Dynamics (CFD) Modeling

Computational fluid dynamics involves solving equations or motion, or Navier-Stokes equations, using finite element methods (FEM). While we do not present results at this time, on-going work involves utilizing the imaged before- and after micro-annuli and using the falling head hydraulic conductivity measurements to validate the modeling. These results were presented at the American Geophysical Union Conference in December, 2018, utilizing the FEM code COMSOL Multiphysics^{TM}. A parallel effort involves using COMSOL to model elastic compression of the microannuli, and comparing CFD results to hydraulic conductivity measurements utilizing pressure and flow rate measurements during the flow-through experiments. The experimental results will be used to validate the compression numerical experiments. COMSOL also allows the modeling of elastic wave propagation, and we are considering using this capability to compare to ultrasonic measurements presented later in this section. Linking the guided wave speed attenuation to the chemical alteration/measured changes in elastic moduli via coupled modeling would be an ideal approach to advancing use of guided waves to assess presence and degradation of microannuli for wellbore integrity.

Finally, we are applying a new coupled modeling approach advanced by the consulting company AMPHOS21 (2018; Nardi et al., 2014) that combines the Multiphysics capability of COMSOL with the chemical modeling capability of PHREEQC (a USGS code developed by D. Parkhurst and others; Parkhurst and Appelo, 1999), applying a THMC modeling approach to micro-annuli degradation. A new chemical database for cement/concrete was released earlier this year that has been adopted into the PHREEQC code formatting (Lothenbach et al., 2019). We have applied this coupled modeling approach to the calcium leaching observed within the micro-annuli in our experiments, and a two-dimensional approach has shown promising results.

2.5 Results

2.5.1 Imaging Results from Tests 1 and 2

μCT imaging results of micro-annuli degradation for the Test 1 and Test 2 experiments are shown in Figures 2-4 through 2-6. Figure 2-4 shows the "before" (Fig. 2-4A and C) and "after" (Fig. 2-4B and D) tomographic reconstructions for the Test 1 and Test 2. The labels 'C' and 'G' refer to cement and granite constituents; in particular the cement phases are recognizable by the large black dots, which are air bubbles in the cement, while the granite is delineated by the white dots which are iron oxide phases. The dark shaded portions are the micro-annuli, and it is observed that the "after" results show quasi-linear traces of heightened void space (shown by the dark shading) that emanate from the inlet (in Figure 2-4B, this is at the bottom of the sample, while in 2-4D, it is at the top). The plane of the imaging intersects the approximate plane of the micro-annuli, and thus the intersection shows as a broad shaded patch in the images. The leaching of cement by the HCl has led to the development of so-called "wormholes", an example of flow-self focusing. It is evident that initial scratches on the surfaces of the cement from saw preparation have been used to initiate the wormhole localization. In Test 2, the worm hole initiation occurs near the inlet but advances to the edge of the sample, taking advantage of the initial mismatch between the granite and cement half-cylinders.

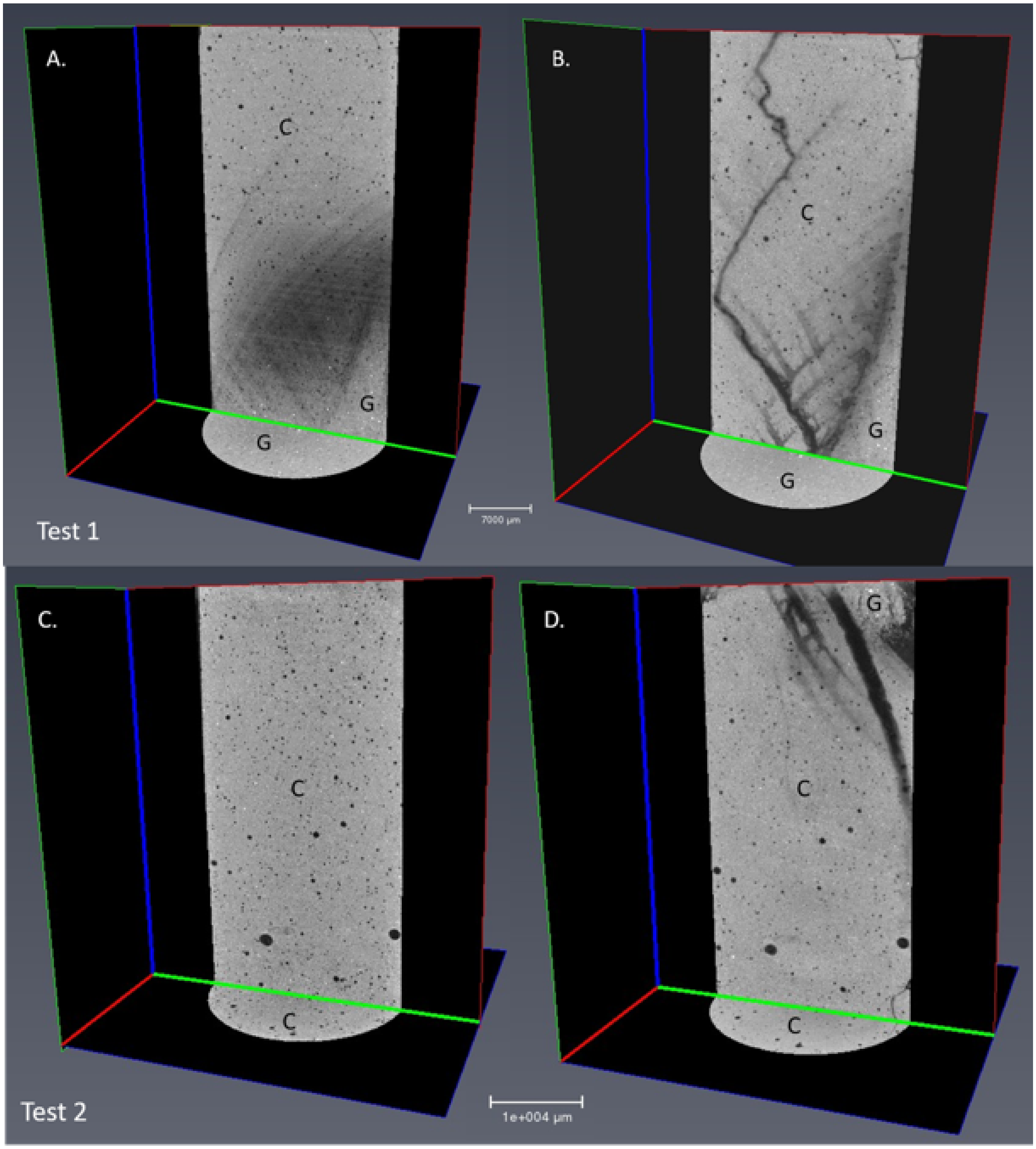

Figure 2-4. µCT imaging of micro-annuli degradation in Test 1 and Test 2. The HCl leaching of cement phases has led to the development of localized pathways, or so-called 'wormholes'.

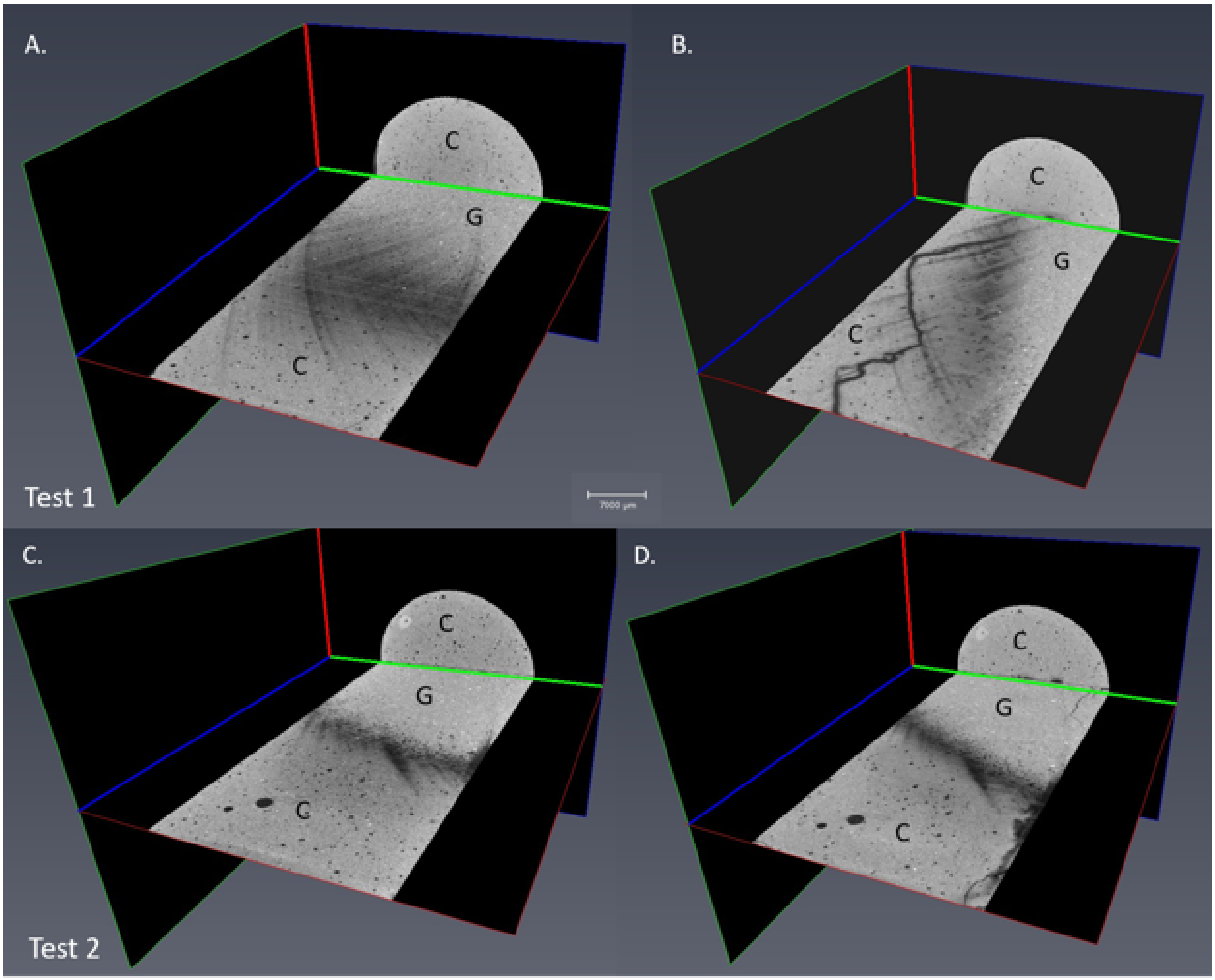

Figure 2-5. μCT imaging of micro-annuli degradation in Test 1 and Test 2.

Figure 2-5 shows the differences between the "before" (left side of figures) and "after" (right side of figures) cement-granite samples from an alternative perspective from Figure 2-4. For these images, the sample inlet is away from the viewer and the outlet is near the viewer. The position of the interface is approximated by the position of the green line, and as is particularly evident for Test 2, the degradation is evident not only in the form of dissolved cave-like pathways, but also as grey solid regions likely signifying the leaching of portlandite leaving behind residual CSH phases.

Figure 2-6 shows segmented μCT images of the connected pore space within the micro-annuli, as 'before' and 'after" images for Test 1 and Test 2. A widening of the entire micro-annulus, as well as the localized wormholes, are evident by comparison of the 'before' and 'after' images. Although it is observed here only in patches, such as the lower right near-corner of the Test 1 'after' image, we observe regions where the micro-annulus has closed, shown by the absence of blue void space in the segmented volume. We believe that these regions are locations of heightened creep closure of the micro-annuli, accelerated by the degradation. While not discussed further here, the image sets also show micro-fracturing localization in regions associated with the degradation, suggesting a large degree of mechanical-chemical coupling during the micro-annuli evolution.

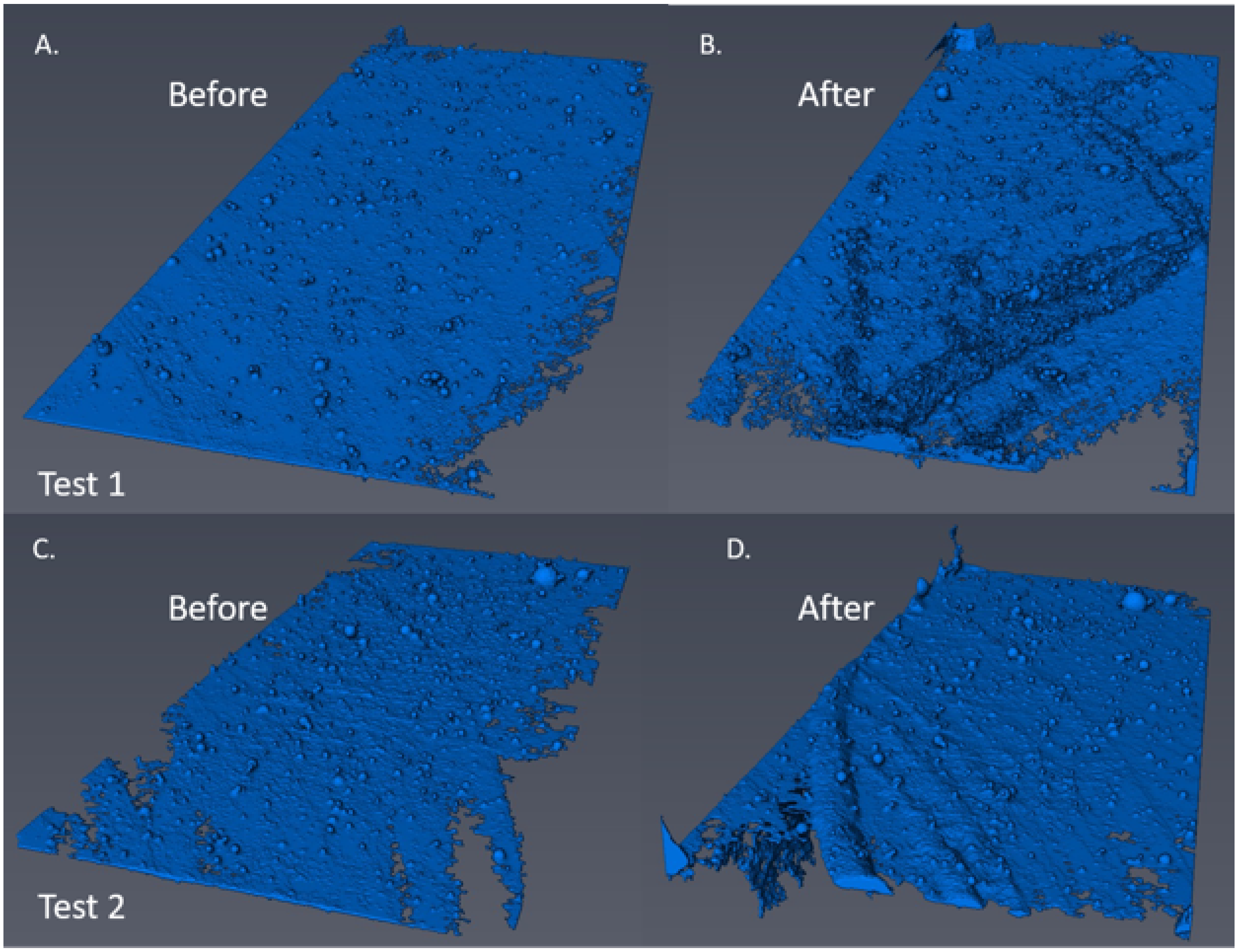

Figure 2-6. Segmented regions of void volume associated with the micro-annuli evolution in Test 1 and Test 2. Comparison of the 'before' and 'after" image sets show enlargement of void space associated with localized leaching, but also closure (absence of voidage) of the microannuli, particularly near the inlet.

2.5.2 Evolution of Effluent Chemistry in Tests 1 and 2

The pH and calcium and silicon concentration were monitored the duration of Test 2. The results from the chemical analysis are in line with the cement-acid chemical reaction results from other studies. The pH quickly spiked upwards from 3.1 to 7 as the acid started to react with the cement. The pH reached a peak of 8 about 90 hours into the experiment and then dropped to a resting pH of about 3.5 over the next 110 hours of the experiment. This data is extremely significant because it gives insight to when the reaction transitioned from a fast surface-controlled reaction to a slower diffusion based reaction. Over the first 120 hours of the experiment, the acidic solution reacted heavily with the cement, creating a preferential pathway through the cement-granite interface. The drop in calcium being leached out signals that a layer of less reactive amorphous silica gel has been formed in the preferential channel. While the amorphous silica gel is still reactive it is much less so than the cement which is suggested by the monitoring of the effluent solution chemistry.

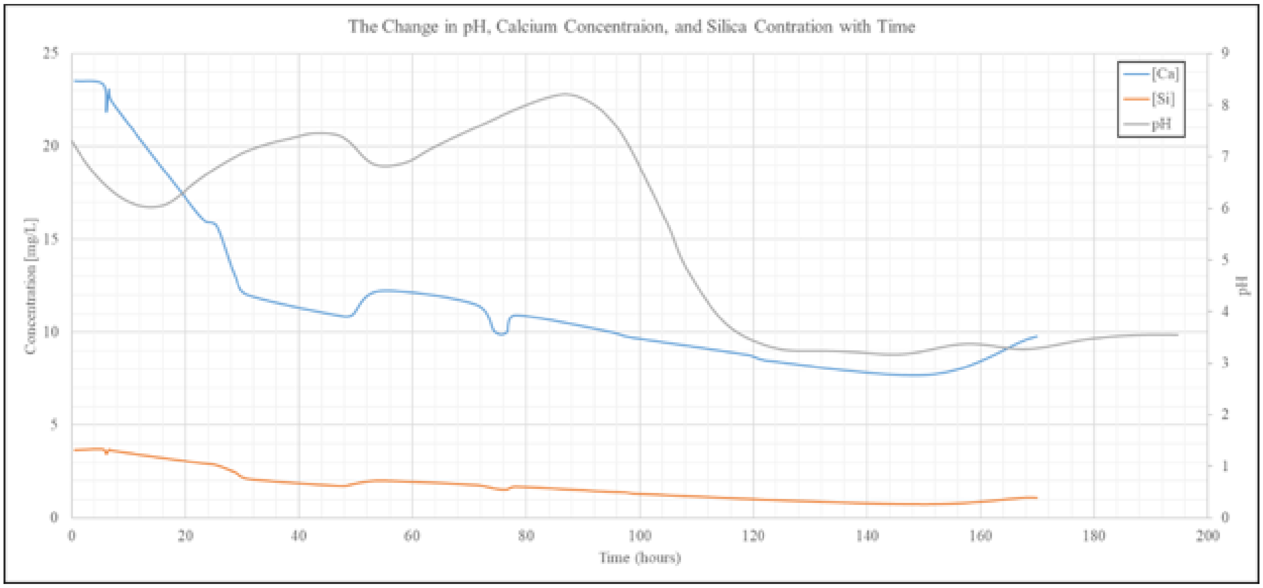

Figure 2-7. The effluent out calcium and silicon concentration compared against with the change in pH.

Not only does the chemical data give us insight to how quickly the reaction reaches steady state. It also gives us confidence that a quantifiable change happened in the cement over time as seen in calcium being continuously leached out from the cement throughout the experiment. This will help correlate a change in the acoustic waveforms to a chemical change taking place in system, examined in the next section.

2.5.3 Changes in Acoustic Response in Test 2

The Test 2 experiment was used to monitor the evolution of acoustic waves associated with the degradation of the micro-annuli. Figures 2-8 – 2-10 shows the measurements over 8 days.

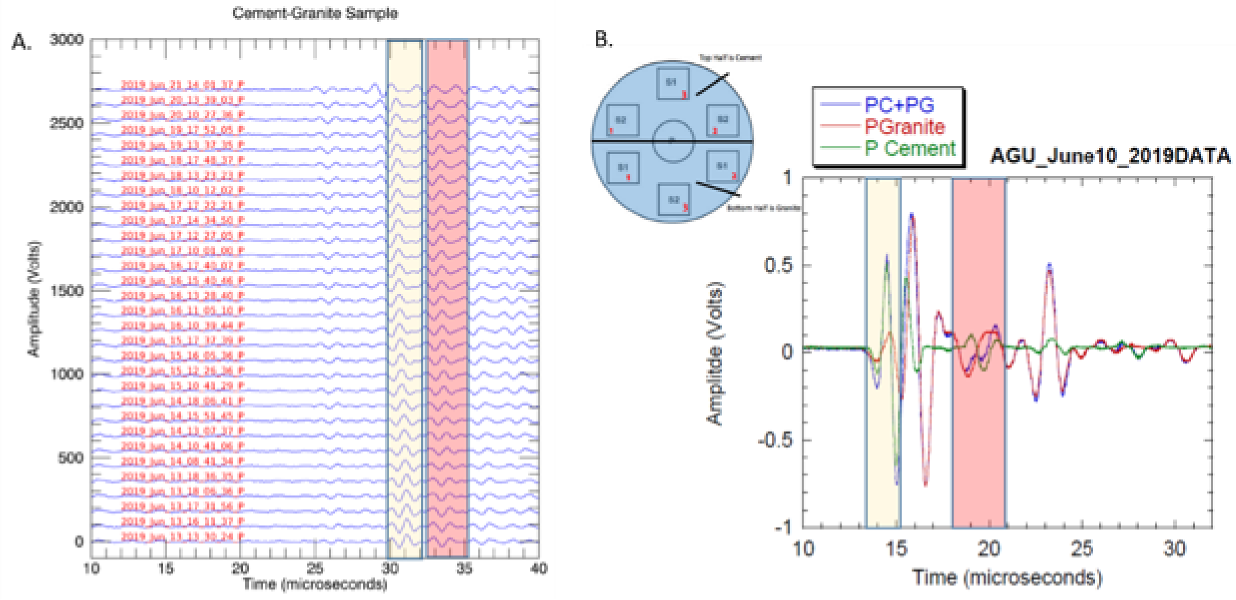

Figure 2-8. P-wave data during 8 days of Test 2 showing small measured changes associated with micro-annuli degradation.

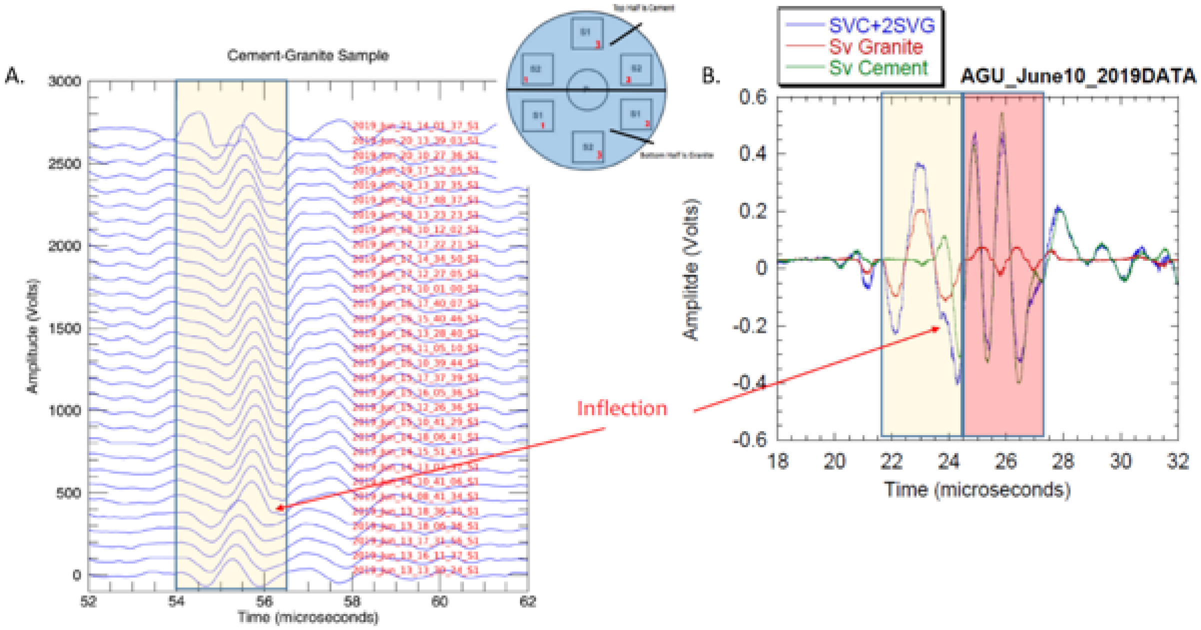

Figure 2-9. S1-wave data during 8 days of Test 2 showing small measured changes associated with micro-annuli degradation.

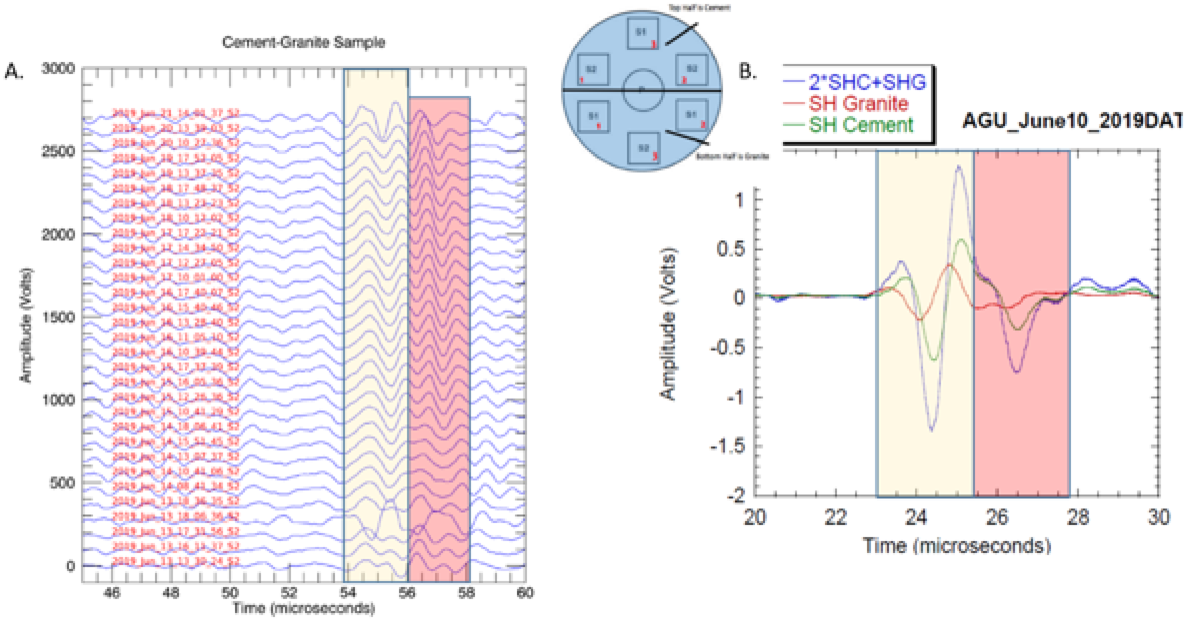

Figure 2-10. S2- wave data during 8 days of Test 2 showing small measured changes associated with micro-annuli degradation.

Interpretation of the full waveforms were conducted by Professor Laura Pyrak-Nolte and Dr. Chaoyi Wang of Purdue University and they contributed to the text in this paragraph. In Figure 2-8, the first arriving P wave appears to be associated with the cement (yellow region in the figure), and the second arrival (rose region) also is consistent with measured responses from solid cement samples. The plots on the right are from measurements taken outside the core holder system by Pyrak-Nolte. In Figure 2-9, the yellow region is consistent with the Rayleigh phases (the interface or guided waves through the cement-granite micro-annuli in the compressed system) for granite measured outside the core-holder system shown on the right. The first arriving S1 is dominated by the granite system until the fifth waveform (shown by red arrow), showing an inflection which might indicate a coupling between the two surfaces of cement and granite in the compressed state. The rose region in the figure to the right, taken for the uncompressed micro-annuli measured outside the core-holder system, indicates a waveform only present in the uncompressed system and was not observed for the Test 2 sample under compression. For the polarized S2 waveforms plotted in Figure 2-10, the yellow demarcated region can be either granite, cement, or a combination of both. The rose region is consistent with wave components from the cement phases. A closer examination of the rose region shows that the signal here widens with time for the Test 2 results, and thus is perhaps an indicator of the associated degradation.

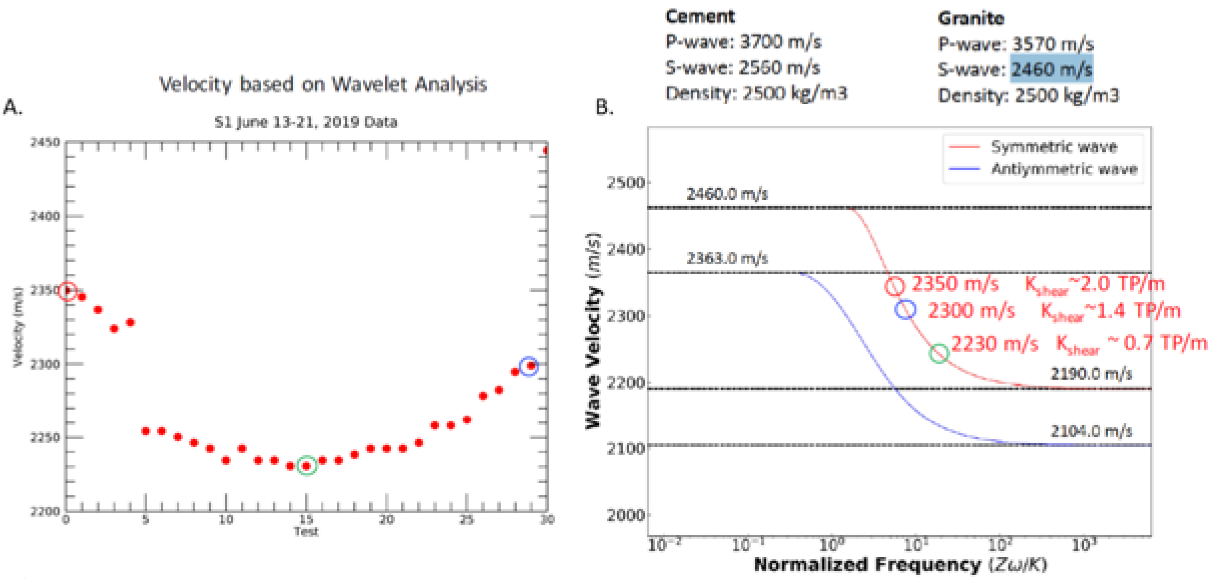

Figure 2-11. S2- wave data during 8 days of Test 2 showing small measured changes associated with micro-annuli degradation.

Figure 2-11 plots interface wave speeds calculated by Dr. Wang. These are based on the P- and S-arrival times measured outside the core-holder system for cement and granite separately, assuming a density of 2500 kg/m^3 for both cement and granite. During the course of Test 2, the interface wave velocity is observed to greatly decrease in the first three days of the test, but then shows a slight recovery. These results suggest that an ultrasonic interface wave can be measured for the micro-annuli in this system, and shows attenuation associated with the cement leaching that occurred most strongly during the first three days of Test 2, consistent with the chemical results. The remaining portion of Test 2, which showed a lessened degradation evident from the chemistry, probably shows a creep consolidation of portions of the micro-annuli interfacial region (consistent with the imaging results) that results in the slight speed-up of interfacial waves.

2.6 Conclusions

Two cement leaching tests were conducted in a pressurized core-holder at 70^{o}C and roughly 2000 psi confining pressure. HCl solutions with initial pH of 3 were flowed though a cement-granite micro-annulus over the course of 8 days (Test 2) and 10 days (Test 1). μCT imaging of the 'before" and 'after" cores show that the micro-annulus experiences widening, and in particular a flow-self-focusing (much like in the development of caves in limestone), leading to the development of a localized channel flow. This serves to lessen the degradation rate over the whole surface area of the micro-annuli, but greatly increases the hydraulic conductivity of the micro-annuli region. Cement leaching results in this void creation, but also leaves behind a residual CSH and/or silica gel region, that also armors the unaltered cement from contact with the bulk HCl reactive solution and slows the overall rate of degradation. Ultrasonic measurements taken during the cement degradation in Test 2 show a slight attenuation in body waves during the course of the test, but also show propagation of an interfacial wave that we believe could be useful in monitoring wellbore micro-annuli evolution. The interface wave velocity shows an attenuation associated with the leaching, abut also shows a slight recovery that is believed to be associated with creep closure of the micro-annuli during the later stages of the Test 2 following the bulk of the degradation. Together with observed zones of micro-fracturing that occur syn- or post-leaching, these results show that the evolution of a cement-rock micro-annulus is a coupled chemical and mechanical phenomena. Near-future measurements are begin taken, including SEM-EDS and micro-indentation of altered and unaltered zones, that will augment the data set presented here.

Current work associated with this experimental and imaging project are parallel modeling studies examining the chemical, mechanical, and acoustic evolution of the micro-annulus, and the data set presented here will be used in a validation exercise for the models.

2.7 Acknowledgements

The interface wave analysis by CW & LJPN was based upon work supported by the U.S. Department of Energy, Office of Energy Efficiency and Renewable Energy (EERE), Office of Technology Development, Geothermal Technologies Office.

3. GAS FLOW THROUGH CEMENT-CASING MICROANNULI UNDER VARYING STRESS CONDITIONS

3.1. Overview

The cement-casing interface, or microannulus, has been identified as a common pathway within wellbores for leakage of fluids yet little is known about its size or character. We conducted laboratory measurements of gas flow through microannuli under varying confining, casing and pore pressures to provide insight into how microannuli respond to a range of stress conditions. Wellbore specimens consisting of a cement sheath cast on steel casing were produced with microannuli between the steel casing and the cement. Gas flow through these specimens was measured under varying confining, casing and pore pressures. After accounting for nonlinear flow, we interpreted the measured gas flow as providing the effective wellbore permeability from which the hydraulic aperture of the microannulus was calculated using the cubic law. Results are presented as hydraulic aperture as a function of confining, casing and pore pressure for wellbore specimens with different microannuli. We found that microannuli are fracture-like in how they deform in response to stress changes. Even when loaded to large external pressures, microannuli remain open and capable of conveying significant flow. The microannuli response was less sensitive to casing pressure changes compared to confining pressure. We also demonstrated that the hydraulic aperture of the microannulus is sensitive to temperature changes within the casing. We made measurements of the actual (mechanical) aperture around the entire circumference after injecting epoxy into a microannulus and sectioning the specimen. These results indicate that the microannulus is not a uniform annular gap but is highly variable around the circumference. In addition to testing specimens with discrete microannuli, we also found that specimens with corroded casing were many orders of magnitude more permeable than intact specimens presumably due to flow through the corrosion product.

3.2. Introduction

The integrity of wellbore systems—consisting of the wellhead, casing, cement sheath and adjacent rock formation—is of critical importance to many subsurface operations including CO_2 sequestration (Zhang and Bachu 2011), oil and gas exploration and production (Davies et al. 2014), geothermal energy development (Shadravan et al. 2015), and fluid storage (Miyazaki 2009). As a wellbore is being advanced, drilling operations are periodically stopped and steel casing is placed in the wellbore and cemented in place. Cement slurry is pumped down the casing and up into the annular space behind the casing, displacing the drilling fluid and creating a cement sheath intended to fully fill the annular space. The principal function of the cement is to seal the annular space between the host rock and casing, thereby impeding fluid communication between the different strata penetrated by the wellbore. In addition, wellbore cement protects the casing from corrosion and provides structural support for the casing. Although intact wellbore cement has low permeability[1] (typically $<10^{-17}$ m^2; Nogues et al. 2011), the effective permeability of the wellbore system can be dramatically increased by the presence of various flaws, including poor cement-formation and cement-casing bonds, fractures within the cement, and channels from poorly emplaced cement (Bonett and Pafitis 1996; Gasda et al. 2004; Viswanathan et al. 2008; Dusseault et al. 2014; Watson and Bachu 2008). Effective wellbore permeabilities interpreted from gas leakage and pressure build-up records (Kang et al. 2015; Checkai et al. 2013) or from specialized wellbore

---

[1] Permeabilities are given here with units of m^2; to convert to units of Darcy multiply by 1.013×10^{12}.

permeability measurements (Crow et al. 2010; Gasda et al. 2013) range from $<10^{-18}$ m^2 to 10^{-12} m^2 (Kang et al. 2015; Checkai et al. 2013; Crow et al. 2009; Gasda et al. 2013), indicating that flaws can dominate the permeability of a wellbore system. Estimates of the frequency and impact of leaky wellbores can vary widely depending on the type and age of the wells considered as well as the data used and assumptions underlying these estimates (Davies et al. 2014; King and King 2013; Ingraffea et al. 2014; Vidic et al. 2013; Jackson 2014). Regardless of the exact number of wells that are affected, the common occurrence of gas present in the cemented annulus at the surface of many oil and gas wells highlights that gas flow through cemented wellbores is a widespread issue that requires more understanding (Dusseault et al. 2000; Rusch et al. 2004).

The environmental and economic consequences of leaky wellbores are large. Wellbore integrity is considered to be the greatest environmental risk factor for hydrofracturing and other nonconventional energy extraction (Jackson 2014). In gas wells, wellbore leakage can lead to methane migration into groundwater supplies and/or to the surface (Ingraffea et al. 2014; Vidic et al. 2013) where it is an explosive hazard and a powerful greenhouse gas in the atmosphere. Wellbore integrity issues can be severe enough to require expensive well remediation (Rusch et al. 2004) or even force abandonment of the well (Rocha-Valadez et al. 2014). Gas pressure behind casing can become great enough to fail the casing, and result in catastrophic well failure (Bourgoyne et al. 1999). Loss of wellbore integrity in geothermal wells can result in lost production and catastrophic well failure with associated risks from high pressure water or steam (Southon 2005).

The cement-casing interface, herein referred to as the microannulus, has been identified as a common wellbore leakage pathway (Zhang and Bachu 2011; Gasda et al. 2004; Dusseault et al. 2014; Duguid et al. 2013). Sonic logging within wellbores often detects the presence of microannuli at the casing-cement interface (Brufatto et al. 2003; Bellabarba et al. 2008; DeBruiin et al. 2009). Microannuli can be formed from thermal stresses from cement hydration or wellbore operations, or from mechanical stresses which arise from fluid pressure changes within the casing due wellbore operations (Bonett and Pafitis 1996). An additional mechanism may be fluid (pore) pressures sufficient to de-bond the cement from the casing (Lecampion et al. 2013; Feng et al. 2017). Conditions that produce microannuli have been evaluated in laboratory investigations that used test systems consisting of a central casing surrounded by cement (Boukhelifa et al. 2004; Jackson and Murphey 1993; Goodwin and Crook 1992). Conditions related to various wellbore operations were simulated by changing casing pressures or temperatures, and microannuli formation was detected by measuring flow along the wellbore axis. A principal conclusion from these studies was that large stresses in the casing can plastically deform the cement; when these stresses are reduced, a microannulus may be created. Bois et al. (2011) analyzed various conditions for microannulus formation, and suggested that the stiffness of the cement and formation may be important considerations in the location and magnitude of microannulus formation. They concluded that cement hydration along with wellbore pressure and temperature cycling are the most important mechanisms for microannulus formation.

Because microannuli are considered discrete, fracture-like flaws, they can be described in terms of their aperture, similar to how rock fractures are characterized (National Academies of Sciences 2015; Berkowitz 2002). The mechanical aperture (d) is the distance across the opening of the microannulus. The hydraulic aperture (h) is the spacing between smooth-walled parallel plates that produces the equivalent steady-state flow as the microannulus. The hydraulic aperture of a microannulus that corresponds to the effective permeability (k) of a wellbore system can be approximated by the so-called cubic law (Witherspoon et al. 1980) if it is assumed that all of the flow occurs through the microannulus (Dusseault et al. 2015; Seidel and Greene 1985):

$$h^3 = \frac{12kA}{w} \qquad \textit{Equation 3-1}$$

where A is the wellbore annular area and w is the length of the hydraulic aperture which, if flow is assumed to occur through the cement-casing microannulus, can be approximated by the circumference of the outside of the casing. As shown in Section 3.7, although the cubic law was derived for flow between planar parallel plates, it provides a very close approximation for flow through an annulus for geometries typical for a wellbore microannulus. The relationship between the effective wellbore permeability and the corresponding microannulus hydraulic aperture for a typical wellbore configuration given in Figure 3-1 reveals that the effective wellbore permeability can be greatly increased by the presence of a microannulus with a relatively small hydraulic aperture, consistent with the observations of others. Seidel and Greene (1985) state that a microannulus of 25 μm is sufficiently problematic for gas flow along a well, whereas Dusseault et al. (2014) indicated that microannuli as small as 10 to 15 μm will provide a pathway for gas movement. Bachu and Bennion (2009) cast steel rods in cement cores, and created annular gaps between the cement and steel to simulate microannuli. They reported that annular gaps that were 10 to 30 μm wide increased the permeability of the cement-steel system to approximately 10^{-15} m^2, many orders of magnitude above that for an intact or perfectly bonded system. While hydraulic aperture is a convenient term to describe a microannulus and reflects its impact on the leakage potential of a wellbore, it does not describe the mechanical aperture around the casing circumference or how the mechanical aperture may behave under different operational and in situ stress conditions.

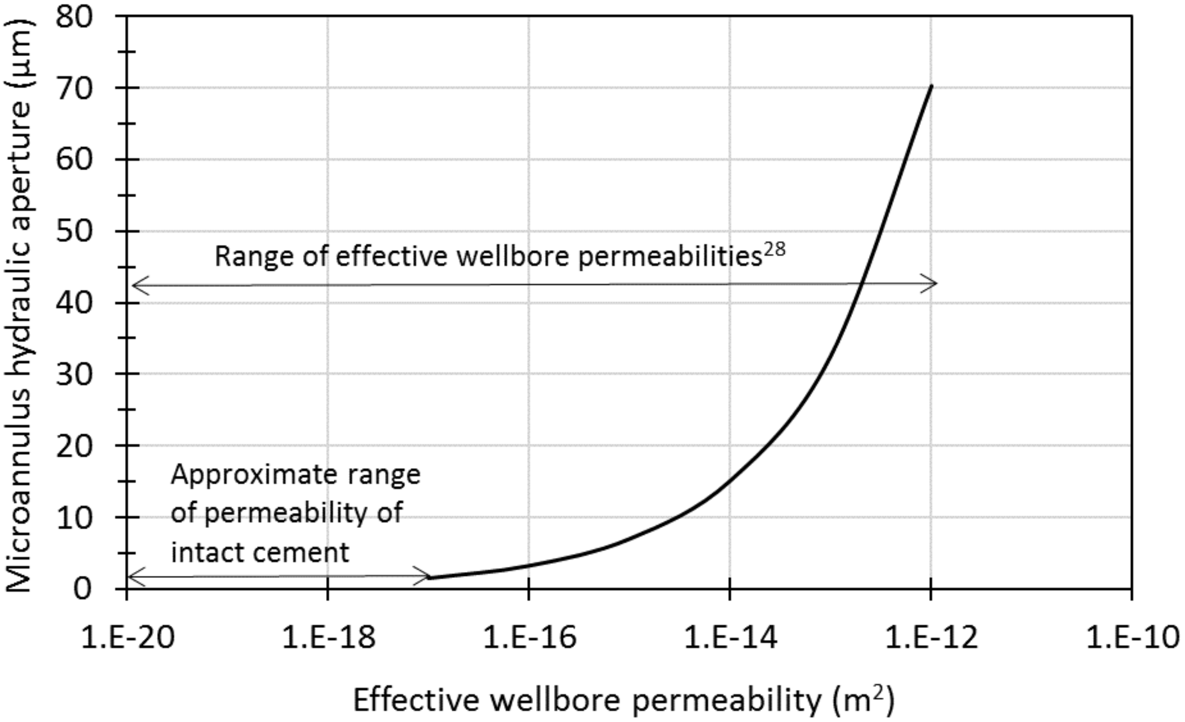

NOTE: Relationship is calculated using the cubic law (Equation 3-1) and assumes all of the wellbore permeability can be attributed to the microannulus. The wellbore diameter is assumed to be 0.23 m, and the outer casing diameter is assumed to be 0.18 m.

Figure 3-1. Hydraulic aperture of microannulus as a function of effective wellbore permeability

Stresses acting on the wellbore system, either from the formation or from within the casing, may significantly affect wellbore integrity as these stresses can tend to open or close wellbore flaws including microannuli (Dusseault et al. 2014; Manceau et al. 2015; Carroll et al. 2017). The casing will expand or contract based on changes in the fluid density, pressure and temperature within the casing, and this expansion or contraction may affect the microannulus. Sonic logs conducted first with no casing pressure and then repeated with casing pressure indicate that casing pressure tends to close microannuli (Brufatto et al. 2003). In laboratory tests, Jackson and Murphey (1993) found that re-pressurizing the casing after a microannulus had been formed could eliminate flow, presumably due to the microannulus closing. Temperature changes in the casing fluids may also induce casing expansion and contraction, imposing stresses on the cement-casing interface (Lavrov et al. 2015). Microannuli may also deform in response to changes in the external stresses that act on the wellbore system. These stresses are a function of many factors, including the overburden pressure, the tendency of the host rock to creep, deformations due to reservoir compaction or expansion, changes in formation pore pressure, and expansion/contraction of the cement (Hawkes et a. 2005; Orlic 2009). In spite of the many ways that stress conditions may affect the microannulus, there have been no studies that have quantified the response of microannuli to stress.

Understanding how microannuli respond to stress will improve our ability to estimate wellbore leakage and the resulting environmental consequence. Currently, estimates of flow through leaky wellbores are used to assess the environmental risk and performance of subsurface operations including CO_2 sequestration (Celia et al. 2011), disposal of hazardous materials by deep underground injection (LeNeveu 2011), abandonment of oil and gas wellbores (Lavasani et al. 2015), and storage of fluids in caverns (van Thienen-Visser et al. 2014). However, these calculations do not include the significant influence that the stress conditions may have on the effective wellbore permeability. Thus, estimates of flow through wellbore systems with a microannulus will be improved if the effect of stress acting on the microannulus was known and accounted for. Additionally, the impact of well operations on wellbore integrity could be better understood and perhaps managed if the microannulus response to stress was accounted for (Bois et al. 2011; Manceau et al. 2015; Carroll et al. 2017; Zhang et al. 2017). This knowledge would also inform efforts to repair leaky wellbores that often involve attempts to "squeeze" repair materials into the microannulus under pressure in order to restore the functionality of the wellbore (Saponja 1999). Pressurizing repair material in the casing to force it out through perforations into the cemented wellbore annulus may tend to close microannuli; once this pressure inside the casing is relieved at the end of the repair effort, the microannuli may re-open. An improved understanding of microannuli response to stress will lead to better repair efforts, which in turn results in less potential contamination from leaky wells and increased efficiency of wellbores used for energy production.

Models of wellbore system behavior have been developed which include the effects of formation stresses, cement shrinkage and expansion, hardening, and microannulus formation through interfacial debonding (Zhang et al. 2017; Gray et al. 2009; Schreppers 2015). These models can be used to investigate the conditions that produce microannuli during wellbore construction and subsequent operations. However, these models represent the microannulus as a uniform, smooth-walled, annular gap in contrast to a typical fracture in a brittle material that has a variable aperture that produces a rough surface and partial contact that controls its response to stress changes (Zimmerman and Bodvarsson 1996). There have been no direct measurements of aperture size (mechanical aperture) around the cement-casing interface to characterize the roughness of a microannulus. Measurements using X-ray computed tomography of wellbore systems of cement, rock and casing (Vrålstad et al. 2015; Roy et al. 2017; Kjøller et al. 2016) suggest that defects that develop at the cement-casing microannulus are nonuniform; however, these measurements have a resolution of >100 µm which is an order of magnitude greater than the size of apertures that can have a large impact on the effective wellbore permeability (refer to Figure 3-1).

We report on laboratory measurements of gas flow through wellbore specimens that contain microannuli under various combinations of confining, casing and pore pressures to provide insight how microannuli respond to a range of stress conditions. We interpreted the gas flow data as providing the hydraulic aperture of the microannulus. We also measured the microannulus size (mechanical aperture) around the circumference of a casing on one specimen. These measurements are directed at determining whether the microannulus response and character is similar to that of fractures in rock and other brittle materials, or whether the microannulus behaves as a uniform annular gap. Understanding the microannulus response to changing stress conditions is important for energy production and storage applications as wellbore leakage through the microannulus can reduce the efficacy of engineered systems as well as result in environmental impacts such as contamination of potable groundwater.

3.3. Materials and Methods

3.3.1. Specimen Preparation

3.3.1.1. Cement Preparation

Wellbore system specimens were created by casting a sheath of conventional oil well cement (OWC) onto a steel casing. The casing was a thin-walled (2.35-mm thick) mild carbon steel (A36) cylinder with an inner diameter of 53 mm. The diameter to thickness ratio of the casing, which controls stresses and strains in the casing, is consistent with the range used in many oil and gas wells (Gatlin 1960). The casing was fixed in the center of a mold with a cap and plug, and cement was poured into the mold. The cement was American Petroleum Institute (API) Class G with a water/cement ratio of 0.33 and was mixed following American Society for Testing and Materials (ASTM) C305-14 (ASTM 2014). Specimens were cured in a 55°C hot water bath for 7 days, and stored in a 100% humidity curing room until tested. The specimens had nominal cured dimensions of 203-mm length, outer diameter of 96 mm, and inner diameter of 53 mm. The 19-mm thickness of the cement sheath is within the range of cemented annuli in many oil and gas wells (Gatlin 1960). A cured specimen is shown in Figure 3-2.

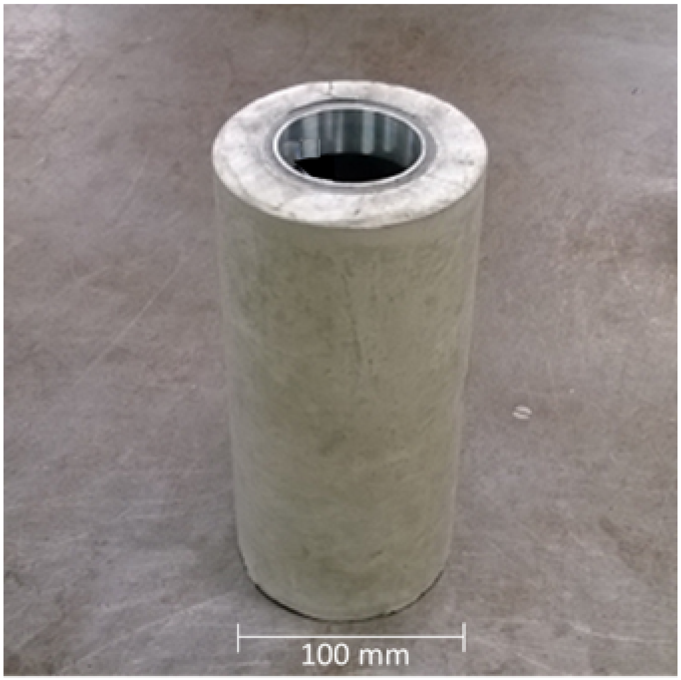

Figure 3-2. Wellbore specimen consisting of cement sheath cast on steel casing

3.3.1.2. Microannuli

Two methods were used to create microannuli within specimens. One method involves first wrapping the casing with release film (25-μm thick) prior to casting the specimen. After 24 hours of curing, the casing was removed from the cement sheath and the release film was discarded. The specimen was then reassembled and allowed to continue to cure. At the end of curing, the steel casing could be moved by hand within the cement sheath. This method produced a relatively large microannulus. The other method to produce microannuli within specimens was to thermally de-bond the casing from the cement. After curing, the casing was cooled with dry ice for 5 minutes so that it contracted and de-bonded from the adjacent cement. This method produced a relatively tight interface between the casing and cement with a relatively small microannulus.

Specimens were also produced with corroded casing (Figure 3-3). The casing was corroded by placing it in a concrete curing room with 100% humidity for 5 days prior to casting the specimen.

Figure 3-3. Casing with (left) and without (right) corrosion

3.3.2. Experimental System

The pressure vessel used to test the wellbore specimens, shown in Figure 3-4a and Figure 3-4, is capable of applying independent confining pressures up to 35 MPa, internal casing pressures up to 20 MPa, and pore pressures within the specimen up to 15 MPa. A hydraulic pump connected to a port in the sidewall of the vessel was used to introduce and control the confining pressure. The end caps of the pressure vessel include ported bosses that were designed to fit inside the casing of the wellbore specimens to allow the interior space of the casing to be isolated. In some tests, gas was used to pressurize the casing. Access to the casing was also used to circulate heated or cooled water through the casing. The annular surface of the specimen top and bottom are accessible from ports on both end caps, and were connected to the permeameter to establish a gas pore pressure within the specimen and induce and measure gas flow through the specimen.

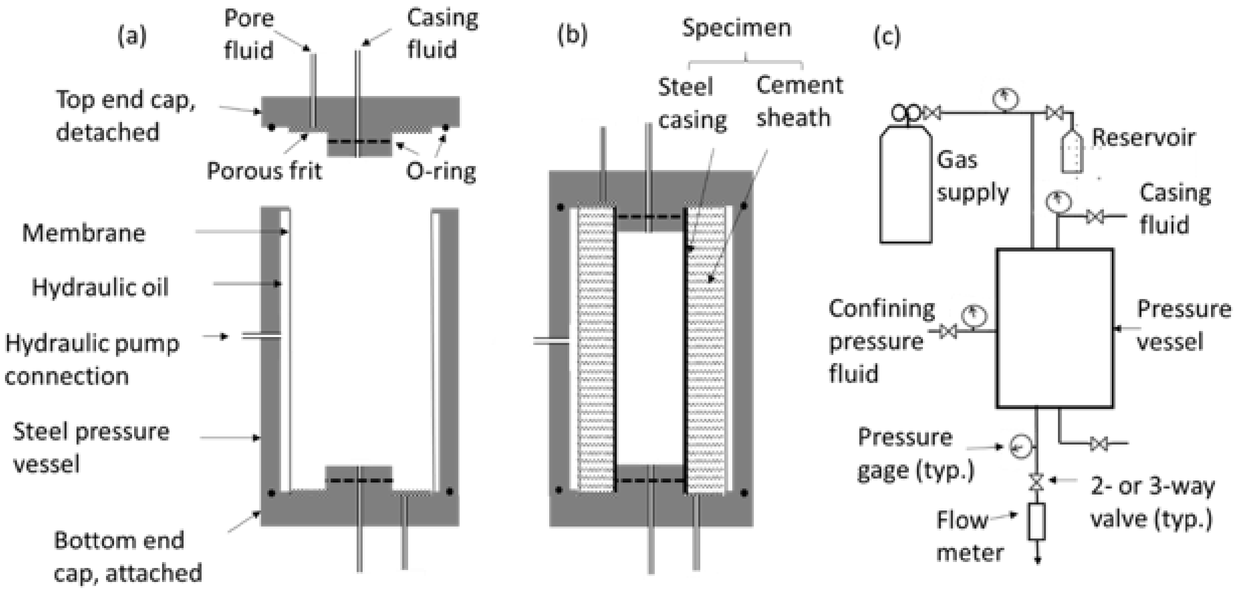

Figure 3-4. (a) Cross-section of empty pressure vessel with top end cap detached and bottom end cap attached, (b) cross-section of assembled pressure vessel containing wellbore specimen, and (c) schematic of permeameter and components

The permeameter system (Figure 3-4c) is the series of valves, tubing and measurement devices used to supply and measure gas pressure and flow through the wellbore specimens while in the pressure vessel. All tests reported here were conducted with nitrogen. To cover the wide range of possible wellbore specimen permeabilities, the system can utilize three different permeability measurement methods. Steady-state flow rates in the range of 5 to 150 standard cm^3/s were made with flow meters with an accuracy of 1% of full-scale. The regulator was adjusted to provide a constant pressure to the upstream side of the permeameter. The flow meter could be connected to either the upstream or downstream side of the specimen to measure the flow that passes through the specimen. Most tests vented the downstream to atmosphere. For some tests, it was desirable to maintain a backpressure above atmospheric so that larger pore pressures could be developed within the specimen. The backpressure system consists of a valve that was adjusted to maintain the desired downstream pressure (typically within ± 7 kPa). Pressure differences across the specimen were usually less than 100 kPa. The pressure on the upstream side (on the side with the gas supply) and downstream side were measured with pressure gauges with an accuracy of 1% of full-scale.

For flow rates between 0.02 to 5 standard cm^3/s, a quasi-steady method was used. With the downstream at a constant pressure (either atmospheric or with a backpressure), the upstream pressure was increased and then isolated from the pressure supply. The flowrate from the upstream volume, Q, can be found from the rate of change of the pressure in the upstream volume (dP/dt) for an isothermal process from (Jannot and Lasseux 2012)

$$Q = \frac{VdP}{Pdt} \qquad \textit{Equation 3-2}$$

where V and P are the volume and pressure of the upstream, respectively. The upstream volume of 158 cm^3 can be increased by including a 1-L reservoir to change the sensitivity of the pressure response to volumetric flow. Pressure differences across the specimen were usually less than 1 MPa. A soap-film flowmeter was used to calibrate the pressure fall-off method for flows less than 5 standard cm^3/s. The pressure fall-off method was found to be within 2% of the measurements taken with the soap-film flowmeter. For lower flow rates, transient measurements can be made using pulse decay methods. Because of the relatively large flow rates through the microannuli, no transient measurements were made on these specimens.

The system was tested with an empty pressure vessel to test for the effective upper bound of permeability that the system can measure. At 14-kPa inlet pressure and no backpressure, the flow rate was 125 standard cm^3/s and the equivalent system permeability was calculated to be 1.5×10^{-11} m^2.

3.3.3. Interpretation of Flow Measurements

Large flow rates may include both viscous (Darcy) flow as well as nonlinear (inertial) flow and can be described by Forchheimer's equation (Forchheimer 1901)

$$-\nabla P = \frac{\mu}{kA}Q + \frac{\beta\rho}{A^2}Q^2 \qquad \textit{Equation 3-3}$$

where ∇P is the gradient, Q is the volumetric flowrate, k is the permeability, A is the cross-sectional area involved in the flow, μ is fluid viscosity, β is the inertial coefficient and ρ is the fluid density. For steady-state isothermal gas flow, Equation 3-3 can be rewritten as (Bellabarba et al. 2008)

$$\frac{MA(P_u^2 - P_d^2)}{2zRT\mu L\rho Q} = \frac{1}{k} + (\frac{\rho Q}{\mu A})\beta \qquad \textit{Equation 3-4}$$

where M is the molecular weight of the gas, L is the is the specimen length, z is the gas compressibility factor, R is the universal gas constant, T is temperature, and the subscripts u and d stand for upstream and downstream, respectively. This equation can be rewritten as $y = (1/k) + x\beta$, where y is the left-side of Equation 3-4 and x is the term in parentheses on the right-hand side of Equation 3-4. Flow measurements made at different pressures will generate (x,y) pairs, which can be plotted. The plotted data should produce a straight line with a slope that is a function of the inertial coefficient β and an intercept inversely proportional to permeability. In the case of linear, viscous flow, the slope will be zero and Equation 3-4 reduces to Darcy's Law. The Forchheimer equation has been effectively used to interpret flow through discrete fractures in addition to more uniform porous media (Zhang and Nemcik 2013; Nowamooz et al. 2009; Javadi et al. 2014).

Data from two series of measurements are given in Figure 3-5 to illustrate the data interpretation method. Each measurement series consisted of seven (x,y) pairs which were generated by varying the pressure conditions to produce different flow rates. The permeability for each measurement series is the inverse of the intercept of the straight line fit to these data. This corrected permeability is greater than the permeability interpreted from individual measurements assuming only viscous flow; the correction for nonlinear flow can increase the interpreted value of permeability by more than 100%. For typical pressure conditions used in our measurements, nonlinear flow was not detectable for flow rates less than approximately 0.1 standard cm^3/s.

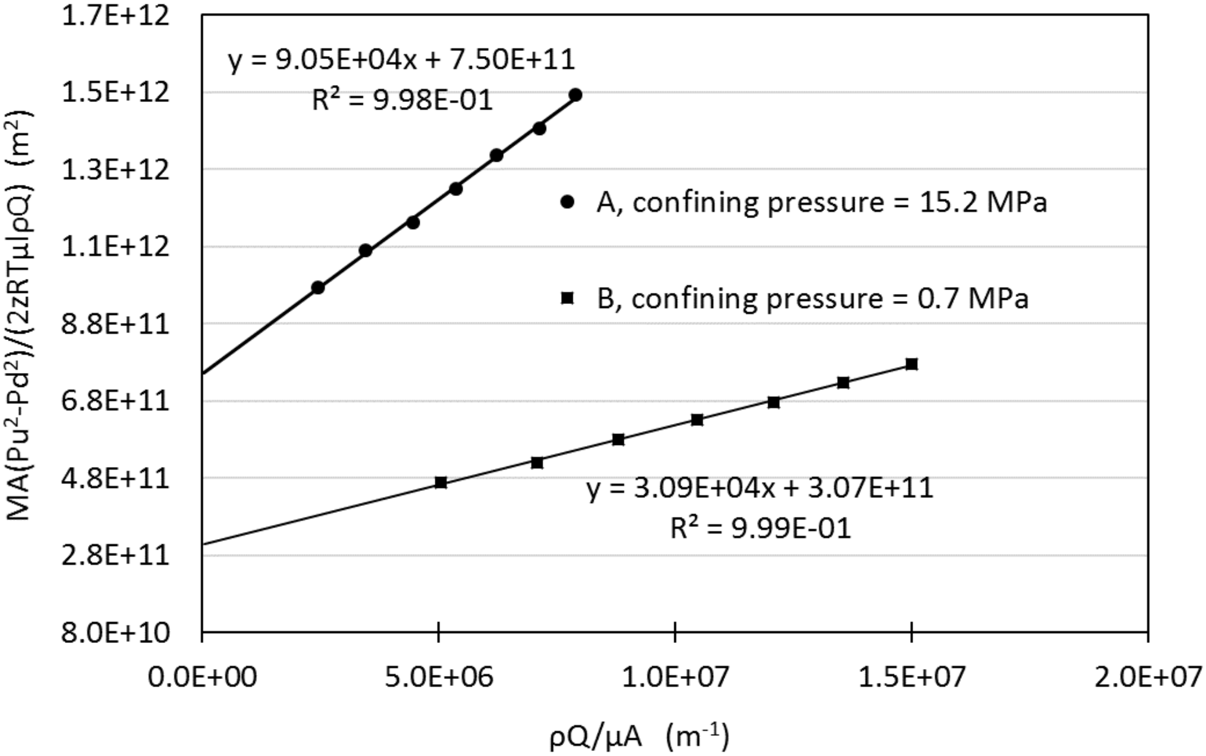

NOTE: In both measurement series, upstream pressures were varied over the range of 98 to 139 kPa while the downstream pressure was held constant (atmospheric); the resulting flow rates ranged from 18 to 58 standard cm^3/s for series A and 37 to 111 standard cm^3/s for series B.

Figure 3-5. Results from two measurement series with different confining pressures conducted on specimen R1

The permeabilities determined from the above analyses were then used to determine the hydraulic aperture of the microannulus. The permeability of the specimens with microannuli were mostly in the range of 10^{-12} to 10^{-15} m^2. In contrast, the intact specimen's permeabilities were on the order of 10^{-18} m^2. It was therefore assumed that flow occurred exclusively through the microannulus, and the permeability was interpreted as the hydraulic aperture (h) using the cubic law (Equation 3-1). From uncertainties in measured quantities, the error in the reported hydraulic aperture is ± 5% for each series of measurements.

Gas slip effects were evaluated from data collected at different mean gas pressures and from data collected with different gases. In the tests reported here, the flow paths were sufficiently large that gas slip effects were not observed.

3.3.4. Post-test Observations of Microannulus

After testing in the pressure vessel, epoxy was injected into the microannulus of one specimen and subsequently used to physically measure the microannulus size or mechanical aperture. To aid in the visual observation, the epoxy was mixed with Rhodamine B (Sigma R6626), a bright pink dye which is also fluorescent, to provide contrast in both visible and ultraviolet light. The epoxy was injected into the specimen by placing the specimen in a tight-fitting, thick-walled, polyvinyl chloride (PVC) pipe which was capped at both ends. Epoxy was placed on top of the specimen after the casing was plugged. A port on the top cap allowed the epoxy to be pressurized with air (up to 100 kPa) for 15 minutes to force epoxy into the microannulus. After the epoxy cured, the specimen was wet cut with a masonry saw to expose an interior surface. Microphotographs of the cement-steel interface were taken every 1° along the circumference of the casing and merged together using Photoshop™. The size of the microannulus around the casing circumference was interpreted using image processing software (ImageJ). The resolution of the imaging method was 3 μm.

3.4. Results and Discussion

Gas flow measurements were made on twelve wellbore system specimens. Table 3-1 provides a summary of the specimen label, the type of microannulus, and the confining pressure and casing pressures used in the measurements. The range of hydraulic apertures interpreted from the flow measurements is given for each specimen. In addition, the principal parameter varied when testing each specimen is given. Results from testing these specimens are subsequently presented and discussed.

Table 3-1. Summary of specimens, test conditions and range of permeabilities and hydraulic apertures interpreted from flow measurements.

Specimen Label	Method to Create Microannulus	Confining Pressure (MPa)	Casing Pressure (MPa)	Range of Permeabilities (m²)	Range of Hydraulic Apertures (μm)	Principal Parameter Varied
I1	N/A	0.7–34.5	0	$< 1\times10^{-18}$	<0.6	Confining pressure
I2	N/A	0.7–34.5	0	$< 1\times10^{-18}$	<0.6	Confining pressure
R1	Release film	0.7–34.5	0	6.9×10^{-13} – 3.1×10^{-12}	58–95	Confining pressure
R2	Release film	4.1–17.9	0	1.1×10^{-13} – 5.2×10^{-13}	32–53	Confining pressure
R3	Release film	5.5–13.8	0–13.8	3.0×10^{-13} – 8.4×10^{-13}	44–62	Casing pressure
R4	Release film	6.9	0	4.6×10^{-12} – 5.8×10^{-12}	109–118	Casing fluid temperature
R5	Release film	0.7–34.5	0	7.5×10^{-14} – 4.9×10^{-13}	28–52	Effective stress
R6	Release film	0.1	0	1.9×10^{-11}	175	Post-test observations
T1	Thermally	4.1–29.0	0	5.9×10^{-16} –	5–12	Confining

Specimen Label	Method to Create Microannulus	Confining Pressure (MPa)	Casing Pressure (MPa)	Range of Permeabilities (m^2)	Range of Hydraulic Apertures (μm)	Principal Parameter Varied
	de-bond			6.7×10^{-15}		pressure
T2	Thermally de-bond	4.1–12.4	0–21.0	6.5×10^{-16} – 9.6×10^{-15}	5–14	Casing pressure
C1	Corroded casing	2.1–9.7	0	3.2×10^{-15} – 6.0×10^{-15}	10–12	Confining pressure
C2	Corroded casing	0.7–20.7	0	1.6×10^{-16} – 4.3×10^{-15}	4–11	Confining pressure

3.4.1. *Intact Specimens*

Two intact wellbore system specimens were tested. These specimens were prepared in the same manner as other specimens in Table 3-1 but without a microannulus. The effective permeability of these specimens was $< 1\times10^{-18}$ m^2, which is given as an upper bound as steady flow was not confirmed in these measurements. The effective permeability of the intact wellbore specimens is consistent with permeability of intact cement, and corresponds to a hydraulic aperture of <0.6 μm from Equation 3-1; this value is for comparative purposes only as there was no indication of a discrete flow path through the intact specimens for which the concept of a hydraulic aperture would apply. Testing of specimens with microannuli (described subsequently) resulted in orders of magnitude greater gas flows at comparable conditions and consequently much greater hydraulic apertures and effective permeabilities (Table 3-1). These results confirm the assumption that, for specimens with a microannulus, essentially all of the flow occurred through the microannulus and that it is reasonable to use the cubic law (Equation 3-1) to interpret the hydraulic aperture of these specimens.

3.4.2. *Microannuli Response to Confining Pressure*

Effective wellbore permeability and hydraulic aperture as a function of confining pressure are given in Figure 3-6 for three different specimens with a microannulus. The results reveal that the presence of microannuli had a significant effect on the flow characteristics of the wellbore specimens. Although there is considerable variability between specimens, all specimens had an effective permeability more than three orders of magnitude greater than that of the intact specimens.

Subsequent discussions in this paper will largely focus on hydraulic aperture rather than effective permeability because the term is widely used to describe fractures in rock and cement, it conveys a sense of the discrete nature of the microannulus, and it serves as a first order estimate of the actual or mechanical aperture (Zimmerman and Bodvarsson 1996). Further, hydraulic aperture is independent of the dimensions of the wellbore specimens and therefore can be readily applied to different configurations. We reiterate that the hydraulic apertures were calculated from the effective wellbore permeabilities using the cubic law (Equation 3-1) assuming all flow is through the microannulus. Effective wellbore permeabilities can be found from the reported hydraulic apertures by rearranging Equation 3-1 and solving for effective wellbore permeability.

Specimen R1 was subjected to confining pressure cycles with progressively greater confining pressures to a maximum of 35 MPa. The hydraulic aperture decreased with an increased confining pressure; at confining pressures above approximately 20 MPa, the rate of change of the hydraulic aperture with confining pressure (i.e., the slope in Figure 3-6a) decreased by approximately an order of magnitude. Unloading largely followed the loading path, with hysteresis of variable strength observed. Between the first and last loading-unloading cycle, the hydraulic aperture decreased by 10 µm. During the initial loading of specimen R2, the hydraulic aperture decreases in a nonlinear manner. The first loading-unloading cycle induced a nonrecoverable change in the hydraulic aperture of 15 µm. The second loading-unloading cycle indicates no appreciable hysteresis. Although both specimens R1 and R2 had a microannulus created using the release film method, their effective permeability and hydraulic aperture are significantly different. These results indicate that there may be considerable variability between specimens with the same type of microannulus. For specimen T1, the hydraulic aperture changed less with confining pressure compared to the results from the other specimens. Upon unloading, the hydraulic aperture increases only slightly and is smaller than that on the loading path. These hydraulic apertures for specimen T1 are approximately one order of magnitude smaller than those measured for specimen R1 at comparable confining pressures. In terms of permeability (Figure 3-6b), changes with confining pressure are more evident for specimens with smaller hydraulic apertures.

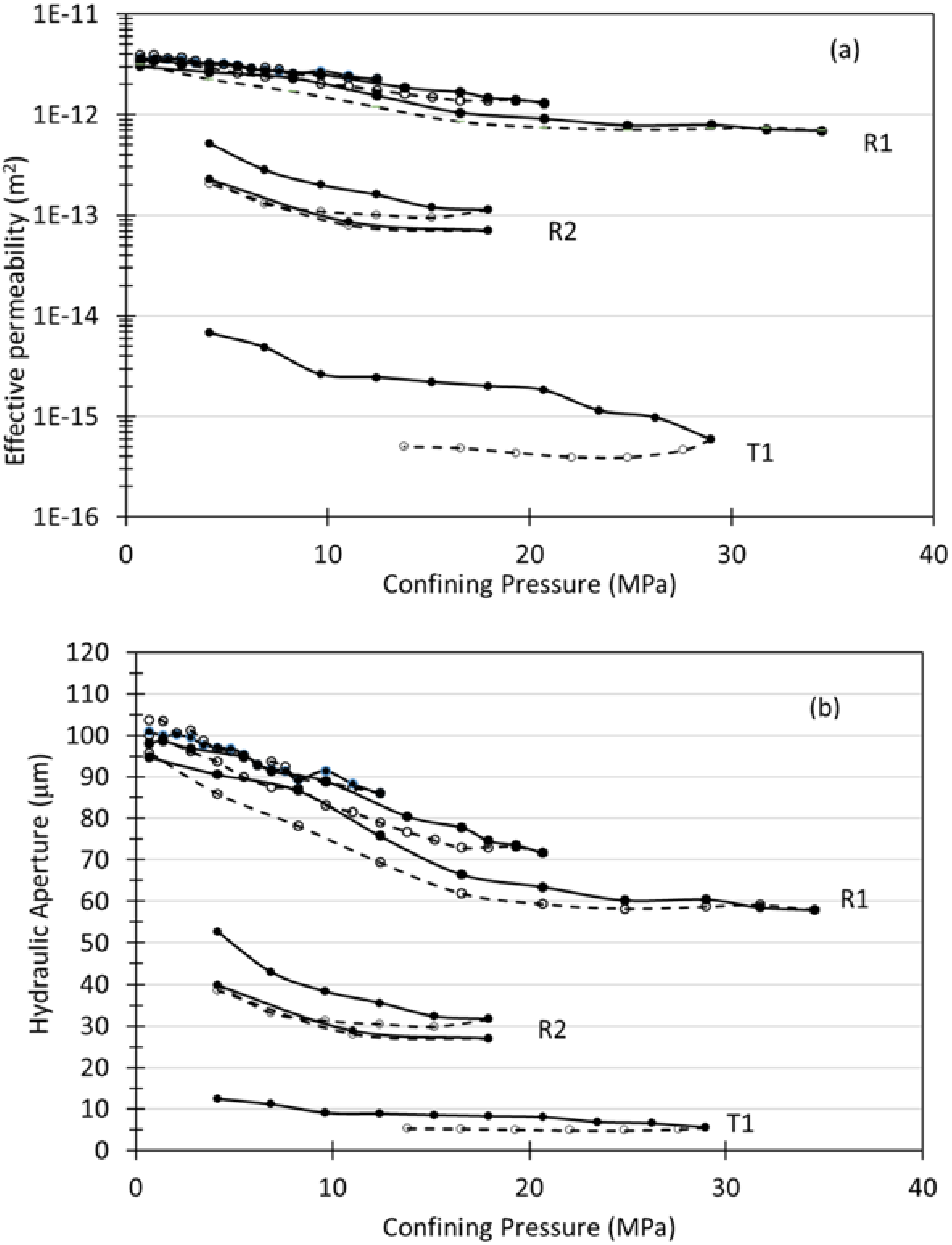

NOTE: In both figures, loading (increasing confining pressure) is shown with the solid lines and circles; unloading is denoted by the dashed lines and open circles.

Figure 3-6. (a) Effective permeability and (b) hydraulic aperture as a function of confining pressure for three specimens with microannuli

The three specimens, which included hydraulic apertures which varied by approximately an order of magnitude, exhibited similar behavior. The hydraulic aperture decreased with increased confining pressure; yet even under the largest confining pressures applied, the hydraulic apertures remained a significant fraction of their initial value and were much greater than that for intact cement-casing specimens. For the specimens with the larger microannuli (R1 and R2), the change in hydraulic aperture with confining pressure was noticeably nonlinear. At larger values of confining pressure, the rate of change in hydraulic aperture with confining pressure was nearly the same for all three specimens.

The response of microannuli to external stress is consistent with their surfaces having some degree of roughness with a distribution of asperity sizes. The behavior of microannuli to stress is similar to that of fractures in rock and cementitious materials (Bandis et al. 1983; Baghbanan and Jing 2008; Lange et al. 1993). Increased normal stress across a microannulus results in more contact between the two surfaces with a corresponding increase in stiffness, resulting in a nonlinear fracture closure and consequently nonlinear hydraulic aperture and permeability decrease with stress. Microannuli could not be completely closed even at relatively large normal stresses because asperities along the microannuli would not allow the cement and casing to perfectly mate together. These results indicate de-bonding cement from casing generates a surface that is sufficiently rough to remain conductive under large normal stresses. Hysteresis in the response of microannuli is consistent with plastic deformation of asperities in contact along the cement-casing interface. Plastic deformation of asperities would give rise to an increased stiffness after the initial loading as was clearly observed in the response of specimen R2. Further, plastic deformation of asperities would produce the nonrecoverable reduction in the hydraulic aperture as observed in these results. The results given in Figure 3-6 are consistent with microannuli having a rough surface that will govern their mechanical and hydraulic response to stress.

3.4.3. Specimens with Corroded Casing

In Figure 3-7, the hydraulic aperture is given as a function of confining pressure for two specimens that were created with corroded casing but otherwise were intact. Both specimens had a hydraulic aperture significantly larger than would have been interpreted for an intact specimen created with noncorroded casing (much less than 1 μm). The hydraulic aperture decreased upon the initial loading for both specimens, although the rate of change of the hydraulic aperture for confining pressures less than 10 MPa is noticeably different for the two specimens. The initial loading of specimen C1 is slightly concave in contrast to that for specimen C2 and the specimens given in Figure 3-6. It is not obvious that the response of C1 is fundamentally different than C2 beyond the variability between specimens. The initial loading of C2 had a nonlinear response. Upon unloading, the hydraulic aperture did not recover to its initial value. Subsequent loading followed the unloading path. The response of these specimens with corroded casing was approximately comparable to thermally de-bonded specimen (T1 in Figure 3-6a), and implies that the corrosion product deforms significantly under initial loading.

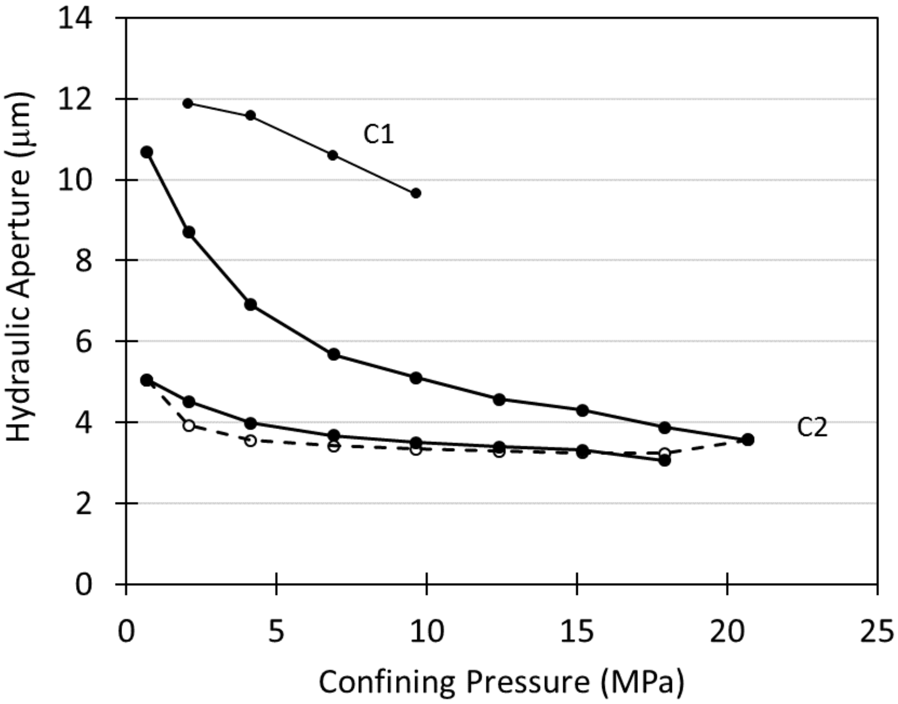

NOTE: Loading (increasing confining pressure) is shown with the solid lines and circles; unloading is denoted by the dashed lines and open circles.

Figure 3-7. Hydraulic aperture as a function of confining pressure for two specimens (C1 and C2) with corroded casing

3.4.4. Response of Microannuli to Casing Pressure

The response to variations in casing pressure was measured for a number of specimens with different hydraulic apertures. Compared to changes in confining pressure, the hydraulic aperture was much less sensitive to changes in casing pressure largely because of the relative stiffness of the steel compared to that of the cement. Moreover, the response of hydraulic aperture to variations in casing pressure was found to be a strong function of the confining pressure. When the confining pressure was large (>15 MPa), the hydraulic aperture changed only slightly (often less than 1 µm) with casing pressure variations of more than 20 MPa. The hydraulic aperture was more responsive to casing pressure when the confining pressure was lower. The hydraulic aperture of R3 is given in Figure 3-8 as a function of casing pressure for two different values of confining pressures (5.5 MPa and 13.8 MPa). At a lower confining pressure, the hydraulic aperture changed more with changes in the internal casing pressure.

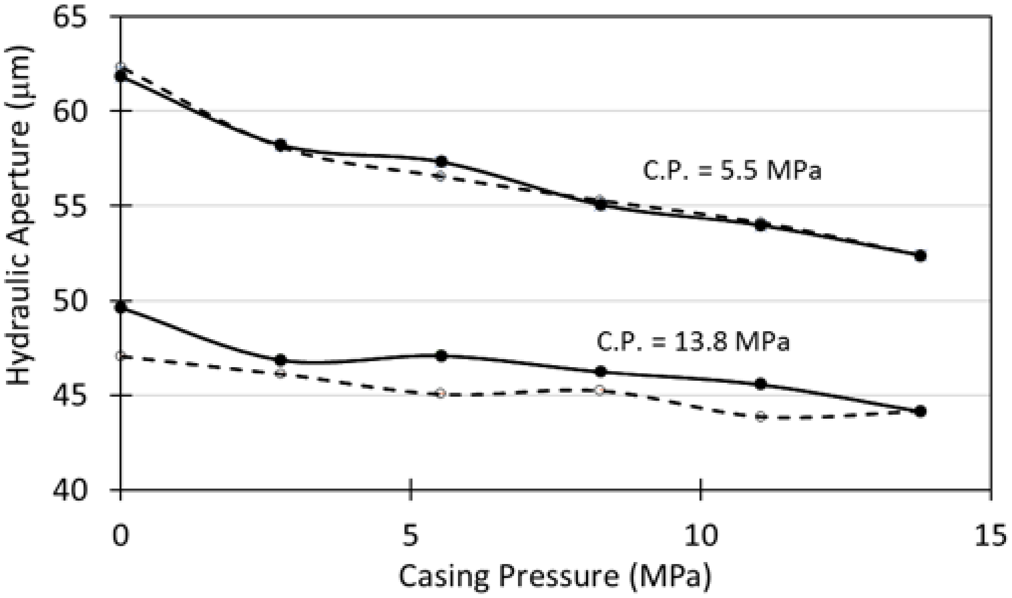

NOTE: Loading (increasing casing pressure) is shown with the solid lines and circles; unloading is denoted by the dashed lines and open circles. C.P. denotes confining pressure.

Figure 3-8. Hydraulic aperture as a function of casing pressure for R3 at two different confining pressures

Results from another specimen (T2) tested under variable casing pressure is shown in Figure 3-9. For the tests at both confining pressures, the casing pressure was increased above that of the confining pressure. At the larger value of confining stress, the hydraulic aperture did not significantly change with casing pressure. However, at the lower value of confining pressure, the hydraulic aperture increased. This behavior is attributed to the development of tensile stresses in the cement sufficient to fail the cement. An elastic solution for a bi-material hollow cylinder (Bois et al. 2011) applied to these test conditions indicates that the circumferential stress becomes negative at a casing pressure of approximately 10 MPa, consistent with the cement having failed in tension. Indeed, a fracture in the cement was observed upon removing the specimen from the pressure vessel. Thus, the apparent increase in hydraulic aperture is not due to increased flow in the microannulus but rather from flow through a newly created fracture in the cement.

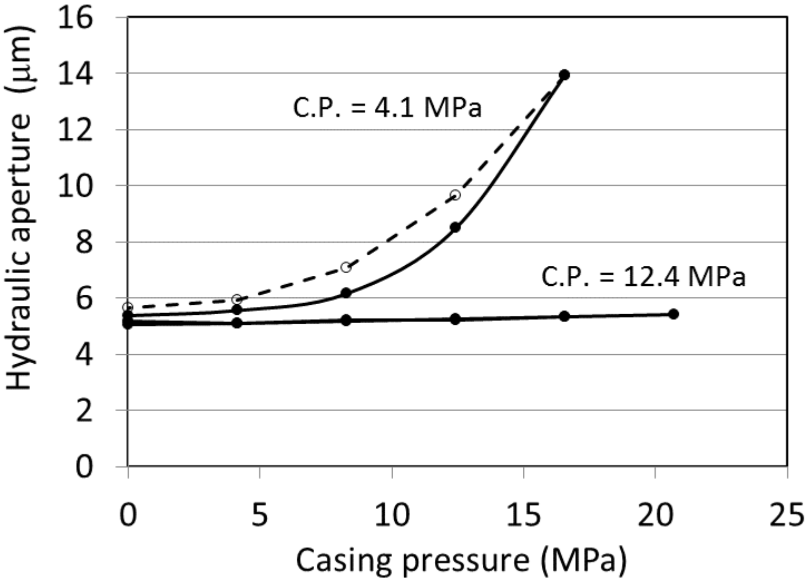

NOTE: Loading (increasing casing pressure) is shown with the solid lines and circles; unloading is denoted by the dashed lines and open circles. C.P. denotes confining pressure.

Figure 3-9. Hydraulic aperture as a function of casing pressure at two values of confining pressure for T2

3.4.5. Response of Microannuli to Casing Temperature

In Figure 3-10, the hydraulic aperture of specimen R4 is given a function of the temperature of the fluid within the casing. After an initial measurement of the hydraulic aperture at ambient conditions, hot water was circulated through the casing with a peristaltic pump (10 mL/min) at ambient pressure. The temperature of the influent and effluent water was measured, along with the influent and effluent gas temperatures. After the mean temperature of the influent and effluent fluid stabilized at its maximum value (78°C), the hydraulic aperture was again measured. Cold water was then circulated through the casing, and the hydraulic aperture was measured after the mean temperature stabilized at its minimum value (8°C). An increasing hydraulic aperture with decreasing casing fluid temperature is consistent with the thermal contraction of the casing enlarging the microannulus. The radial contraction of the casing calculated from linear thermoelastic theory (Tipler and Mosca 2007) from the hot to cold condition was 3 μm, less than the measured change in hydraulic aperture.

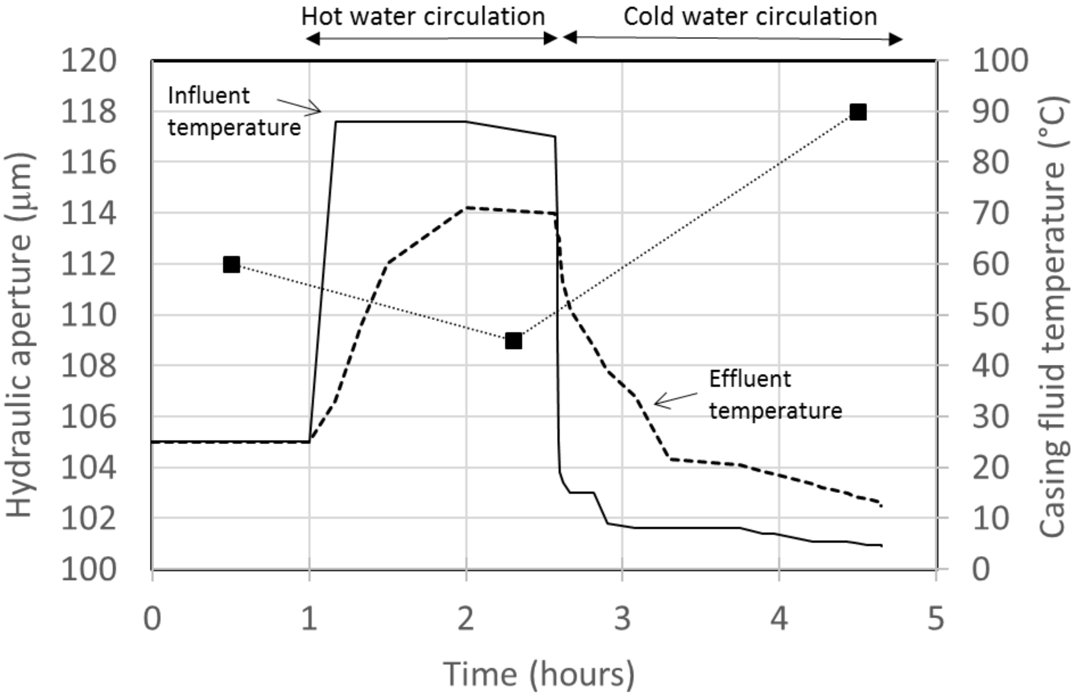

NOTE: Solid squares denote measured hydraulic apertures.

Figure 3-10. Hydraulic aperture measured as a function of casing fluid temperature for specimen R4

3.4.6. Response of Microannuli to Pore Pressure

In Figure 3-11, the hydraulic aperture is given as a function of effective stress (defined here as confining pressure minus pore pressure) from the test on specimen R5. Backpressure was used to control the pore pressure. Effective stress was changed in three different stages during this test. During the initial stage, the confining pressure was progressively increased to 3.4 MPa with a pore pressure near zero. Confining pressure and pore pressure were then simultaneously increased to 6.9 MPa and 3.5 MPa, respectively, to maintain a constant effective stress of 3.5 MPa. During the second stage, the effective stress was changed by progressively reducing the pore pressure to near zero while maintaining a constant confining pressure. During this stage, the hydraulic aperture decreased in a response to a decrease in the pore pressure. In the final stage, the confining pressure was reduced with a pore pressure of near zero. Taken together, these results indicated that the hydraulic aperture can change in response to varying the pore pressure. Further, the changes in hydraulic aperture from changes in pore pressure are consistent with those induced by changes in confining pressure.

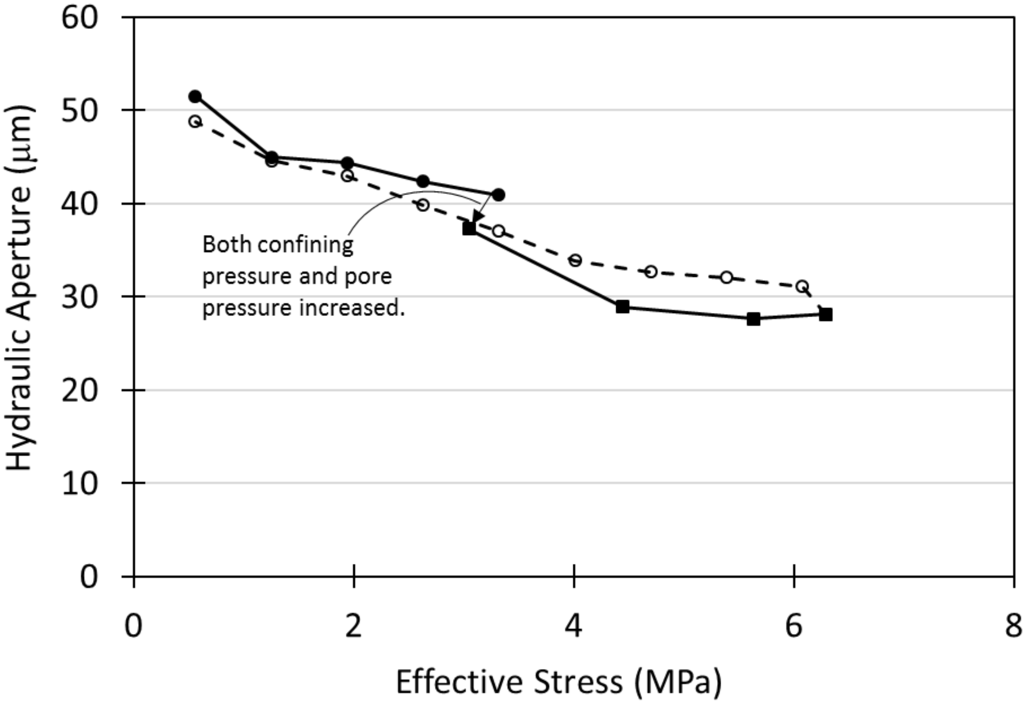

NOTE: Effective stress is defined as confining pressure minus pore pressure. First stage (solid circles): effective stress increased by changes in confining pressure. Second stage (solid squares): effective stress increased by decreasing pore pressure. Third stage (open circles): effective stress decreased by reducing confining pressure.

Figure 3-11. Hydraulic aperture as a function of effective stress acting on specimen R5

3.4.7. Post-test Measurement of Aperture at Cement-Casing Interface

After flow testing, specimen R6 was injected with epoxy, sliced and microphotographs were taken at the cement-steel interface at equal 1° intervals around the casing circumference. A typical microphotograph is shown in Figure 3-12. The microannulus aperture was measured in each microphotograph; the measured apertures are given as a function of the distance around circumference of the cement-casing interface in Figure 3-13. The data clearly reveal that the microannulus is not a uniform annular gap but is highly variable around the circumference. The measured apertures ranged from 0 (no aperture) to 560 μm. The cement and steel were in contact 18.6% of the circumference. The mean mechanical aperture was 132 μm if measurements of zero aperture are included and 163 μm if only nonzero apertures are considered. Forty eight percent of the measured apertures were less than 100 μm. The gas flow measurements made on specimen R6 at a 0.1 MPa confining pressure yielded a hydraulic aperture for the entire specimen of 175 μm.

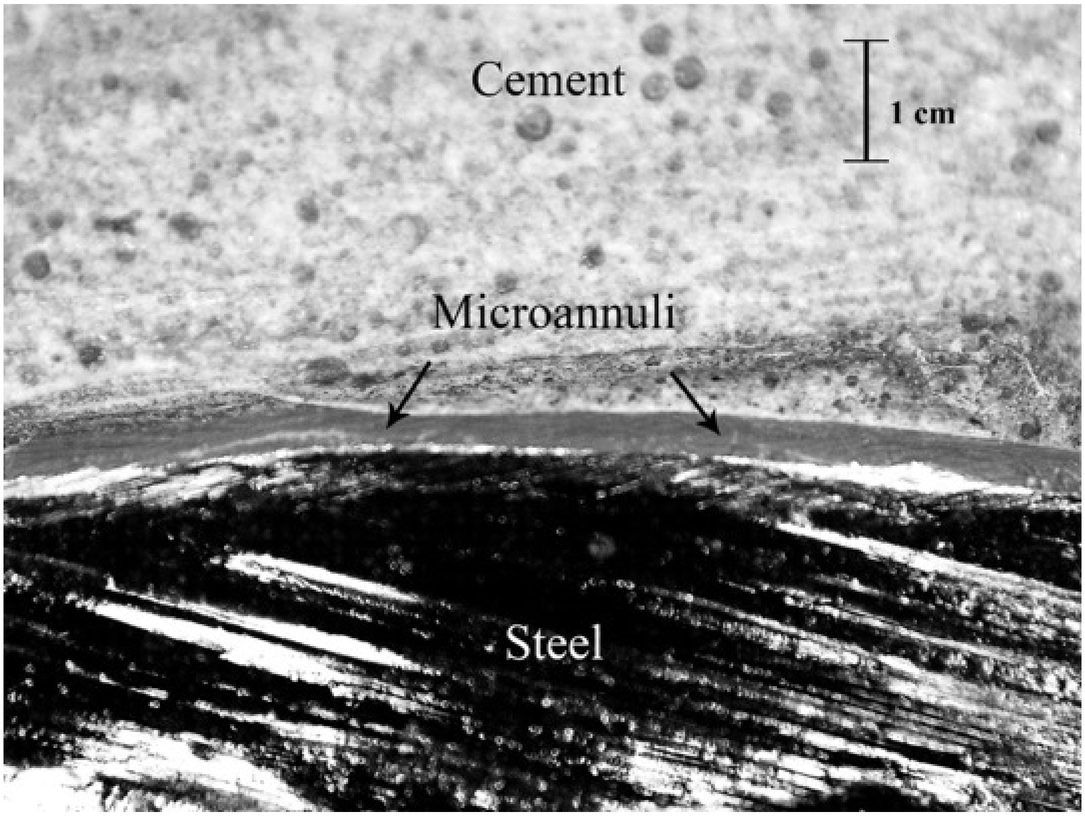

Figure 3-12. Photomicrograph of microannulus of specimen R6 injected with dyed epoxy

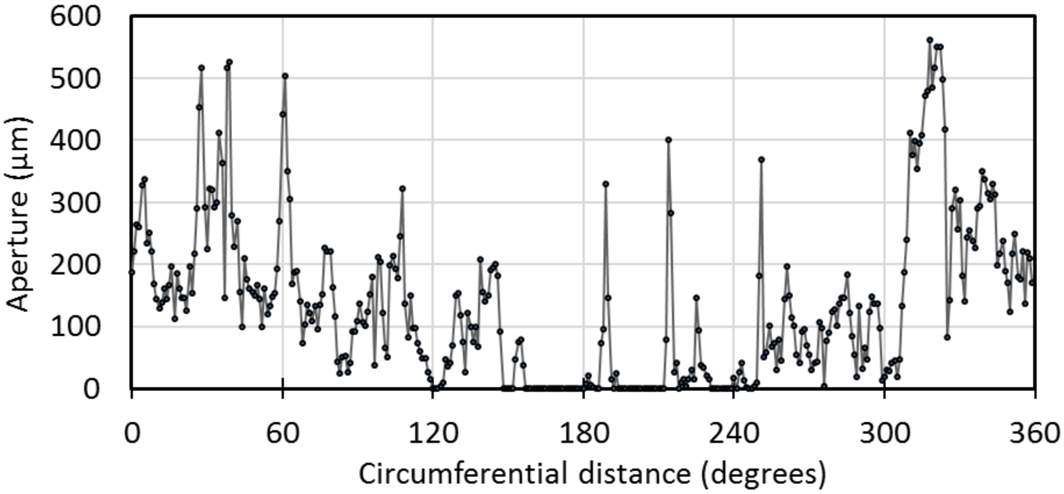

NOTE: Measurements (solid circles) were made at equal arc angle intervals of 1°.

Figure 3-13. Aperture vs. circumference distance expressed as arc angle on slice from specimen R6

The method of epoxy injection and microphotographs allows for detailed and high-resolution measurements of the microannulus. However, this is a destructive method and only provides information at discrete sections where the specimen has been sliced. Further, injecting epoxy under pressure could potentially propagate fractures within the specimen. It would be useful to compare results from this method with those from nondestructive methods, such as nonlinear acoustic imaging and X-ray computed tomography, to determine the relative attributes of the various methods.

3.4.8. Implications for Well Integrity

Microannuli at the cement-casing interface are a challenge for wellbore integrity. The continuous cement-casing contact along the length of a wellbore provides a potential connection from gas-bearing zones to overlying strata and the surface. Hydraulic apertures of cement-casing microannuli measured under varying stress conditions are in a range that can account for flow observed through leaky wellbores (refer to Figure 3-1). Corroded casing in contact with cement can also permit significant gas flow. These measurements suggest microannuli can permit sufficient flow to have a significant environmental impact by allowing contamination of water-bearing strata or by releasing gas to the surface.

While microannuli may permit undesirable gas flows in wellbores, their apertures can be small enough to be difficult to detect except by the presence of flow. In reviewing the current state of acoustic logging in wellbores, Wang et al. (2016) noted that detecting microannuli less than 100 μm is a challenge. Thus, there is a need to improve technologies to identify the presence of microannuli that are below current detection limits but are large enough to allow significant flow in wellbore systems.

Microannuli deform in response to casing pressure and temperature changes that will occur as a result of wellbore operations. Cycles of stress, as would be expected for many operations, may alternatively increase and decrease the hydraulic aperture of the microannuli. We found that microannuli never completely closed and remained capable of conveying significant flow under the range of stresses applied in this study. Thus, even when conditions in the wellbore system produce large compressive stresses across the cement-casing interface, the microannulus will likely remain conductive and a potential pathway for wellbore leakage.

Furthermore, it may be difficult to inject conventional cementitious-based materials to repair these very small leakage pathways. The penetration of cementitious materials into fractures is a function of the particle size of the cement (Axelsson et al. 2009; Jorne and Henriques 2016; Mirza et al. 2013). A common criterion for cement-based grout fracture penetration is that the aperture to be filled must be at least three times the maximum particle size of the cement (Eklund and Stille 2008). Using this criterion, a typical microfine cement with a maximum particle size of about 30 μm (Hansen et al. 2003) would not be expected to be an effective material for sealing the microannuli tested in this study. Microfine cement would not penetrate more than 30% of the mechanical apertures of specimen R6 (see Figure 3-13), which had the largest hydraulic aperture of all microannuli tested in this study. These results suggest that alternative repair materials such as polymers may be required to effectively penetrate microannuli and restore wellbore integrity.

Models of wellbore systems are being used to estimate the impact of design and operations on wellbore integrity (Zhang et al. 2017; Gray et al. 2009; Schreppers 2015), including microannuli formation and behavior. The usefulness of such models depends in part on how realistically they describe the behavior of components of the wellbore system. Results from this study suggest that these models should represent microannuli similar to a fracture with a rough surface that controls its response to stress changes and not as a uniform, smooth-walled annular gap. Models of microannuli should include the nonlinear and hysteretic response of the hydraulic aperture with stress.

3.5. Conclusions

We used a specially designed pressure vessel to obtain a unique data set of gas flow measurements through cement-casing microannuli as a function of external confining pressure, internal casing pressure and temperature, and pore pressure. Because the specimens were relatively permeable, the measured gas flow often included both viscous and inertial components. The flow was well described by the Forchheimer equation, which reduces to Darcy's equation when the inertial flow is negligible. Permeabilities derived from the Forchheimer equation yielded values that were often significantly larger (>100%) than would be interpreted if inertial flow was ignored.

Our results indicated that wellbore specimens with microannuli generated relatively large effective wellbore permeabilities compared to intact specimens, and consequently are capable of transmitting large amounts of flow. The flow rate through specimens with microannuli was approximately 10^3 to 10^5 times the flow rate of intact wellbore cement under comparable conditions. The interpreted hydraulic aperture of the microannuli ranged from less than 10 μm to more than 100 μm which is in the range of hydraulic apertures interpreted for some leaky wellbores (Checkai et al. 2013). We found there can be considerable variability between specimens that have a microannulus created in the same manner, such as those formed by release film or with corroded casing.

We found that microannuli are fracture-like in how they deform in response to stress changes. Increased normal stress across a microannulus results in more contact between the two surfaces with a corresponding increase in stiffness, resulting in a nonlinear fracture closure and consequently a nonlinear hydraulic aperture and permeability decrease with stress. Hysteresis in the response of microannuli is consistent with plastic deformation of asperities.in contact along the cement-casing interface. Plastic deformation of asperities would give rise to an increased stiffness after the initial loading and would produce the nonrecoverable reduction in the hydraulic aperture often observed after the initial loading. The hydraulic aperture changes from subsequent loading and unloading tended to be largely recoverable. Even when loaded to large external pressures, the hydraulic apertures remained open and capable of conveying significant flow. Once de-bonded, the microannuli remained significantly more permeable than the wellbore cement and application of stresses across the microannuli did not completely close the microannuli.

The lower the external confining pressure, the more effect casing pressure had on the hydraulic aperture of the microannulus. The microannuli response was less sensitive to casing pressure changes compared to confining pressure changes due to stiffness and geometric differences between loading the exterior of the cement sheath and loading the interior of the casing. In one instance, the cement sheath failed when the casing pressure was increased significantly above the confining pressure, consistent with tensile stresses being induced in the cement sheath from casing pressures. We also demonstrated that the microannulus was sensitive to temperature changes within the casing; the hydraulic aperture of the microannulus increased in response to a temperature decrease inside the casing. We found that the hydraulic aperture of the microannulus was affected by changes in the pore pressure within the specimen. The hydraulic aperture decreased as pore pressure was decreased and confining pressure was held constant, consistent with the microannulus deformation responding to an effective stress. We also found that specimens created with corroded casing had flow rates that were much greater than that for intact specimens, implying that the corrosion at the contact between the cement and casing created a flow path comparable to a microannulus from de-bonding.

Microphotographs of the cement-casing interface at one cross-section were used to provide measurements of the actual (mechanical) aperture around the entire circumference. These data reveal that the aperture was highly variable along the circumference, and over some portion of the circumference there was a tight contact between the cement and casing; that is, at that location there was no discernable microannulus. These results indicate that the microannulus is not a uniform annular gap but is highly variable around the circumference.

The measurements and observations reported here only apply to the types of microannuli and the range of stress conditions used in this study. Some wellbores may be subjected to greater external confining pressures, internal casing pressures and temperatures than those used herein. Further, microannuli may be formed by mechanisms different than used in this study, such as cement shrinkage. Additional wellbore testing that incorporates other realistic conditions and configurations including curing under downhole conditions is suggested. A numerical model of wellbore behavior that includes the behavior observed in this study would allow extrapolating these results to other geometries and conditions.

3.6. Acknowledgements

This material is based upon work supported by the U.S. Department of Energy (DOE) National Energy Technology Laboratory (NETL) under Grant Number DEFE0009562. We acknowledge the contributions of Rashid Ahmad and Joshua Ellison to the conduct of the laboratory measurements.

3.7. Supplemental Material

An expression analogous to the cubic law for flow between parallel plates is derived for flow through an annular gap between two concentric cylinders. This derivation follows directly from the derivation of the cubic law for flow between parallel plates given by Zimmerman and Bodvarsson (1996). The problem geometry is illustrated in Figure 3-14.

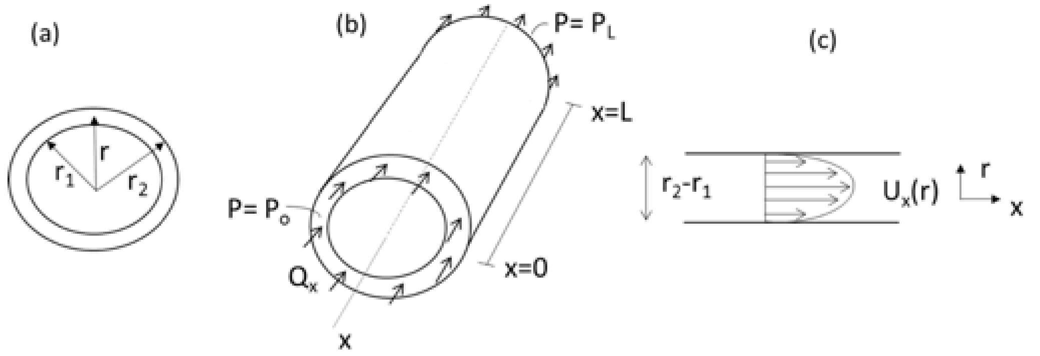

Figure 3-14. (a) Cross-section of concentric cylinders in *r-θ* plane; (b) perspective view of concentric cylinders identifying constant pressure boundary conditions and showing flow in annular gap; and (c) profile of flow velocity in annular gap

Flow is modeled using the steady-form of the Navier-Stokes equation and laminar flow is assumed. Constant pressures are assumed at $x=0$ and $x=L$, and a uniform pressure gradient (∇P) parallel to the x-axis is assumed within the annular gap. In this case, the flow velocity exists only in the x-direction, and the Navier-Stokes equation reduces to

$$\nabla^2 u_x(r) = \frac{\nabla P}{\mu}$$ *Equation 3-5*

Using no-slip boundary conditions at r_1 and r_2, the velocity profile within the annular gap is

$$u_x(r) = \frac{\nabla P}{2\mu}\left(r^2 - (r_2 + r_1)r + r_1 r_2\right) \qquad \textit{Equation 3-6}$$

The flow rate (Q_x) through the annular gap is found by integrating this velocity over the area of the annular gap

$$Q_x = 2\pi \int_{r_1}^{r_2} u_x(r)\, r\, dr = -\frac{\nabla P}{12\mu}\pi\left(r_2^4 - r_1^4 + 2\, r_1^3\, r_2 - 2r_2^3 r_1\right) \qquad \textit{Equation 3-7}$$

The flow rate through the annular gap using the cubic law approximation is given by

$$Q_x = -\frac{\nabla P}{12\mu} w\, h^3 \approx -\frac{\nabla P}{6\mu}\pi\, r_1 (r_2 - r_1)^3 \qquad \textit{Equation 3-8}$$

where the hydraulic aperture h is $(r_2 - r_1)$ and the length w is $2\pi\, r_1$. The error in using the cubic law approximation is given in Figure 3-15 as a function of the casing radius (r_1) for 3 different annular gap sizes. This error is considerably less than 1% for the casing dimensions and microannuli sizes for typical field conditions as well as the laboratory tests reported here.

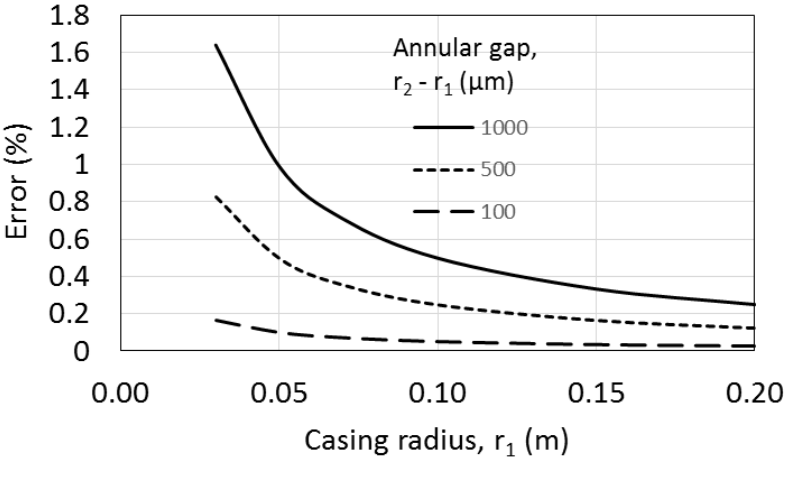

Figure 3-15. Error from using cubic law approximation as a function of casing radius and annular gap size

4. CHARACTERIZATION OF WELLBORE MICROANNULI

4.1. Overview

Wellbores are comprised by a steel casing surrounded by a cement sheath. The microannulus is the typically very small annular or degraded space that may develop between cement and casing that has been identified as a common leakage pathway in wellbore systems. Although data regarding the actual size and character of wellbore microannuli are limited, the hydraulic aperture of the microannulus can be estimated from pressure build up or flow measurements at the wellhead. Such information can be misleading, however, as it represents microannuli as uniform annular gaps along the wellbore. This study aims to provide a quantitative measure of the variability of the microannuli. We generated wellbore-based samples with microannuli between the steel casing and cement, and calculated their hydraulic aperture and permeability by flowing gas through the microannuli. We then injected dyed epoxy into the microannuli, cut the specimens into five circumferential sections per sample, and used microphotographs to measure microannulus aperture size and contact between the steel and the cement to generate microannulus profiles for each section. These measurements are unique as they provide a quantitative measure of the variability of the microannulus with a resolution as low as 3 μm. Aperture sizes were fitted to different statistical distributions, most frequently lognormal and gamma. Capillary entry pressure (*CEP*) for gas displacing brine in the microannulus was estimated from measured aperture size. *CEP* estimated from actual aperture size was generally much greater than that estimated from the hydraulic aperture of the entire specimen, resulting in a wide range of values. Measured aperture sizes were used to evaluate possible microannulus repair by estimating the penetration of cementitious materials. The data showed that the repair using cementitious materials is unlikely to be effective for microannuli with a hydraulic aperture <50 μm.

4.2. Nomenclature

α	fitting criteria
$\bar{z}$	arithmetic mean (L)
β	inertial coefficient
χ^2	statistical value $\Gamma(A)$ gamma function
γ	continuous location parameter
λ	interfacial tension between phases (MT^{-2})
μ	fluid viscosity ($ML^{-1}T^{-1}$)
∇	gradient
ρ	density (ML^{-3})
σ	standard deviation (L)
σ^2	variance of the mechanical aperture (L^2)
θ	contact angle (degrees)
A	cross-sectional area involved in the flow (L^2)

a	aperture size (L)
B	continuous scale parameter
C	continuous shape parameter
CEP	capillary entry pressure ($ML^{-1}T^{-2}$)
CEP_h	capillary entry pressure from hydraulic aperture ($ML^{-1}T^{-2}$)
CEP_i	capillary entry pressure from individual aperture measurements ($ML^{-1}T^{-2}$)
E_i	expected aperture value for a given distribution (L)
h	aperture measurement in image processing (L)
h_a	hydraulic aperture (L)
i	hydraulic gradient ($MT^{-2}L^{-2}$)
K	continuous shape parameter
k	permeability (L^2)
l	length of the specimen (L)
M	molecular weight (M/mol)
O_i	discrete value (L)
P	pressure ($ML^{-1}T^{-1}$)
p_1	upstream pressure ($ML^{-1}T^{-2}$)
p_2	downstream pressure ($ML^{-1}T^{-2}$)
Q	volumetric flow rate (L^3/T)
R	universal gas constant ($ML^2T^{-2}K^{-1}mol^{-1}$)
T	temperature (K)
t_w	width of the flaw (L)
w	width of each measurement in the image processing (L)
x	nonlinear term (L^{-1})
y	left-hand side of Forchheimer's equation (L^{-2})
z	discrete value (L)

4.3. Introduction

Wellbores are constructed for access to the subsurface for a wide variety of purposes, including gas and hydrocarbon storage, energy production and waste disposal. In the United States alone, over 2.6 million wellbores have been drilled since 1947 (Davies et al. 2014). The most common wellbore configurations comprise a steel casing surrounded by an annular cement sheath. A main function of the cement is to seal the annular space between the casing and the host rock formation, preventing any fluid flow along the wellbore. The cement also protects the casing from corrosion and makes the wellbore more structurally sound.

The sealed annular spaces within many wellbores leak; leakage is often detected through pressure building behind the casing (i.e., sustained casing pressure) and surface casing vent flow (Checkai et al. 2013). The percentage of leaky wellbores varies with the type of wellbore (e.g., onshore-offshore) and age, but several studies have reported rates of barrier failure higher than 30% (Peng et al. 2007; Brufatto et al. 2003; Chilingar and Endres 2005; Vignes 2011; Yuan et al. 2013).

Gas leakage can create hazardous surface conditions (Bielicki et al. 2014; Gasda et al. 2004). Wellbore leakage may also serve as a pathway for contamination of groundwater resources by fluids from hydrofracturing operations in underlying gas-bearing strata. Several studies (Jackson et al. 2013; Osborn et al. 2011) found gas contamination in drinking water near hydrofracturing operations, and suggested wellbore leakage was one of the likely causes. Geologic CO_2 sequestration, a strategy for reducing greenhouse gases in the atmosphere, also relies on wellbore integrity. Confinement of CO_2 within the intended host formation is a fundamental requirement for successful CO_2 sequestration which depends in large part on the hydraulic seal of wellbores associated with these facilities (Bachu and Bennion 2009; Carey et al. 2007; Zhang and Bachu 2011). Poor wellbore integrity can also compromise the function of facilities for the underground storage of fluids (LeNeveu 2011; Berest et al. 2007) and the production of geothermal energy (Southon et al. 2005).

Potential leakage pathways in a wellbore system include the interfaces along casing-cement and cement-rock contacts, fractures and voids within the cement sheath and failed casing (Gasda et al. 2004). There are many possible mechanisms for creating these leakage pathways in wellbore systems. Thermal stresses that arise from cement hydration or wellbore operations could debond interfaces or affect the integrity of the cement (Bois et al. 2011; Kjller et al. 2016; Lavrov et al. 2015; Viswanathan et al. 2008; Vralstad et al. 2015). Flaws introduced during construction, such as mud channels, could also be leakage pathways (Lecampion et al. 2013). Excessive fluid pore pressures can debond the cement-casing interface (Feng et al. 2017; Lecampion et al. 2013). Additionally, stresses from the adjacent host rock acting on the cement-casing system can change (e.g., creep) and create fractures or debond interfaces.

The microannulus is the typically very small annular or degraded space that may develop between cement and casing (Gasda et al. 2004) that has been identified as a common leakage pathway in wellbore systems (Gasda et al. 2004; Bellabarba et al. 2008; Huerta et al. 2009). The presence of microannuli is widely referred to in the literature (Gasda et al. 2004; Bellabarba et al. 2008; Huerta et al. 2009; Dusseault et al. 2014), although there is little direct information about their nature and size. Cement bond logs are commonly used in wells to evaluate the quality of the cement behind the casing (Gasda et al. 2004; Bellabarba et al. 2008; Dusseault et al. 2014; Duguid et al. 2014), including inferring the presence of microannuli. These logging methods do not provide a direct measure of the microannulus and generally will not be able to detect microannuli less than about 100 μm (Wang et al. 2016). Specific mechanisms for the formation of microannuli include cement shrinkage and/or from temperature and pressure changes within the casing (Bois et al. 2011; Gray et al. 2009). Laboratory tests on samples of casing set in a cement sheath demonstrated that microannuli can be formed by pressure cycling (Goodwin and Crook 1992; Boukhelifa et al. 2004) and thermal cycling within the casing (Vralstad et al. 2015; Andrade et al. 2015). Stormont et. al. (2018) measured gas flow through microannulli under different confining and casing pressures. They found that microannuli are fracture-like in how they deform in response to stress changes. Even when loaded to large external stresses, microannuli remain open and able to convey significant flow.

Numerical models of wellbore systems that include microannuli formation demonstrate that cycles of casing pressure can induce plastic behavior in the cement sufficient to produce a microannulus (Bois et al. 2011; Gray et al. 2009; Zhang et al. 2017). All these models assumed the microannulus was a smooth gap around the steel casing and did not characterize the likely fracture-like nature of the microannulus. Regarding hydraulic fracturing, Wang and Dahi Taleghani (2017) presented a cohesive zone model to evaluate the cement sheath integrity, which will likely result in a nonuniform microannulus geometry.

Microannulus size can be estimated from leakage observed through the wellbore. If all of the flow is assumed to occur through the microannulus and it is assumed to be a smooth, open fracture, then the hydraulic aperture of the microannulus is given by the so-called cubic law (Witherspoon et al. 1980):

$$h_a^3 = \frac{12Q\mu}{twi} \qquad \textit{Equation 4-1}$$

where h_a is the hydraulic aperture, Q is the volumetric flowrate, i is the hydraulic gradient, μ is the fluid viscosity and tw is the width of the flaw which is assumed to be the outer circumference of the casing. Using this approach, Checkai et al. (2013) interpreted surface-casing vent flow data from 238 wells as microannulus hydraulic apertures. They found 85% of the apertures ranged from 5 to 100 μm.

The hydraulic aperture is generally not equivalent to the measured or actual average aperture in fractured cement and rocks (Akhavan et al. 2012; Hakami and Larsson 1996; Renshaw 1995), presumably due to the roughness and tortuosity of the fracture. These studies highlight that the hydraulic aperture derived from flow measurements does not provide a direct measure of the actual (or mechanical) aperture of a microannulus and offers no information about its spatial variability.

A detailed understanding of the nature of the micoannulus formed at the cement-casing interface is important for a number of reasons. The size of the apertures comprising the microannuli is a fundamental factor in understanding flow through the microannulus (single phase or multiphase) of the different possible fluids present (gas, hydrocarbons, brine). For example, the pressure at which gas will displace brine or some other fluid from the microannulus will depend on the aperture size. Repair of microannuli, which is sometimes attempted to restore the integrity of the wellbore, depends on the ability of the repair material to penetrate the apertures that comprise the microannulus. In addition, the response of the microannuli to different stresses (i.e. thermal, operational) will be a function of the contact between the cement and steel surfaces that form the microannuli similar to how fractures in rock and cement behave in response to stress changes.

In order to develop a better understanding of microannuli, wellbore specimens consisting of a steel casing surrounded by a cement sheath were created and tested. Microannuli of different sizes were included in these specimens. Flow through the microannuli was measured, which allowed to calculate the hydraulic aperture. Inviscid epoxy was then injected into the microannuli, and the specimens were sliced to allow microphotographs to be taken continuously around the cement-steel interface. From the high-resolution images aperture as a function of position along the microannuli was measured. The principal advantage of this technique is the resolution (as low as 3 μm); in contrast, X-ray computed tomography measurements have a resolution for samples of comparable size of >100 μm (Crandall et al. 2010), which is an order of magnitude greater than the size of apertures that can have a large impact on the effective wellbore permeability (Stormont et al. 2018).

4.4. Materials and Methods

Specimens of a hollow steel casing surrounding a cement sheath were constructed to simulate a wellbore configuration (Figure 4-1). The casing was carbon steel with an outer diameter of 60 mm and a thickness of 2.35 mm. The ratio between the diameter and the thickness is consistent with the range used in many oil gas wells (Gatlin 1960). The cement was prepared following the American Society of Testing and Materials (ASTM) (ASTM 2014).

American Petroleum Institute (API) Class G cement was mixed with silica fume at a ratio of 0.1 to provide additional strength to the relatively thin sheath. The water/binder ratio was 0.3 and superplasticizer (2% by weight of water) was added. Typically, the water to binder ratio used for wellbore cement is 0.45 (API 2009) and no additives are required. A relatively low water/binder ratio was used to avoid bleeding. The use of different water/binder ratios or different additives could affect the results as they alter the flowability, composition and porosity of the cement. The cement was cast around the steel casing in polyvinyl chloride (PVC) molds. After 24 hours, specimens were unmolded and placed in a curing room for 28 days (100% humidity, 24°C). Specimens were 185-mm long and the cement sheath was 30-mm thick.

Microannuli between the steel casing and cement were created in the wellbore specimens using two different techniques. To create relatively large microannuli, the steel casing was wrapped with a thin (25 μm) plastic release film and the cement was cast around it. After 24 hours, the casing was pulled from the cement sheath, the film removed, the casing reinserted into the cement sheath, and the specimen was cured for an additional 28 days. Subsequent gas flow testing of specimen with microannuli formed by this method indicated hydraulic apertures were greater than 50 μm.

To create microannuli with smaller apertures (hydraulic apertures less than 50 μm), the steel casing was thermally debonded from the cement. Dry ice (−79°C) was placed inside the casing of a cured specimen and both ends of the steel casing were tapped with a rubber plug to preserve the temperature. After 5 minutes, the dry ice was removed and warm water (40°C) was added for another 5 minutes. The low temperature contracts the casing, pulling it apart from the cement, and the elevated temperature expands the casing. The process was repeated 4 times to ensure debonding. Subsequent gas flow testing of specimens with microannuli formed by this method indicated hydraulic apertures were less than 50 μm. Both methods to create the microannuli are summarized in Figure 4-2.

Three wellbore specimens were included in this study (A, B, and C). Wellbore Specimens A and B apertures were generated with the release film method, and the thermal debonding method was used to generate the aperture of Specimen C.

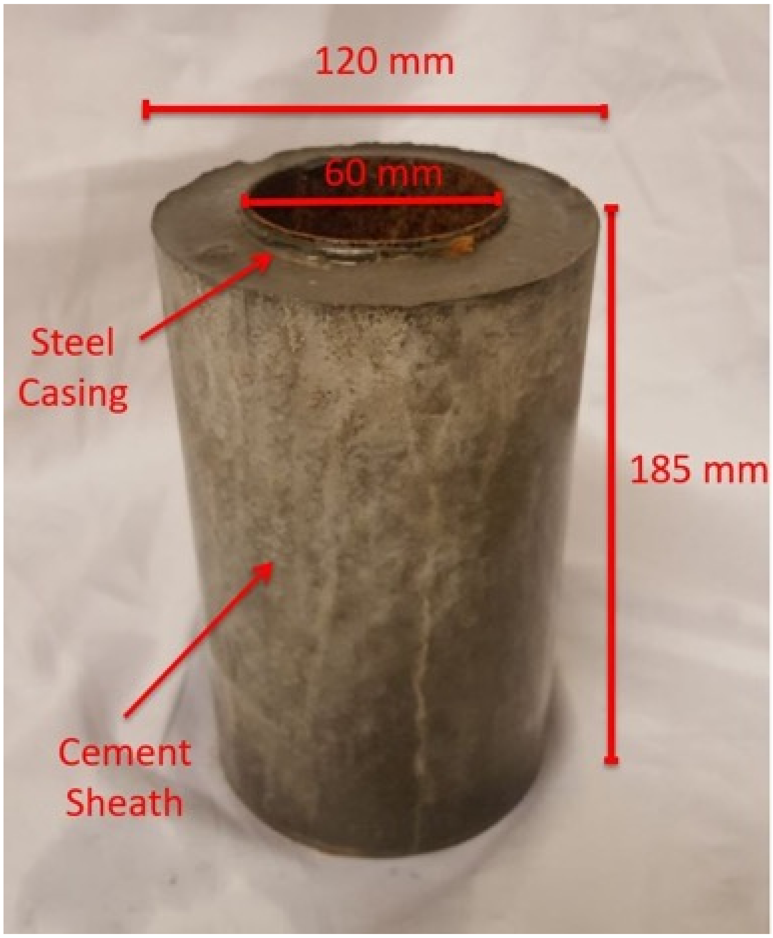

Figure 4-1. Wellbore specimen, comprised of a steel casing and a cement sheath

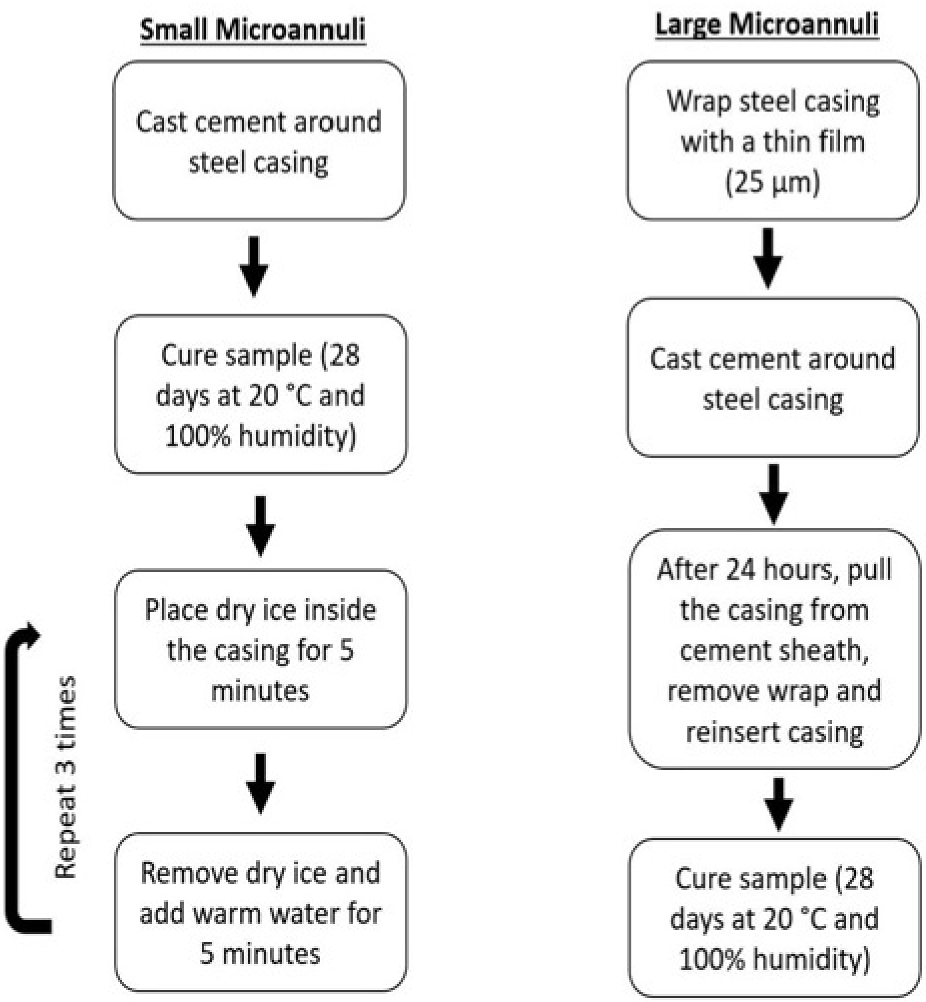

Figure 4-2. Steps to create the microannuli

4.4.1. Gas Flow Measurements

Specimens were placed in a pressure vessel and subjected to hydrostatic stress conditions. Gas flow measurements were made along the axis of the specimens and thus included the microannulus. The test system is shown in Figure 4-3.

The pressure vessel was capable of applying independent confining and casing stress up to 35 MPa and 20 MPa, respectively. Confining stress was regulated through a port on the side of the pressure vessel. Hydraulic oil was pumped, changing the stress applied to a flexible membrane that was in contact with the cement sheath. All gas flow measurements reported here were made with a minimum confining stress (<1 MPa) in order to have a comparable stress condition to that in the subsequent epoxy injection. An additional port in the end caps was used to perform gas flow experiments. Gas was introduced into the pressure vessel using the upstream port and flowed through the cement sheath and the steel-cement interface. Steady-state flow rates were measured using flowmeters (from 5 to 150 standard cm^3/s, full-scale of the flowmeter) with an accuracy of 1% of full-scale connected to the downstream port. The gas pressure applied was read using a pressure gauge before the upstream port.

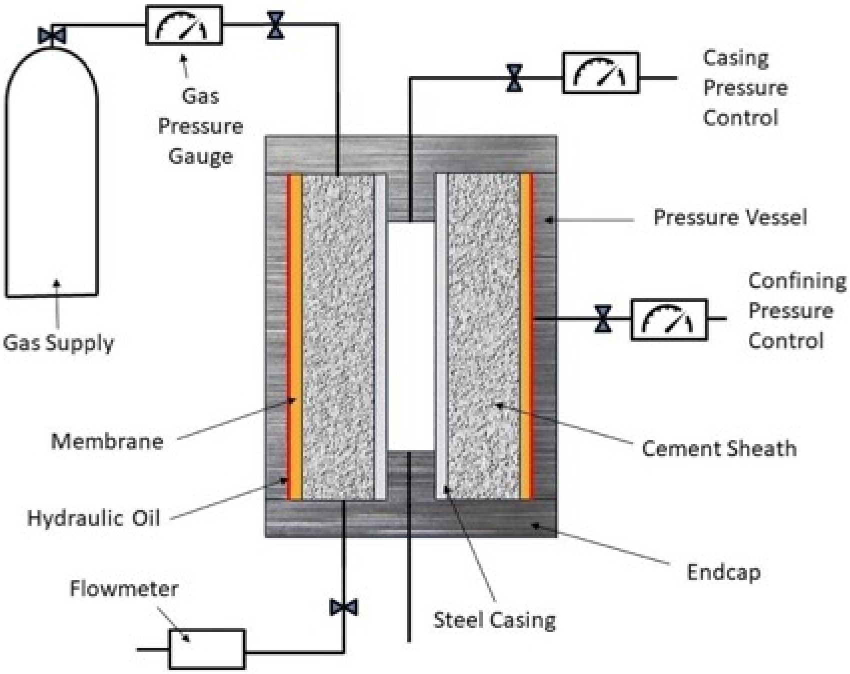

(a)

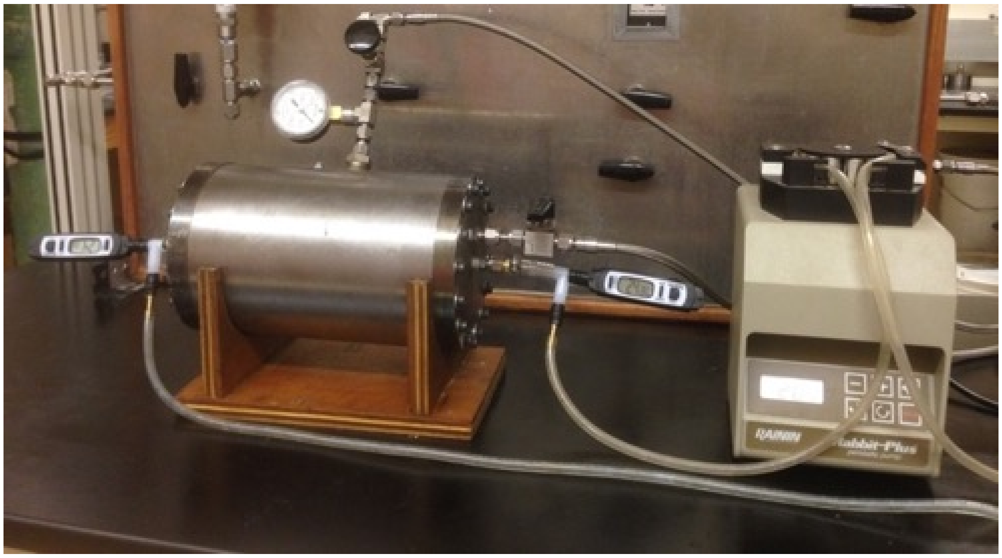

(b)

Figure 4-3. (a) Schematic of the pressure vessel system used to test gas permeability of the wellbore specimens and (b) picture of the pressure vessel used

Permeability was interpreted from the gas flow measurements using Darcy's law.

$$k = \frac{Q\mu}{\nabla PA} \qquad \text{Equation 4-2}$$

where k is the permeability, Q the volumetric flow rate, A the cross-sectional area involved in the flow, ∇P the pressure gradient and μ the fluid viscosity.

Darcy's law states that the flux changes linearly with the change in pressure difference. With the test conditions used, nonlinear or inertial flow often occurred. In these conditions, the flux varied nonlinearly with the pressure gradient and the flow could be described by the Forchheimer equation (Forchheimer 1901):

$$\nabla P = \frac{\mu}{kA}Q + \frac{\beta\rho}{A^2}Q^2 \qquad \text{Equation 4-3}$$

which is Darcy's law plus a term to account for the nonlinearity. β is the inertial coefficient and ρ is the density of the gas. Assuming an ideal gas, this equation can be rewritten as (Zeng and Grigg 2006)

$$\frac{MA\left(p_1^2 - p_2^2\right)}{2RT\mu l\rho Q} = -\frac{1}{k} + \beta\frac{Q\rho}{\mu A} \qquad \text{Equation 4-4}$$

where M is the molecular weight of the gas, R the universal gas constant, T is the temperature, p_1 the upstream pressure, p_2 the downstream pressure, and l the length of the specimen. The terms in Equation 4-4 could be grouped; referring to the left part of the equation y and the nonlinear term x. Equation 4-4 can be expressed as

$$y = -\frac{1}{k} + \beta x \qquad \text{Equation 4-5}$$

which defines a linear relation between x and y. Plotting the x and y terms for a series of measurements allow obtaining the inertial coefficient β as the slope of the straight line and the inverse of k as the intersection of the straight line with the y axis. To obtain the data necessary to determine k and β, a series of flow rates were measured as a function of the gradient. The gradient was changed by adjusting pressures on the upstream and downstream sides of the specimen. Once the permeability value is obtained at the specific stress state, the cubic law (Equation 4-6) is used to interpret this permeability as a hydraulic aperture of the microannulus.

$$h_a^3 = \frac{12kA}{tw} \qquad \textit{Equation 4-6}$$

where h_a is the hydraulic aperture, k is the permeability of the wellbore system estimated from the observed leakage using Forchheimer's correction, A is the cross-sectional area of the entire specimen and w is the width of the microannulus. In this case, w is the circumference of the outer diameter of the steel casing. Use of Equation 4-6 implies that all of the flow passes through the microannuli. This assumption is based on our experimental data; microannuli have a transmissivity many orders of magnitude higher than the intact cement. Another assumption is that the flow between two parallel plates is equivalent to the flow between two concentric cylinders; this assumption produces negligible error (Stormont et al. 2018).

4.4.2. Specimen Preparation for Image Analysis

At the conclusion of the gas flow measurements, the specimen was removed from the pressure vessel and Novolac epoxy was injected in the microannulus and allowed to harden. Novolac epoxy was used for its excellent flowability. The injection was conducted outside of the pressure vessel to avoid the epoxy hardening withing the access tubing of the pressure vessel. Novolac is a two-component epoxy mixed at a 2.2:1 resin-hardener ratio. The resin is a mixture of Novolac backbones with epichlorohydrin epoxy resin including silane. The hardener is diethylenetriamine (DETA), phenol, 4,4-(1-methylethylidene)bis-, and tetraethylene-pentamine. Rhodamine B was added (0.1% of the epoxy weight) to epoxy to yield bright pink fluorescence color, which aided microannulus characterization by improving the epoxy contrast with the cement and the steel.

To prepare for the epoxy injection, samples were placed into 101.6-mm diameter PVC molds and epoxy was poured to surround the sample to ensure the sealing between the specimen and the PVC mold and assuring the integrity of the specimen during the subsequent cutting. Rubber caps were placed inside the hollow steel casing, thus the only flow path available for epoxy with rhodamine B was the microannulus along the cement-steel interface (Figure 4-4).

The epoxy-rhodamine B preparation was poured over the top surface of the sample, which was placed in the injection setup. Air pressure (65 kPa) was applied through the top endcap to squeeze the epoxy into the microannulus.

After injection, some epoxy was visible on the bottom of the specimen, which indicated that epoxy travelled through the length of the specimen along the microannulus. Once injected, the epoxy cured for a week and then specimens were sectioned horizontally and polished to remove imperfections. A brick saw (MK Diamond Products, Inc.), equipped with a 355.6-mm diameter, 3.5-mm-thick concrete blade was used to section the specimens which were held in a vise. The sectioned specimens were polished with a belt sander. Progressively finer sandpaper was used (grit sizes from 50 to 120). It was necessary to polish the specimen from the casing outward to preserve the microannuli and so that the cement was not smeared over the microannulus.

For the nomenclature of the sectioned specimens, the first letter refers to the Specimen (A, B or C), followed by a digit that indicates the position of the specific circumferential section in the specimen

(1, top, to 5, bottom). This is followed by a letter that defines the face of the piece (a, top face; b, bottom). For instance, A.3.a is the top face of the cross section labeled as 3 of wellbore Specimen A

Figure 4-4. Specimen in the PVC mold with surrounding epoxy, ready to be injected

4.4.3. *Image Analysis*

Microphotographs were taken along the circumference of the steel casing to describe the aperture size and distribution. Photographs of wellbore Specimens A and B were taken with a universal serial bus (USB) camera with 5 MegaPixels (MP) using 100× magnification and 3-µm resolution. Microphotographs of Specimen C were taken with an USB 5-MP camera and 220× magnification, which results in a (0.4 µm resolution). The higher magnification was needed to accurately measure the small apertures in this specimen. For Specimen C, an automated rotating photography system setup (Figure 4-5) was constructed. A servo motor was attached to a mount that fit into the steel casing of the sectioned specimen and, controlled by an Arduino Uno R3 Microcontroller, was set to rotate 1.5° and stop for 5 seconds. The camera automatically acquired an image while the specimen was not moving.

The series of images taken along the circumferential section were merged using the built-in Adobe Photoshop 2014 photomerge function (Figure 4-6). This function becomes more computationally expensive as the number of photographs increases, since it gathers all photographs simultaneously and attempts to find matching parts. The function worked efficiently with circumferential sections of Specimens A and B, but for the Specimen C (with twenty times as many images per circumferential section), computational time increased substantially and unsuccessful merges were more frequent.

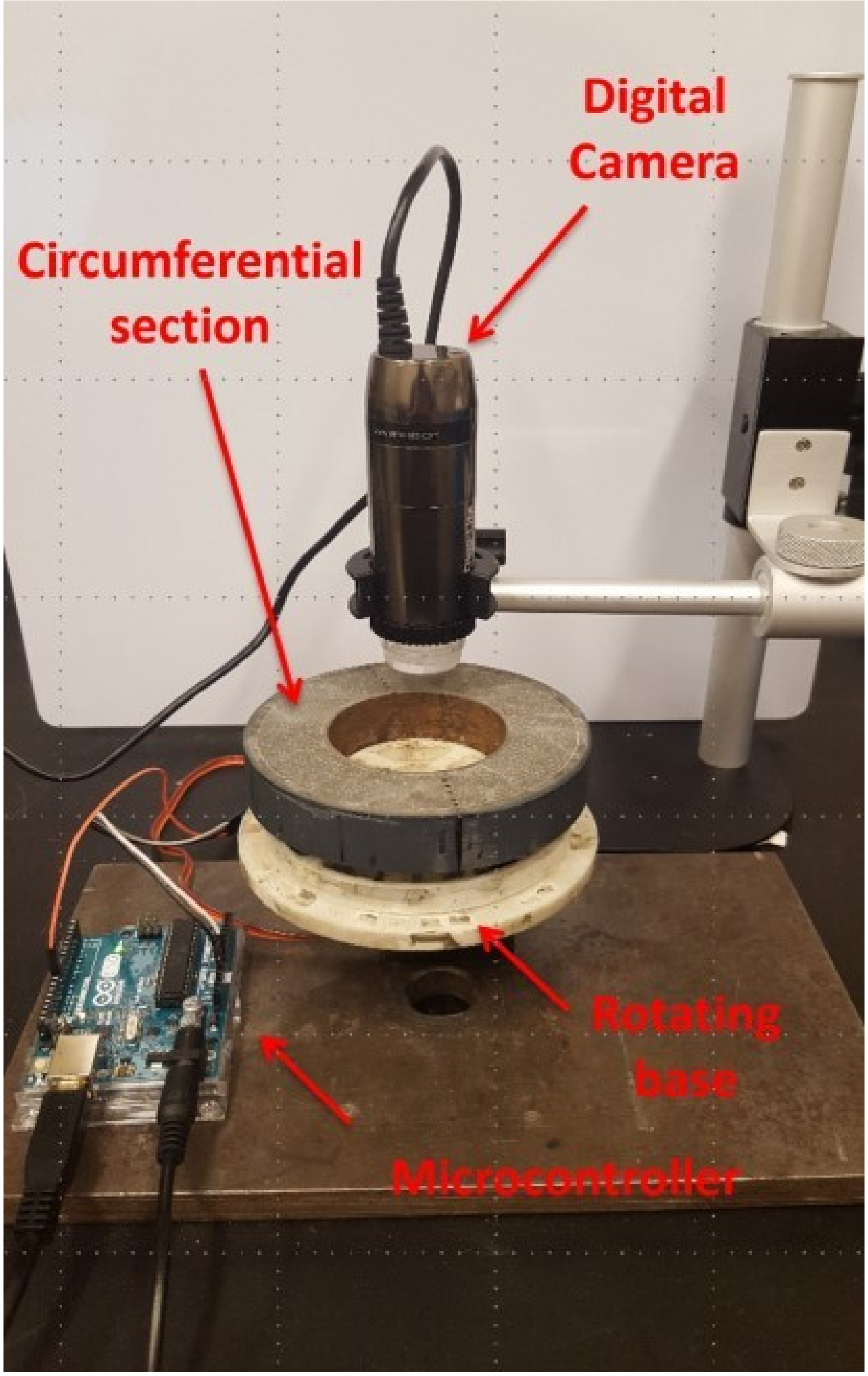

Figure 4-5. Automated rotating photographic system, comprised by a servo motor.

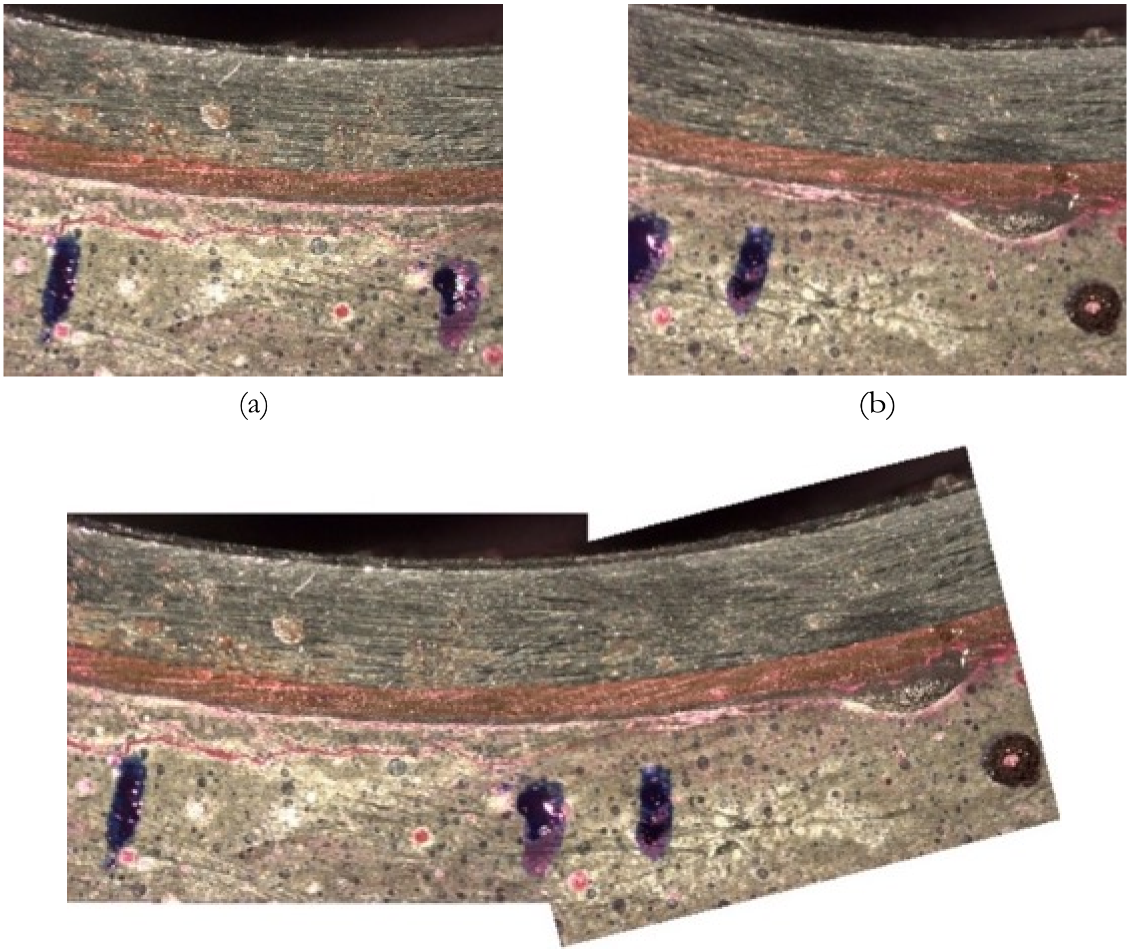

(a)

(b)

(c)

Figure 4-6. Example showing two consecutive images ([a] and [b]) and the merged image (c) done using Photoshop function photomerge

4.4.4. Aperture Measurement

After the photograph merger, ImageJ software version 1.51r (National Institutes of Health, Bethesda, MD) was used for the remainder of the processing. The merge was split into smaller sections of equal width (represented as w in Figure 4-7). The fluorescent rhodamine B in the epoxy served as a tracer of the filled microannulus, which allowed us to establish a color threshold to select the microannulus color. The ImageJ function,"Analyze particle", was used to measure the area (in pixels) within the threshold, which provided a precise measurement of the microannulus area. Dividing this area by the width of the split (w) yielded an average height of the microannulus for each section.

The width size was selected to be small enough to capture variability of the aperture yet as long as possible to minimize computational cost. Wellbore Specimens A and B were split in 360 equal sections (each 510 μm) and C was split in 7200 equal sections of width w (25 μm). Wellbore Specimen C was split in smaller w than Specimens A and B because the aperture size was considerably smaller and less continuous.

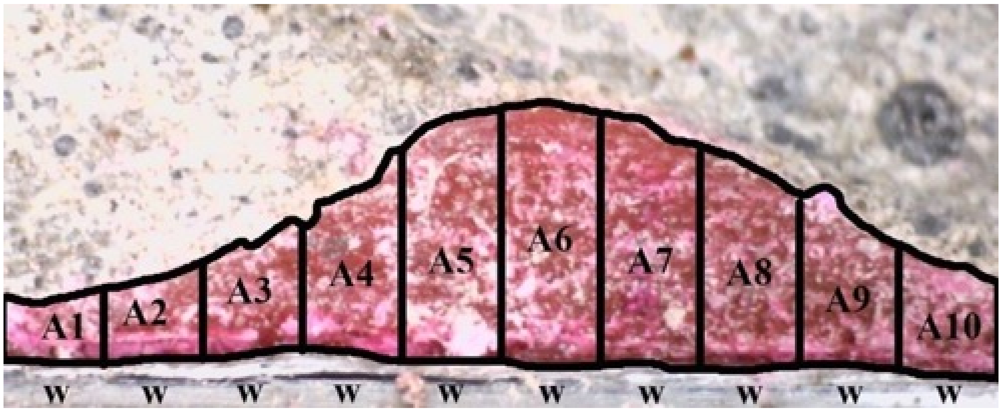

(a)

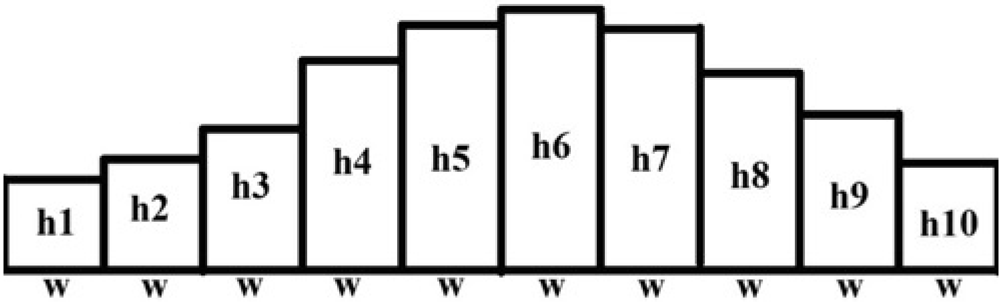

(b)

NOTE: The areas measured (a) over constant widths w (A1, A2, A3...) are divided by the total width to obtain height measurements (h1, h2, h3...) (b). The aperture is interpreted as different heights, spaced at constant w.

Figure 4-7: Interpretation of the apertures

4.4.5. Information Obtained from This Analysis

Aperture size as a function of circumferential distance was obtained using the method indicated above. To describe each circumferential section, contact percentage, average mechanical aperture with and without zeros, geometric mean, hydraulic aperture calculated from the cubic law (Equation 4-6), and the modification of the cubic law that accommodate surface roughness (Equation 4-8), developed by Renshaw et al. (Renshaw 1995). Contact is defined as the absence of an observable aperture. Contact percentage is the number of splits with no area divided by the number of measurements made (360 for Specimen A and B, 7200 for Specimen C). Mechanical mean with and without zeros is presented here to show a meaningful conceptual difference; that is, to define whether we refer to the microannulus alone or to the cement-casing interface. When referring to the microannulus only, the zero values should not be included. By definition, the microannulus is the space between the cement and the steel casing; if there is no aperture, there is no microannulus. If the entire cross-section was discussed, the zero values should be included. Piggot and Elsworth (1993) showed that the hydraulic aperture could be represented by the geometric mean and Dagan (1993) proved that it could be accurate for lognormal aperture distributions, which is a reasonable approximation of the distributions that were found (refer to section “Fitting aperture data to distributions” for more information). The hydraulic aperture is obtained from the cubic law using the equation:

$$h_a = \frac{\sum_{i=1}^{n} \sqrt[3]{w_i * h_i^3}}{\sum_{i=1}^{n} w_i} \qquad \textit{Equation 4-7}$$

where w_i is the width of the measurement, which is constant in all measurements, h is the measure of aperture, and casing circumference length is the sum of all w_i. Renshaw’s modification of the cubic law was developed under the assumption that apertures follow a lognormal distribution, which seems reasonable from what was observed in our experimental data (refer to section “Fitting aperture data to distributions” for more information). The equation is

$$h_a = \bar{x} * \left(1 + \frac{\sigma^2}{\bar{x}}\right)^{-\frac{1}{2}} \qquad \textit{Equation 4-8}$$

where ¯ is the arithmetic mean of the mechanical aperture and σ^2 is variance of the mechanical aperture.

4.5. Results and Discussion

Microphotographs of cement-steel interfaces in sliced circumferential sections revealed a wide range of geometric characteristics for microannuli (sizes and shapes); Figure 4-8 shows microphotographs illustrating typical characteristics. The observed aperture size varied from a few microns (Figure 4-8(a)) to nearly 1 mm (Figure 4-8(b)). The aperture could be uniform over the circumferential arc of a microphotograph (Figure 4-8(c)) or could show significant variability (Figure 4-8(d)) such as isolated channels. A portion of every circumferential section had perfect contact, that is, there was no detectable aperture and therefore no microannulus (Figure 4-8(e)).

The measured aperture size around the circumference of two representative circumferential sections from Specimens A and B are given in Figure 4-9. The circumferential distance starts at an arbitrary point and goes completely around the circumference along the cement- steel interface. The section from Specimen A has a wide range of apertures that can vary significantly over small distances. The section from Specimen B reveals more contact compared with Specimen A and discrete regions or channels with relatively large, nonuniform apertures. There is no figure presented from Specimen C because the large number of measurements would require to partition the graph in several pieces to be able to observe the size of the apertures.

The aperture data are shown as cumulative distribution functions in Figure 4-10 to provide an indication of the spatial variability of the aperture size for each section as well as differences between samples.

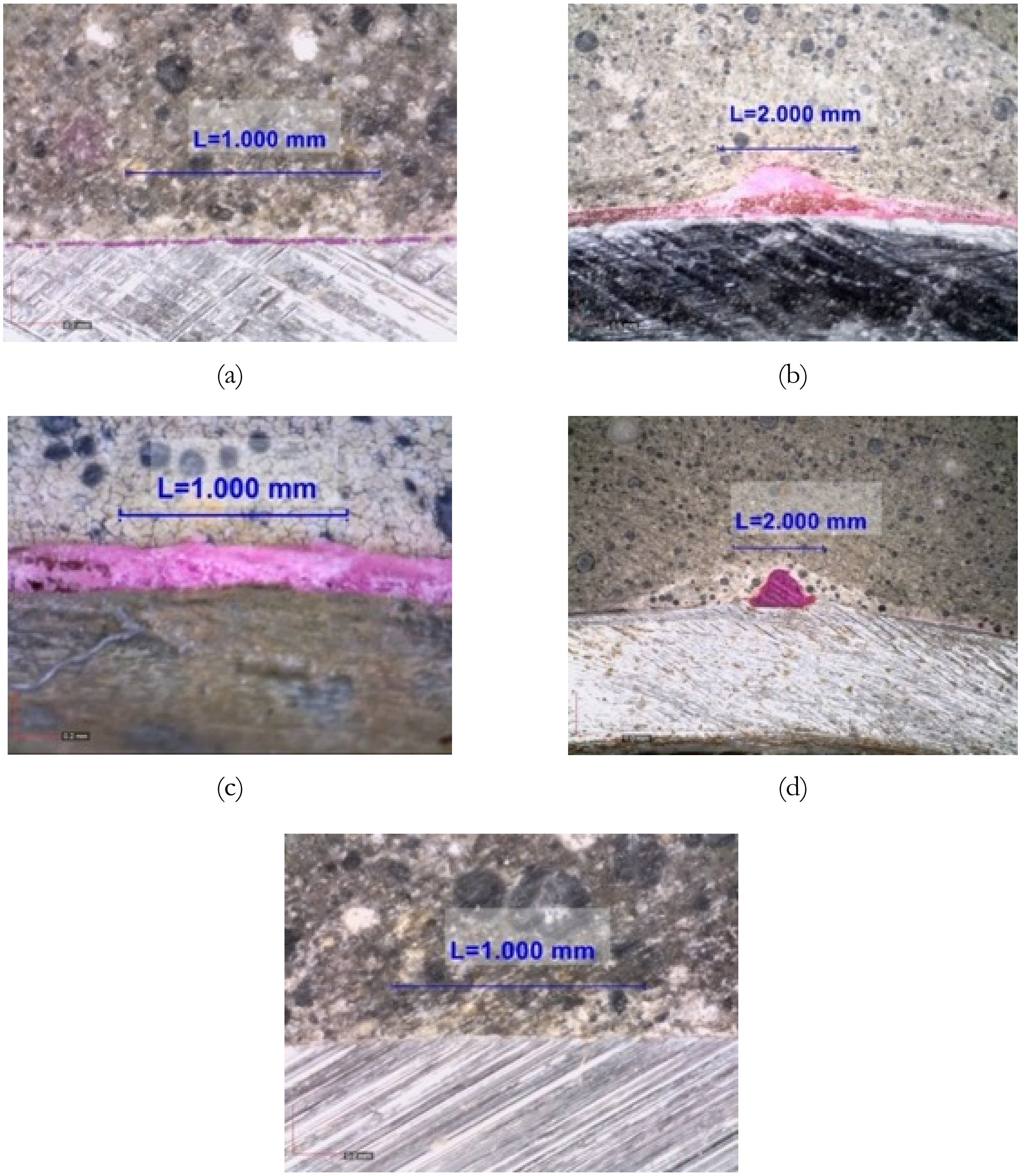

(a) (b) (c) (d) (e)

NOTE: (a) Small continuous aperture (35 μm) in wellbore specimen C. (b) Variability in the aperture size found in wellbore specimen A, where the aperture changes from 203 to 760 μm and then back to 196 μm over a distance of 2 mm. (c) Uniform and continuous aperture 185 μm in wellbore specimen B. (d) Big channel (865 μm), preceded and followed by perfect contact in wellbore specimen B. (e) Perfect contact between the steel and the cement, which indicates the absence of microannulus (wellbore specimen C).

Figure 4-8. Examples of different geometries observed in the microannuli

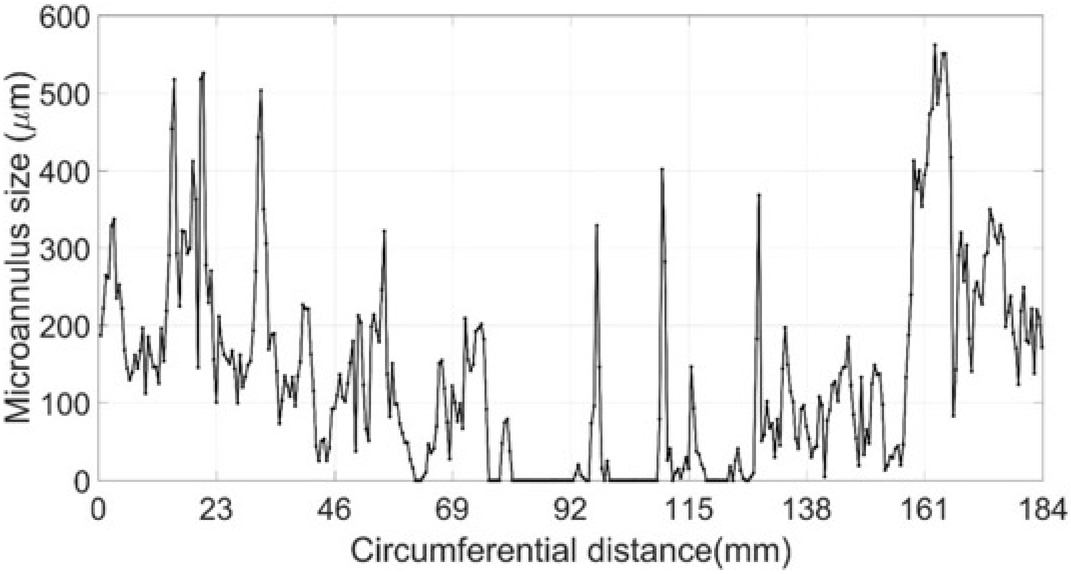

(a)

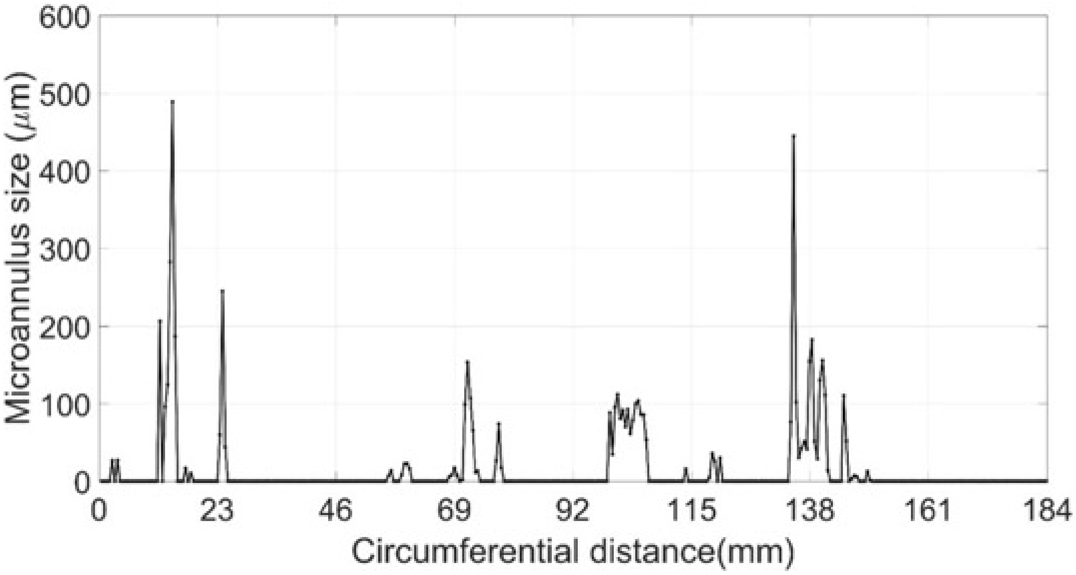

(b)

Figure 4-9. Microannulus size as a function of circumferential distance for two sections: (a) section (A.2.b), (b) section (B.2.b)

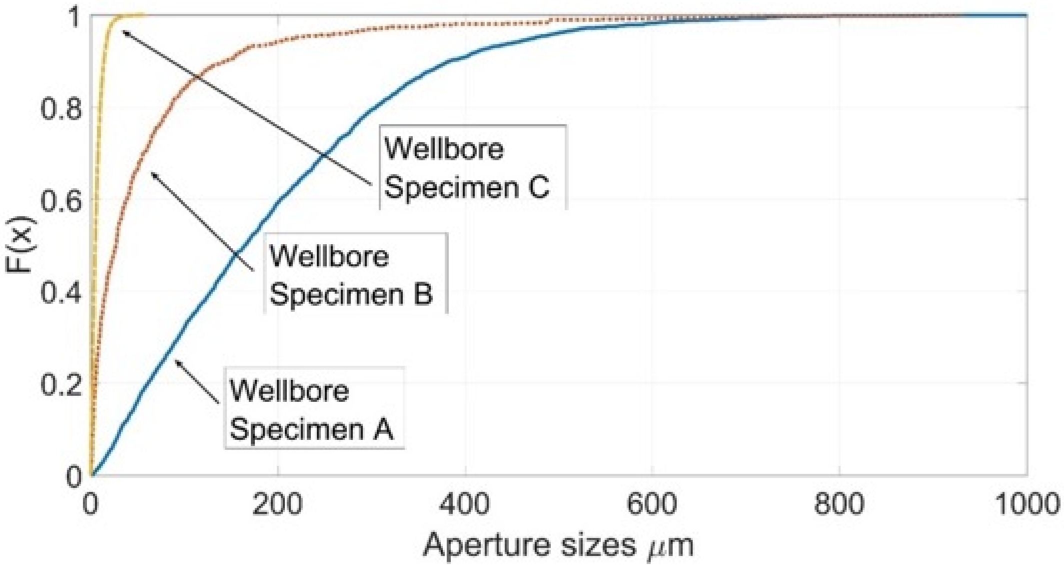

(a)

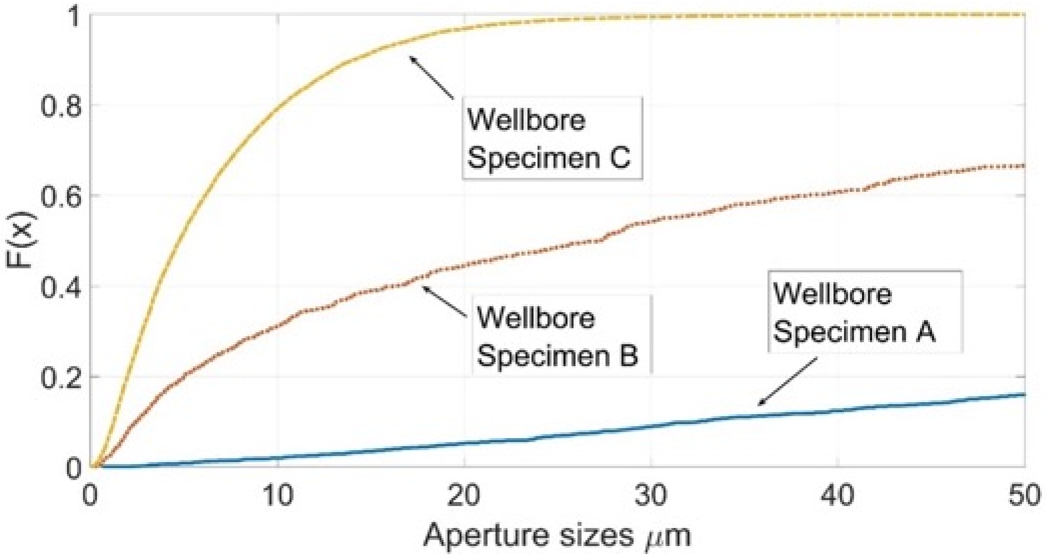

(b)

Figure 4-10. (a) Cumulative distribution function (F(x)) of the aperture size of wellbore specimens A, B and C, and (b) Cumulative distribution function of the aperture size of the wellbore specimens A, B and C zoomed at the range 0–50 µm to show in detail wellbore specimen C

4.5.1. Fitting Aperture Data to Distributions

To describe the measured apertures, some of the distributions used to describe aperture sizes in rock fractures were considered, including lognormal (Bianch 1968; Gale 1987; Johns et al. 1993; Sanei et al. 2015), power law (Barton and Hsieh 1989; Gale et al. 2007), normal (Asadollahi 2009) and gamma (Gentier 1987; Tsang and Tsang 1987). The distributions used for describing rock fracture aperture typically consist of two fitting parameters. In addition to these, modifications of these distributions with additional parameters were used. To fit the data, the software Easyfit, created by MathWave, was used. The parameters of all the distributions used are explained in Section 4.8.

The Chi-square goodness-of-fit test was used to evaluate the fit of the aperture data to different distributions. Every aperture measurement is considered a discrete value (O_i) and the statistical value (χ^2) is obtained from the following equation

$$\chi^2 = \sum_{i=1}^{k} \frac{(O_i - E_i)^2}{E_i} \qquad \textit{Equation 4-9}$$

where E_i is the expected aperture value for a given distribution. The null hypothesis is that the data are consistent with a particular distribution. If the χ obtained from Equation 4-9 is smaller than the threshold χ defined by an assumed significance value (α), it can be confirmed with specific significance that the data fit the distribution. The fitting criteria used was $\alpha = 0.01$. The greater the α value is, the better the data fit the particular statistical distribution

There was not a unique statistical distribution that fit all the data, but it was found that lognormal 3P and generalized gamma 4P were the most successful. Figure 4-11 shows the aperture data fitting to these distributions.

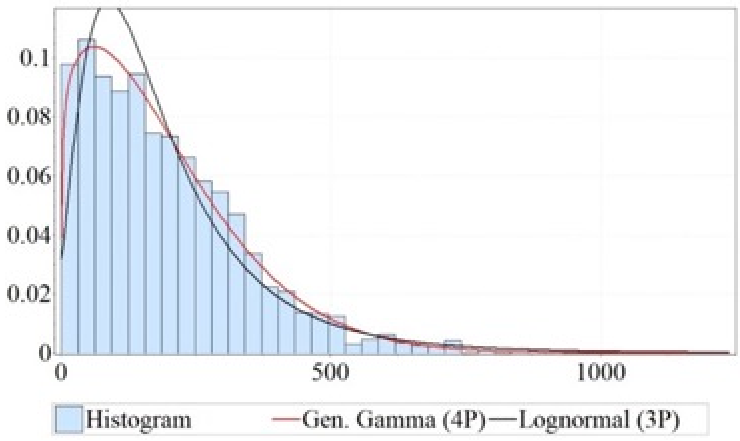

(a)

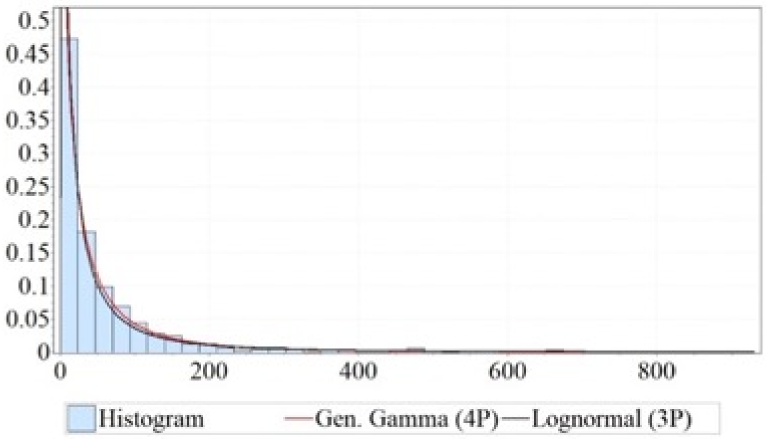

(b)

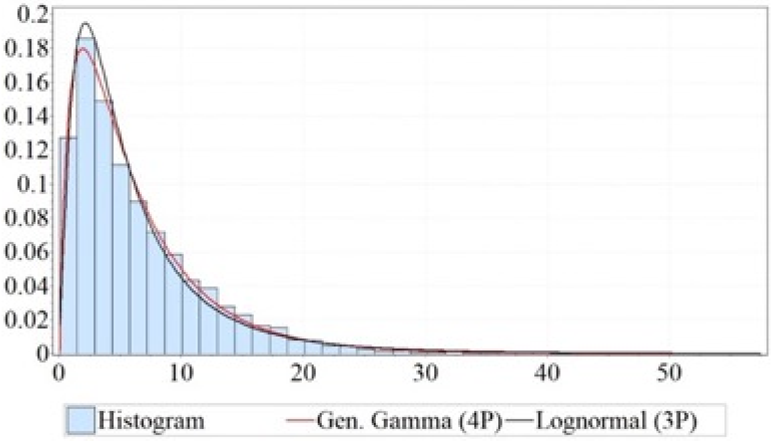

(c)

NOTE: X axis is the aperture size in μm and the Y axis is the percentage of apertures in the specified range over 1.

Figure 4-11. Histograms of aperture size of wellbore specimens (a) A, (b) B, and (c) C, with the fitting of generalized gamma 4P and lognormal 3P

4.5.2. Convergence Study

If the aperture distributions were constant along the axis of the wellbore, a single section would provide a complete description of the microannuli. However, it was found that the aperture distributions varied axially. The convergence study evaluated how the measured apertures and the parameters calculated from the measured apertures varies with the number of sections considered.

Circumferential sections that were as equally spaced as possible were selected. For example, when just one surface was used, it was located at the middle of the specimen and when two surfaces were selected, they were located at 1/3 and 2/3 of the sample length. Results of the convergence study are shown in Table 4-1. In general, it was observed that all parameters were within 100% of the value based on the most sections (8). On average for all parameters there was a 65% error between using just one circumferential section and using eight. Intuitively, it can be postulated that an increase in the number of circumferential sections will result in a more accurate wellbore representation. That said, this convergence study shows that, while there is variability of the parameters used to characterize the circumferential sections as more sections are analyzed, by just analyzing one it is possible to obtain a good first approximation.

Table 4-1. Convergence study of the number of circumferential sections needed to represent and characterize the microannuli of a specimen. Units in μm.

Specimen	Property	1 Surface	2 Surfaces	3 Surfaces	4 Surfaces	8 Surfaces
A	Mechanical Mean	200.5	179.0	190.0	193.7	191.5
	Mean with 0s	166.5	143.0	168.10	167.8	161.3
	LCL	257.8	235.0	260.9	262.7	260.4
	Renshaw	240.5	220.1	231.9	237.4	236.9
	Geometric Mean	141.9	125.6	140.8	139.4	134.0
B	Mechanical Mean	31.2	60.3	70.6	62.7	59.7
	Mean with 0s	8.2	13.4	27.5	21.1	19.7
	LCL	71.2	85.9	144.7	114.9	117.8
	Renshaw	71.8	99.3	132.4	112.0	109.8
	Geometric Mean	9.2	28.6	28.1	26.8	26.0
C	Mechanical Mean	5.3	8.7	7.0	7.5	6.8
	Mean with 0s	0.6	1.3	1.4	1.5	1.2
	LCL	12.5	20.0	17.8	19.1	17.3
	Renshaw	7.3	10.9	9.0	9.6	8.9
	Geometric Mean	3.6	6.8	4.9	5.6	4.9

4.5.3. Comparison of Interpreted Parameters to Hydraulic Aperture

Parameters calculated from the measured apertures were compared to the hydraulic aperture interpreted from flow measurements (h_i); the parameters were averaged from each specimen. Results are shown in Table 4-2.

The mean mechanical aperture with and without zeros were the closest values to the interpreted hydraulic aperture (8% lower and 9% higher, respectively) for wellbore specimen A. LCL overestimated the aperture by 56%, and the geometric mean underestimated it by 24%. For wellbore Specimen B, the mean mechanical aperture is the closest value found compared to the hydraulic aperture interpreted from the flow test-derived value (19% more the calculated than the interpreted). The mechanical mean including the zeros was far from the flow test (19.7 vs. 50 μm), because the percent of contact in this sample was higher than in Specimen A. LCL and Renshaw's equation yielded hydraulic apertures more than twice as large as that interpreted from the flow measurement. The geometric mean underestimated the aperture by 48%. The complicated geometry of the microannuli makes it difficult to define definitive relationships between hydraulic aperture and parameters derived from the mechanical aperture. In the case of wellbore Specimen C, a radial crack was found after testing that might have affected the hydraulic aperture measured in the flow test.

The post-test crack found in Specimen C makes the comparison between flow-derived data and the parameters obtained from the mechanical apertures more difficult. That said, all the information obtained from the mechanical apertures (statistical distribution, *CEP*, repair effectivity and parameters interpreted from the mechanical apertures) are still valid results.

Table 4-2. Averaged parameters of wellbore specimens A, B, and C compared to h_i. Units in μm.

Wellbore Specimen	Contact %	Mechanical Mean	Mean with 0s	LCL (Equation 4-6)	Renshaw (Equation 4-8)	Geometric Mean	Hydraulic Aperture (h_i)
A	0.17	191.5	161.3	272.3	236.9	133.6	175.0
B	0.67	59.7	19.7	117.8	109.8	26.0	50.0
C	0.81	6.8	1.2	17.3	8.9	4.9	32.0

4.5.4. Capillary Entry Pressure

Gas must exceed a displacement or entry pressure in order to displace a wetting fluid (e.g. brine) from a fracture. The *CEP* is inversely related to the fracture aperture size. The *CEP* in a fracture is given by the equation (Pruess and Tsang 1990):

$$CEP = \frac{2\lambda cos\theta}{a} \qquad \textit{Equation 4-10}$$

where *CEP* is in Pascals, λ is the interfacial tension between gas and brine (66.73 mN/m), θ is the contact angle of the brine and the gas (43°), and a is the aperture size. The values used were obtained by Khishvand et al. (2016) in two-phase flow laboratory experiments at underground conditions using N_2 and brine. N_2 was used instead of natural gas because it is safer to work with and the pore-scale capillary interactions are similar for both types of gases.

We calculated the CEP using two different approaches. First, we used the hydraulic aperture as the aperture size in Equation 4-10 to calculate a single capillary entry pressure (CEP_h) for each specimen. Secondly, we calculated the capillary entry pressure for every measured aperture along each circumferential section (CEP_i) of each specimen.

In Figure 4-12 the cumulative distribution function for CEP_i are given for each specimen along with its CEP_h. These data are summarized by the percent of the CEP_i values that are greater than CEP_h (Table 4-3).

The results show that a large percentage of the microannulus can have a local CEP_i that is much greater than the CEP_h estimated from the hydraulic aperture. Thus, a single capillary entry pressure does not accurately represent the range of capillary entry pressures within the microannulus. It is important to note that the percentages presented in Table 4-3 are calculated on the assumption that the apertures are perfectly connected.

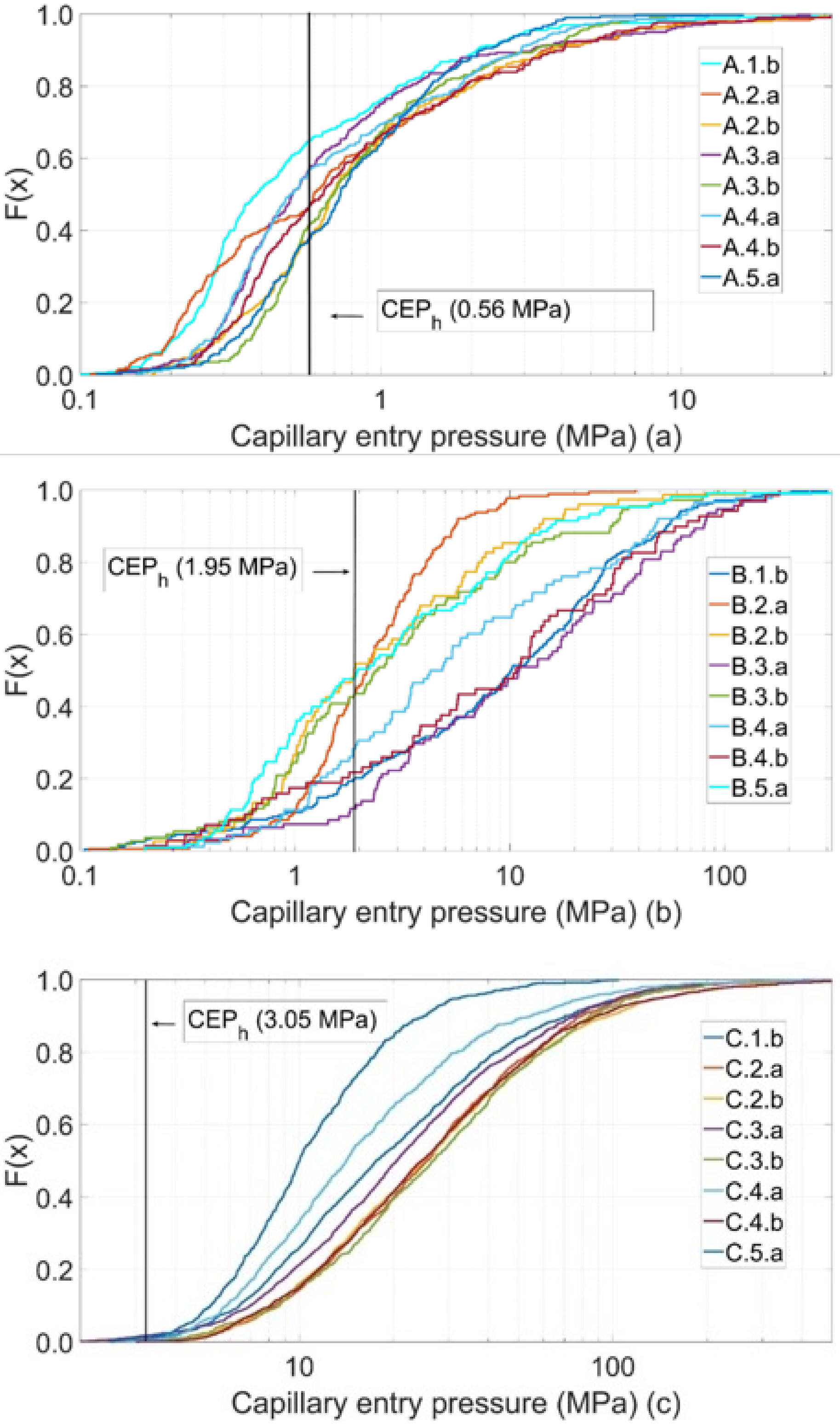

Figure 4-12: CEP_i in all circumferential sections of wellbore specimens: (a) Specimen A, (b) Specimen B and (c) Specimen C

Table 4-3. Hydraulic aperture, CEP_h, and percent of the microannulus with CEP_i greater than the CEP_h

	Specimen A	Specimen B	Specimen C
h_a (μm)	175	50	32
CEP_h (MPa)	0.56	1.95	3.05
% microannuli with $CEP_i > CEP_h$	36–64	48–87	>99

4.5.5. Repair Material Penetrability of Microannuli

Cementitious materials are typically used to repair or enhance the properties of cement, rocks and soils. The purpose of repair is primarily to fill voids so as to reduce the permeability of the host material. For an ideal repair, the cementitious material should penetrate and fill all fractures and voids. From a practical standpoint, simply filling interconnected apertures would be sufficient. Penetrability of the repair material in the host material is therefore a critical issue. Several factors affecting the penetrability of the cement, the most relevant of which are the water/cement ratio and the ratio between the opening size and the grain size of the cement (Jorne and Henriques 2016; Mirza et al. 2013; Axelsson et al. 2009). With regard to the latter, the generally accepted rule of thumb is that the aperture to be filled must be at least three times the grain size of the cement (Mitchell 1981); this is claimed as a general rule in several reviews (Tolppanen and Syrjanen 2003; Exelsson et al. 2009). Recent laboratory tests have supported the rule of thumb and have added that, in specific cases under favorable conditions, could be from two to three times smaller than the aperture (Eklund and Stille 2008).

Microannuli apertures are variable and nonuniform, which could complicate the attempt to seal them. If the microannulus is not filled completely, a permeable path may remain that enables fluid migration. The actual repair could be compromised by a low conductivity section. Both problems have been described in detail by Jorne et al. (2016).

The criterion presented above was used to evaluate the repair of the microannuli using different cementitious materials. On the assumption of perfect connectivity and no plugging nor blockage, the aperture size distribution in all three wellbore specimens were analyzed and the extent to which a microannulus could be repaired was estimated. To evaluate the penetrability, the maximum grain size of the cementitious materials is required. Four different cementitious materials with distinctly different grain sizes were evaluated; three of them were provided by Mirza et al. (2013) and De Neef MC-500 was also considered since it provided a finer granulometry. The d_{99} of the cementitious materials along with the smallest aperture that they could fill following Mitchell's criterion is presented in Table 4-4, representing a range of granulometries from Portland cement to ultrafine cement.

The results of this analysis, given in Table 4-5, indicate that Portland cement is not suitable for repairing microannuli and that microfine cement could leave most of the microannulus unfilled. The variability in aperture size affects the possible repair of microannuli. An example is Specimen B, which had a hydraulic aperture of 50 μm. If a uniform aperture is assumed, it could be considered that both UFCs would penetrate the microannulus, whereas the measured apertures indicate that, in the best of cases, only 50% of the microannulus would be filled. Penetrability would be further hindered by the variability of the aperture size as small apertures will likely restrict access to some larger apertures. Changes in the water/cement ratio would improve the penetrability, but this factor is not considered in this study.

Table 4-4. Particle size (μm) of the cementitious materials

	d_{99} (μm)	Minimum Aperture Size That Could Be Filled (μm)
Portland cement	100	300
Microfine cement	32	96
Ultrafine cement 1	15	45
Ultrafine cement 2	11	33

Table 4-5. Percentage of apertures not filled by the sealing materials using Mitchell's criterion

	Specimen A %	Specimen B %	Specimen C %
Portland cement	79.5	96.9	100.0
Microfine cement	30.7	83.1	100.0
Ultrafine cement 1	14.0	64.5	99.9
Ultrafine cement 2	10.2	56.2	99.6

4.6. Conclusion

Microannuli are often described as a hydraulic aperture, which is a single-valued parameter derived from a flow test. In contrast to this conventional description, we measured the microannuli apertures with a resolution as low as 3 μm and found them to be highly variable. Microannuli produced in laboratory wellbore specimens were found to have apertures that vary orders of magnitude in a single circumferential section. Even in specimens with relatively large hydraulic apertures interpreted from flow measurements, perfect contact (no aperture) exists over portions of the steel-cement interface. This complex geometry produces tortuous flow paths through the microannulus, far from the assumption of flow between parallel plates used to interpret the hydraulic aperture of the microannulus. This result suggests that, while the hydraulic aperture provides a useful parameter to characterize flow, describing the microannulus with this single-valued parameter may be inappropriate for some applications. For example, because of the variable aperture sizes within a microannulus, we estimated that cementitious materials will not effectively penetrate and repair microannuli with hydraulic apertures less than about 50 μm.

Lognormal 3P and generalized gamma 4P statistical distributions provided a good representation of the microannuli's apertures. Implementing these statistical distributions (plus contact areas) in computational models when dealing with the microannuli would provide a more physically realistic representation compared to assume a uniform gap, hence facilitating matching stresses in the wellbore with the change in the microannuli's aperture size and the flow through it.

4.7. Acknowledgements

This material is based upon work partially supported by the U.S. Department of Energy (DOE) National Energy Technology Laboratory (NETL) under Grant Number DEFE0009562.

4.8. Supplemental Material

The statistical distributions were obtained from Easyfit manual. The normal distribution has two parameters: the mean value ($\bar{z}$) and the standard deviation (σ). The probability density function is

$$f(z) = \frac{exp\left(\frac{-1}{2}\left(\frac{z-\bar{z}}{\sigma}\right)^2\right)}{\sigma\sqrt{2\pi}} \qquad \textit{Equation 4-11}$$

Lognormal distribution has two or three parameters: the mean value ($\bar{z}$) and the standard deviation (σ) and the continuous location parameter (γ). $\gamma=0$ yields the two parameter (2P) lognormal. The probability density function is

$$f(z) = \frac{exp\left(\frac{-1}{2}\left(\frac{ln(z-\bar{z})}{\sigma}\right)^2\right)}{(z-\gamma)\sigma\sqrt{2\pi}} \qquad \textit{Equation 4-12}$$

The gamma distribution has two or three parameters: continuous shape parameter ($C > 0$), continuous scale parameter ($B > 0$) and continuous location parameter ($\gamma = 0$ yields the gamma 2P). The probability density function is

$$f(z) = \frac{(z-\gamma)^{C-1}}{\Gamma(C)B^{C}} exp\left(-\left(\frac{z-\gamma}{B}\right)\right) \qquad \textit{Equation 4-13}$$

The generalized gamma distribution has three or four parameters: continuous shape parameters ($C > 0$ and $K > 0$), continuous scale parameter B ($B > 0$) and continuous location parameter γ ($\gamma = 0$ yields the generalized gamma 3P). The probability density function is

$$f(z) = \frac{k(z-\gamma)^{C-1}}{\Gamma(C)B^{KC}} exp\left(-\left(\frac{z-\gamma}{B}\right)^{K}\right) \qquad \textit{Equation 4-14}$$

5. ALBANY-PFLOTRAN COUPLING

5.1. Introduction

In this chapter, we describe the Albotran application code that was developed as part of this LDRD effort. Albotran is a multiphysics solver that couples the thermal subsurface hydrological flow and reactive transport (THC) code PFLOTRAN (Hammond et al. 2014) and the implicit, unstructured grid finite element code Albany (Salinger et al. 2016). Albotran imbeds PFLOTRAN in Albany as a pore pressure evaluator. The split-stress (Kim 2010) coupling scheme is employed to combine results from each code and the Data Transfer Kit (Slattery et al. 2013) is used to transfer data from one code to another.

5.2. Background and Motivation

The problem of coupling mechanical compaction and fluid transport in porous media where hydrological interactions between fluid-saturated pores and the bulk solid results in complex poromechanical responses is relevant to many natural and engineered problems in soil mechanics, oil/gas reservoir evaluation, and the assessment of clay barrier performance. This type of coupling has been theoretically assessed to various levels of complexity through the development of mathematical and computational approaches in the last few decades (Karrech 2013; Sun 2015). Sun (2015) discusses the highlights of some of the various theoretical approaches and their numerical implementations whether these couplings are monolithic (fully coupled multiphysics) or sequential (decoupled multiphysics). Both types of approaches have their advantages and disadvantages when applied to poromechanical problems. For example, in the monolithic approach the physics of interest is tightly coupled in a single application library, but tends to suffer from numerical stability issues (Sun 2015). On the other hand, sequential approaches combine two or more existing application libraries, bringing with them specialized domain expertise, but require complex data transfer mechanisms between the libraries; this is in addition to the potentially prohibitive computational expense of running and combining results from multiple simulations (Kim 2010; Sun 2015).

Coupled multiphysics modeling, such as thermal-hydrological-mechanical-chemical (THMC) can result in highly complex phenomena that is very challenging to handle numerically often requiring treating model components separately to allow for their rigorous numerical treatment. The last several decades have seen significant advances in the simulation of coupled THC processes through geochemical modeling of fluid/mineral interactions with hydrological transport in porous media (Lichtner, 1996; Lichtner et al. 2018). Poromechanical modeling have also seen advances in the simulation of coupled processes relevant to soil consolidation and compaction of clay-bearing materials (Alonso and Olivella, 2006; Alonso et al. 1990; Collin et al. 2006; Guimarães et al. 2006; Olivella et al. 1996; Sanchez et al. 2010). An example of such type of code coupling is TOUGHREACT-FLAC (Rutqvist et al. 2011). One key drawback of these code couplings are the expected computational inefficiencies due to code communication in the coupling scheme but also the lack of leveraging high performance computing (HPC) resources exploited by massively-parallel computer codes. Also, the numerical implementation of key aspects of the mechanics and/or chemistry are often suitably treated in sequentially coupled codes. As described in the previous section, here we combine the use of two open-source HPC codes (Albany and PFLOTRAN) to simulate isothermal consolidation phenomena in a porous solid. This code coupling problem will be later extended to include reactive transport by simulating leaching in cementitious material.

5.3. Background and Theory

The solution of the coupled stress-diffusion equation that describes the behavior of fluid-saturated solid media is approximated by the effective stress principle. Accordingly, the total stress at a material point is assumed to be the sum of an "effective stress" carried by the solid skeleton and the pressure in the fluid occupying pore space within the solid. The stress-displacement behavior of the solid skeleton is governed by the balance of linear momentum along with the constitutive assumption of linear elasticity. The motion of the fluid through pore space is governed by the balance of mass along with the constitutive assumption that flow velocity is proportional to gradients in the fluid pressure as described by Darcy's law.

The computational model described herein assumes a two-phase porous medium with constituents $\alpha = \{s,f\}$, where s and f represent the solid matrix and fluid phases, respectively. A representative volume element (RVE) of material with volume dV and mass dm is composed of each constituent such that

$$dV = dV^s + dV^f \ \ and \ \ dm = dm^s + dm^f \qquad \textit{Equation 5-1}$$

The volume fraction of each constituent is defined in the usual way,

$$f^\alpha = \frac{dV^\alpha}{dV} \qquad \textit{Equation 5-2}$$

so that $\Sigma f^\alpha = 1$.

For the two-phase medium, the volume fraction of the solid constituent is

$$f^s = 1 - \phi \qquad \textit{Equation 5-3}$$

where ϕ is the porosity

$$\phi = \frac{dV^s}{dV} \qquad \textit{Equation 5-4}$$

5.3.1. Balance of Mass

The behavior of the fluid constituent is governed by the conservation of mass for single-phase flow through porous media

$$\frac{\partial(\rho^f \phi)}{\partial t} + \nabla \cdot (\rho^f \phi v) = 0 \qquad \textit{Equation 5-5}$$

where ρ^f is the density of the fluid and v is the Darcy superficial velocity

$$v = \frac{k}{\mu}(\nabla p - \rho^f g) \qquad \textit{Equation 5-6}$$

Here, k is the permeability, μ is the viscosity of the single-phase fluid, p is the pore pressure, and g is the gravity vector. The porosity of the solid matrix varies according to

$$\Delta\phi = \alpha\Delta\epsilon_v + \frac{1}{N}\Delta p \qquad \textit{Equation 5-7}$$

where α is the Biot coefficient and ϵ_v is the volumetric strain. The Biot coefficient, which is a measure of the sensitivity of the elastic response to porosity, is defined as

$$\alpha = 1 - \frac{K}{\hat{K}} \qquad \textit{Equation 5-8}$$

K is the *drained* bulk modulus of the porous solid and $\hat{K}$ is the bulk modulus of the solid matrix (typically $\hat{K} \gg K$). The quantity $1/N$ in Equation 5-7 is defined as

$$\frac{1}{N} = \frac{1}{\alpha - \kappa\phi_0} = \frac{\alpha - \phi_0}{\hat{K}} \qquad \textit{Equation 5-9}$$

where κ is the fluid compressibility.

5.3.2. Balance of Momentum

The behavior of the solid constituent is governed by the conservation of linear momentum

$$\nabla \cdot \sigma + \rho^s g = 0 \qquad \textit{Equation 5-10}$$

where σ is the Cauchy stress tensor and ρ^s is the density of the solid matrix. In the following, we assume that the response of the solid matrix to deformation is that of an ideal isotropic-poroelastic solid wherein the incremental stress tensor $\Delta\sigma$ is related to the incremental strain tensor ϵ and pore pressure by

$$\Delta\sigma = C{:}\Delta\epsilon - \alpha\Delta p I \qquad \textit{Equation 5-11}$$

where C and I are the fourth-order elasticity and second-order identity tensors, respectively.

The porosity in the idealized poroelastic solid evolves according to Kim (2010)

$$\Delta\phi = \alpha\Delta\epsilon_v + \frac{\alpha - \phi}{\hat{K}}\Delta p \qquad \textit{Equation 5-12}$$

5.3.3. Coupling Mass and Momentum Conservation

The goal of the coupled poromechanics problem is to determine the flow of fluid through pore space and deformation of the solid matrix such that the governing equations of each phase (Equation 5-5 and Equation 5-9, respectively) are satisfied. The implementation, however, is far from trivial. The difficulty in implementing a coupled poromechanics solver arises from several sources. Firstly, the solution of even a single phase requires a significant computational infrastructure and complex constitutive routines requiring a high level of domain expertise in several areas of computation sciences. Developing a fully implicit monolithic solver for the coupled system requires writing a new solver, or making significant modifications to existing solvers. Either option would adopt all of the risks and costs of each single-phase solver, plus the additional costs associated with their coupling. (Sun et al. 2013a; Sun et al. 2013b).

Alternatively, existing solvers can be coupled in a sequential fashion. Sequentially coupled solvers have the advantage of being able to leverage existing solvers and domain expertise, at the expense of having to develop methods for the individual solvers to communicate results and data. Sequentially coupled solvers come in several variations. The simplest, a loosely coupled staggered solve, has the mass and momentum conservation solved in sequence one time step after another until the final time is reached. A modified version of this technique that conserves computational resources has the momentum solver called periodically during the solution procedure instead of after each mass conservation evaluation. Contrast that with the more complicated iterative-sequential solve wherein a new time step is not started until the momentum and mass conservation solves have converged in some sense. Figure 5-1 depicts the idea of iterative-sequential.

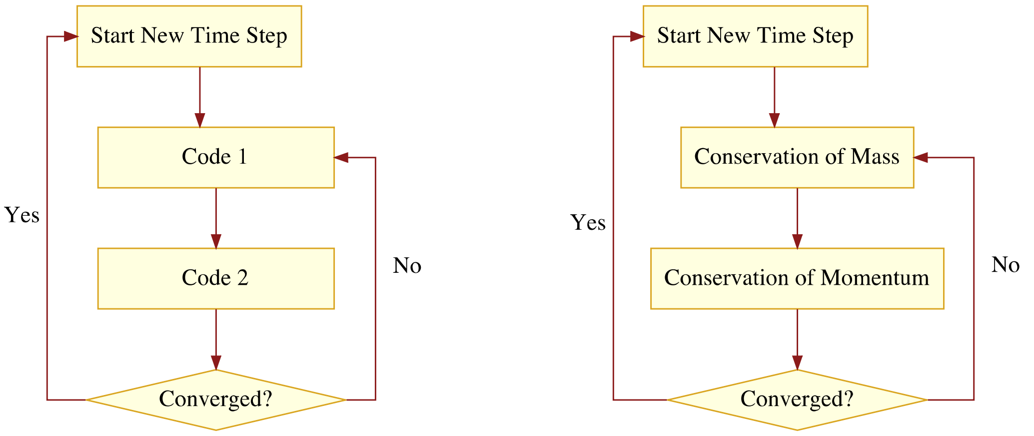

Figure 5-1. Graphical depiction of the iterative-sequential code coupling algorithm

Four iterative-sequential coupling methods have emerged in the literature: drained, undrained, fixed-strain, and fixed-stress operator splits (Figure 5-1). In the drained and undrained splits, the solution to the stress-displacement problem is obtained first, after which the solution to fluid flow problem is found. The drained split holds the pore pressure constant during the solution of the fluid problem while the undrained split holds the fluid mass constant. Kim (2010) showed that the drained operator split results in solutions that are only conditionally stable, while the undrained operator split produces unconditionally stable solutions.

In the fixed-strain and fixed-stress operator splitting methods, the solution to fluid flow problem is found and then the solution to stress-displacement problem. The fixed-strain operator split holds the solid matrix deformation fixed during the flow solution while the fixed-stress operator split holds the stress fixed. Like the drained split, the fixed-strain split is only conditionally stable, while the fixed-stress operator split is unconditionally stable (Kim 2010). In addition to unconditional stability, Mikelić et al. (2014) demonstrated superior convergence characteristics of the split-stress split over the undrained split under certain conditions.

In this work, we adopt the fixed-stress operator split. The fixed-stress operator split is achieved by fixing the mechanical stress during each flow solution. Under this condition, Equation 5-10 gives for the increment of volume strain during the flow solve as

$$\Delta\epsilon_v = \frac{\alpha\Delta p}{K}$$ *Equation 5-13*

so that the increment in porosity during the fluid solved in Equation 5-7 can be expressed as

$$\Delta\phi^f = \left(\frac{\alpha^2}{K} + \frac{1}{N}\right)\Delta p$$ *Equation 5-14*

Here we use the superscript f to distinguish the porosity tracked by the flow solver from the porosity tracked by the stress-displacement solver ϕ^s.

Thus, the updated porosities are

$$\phi_{k+1}^{f} = \phi_k^s + \Delta\phi_{k+1}^{f} = \phi_k^s + \left(\frac{\alpha^2}{K} + \frac{1}{N}\right)\Delta p_{k+1}$$

Equation 5-15

$$\phi_{k+1}^{s} = \phi_k^s + \Delta\phi_{k+1}^{s} = \phi_k^s + \alpha\epsilon_{vk+1} + \frac{1}{N}\Delta p_{k+1}$$

Equation 5-16

and the criterion for convergence can be chosen to be

$$\frac{\left|\phi_{k+1}^{f} - \phi_{k+1}^{s}\right|}{\phi_{k+1}^{s}} < \varepsilon$$

Equation 5-17

where ε is an appropriate convergence tolerance.

5.4. Numerical Implementation

The implementation of the fixed-stress operator split is achieved by coupling the responses of the flow simulator PFLOTRAN (Hammond et al. 2014) with the abstract finite element code Albany (Salinger et al. 2016). The responses from each simulator are communicated to each other using the Data Transfer Kit (Slattery et al. 2013).

5.4.1. PFLOTRAN

PFLOTRAN is a massively parallel reactive multiphase flow and transport code employed to simulate physical and chemical processes in the Earth's subsurface (Hammond et al. 2014). The (GNU LGPL) open source code is founded upon data structures and solvers from the PETSc library with parallel IO through HDF5. PFLOTRAN is written in object-oriented Fortran 2003/2008, leveraging modern Fortran's modularity, inheritance and polymorphism extensively. PFLOTRAN has been executed on up to 2^{18} processor cores on problems composed of several billion degrees of freedom.

At each time step, the porosity computed in PFLOTRAN is computing according to Equation 5-7 as

$$\phi_{k+1}^{f} = \phi_0^s + \alpha\epsilon_{vk} + \frac{1}{N}(p_k - p_0) + \left(\frac{\alpha^2}{K} + \frac{1}{N}\right)(p_{k+1} - p_k)$$

Equation 5-18

were ϵ_v is the volume strain computed by Albany.

5.4.2. Albany

Albany is a highly abstracted C++ framework using template based generic programming practices. In Albany, necessary physical quantities such as the deformation gradient, stress, porosity, etc., are implemented as "evaluators", with each evaluator specifying well-defined dependencies. During a simulation, a directed acyclic graph (DAG) representing the collection of evaluators making up the simulation is built, traversed, and evaluated during the computation of finite element residuals and Jacobians. Albany leverages nonlinear solvers, distributed linear algebra, automatic differentiation, and other sophisticated components from the Trilinos library (Heroux et al. 2005). In this framework, PFLOTRAN is implemented as an evaluator that depends on the deformation and material properties from which the pore pressure is evaluated. A simplified DAG for the code coupling performed in this work is shown in Figure 5-2.

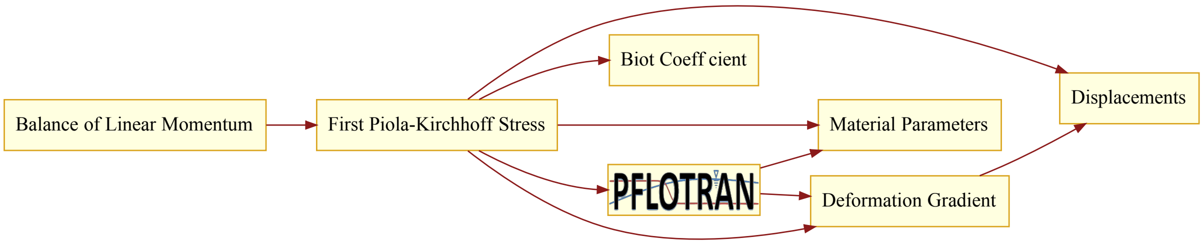

Figure 5-2. Simplified DAG of the Albany-PFLOTRAN code coupling

Unlike typical evaluators, which only compute the quantity of interest over a collection of elements, the PFLOTRAN evaluator first runs the flow simulation to the end of the current time step and then transfers pore pressure from PFLOTRAN to Albany. Implemented in this way, we take advantage of Albany's use of automatic differentiation (AD) in the computation of the Jacobian. Computing the Jacobian, or, sensitivities of the residual to the indepedent variables (the degrees of freedom), is simply the result of computing the residual by using AD types. See Bartlett et al. 2006 for more information on Albany's use of AD and the implementation of AD in Trilinos.

The coupled poromechanics formulation discussed in the present work can be viewed as a hybrid of a fully coupled monolithic system and an iterative-sequential system. On the one hand, standalone solvers for each solution phase are employed (flow and mechanics) while on the other, tight integration of the flow solution in to Albany's graph-based assembly produces solutions comparable to fully-coupled systems. Managed dependencies, graph-based assembly, and embedded AD proves a powerful framework for finding solutions to strongly coupled physical systems.

5.4.3. Data Migration

Unifying the PFLOTRAN flow response in to Albany's residual minimization is made possible by employing the Data Transfer Kit (DTK) (Slattery et al. 2013) to communicate necessary data between the two codes' meshes. DTK transfers data between arbitrary physics components by repartitioning the domains such that they have a common geometric domain on each parallel process. Parallel maps from each physics' domain to the common geometric domain are used to efficiently transfer data between the two solvers. In Albotran, volume strain is transferred from Albany to PFLOTRAN and pore pressure is transferred from PFLOTRAN to Albany.

5.5. Verification

In the following sections, we demonstrate the correctness of the code coupling strategy by comparing solutions with analytic solutions.

5.5.1. Data Transfer

Verification of proper data transfer between PFLOTRAN and Albany was performed by a simplified simulation performed on 4 cores. Each code partitioned its mesh using its default approach. In the simulation, a block of material is injected on its top and left-hand sides at a constant injection rate. Dirichlet boundary conditions in Albany hold the block fixed in time. Neumann boundary conditions in PFLOTRAN on the bottom and right-hand sides do not permit flux of pressure through those boundaries. The pore pressure in the block is initially at atmospheric pressure. Figure 5-3 and Figure 5-4 show that pressure is transferred correctly from PFLOTRAN to Albany for the case of matching (Figure 5-3) and nonmatching (Figure 5-4) meshes. The results demonstrate that data is transferred correctly between the two meshes (matching and nonmatching) by DTK.

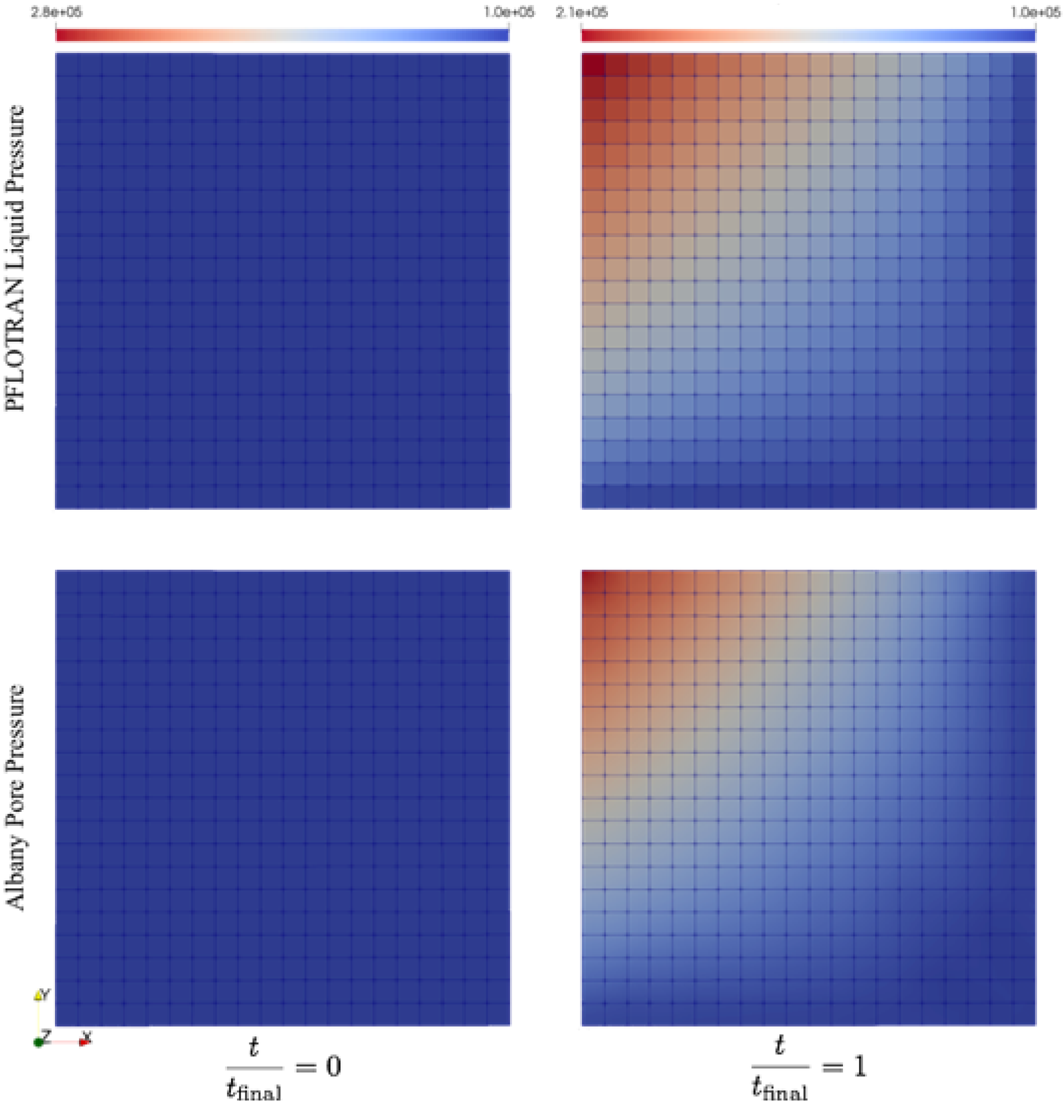

NOTE: (Left) Pressure distribution in the PFLOTRAN (top) and Albany meshes at time t=0. (Right) Pressure distribution in the PFLOTRAN (top) and Albany meshes at the end of the simulation.

Figure 5-3. Data transfer verification simulation consisting of a solid skeleton with 30% porosity permeated by fluid with atmospheric pore pressure at time t=0

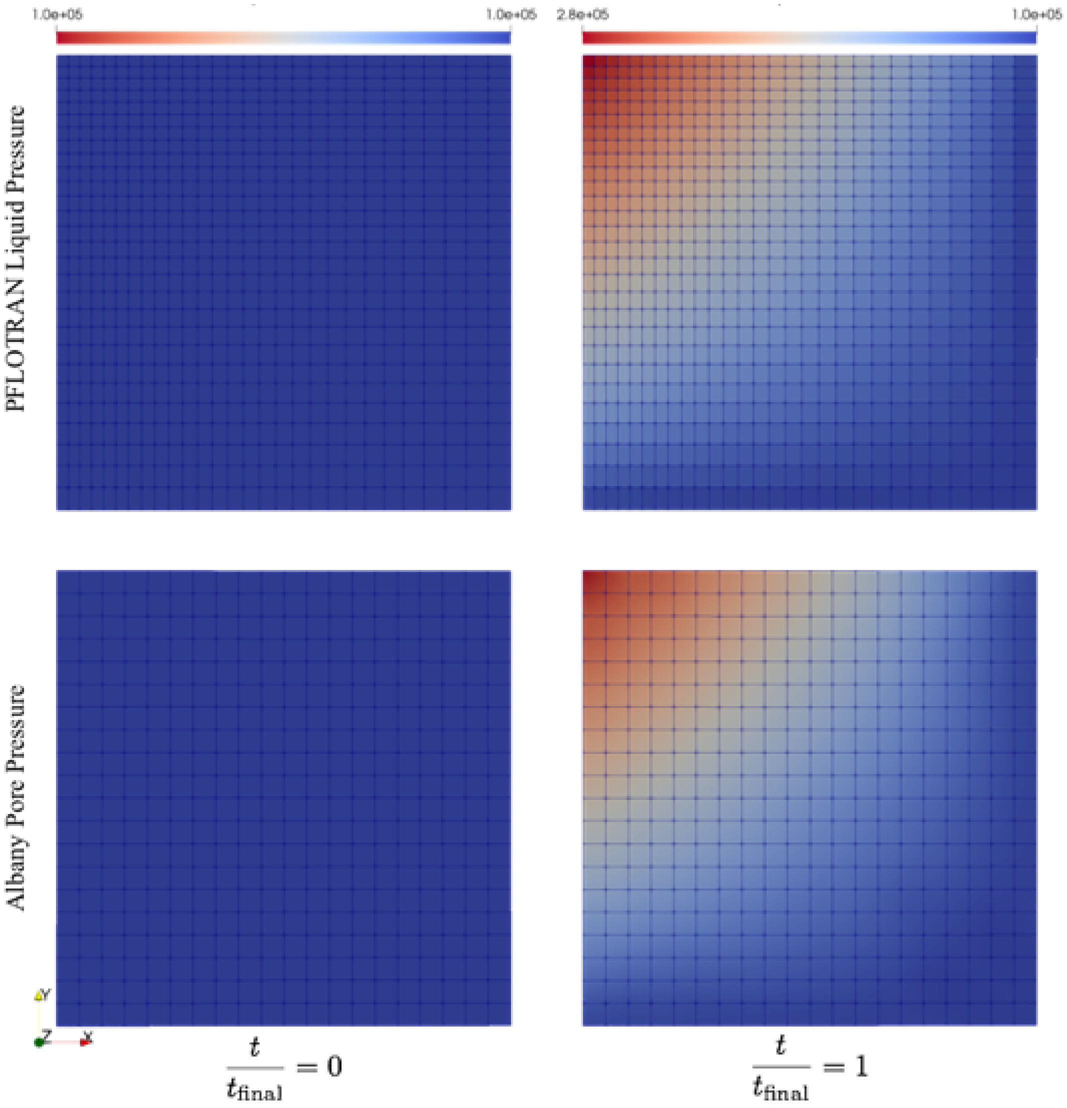

NOTE: In this verification test, meshes are nonmatching. (Left) Pressure distribution in the PFLOTRAN (top) and Albany meshes at time t=0. (Right) Pressure distribution in the PFLOTRAN (top) and Albany meshes at the end of the simulation.

Figure 5-4. Data transfer verification simulation consisting of a solid skeleton with 30% porosity permeated by fluid with atmospheric pore pressure at time t=0

5.5.2. *Terzaghi Consolidation*

The Terzaghi consolidation problem (Terzaghi et al. 1996) is a one dimensional consolidation problem wherein a column with height h of saturated soil with initial pressure p_0 is loaded suddenly by load q. The sudden loading causes an abrupt increase in fluid pressure. As fluid escapes through the column's permeable top surface, fluid pressure decays and the soil consolidates as load is transferred from the fluid to the solid skeleton. The Terzhagi consolidation problem is depicted in Figure 5-5.

5.5.3. Results

The results of the Terzhagi consolidation simulation are summarized in Figure 5-6 and Figure 5-7. Figure 5-6 shows pore pressure profiles at various stages of the simulation. The value of $p/q \approx 0.85$ at $t = 0$ is known as the Skempton coefficient and is an important quantity in poromechanics. As we expect, the simulation shows a sudden increase in pore pressure at $t = 0$ followed by rapid drainage from the top (permeable) surface until a total loss of pore pressure in the entire column is obtained. At equilibrium, load is transferred entirely to the effective stress carried by the solid skeleton. Figure 5-7 shows the rapid decrease in pore pressure at the top of the column as calculated in both PFLOTRAN and Albany.

5.5.4. Input files

Input files for the Terzhagi consolidation simulation can be found in Section 5.9.

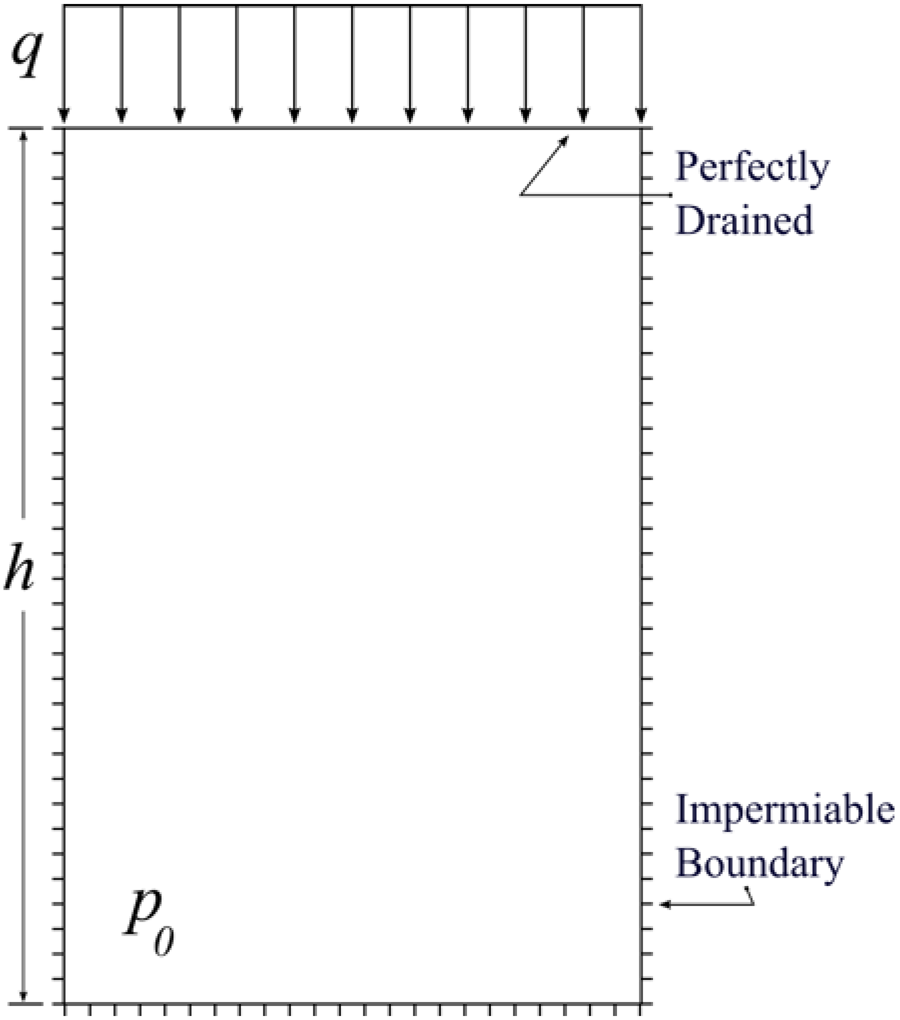

Figure 5-5. Schematic of the one-dimension Terzaghi consolidation problem

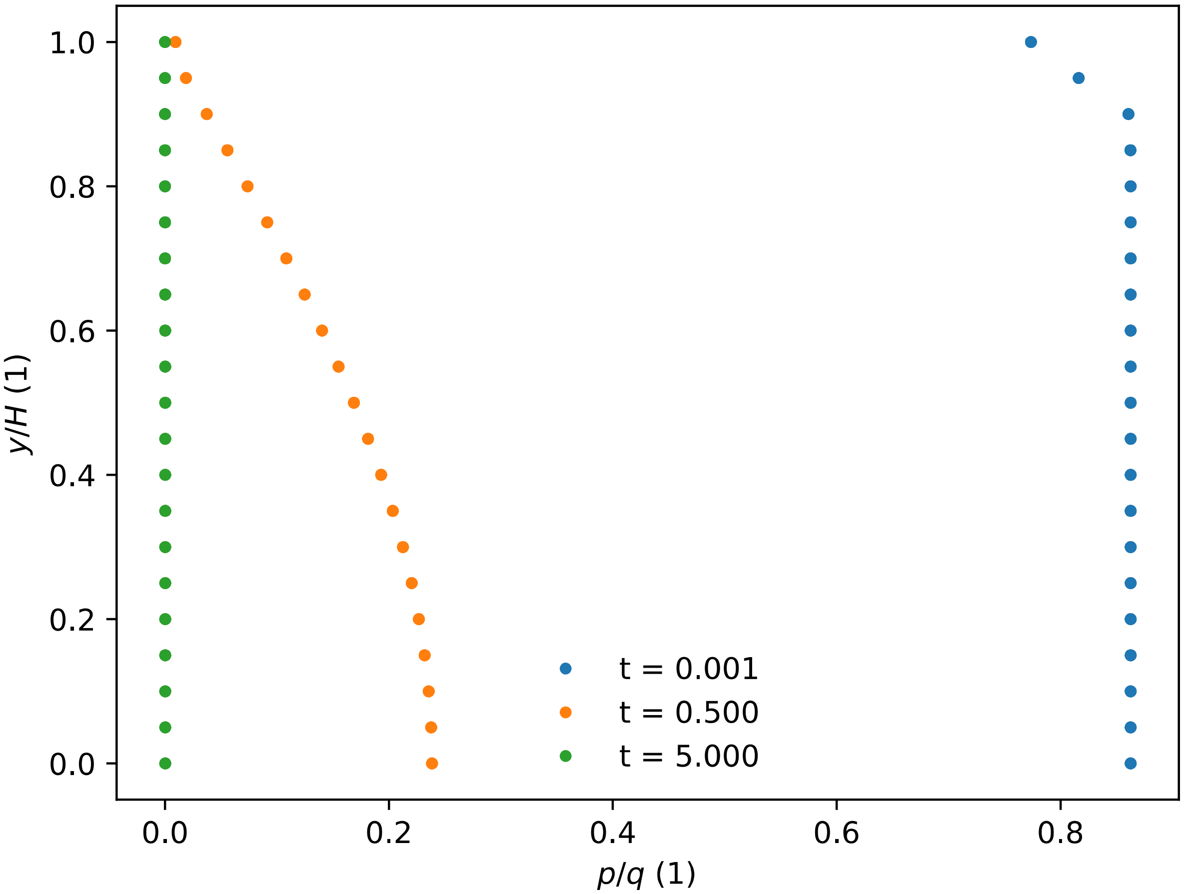

Figure 5-6. Pore pressure profiles at various simulation times

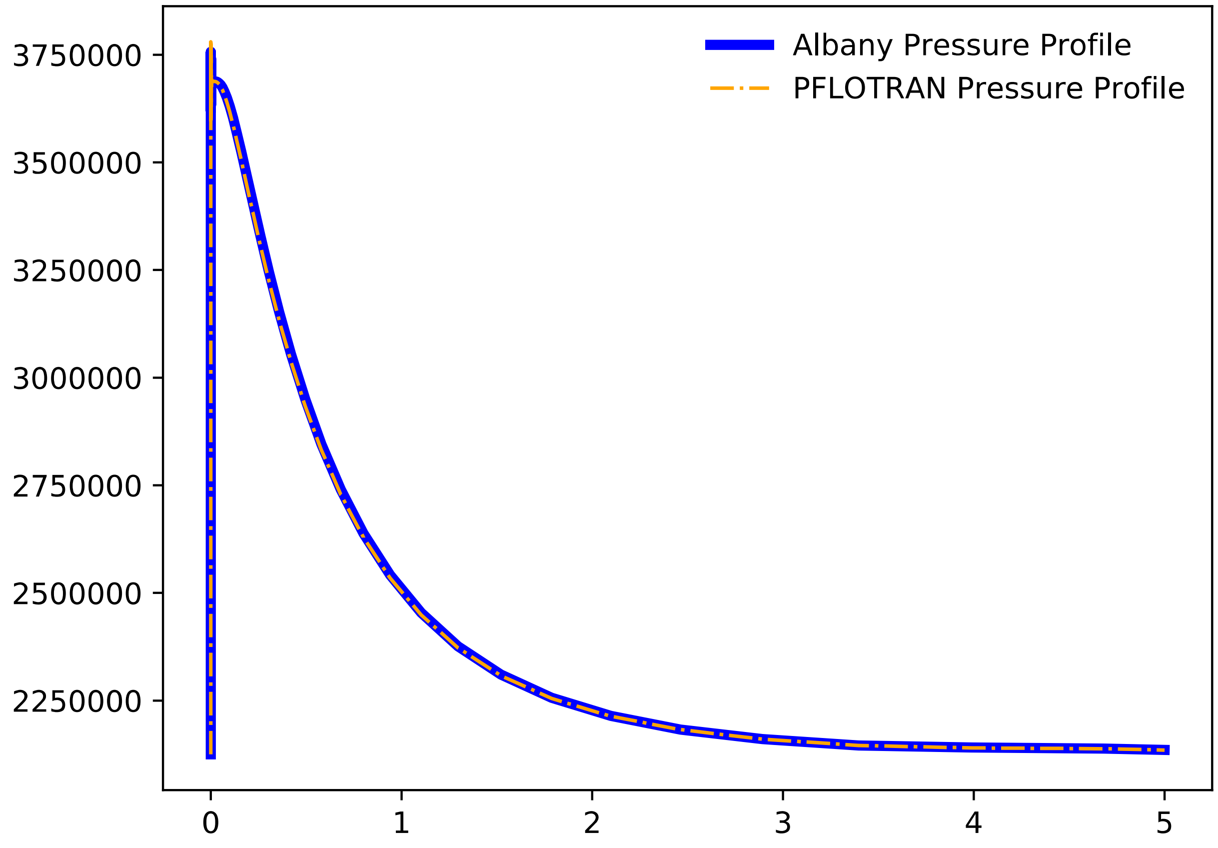

Figure 5-7 Pore pressure at the top of the column vs time

5.6. Obtaining and Installing Albotran

Albotran is a hybrid application combining modified versions of PFLOTRAN and Albany. As such, these versions of PFLOTRAN and Albany must be built and linked to create the Albotran application (binary releases of Albotran do not currently exist). The modified versions of PFLOTRAN and Albany are hosted on a git repository at www.gitlab-ex.sandia.gov/albotran from which each can be downloaded or cloned.

Building Albotran is complicated by the fact that both PFLOTRAN and Albany use their own build systems, require a large number of third-party libraries (TPLs), and custom build instructions are needed for each so that PFLOTRAN and Albany can be linked. For convenience, and repeatability, spack (https://www.github.com/spack) is used to build and install Albotran. spack is the "Super computer PACKage manager" and is actively developed at Lawrence Livermore National Laboratory. spack is similar to other package managers such as Homebrew (https://brew.sh) in that it manages and builds software packages and all of their dependencies. spack has several unique capabilities making it particularly useful for scientific applications and high performance computers.

5.6.1. *Installing Albotran*

Sandia users on a cee-lan machine or Skybridge, see the following section for instruction specific to those machines.

Step 1. Clone both spack and Albotran

At the command line, execute the following

```
$ git clone https://www.github.com/spack/spack
$ git clone git@gitlab-ex.sandia.gov:albotran/Albotran
```

Step 2. Register Albotran with spack as an external repository.

Create file `~/.spack/repos.yaml` with the following contents

```
repos:
- <path to Albotran>/var/albotran/spack-repo
```

Here, `<path to Albotran>` is the directory where Albotran was cloned in Step 1.

Step 3. Build and install Albotran

At the command line, execute the following

```
$ spack install albotran
```

Warning: the build process can take multiple hours depending on the machine.

5.6.1.1. Sandia CEE LAN or Skybridge Users

spack environments have been created that reduce the build time by using software already installed on various cee-lan machines and on Skybridge.

Step 1. Clone Albotran

At the command line, execute the following

```
$ git clone git@gitlab-ex.sandia.gov:albotran/Albotran
```

Step 2: Activate the appropriate spack environment

At the command line, execute the following

```
$ source <path to Albotran>/share/albotran/setup-env.sh <build-name>
```

Here, `<path to Albotran>` is the directory where Albotran was cloned in Step 1.

and `<build-name>` is an appropriate name for the machine you are on. See `<path to Albotran>/share/albotran/setup-env.sh -h` for a list of preconfigured build names.

Step 3:

Build and install Albotran

At the command line, execute the following

```
$ spack install albotran
```

Warning: the build process can take multiple hours depending on the machine.

Note: if `setup-env.sh` will clone spack to `<path to Albotran>/opt`. If you are executing the script behind a company firewall, you may need to set http proxy appropriately. If you have a spack instance that you would like to use, symolically link it to `<path to Albotran>/opt/spack.`

5.7. Running Albotran

Run Albotran using the `AlbanyT` executable.

```
$ mpiexec -np <N> <Albotran prefix>/AlbanyT <filename>
```

where `<filename>` is the name of an *Albany* input file with a PFLOTRAN specification. See Section 5.7 for how to format Albany and PFLOTRAN input files for Albotran.

5.8. Albotran Input Files

Albotran input files are the same as standalone Albany and PFLOTRAN input files, with blocks describing the interaction between the two codes.

5.8.1. Albany

The **Flow Coupling** input section is used to describe the coupling of Albany to PFLOTRAN. Additionally, the **Poro Elastic** material model must be used in the coupled region. Problem and material inputs for the Albotran specification, along with default values (when applicable) are shown in Figure 5-7 and Figure 5-9.

5.9. Supplemental Material

In the PFLOTRAN input file, the SIMULATION, PROCESS_MODELS, and MATERIAL_PROPERTY input decks must be augmented to specify the coupled Albotran problem, as shown in Figure 5-10.

```
ANONYMOUS:
  Problem:
    Name: Mechanics 3D
    MaterialDB Filename: Materials.yaml
    ...
    Flow Coupling:
      Pore Pressure Evaluator:
        Verbosity: 0
      Manager:
        Verbosity: 0
      BlackBox:
        Verbosity: 0
      PFLOTRAN:
        Verbosity: 0
        Input Filename: pflotran.in
      DataTransferKit:
        Map Type: Point Cloud
        Point Cloud:
          Map Type: Spline Interpolation
          Basis Type: Wu
          Basis Order: 4
          Spatial Dimension: 3
          Type of Search: Nearest Neighbor
          Num Neighbors: 4
        L2 Projection:
          Integration Order: 2
        Consistent Interpolation:
          Range Entity Dimension: 3
        Search:
          Track Missed Range Entities: false
```

Figure 5-8. Flow coupling input section used to describe the coupling of Albany and PFLOTRAN

```
Materials:
  <material name>:
    Material Model:
      Model Name: Poro Elastic
      Reference Pore Pressure: <P0>
      Reference Porosity: <PHI0>
      Biot Coefficient: 1
      Verbose: false
      PFLOTRAN Evaluation Mode: 1
    Elastic Modulus:
      Elastic Modulus Type: Constant
      Value: <E>
    Poissons Ratio:
      Poissons Ratio Type: Constant
      Value: <Nu>
```

Figure 5-9. In regions where Albany is coupled with PFLOTRAN, the Poro Elastic model must be defined

```
SIMULATION
  SIMULATION_TYPE COUPLED_GEOMECHANICS
  PROCESS_MODELS
    MECHANICS
      SOLVER Albany
      COUPLING_TYPE TWO_WAY_COUPLED
    END
  END
END

MATERIAL_PROPERTY <NAME>
  ...
  COUPLED_GEOMECHANICS
    BIOT_COEFF <ALPHA>
    DRAINED_BULK_MODULUS <K>
  END
END
```

NOTE: Text in bold denotes Albotran specific input blocks and cards.

Figure 5-10. Modifications to the PFLOTRAN input file needed to run the coupled Albotran problem

6. A NEW POLYMER NANOCOMPOSITE REPAIR MATERIAL FOR RESTORING WELLBORE SEAL INTEGRITY

6.1. Overview

Seal integrity of functional oil wells and abandoned wellbores used for CO_2 subsequent storage has become of significant interest with the oil and gas leaks worldwide. This is attributed to the fact that wellbores intersecting geographical formations contain potential leakage pathways. One of the critical leakage pathways is the cement-shale interface. In this paper, we examine the efficiency of a new polymer nanocomposite repair material that can be injected for sealing micro annulus in wellbores. The bond strength and microstructure of the interface of Type G oil well cement (OWC), microfine cement, Novolac epoxy incorporating Neat, 0.25%, 0.5%, and 1.0% aluminum nanoparticles (ANPs) with shale is investigated. Interfacial bond strength testing shows that injected microfine cement repair has considerably low bond strength, while ANPs-epoxy nanocomposites have a bond strength that is an order of magnitude higher than cement. Microscopic investigations of the interface show that micro annulus interfacial cracks with widths up to 40 μm were observed at the cement-shale interface while these cracks were absent at the cement-epoxy-shale interface. Fourier transform infrared (FTIR) and dynamic mechanical analysis (DMA) measurements showed that ANPs improve interfacial bond by limiting epoxy crosslinking, and therefore allowing epoxy to form robust bonds with cement and shale.

6.2. Introduction

Seal integrity of both production wells and abandoned wells is critical to a variety of subsurface applications, including geologic storage of CO_2. Loss of zonal isolation is a serious issue and is integral to ensuring protection of human health and the environment. Wellbores intersecting geological formations contain potential leakage pathways that exist due to either well-completion process or degradation of the cement and steel casing (Zhang and Bachu 2011). Among the potential leakage pathways in wellbores as summarized schematically in Figure 6-1 (Celia et al. 2005), the steel-cement and rock-cement interfaces are two of the most critical leakage pathways (Carey et al. 2007). While considerable attention has been given to the steel-cement interface (Baldan, 2004; Nakayama and Beaudoin 1987; Zhai et al. 2006), little effort has been focused on studying the rock-cement interface. This article focuses on repair of the rock-, specifically shale, cement interface for seal integrity. Due to their low permeability, shale layers often serve as cap rocks for underlying hydrocarbon reservoirs. Ensuring the integrity of wellbores at locations where they penetrate these layers is important for the containment and control of reservoir fluids.

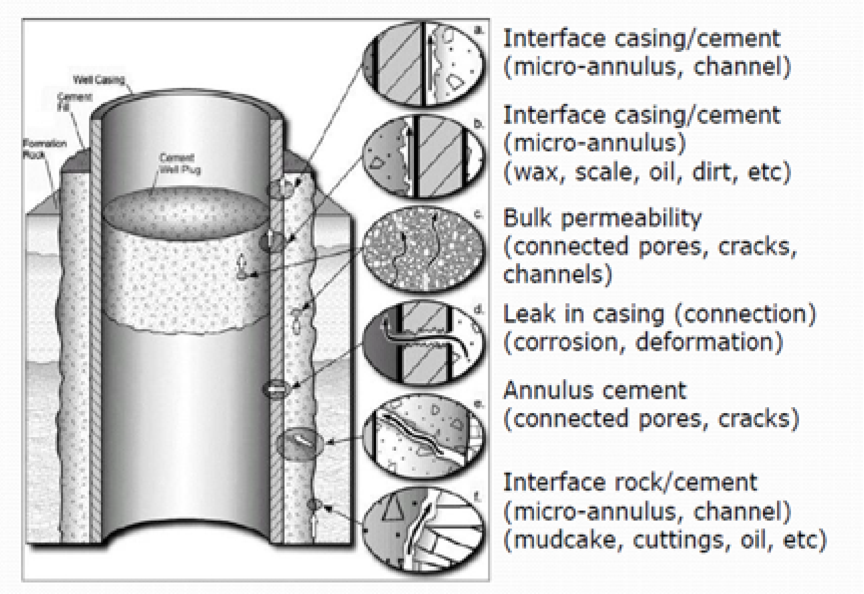

Source: (Celia et al. 2005)

Figure 6-1. Schematic representation of zonal isolation and potential leakage pathways

Prior investigations have shown that the cement-shale bond is affected by both cement and shale. Cement shrinkage and growth of the calcium hydroxide crystals at the interfacial zone of cement-bonded surfaces are well-known reasons to weaken cement bond with most interfaces including the cement-shale interface (Nakayama and Beaudoin 1987; Mehta and Monteiro 2013). Moreover, the swelling coefficient of the shale formation has a significant impact on interfacial bond between the cement and shale. The higher the swelling coefficient, the weaker the bond-strength is between the cement and shale (Ladva et al. 2005). The morphology of the rock surface also significantly affects the bond strength of the cement-shale interface. Shale formation with higher surface roughness would tend to have higher bond strength with cement compared with smooth shale formations (Nasir and Fall 2008). The presence of carbonated brine can significantly deteriorate cement and affect the wellbore seal integrity (Carey et al. 2007; Duguid and Scherer 2010; Huet et al. 2010; Kutchko et al. 2077; Kutchko et al. 2008; Liteanu et al. 2009; Matteo and Scherer 2012; Rimmelé et al. 2008). The above factors favor debonding between cement and shale over the long-term.

Repair of the cement-shale bond requires injecting a repair material that can fill the interfacial contact and improve seal integrity. A repair material should have a relatively low viscosity so it can flow during injection to penetrate microannulus cracks (micro cracks along a cement-shale contact interface). Such material should have minimal shrinkage to reduce the likelihood that a new flow path will develop between the repair material and the cement and/or shale. Furthermore, the repair material should also be flexible to prevent debonding due to further cement shrinkage, shale swelling, temperature changes and/or shock waves.

We suggest that polymer-based materials are optimal repair materials to achieve these requirements. Polymers have shown very high bond strength with metallic surfaces (Baldan 2004). Thermoset polymers, specifically Novolac-based epoxies, show very high bond strength with different surfaces. Moreover, incorporating nanomaterials such as ANPs in polymers was able to improve their mechanical properties and durability (Pocius 2012; Salemi and Behfarnia 2013; Shokrieh et al. 2012; Wetzel et al. 2006). Zhai et al. (2006) reported improved bond between polymer matrices and metallic surfaces when nanomaterials were dispersed in the polymer matrix. Our prior investigations showed that Novolac epoxy incorporating ANPs significantly improved the bond strength of the cement-steel interface (Genedy et al. 2014).

In this study, we investigate the efficiency of using Novolac epoxy incorporating ANPs as a repair material for sealing cement-shale microannulus. The bond strength of ANPs-epoxy nanocomposites incorporating different content of ANPs is investigated using push-out tests. In these tests, ANPs-epoxy nanocomposites were injected into an 800 μm artificial gap created between an inner shale cylinder and an outer cured cement socket. The ANPs-epoxy nanocomposites were compared to a standard microfine cement repair material, typically used in the industry, which was injected to fill the same above gap. The bond strengths of ANPs-epoxy polymer nanocomposites as well as the microfine cement repair materials were compared with the bond strength of a reference case where Type-G OWC was cast around shale and fully cured to achieve the highest possible bond strength. Microstructural analysis including DMA and FTIR analysis as well as light microscope investigations were conducted to understand the significance of nanomaterials on epoxy behavior.

6.3. Experimental Methods

6.3.1. Materials

The shale used in this investigation was Mancos Shale. Type G (American Petroleum Institute [API] Class G) OWC was used as the reference cement material. Microfine cement, generally used to repair cracks in oil wells, provided by the manufacturer was used. The microfine cement has a composition that is comparable to high sulfate-resistant cements and grain size (d_{95}) of 9.5 μm. The mix used for the microfine cement has water-to-cement (w/c) ratio of 0.7 and 2.0% of the dry cement weight super plasticizer (recommended by the manufacturer). Novolac epoxy was selected as the repair material due to its high chemical resistance, relatively high thermal performance and good flowability. Novolac epoxy system is a low viscosity cycloaliphatic polyamine blend with low viscosity hardener. Researchers showed water, acids (such as carbonated water) and saline solutions to have negligible effect on hardened Novolac epoxy (Atta et al. 2008, Tchoquessi Doidjo et al. 2013, Soares-Pozzi et al. 2016). ANPs were used to modify the epoxy matrix. ANPs are aluminum oxide (Al_2O_3) with maximum particle size of 50 nm were obtained from Sigma Aldrich, Inc. Microscopic image of ANPs using transmission electron microscope (TEM) is shown in Figure 6-2. Three weight contents of ANPs were examined in addition to neat epoxy being 0.25%, 0.50% and 1.0% by weight of the epoxy resin.

6.3.2. Polymer Nanocomposite Preparation

To prepare the polymer nanocomposite, the ANPs were added to the required amount of the resin, and the mix was stirred for 2 hours at 110ºC using magnetic stirring. This relatively high mixing temperature was used to reduce the resin viscosity and improve the dispersion of ANPs. The mix was then sonicated for 2 additional hours at 65ºC using an ultrasonic homogenizer. The polymer resin nanocomposite was left to cool and reach room temperature and then mixed with the hardener with mixing ratio 2.2:1 (Resin:Hardener) for 3 minutes using low speed mixer until a uniform mix was obtained. It is important that the nanomaterials are very well dispersed in the mixture to prevent gravity settling. This was achieved by the interaction of ANPs with the polar groups of the epoxy resin.

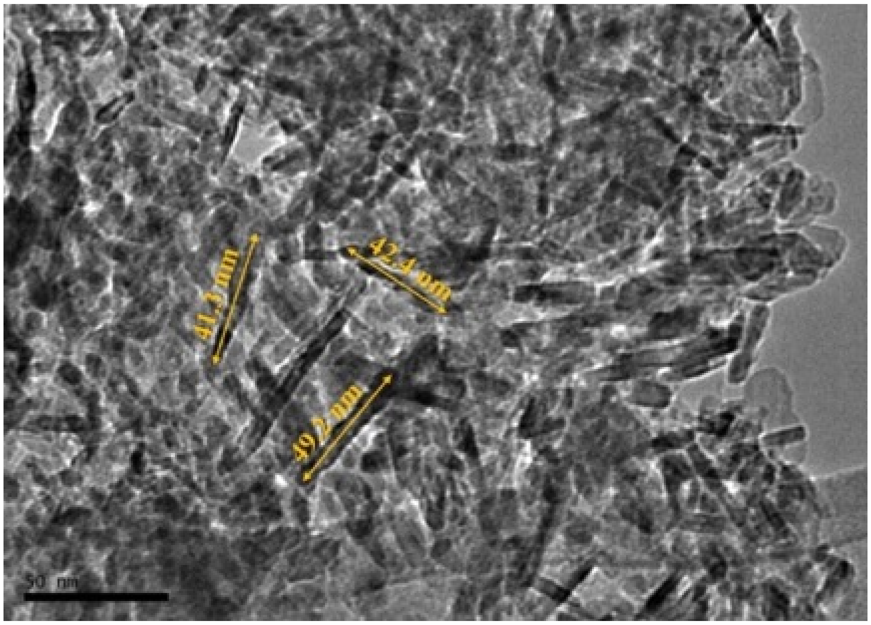

Figure 6-2. TEM micrograph showing ANPs and their size

6.3.3. Viscosity of Repair Materials

Viscosity test was conducted using rotational Viscometer following AASHTO T316 (AASHTO 2013). The viscosity was measured for all material at room temperature (22ºC). SC4-21 needle spindles, rotating at 20 rpm, were used for viscosity measurements. The spindles were allowed to rotate for 1 minute, after which three readings were taken at 15-second intervals. The test was performed as per the AASHTO standard.

6.3.4. Interfacial Bond Strength Testing (Push-out Test)

Two sets of specimens were prepared for push-out tests (Figure 6-3). The first set was used to measure the bond strength between the shale and Type G cement. A shale core of 25.4-mm diameter and a length greater than 30 mm was fixed in the center of a steel cylinder with an outer diameter of 100 mm and thickness of 3.2 mm; cement paste was then cast around the shale to produce cylindrical specimens with a diameter of 101.4 mm and height of 50.8 mm. The second set of specimens was prepared to investigate the bond strength of the repair materials injected in an artificial microannulus between cement and shale. Hollow Type G cement cylindrical specimens confined with steel cylinders with inner diameter of 27 mm, total outer diameter of 101.4 mm and height of 50.8 mm were cast first. These specimens were cured at 100% humidity environment at room temperature for 28 days. After the cement cylinder was cured, the shale core with a diameter of 25.4 mm was placed in the center of the hole, which produced a gap or microannulus between the cement and shale of nominally 800 μm. Repair material was then supplied along the top shale-cement contact and allowed to flow by gravity into the microannulus (Figure 6-4). The repair material was added into the crack until the repair material no longer flowed into the crack. Five repair materials were tested in this investigation: standard microfine cement, Novolac epoxy, and Novolac epoxy with 3 different contents of ANPs (0.25 wt.%, 0.5 wt.%, and 1.0 w.%). ANPs were added as a weight percentage of the epoxy total weight.

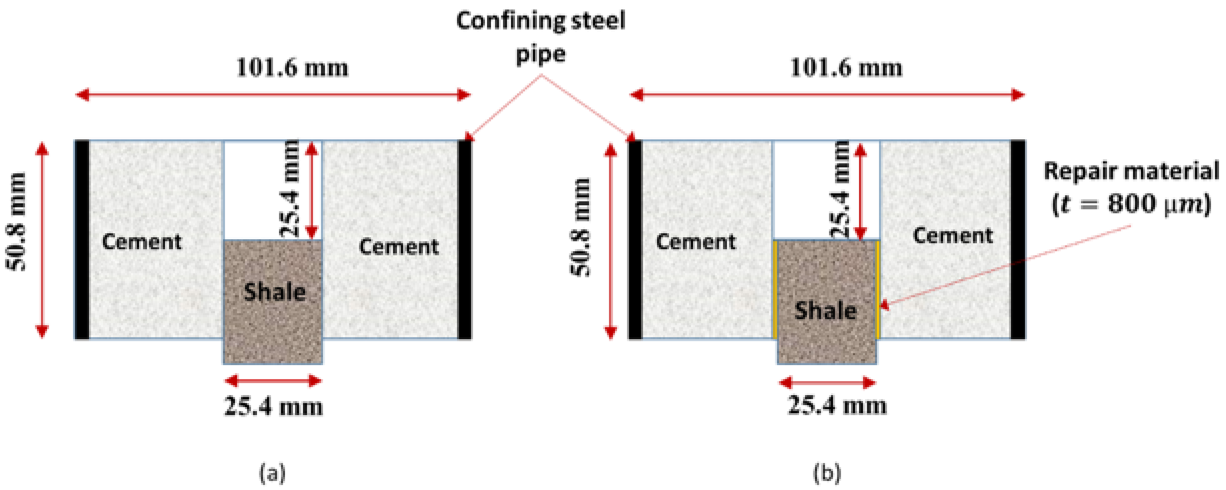

Figure 6-3. Schematic of the push-out test specimens for (a) first set of specimens and (b) second set of specimens

Figure 6-4. Placing repair material at the cement-shale microannulus

All specimens were tested at age 7 days after repair (or curing for reference specimens). Cement specimens were cured in 100% humidity while polymer nanocomposites specimens were air cured at room temperature.

The push-out test setup is shown in Figure 6-5. The push-out test was conducted under two-stage displacement control protocol. The test started with a rate of 0. 1 mm/min for the first 5 mm, after which the loading rate was increased to 1.0 mm/min. Test load and displacement were recorded using sampling rate of 1 Hz. The initial lower displacement rate allowed bond failure to take place at low strain rate. The greater displacement rate post-peak reduced the total test time to about 1 hour. The bond strength was calculated using Equation 6-1.

$$\tau = \frac{P}{\pi D L} \qquad \text{Equation 6-1}$$

where τ is the interfacial bond strength, P is the peak load, D is the diameter of the shale core of 25.4 mm, and L is the embedment length of 25.4 mm.

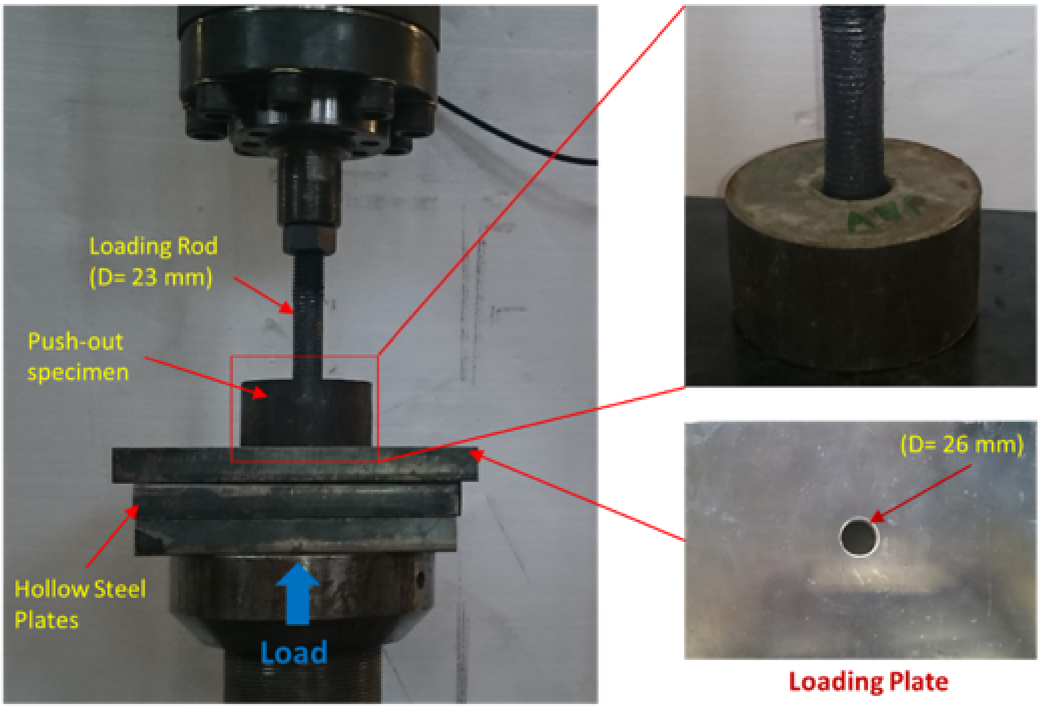

Figure 6-5. Push-out test setup

6.3.5. *Microstructure Investigations*

Microstructure investigations were conducted to gain insight into the bond strength developed in the repaired systems. The effect of ANPs on epoxy matrix was examined using FTIR Analysis and DMA. Microscopic images of the shale-cement interface with the different repair materials were also examined.

6.3.5.1. Fourier Transform Infrared Analysis

FTIR analysis was conducted on the polymer specimen with (1%) and without ANPs. A PerkinElmer FTIR with the universal attenuated total reflectance (UATR) accessory was used for the analysis. The spectra were recorded with a horizontal ATR accessory and a DiComp crystal (composed of a diamond ATR with a zinc selenide focusing element). For each sample, 4000 scans were collected at a resolution of 4 cm^{-1}. The spectra were then converted to absorbance using the Kramers-Kronig equation for FTIR analysis (Griffiths and de Hasseth 2007).

6.3.5.2. Dynamic Mechanical Analyses

The effect of ANPs on crosslinking of epoxy was investigated using DMA. The crosslinking density was determined by applying the theory of rubbery elasticity (Hill 1997) using Equation 6-2.

$$v_e = \frac{E^{'}}{3RT} \qquad \textit{Equation 6-2}$$

v_e is the crosslinking density, $E^{'}$ is storage modulus in the rubbery plateau, T is the temperature in Kelvin corresponding to the storage modulus value, and R is Gas Constant. The rubbery plateau was considered to be at temperature 50ºC above glass transition temperature T_g (Lee and Yee 2000). The storage modulus at rubbery plateau was measured using DMA Q800. The molecular weight between crosslinks can be calculated using Equation 6-3.

$$M_c = \frac{\rho}{v_e} \qquad \textit{Equation 6-3}$$

where M_c is molecular weight between crosslinks and ρ is the density of the polymer nanocomposite. As the crosslinking of a polymer resin increases when the molecular weight between crosslinks decreases (Lee and Yee 2000; Liang and Pearson 2009), A measure for the degree of crosslinking X_{link} is suggested here as an inverse for the molecular weight between crosslinks in a unit volume as in Equation 6-4.

$$X_{link} = \frac{1}{M_c} = \frac{v_e}{\rho} \qquad \textit{Equation 6-4}$$

where X_{link} is a measure of the degree of crosslinking of the polymer nanocomposite.

6.3.5.3. Microscopic Investigation

Light microscopes with two different levels of magnification (100× and 500×) were used to observe the shale-cement interface with the different repair materials.

6.4. Results and Discussion

Median load-displacement curves of specimens with different repair materials are shown in Figure 6-6. It is obvious that microfine cement as repair material has a very low shear capacity and very low energy absorption (represented by the area under the curve) compared with all the epoxy nanocomposite repair materials. Compared to neat epoxy, the nanocomposite with 0.25% ANPs does not appear to have increased shear capacity or energy absorption. However, it is apparent that adding 0.5% ANPs to the epoxy improved both the shear capacity and its energy absorption significantly; little additional benefit appears to be gained by increasing the ANP to 1.0%. Figure 6-6 also shows that the peak displacement for epoxy incorporating ANPs were in the order of 5.0 mm for neat epoxy and epoxy incorporating 0.25% ANPs compared with 3.0 mm for epoxy incorporating 0.5 and 1.0% ANPs compared to 0.7 mm for microfine cement. A very sharp decrease in load carrying capacity was observed for microfine cement compared with a much more gradual decrease observed for epoxy nanocomposites.

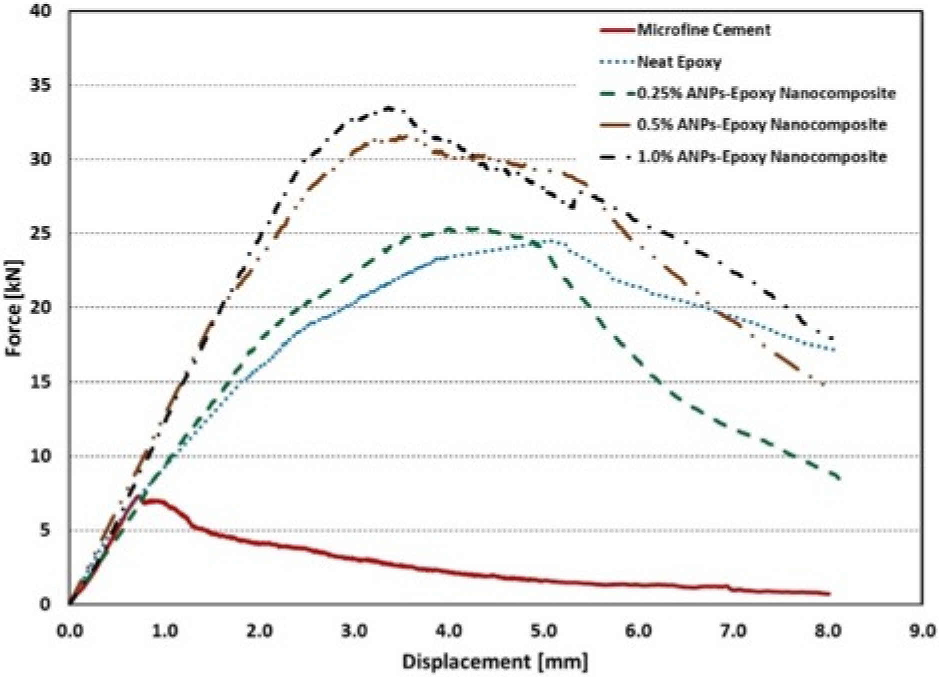

Figure 6-6. Median load-displacement curves of specimens repaired with microfine cement and epoxy-based materials

Figure 6-7 shows the bond strength of the reference case (cement case around shale) and all repair materials. Table 6-1 presents the bond strength for all repair materials compared with reference case. With all failures taking place at the shale epoxy interface, shear effect on epoxy was ignored. Statistical analysis using student t-test with 95% level of confidence shows that the reduction of bond strength of microfine cement was statistically insignificant. However, the increase in the bond strength of all ANPS-epoxy nanocomposites is statistically significant when compared with the reference case or the microfine repair cement.

Table 6-1. Bond strength of repair material compared with reference case

Material	Reference	Microfine cement	Neat Epoxy	0.25% ANPs	0.5% ANPs	1.0% ANPs
Bond Strength [MPa]	4.5±0.1	3.5±0.8	12.3±0.9	12.6±0.1	15.4±0.3	15. 9±0.9

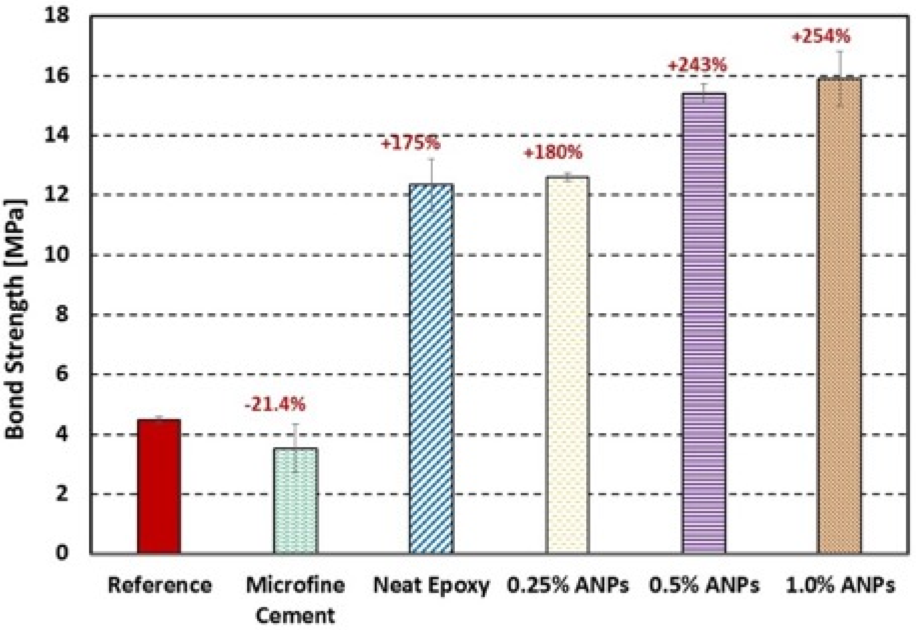

NOTE: % above the bars represents the difference of bond strength of repair material compared with the reference case.

Figure 6-7. The bond strength of the reference case and all repair materials.

Table 6-2 summarizes viscosity measurements, shear stiffness defined as the slope of the linear part of the load-displacement curve, displacement at peak load, and toughness calculated as the area under load-displacement curve for all repair materials.

Table 6-2. Viscosity, shear stiffness, displacement at peak load, and toughness for all repair materials

Material	Microfine cement	Neat Epoxy	0.25% ANPs	0.5% ANPs	1.0% ANPs
Viscosity [cps]	250±52	204±8	209±8	216±10	221±8
Shear stiffness [kN/mm]	11.0±0.09	10.9±0.49	10.7±0.8	11.1±0.1	11.2±0.5
Displacement at peak load [mm]	0.75±0.01	4.84±0.20	4.09±0.13	3.54±0.06	3.39±0.04
Toughness [N.ma]	21.7±0.4	145.7±0.5	141.4±1.2	180.7±1.9	186.7±2.4

Figure 6-8 shows the viscosity measurements for ANPs-epoxy nanocomposites compared with microfine cement. It was found that all ANPs-epoxy nanocomposites have viscosity lower than microfine cement. It was also found that incorporating ANPs in epoxy resin have a minor effect on epoxy viscosity. The maximum increase in viscosity of ANPs-epoxy polymer nanocomposite was found to be 8.2% compared with that of neat epoxy. The displacement at peak load for microfine cement and ANPs-epoxy nanocomposites is shown in Figure 6-9. Although the results show that incorporating ANPs in the epoxy resin significantly reduces the displacement at peak load, the displacement at peak load of all ANPs-epoxy nanocomposites is significantly higher than microfine cement. Figure 6-10 shows the toughness of ANPs-epoxy nanocomposites compared to microfine cement.

Statistical analysis using student t-test with 95% level of confidence shows that the difference in viscosity of ANPs-epoxy nanocomposites was significantly different than that of microfine cement. Statistical analysis also shows that the difference of stiffness among all repair material was insignificant. It was also found that the difference in toughness between all ANPs-epoxy nanocomposites and microfine cement was statistically significant. However, there was no significant difference in toughness between neat epoxy and 0.25% ANPs-epoxy nanocomposite.

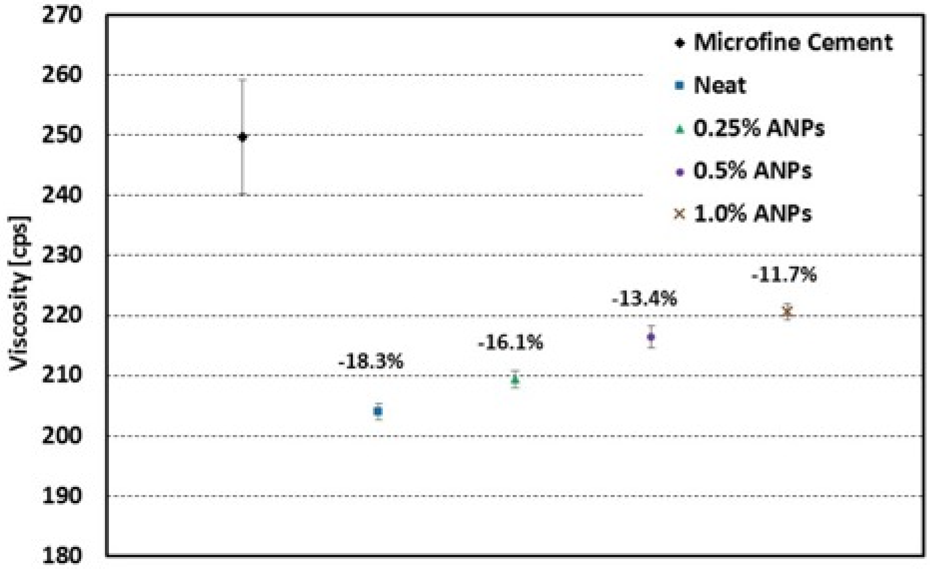

NOTE: % represents the difference in viscosity of polymer nanocomposites compared to the microfine cement.

Figure 6-8. Comparison of the viscosity between polymer nanocomposites incorporating 0% (Neat) 0.25%, 0.5%, and 1.0% ANPs and microfine cement

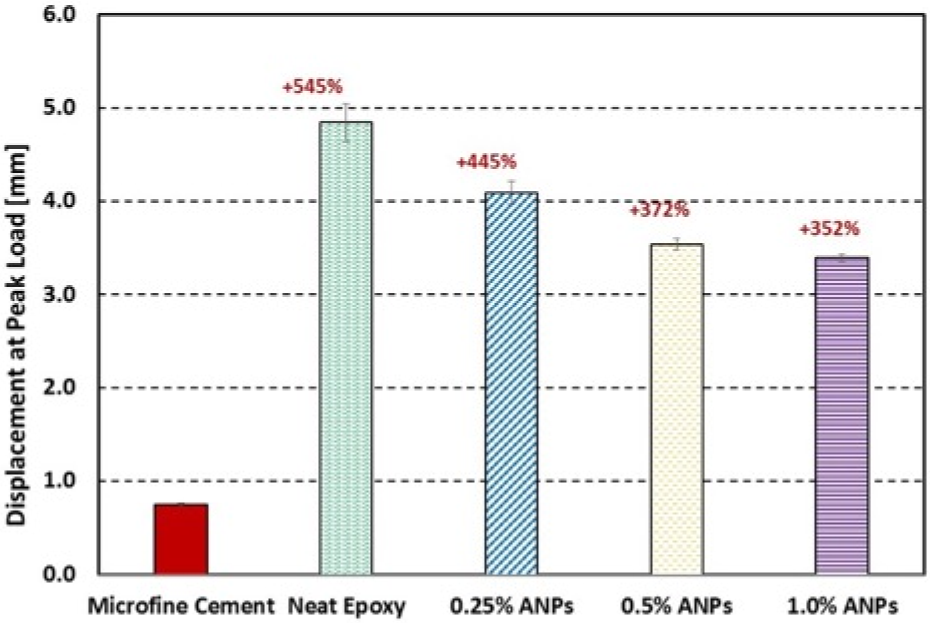

NOTE: % above the bars represents the difference of displacement at peak load of ANPs-epoxy nanocomposites compared with the microfine cement.

Figure 6-9. Displacement at peak load of the microfine cement and all ANPs-epoxy nanocomposites

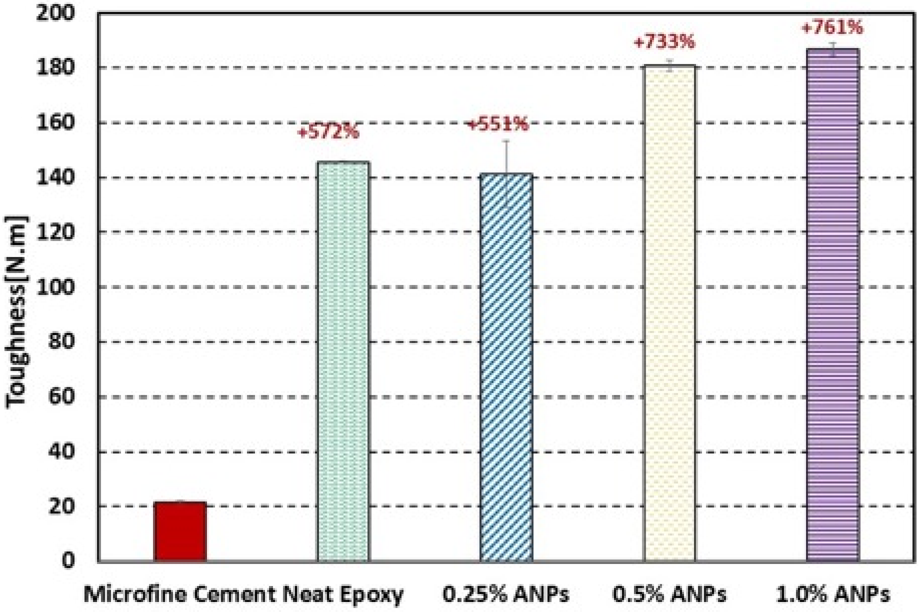

NOTE: % above the bars represents the difference of toughness of ANPs-epoxy nanocomposites compared with the microfine cement.

Figure 6-10. Toughness for the microfine cement and all ANPs-epoxy nanocomposites

Photomicrographs of the repaired shale interface with Type G cement using microfine cement, neat epoxy, and 1.0% ANPs-epoxy polymer nanocomposite are given in Figure 6-11, Figure 6-12 and Figure 6-13 respectively. As shown in Figure 6-11, using microfine cement as a repair material a gap at the shale-cement interface can be observed. It is important to note that such gap was not uniform and the width of the gap ranges from 3 μm up to 40 μm along the interface. These gaps might be formed due to shrinkage of microfine cement during its hydration. Such gaps between microfine cement and shale surface could explain the low bond strength in case of microfine cement compared with reference case.

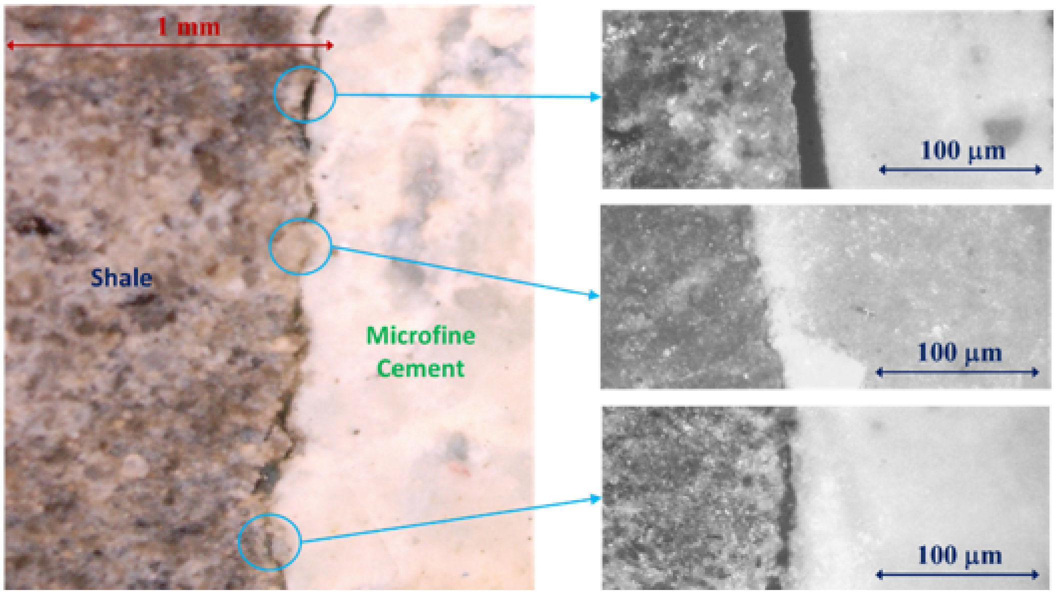

Figure 6-11. Microscopic images of shale-microfine cement interface with two different levels of magnification showing areas with gap between microfine cement and shale

Photomicrographs of the shale-cement interface repaired with the neat epoxy and 1.0% ANPs-epoxy nanocomposite, shown in Figure 6-12 and Figure 6-13, respectively, show no gaps and demonstrate the ability of epoxy with and without ANPs to flow and seal the shale-cement interface. A close look at Figure 6-12 and Figure 6-13 shows the ability of the ANPs-epoxy nanocomposite to infiltrate into the porous shale interface and fill the microcracks at the shale surface. This ability of epoxy and ANPs-epoxy nanocomposite to penetrate the shale microcrack network at the interface enables creating mechanical interlocks in addition to the adhesion between epoxy and shale. These interfacial microcracks at the shale surface also provide potential leakage pathways and thus compromise wellbore seal integrity. The penetration of the epoxy nanocomposite repair material not only improves the shale-cement bond strength, but it also seals leakage pathways adjacent to the interface and thus improves wellbore seal integrity. The improved shale-cement bond strength when epoxy or epoxy-ANPs nanocomposites were used for repair can be attributed to the improved cement-shale interface microstructure.

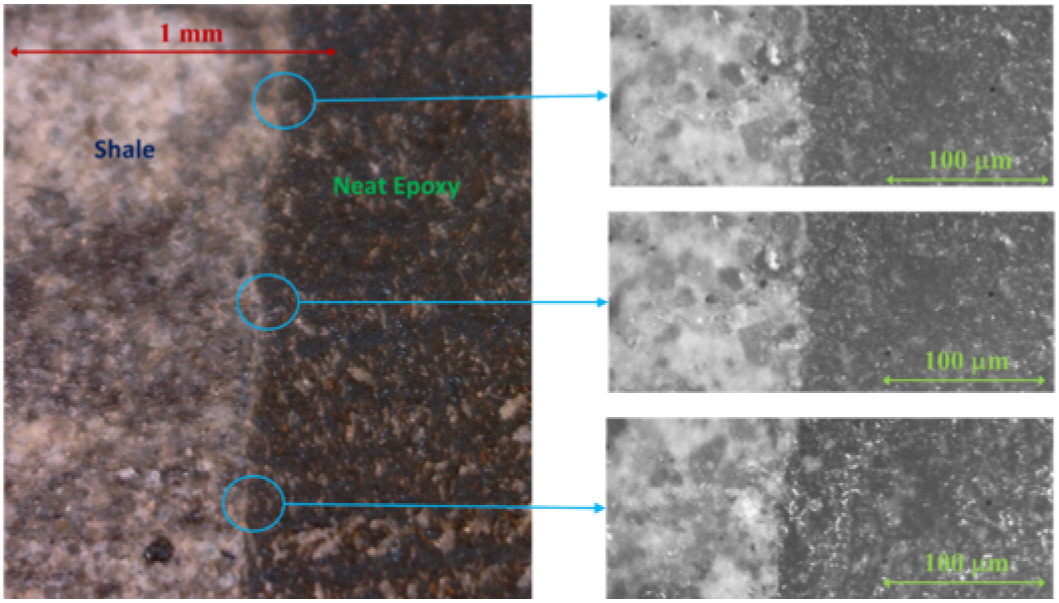

Figure 6-12. Microscopic images of shale-neat epoxy interface with two different levels of magnification showing the ability of the neat epoxy repair material to completely fill the gap at the shale-cement interface

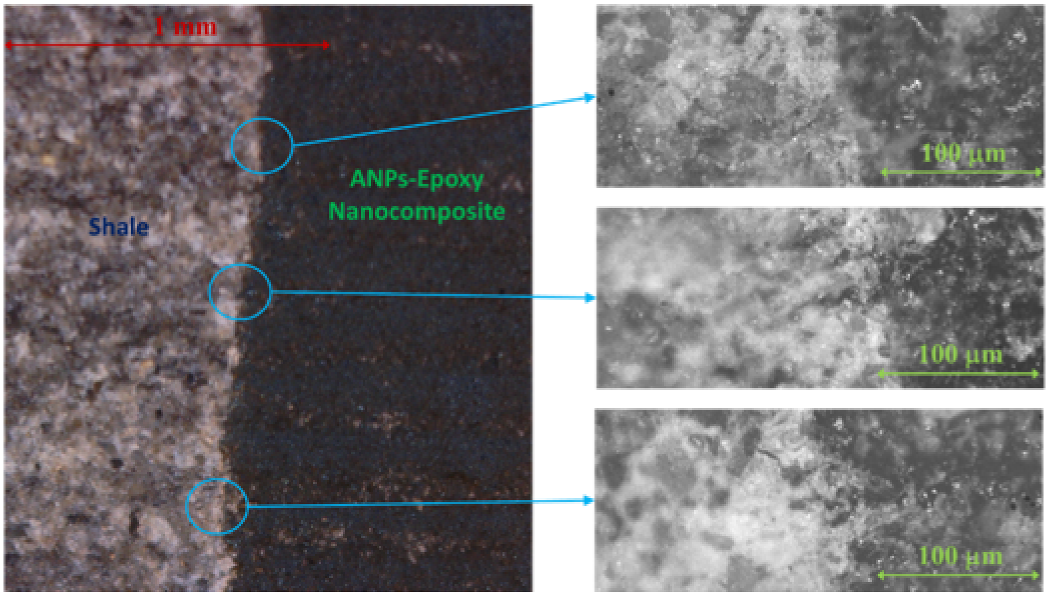

Figure 6-13. Microscopic images of shale-1.0% ANPs-epoxy polymer nanocomposite interface with two different levels of magnification showing the ability of the epoxy repair material to completely fill the gap at the shale-cement interface

FTIR spectra of neat epoxy and epoxy incorporating nano-alumina (0.5% and 1.0% ANPs) were obtained to compare chemical changes of the curing process of epoxy as shown in Figure 6-14. The FTIR spectra show the traditional band of epoxy where absorption bands corresponding to C-H appear at (2850–2930 cm^{-1}), epoxide ring (~825 cm^{-1}), N-H band of primary amines (1585–

1610 cm^{-1}), O-H groups (~3350 cm^{-1}), C-N band (1030–1115 cm^{-1}) and ether bands (~1230 cm^{-1}). The general illustrations of the chemical structures of the Novolac epoxy resin and its curing process can be found elsewhere (Golru et al. 2014). It can be clearly observed that addition of a small amount of ANPS (0.5 or 1.0%) to the epoxy resin caused a significant increase in the epoxy ring, O-H and primary N-H band intensity. This may be attributed to the effect of ANPs on the curing behavior of the epoxy matrix. The curing reaction of the epoxy resin proceeds through the amines presented in the polyamide curing agent (Brand et. al. 2004).

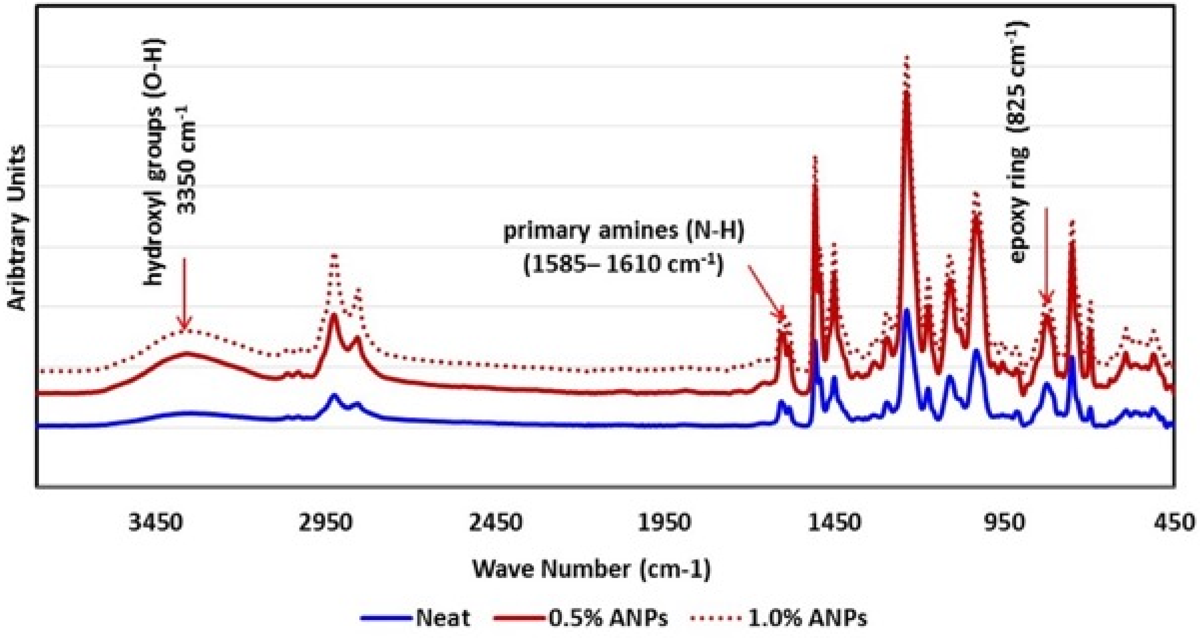

Figure 6-14. FTIR spectra of neat epoxy and epoxy incorporating 0.5% and 1.0% ANPs showing the significant changes appearing in the spectra using ANPs compared to the neat epoxy

It is interesting to note that both ANPs contents give the same effect on the curing process of epoxy. Based on the curing mechanism and the results obtained from FTIR analysis, it can be concluded that the curing reaction was affected by the presence of a relatively small amount of ANPs about 0.50%. This can be understood from the higher peak intensities of the epoxy ring (~830 cm^{-1}) and O-H groups (~3350 cm^{-1}) for the epoxy-ANPs nanocomposite compared with neat epoxy. This can be explained by the ability of ANPs to hinder epoxy curing due to steric hindrance effect of ANPs reported by Ramezanzadeh et. al. (2011). The steric hindrance effect results in decreasing the reactivity between the epoxy functional groups and polyamide hardener. Such effect is attributed to the amphoteric nature of ANPs which (Kardar et al. 2008; Sharifi Golru et al. 2014). The ability of ANPs to limit epoxy curing makes the unreacted epoxy groups available to react with other interfaces that epoxy is adhered to. This explains the ability of ANPs-epoxy nanocomposite to have much improved bond strength to both shale and cement compared with neat epoxy. A schematic of cured neat Novolac epoxy and Novolac epoxy incorporating ANPs based on the above FTIR analysis is shown in Figure 6-15.

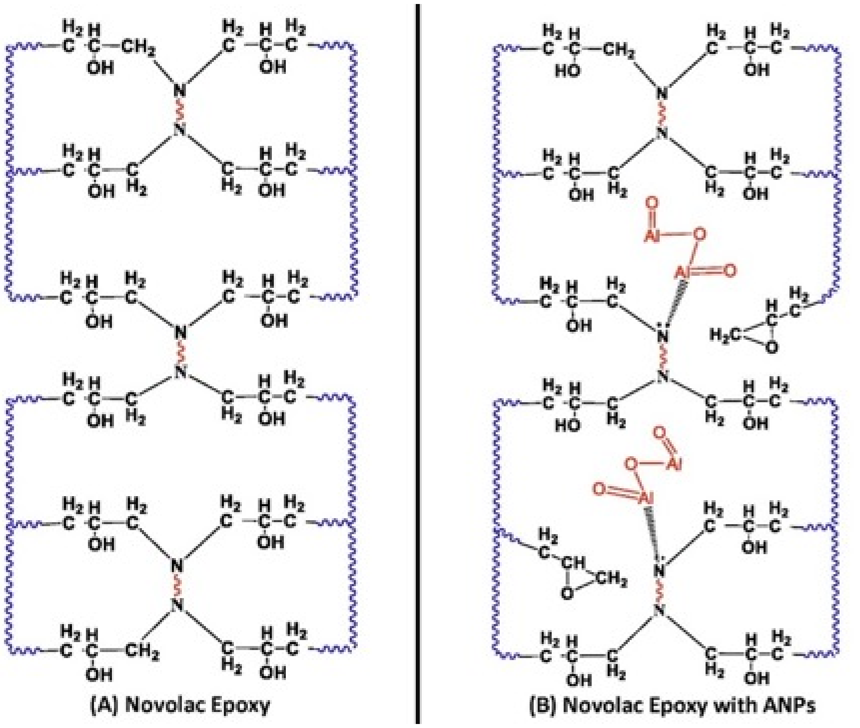

(A) Novolac Epoxy

(B) Novolac Epoxy with ANPs

Figure 6-15. A schematic showing the chemical structure of cured novolac epoxy (A) neat Novolac (B) Novolac epoxy incorporating ANPs

The above FTIR observations explain the increase in the repaired shale-cement bond strength by 29% when ANPs were incorporated in the epoxy resin compared with neat epoxy. Furthermore, limiting epoxy curing using ANPs, enables creating a more flexible ANPs-epoxy compared with neat epoxy. The increase in epoxy-nanocomposite flexibility is represented by the higher toughness (energy absorption) of ANPs-epoxy nanocomposites compared with neat epoxy. The flexibility of the ANPs-epoxy nanocomposite can be explained by a reduced epoxy cross-linking.

To confirm the significance of ANPs on epoxy cross-linking, DMA testing was conducted on neat epoxy and epoxy incorporating 0.25%, 0.5%, and 1.0% ANPs. The suggested degree of crosslinking measure (X-Link) was calculated using Equations (2), (3) and (4). Figure 6-16 shows the degree of crosslinking for neat epoxy, 0.25% ANPs-epoxy nanocomposites, 0.5%-ANPs epoxy nanocomposite and 1.0% ANPs-epoxy nanocomposite. The results show that incorporating 0.25% ANPs in the epoxy resin reduces the cross linking by only 4.9% which can explain the insignificant change in bond strength between ANPs-epoxy nanocomposites incorporating 0% (Neat) and 0.25% ANPs. On the other side, incorporating 0.5% and 1.0% ANPs reduces epoxy crosslinking by 15.8% and 16.4% respectively. The above analysis confirms the FTIR observations and is consistent with the observation that incorporating ANPs results in a more flexible epoxy nanocomposite compared with neat epoxy. A relatively flexible repair material with good bond strength to both shale and cement surface shall provide more stable long-term repair solution for its ability to deform in response to changes in wellbore conditions (stress, temperature, humidity) without cracking. Finally, DMA observations confirm that 0.5% ANPs per weight of the epoxy resin might be the optimal content in producing Novolac epoxy nanocomposite for repair for its limited significance on viscosity and low cost compared with higher ANPs contents. The choice of 0.5% ANPs can be justified by the insignificant improvements observed using1.0% ANPs as confirmed by bond strength testing, FTIR and DMA observations. The use of 0.5% ANPs still provides the necessary strength and flexibility for the repair material.

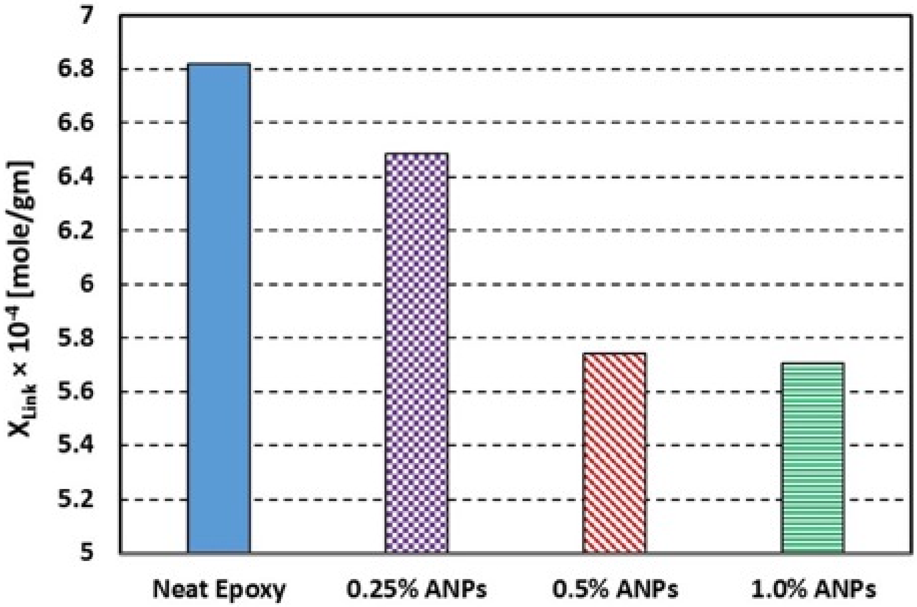

Figure 6-16. X_{link}: A measure of the degree of crosslinking for neat epoxy, 0.25% ANPs-epoxy nanocomposite, 0.5% ANPs-epoxy nanocomposite, and 1.0% ANPs-epoxy nanocomposite

It is important to note that all the experimental investigations presented here were conducted on a smooth shale surface. Shale roughness, temperature and environmental condition (e.g. presence of carbonates) shall be examined in future work. Future experimental program shall also investigate the effect of shale roughness and surface chemical exposure (existence of carbonated brine and effect of salinity) on the bond strength of epoxy nanocomposites. In addition, relatively small crack sizes (10–100 μm) will be examined to investigate the ability of epoxy nanocomposite and microfine cement to flow in much smaller microcracks compared to those reported here. Furthermore, time dependent rheological properties of epoxy nanocomposites including the effect of creep and cyclic loading (fatigue) on cement-shale interfacial bond strength shall also be investigated. Finally, field trials of the proposed polymer nanocomposites will be necessary to identify the optimal content of nanomaterials to achieve field performance needs.

6.5. Conclusions

Novolac epoxy incorporating ANPs is being considered as a repair material for restoring wellbore seal integrity. Novolac epoxy nanocomposite incorporating 0.5% ANPs by weight of the epoxy resin proved to be a good repair material for shale microannulus with improved bond strength and excellent flexibility. Viscosity tests show that all ANPs-epoxy nanocomposites have viscosities that are comparable to that of microfine cement which might enable using ANPs-epoxy nanocomposite as repair material for microannulus cracks. The epoxy-nanocomposite repair material has a bond strength that is an order of magnitude higher than the industry standard for microfine cement repair material. Push-out tests were conducted to examine the bond strength of different repair materials including microfine cement and Novolac epoxy nanocomposites incorporation 0% (Neat), 0.25%, 0.5%, and 1.0% ANPs. The push-out bond strengths were compared with a reference case where Type G cement was cast directly around the shale core. Microstructural investigations were conducted to understand the behavior at the interface using microscopic images, FTIR and DMA.

The experimental investigation showed that microfine cement is unable to completely fill the gap between shale and cement and thus has a bond strength that is 21% lower than the reference case. In contrast, ANPs-epoxy nanocomposites had a bond strength that is 250% higher than the reference case. Microscopic investigation of the shale-cement interface shows microfine cement was unable to completely fill the gap and microcracks along the interface with widths up to 40 μm remaining open. However, no gap was observed with ANPs-epoxy nanocomposites. Furthermore, the ANPs-epoxy nanocomposite was able to penetrate the shale porous surface and establishes an epoxy network inside the shale providing mechanical interlocks that further improves the interface seal by blocking those potential leakage pathways. Moreover, it was found the difference in stiffness of the microfine cement and all ANPs-epoxy nanocomposites was statistically insignificant. In addition, the displacement at peak load and the toughness of ANPs-epoxy nanocomposites were significantly higher than the displacement at peak load and toughness of microfine cement.

FTIR and DMA measurements of ANPs-epoxy nanocomposites showed that ANPs interfere in the epoxy polymerization process and limits the reaction between the resin and the hardener. This was confirmed through FTIR spectra and by estimating epoxy crosslinking using DMA testing. The limited epoxy reactivity in the presence of ANPs leaves the epoxy groups unreacted which improves the bond strength at the cement-shale interface. The limited cross-linking also provides a flexible epoxy that shall enable a good long-term seal with improved ability to respond to shock waves and variability in temperature and humidity.

6.6. Acknowledgements

This material is based upon work supported by the U.S. Department of Energy (DOE) National Energy Technology Laboratory (NETL) under Grant Number DEFE0009562. This project is managed and administered by the DOE/NETL Storage Division and funded by DOE/NETL and cost-sharing partners. This paper was prepared as an account of work sponsored by an agency of the United States Government. Neither the United States Government nor any agency thereof, nor any of their employees, makes any warranty, express or implied, or assumes any legal liability or responsibility for the accuracy, completeness, or usefulness of any information, apparatus, product, or process disclosed, or represents that its use would not infringe privately owned rights. Reference herein to any specific commercial product, process, or service by trade name, trademark, manufacturer, or otherwise does not necessarily constitute or imply its endorsement, recommendation, or favoring by the United States Government or any agency thereof. The views and opinions of authors expressed herein do not necessarily state or reflect those of the United States Government or any agency thereof. The authors thank Epoxy Chemicals, Inc. and Transpo Industries, Inc. for donating epoxy materials to the project.

7. THE SIGNIFICANCE OF NANOPARTICLES ON BOND STRENGTH OF POLYMER CONCRETE TO STEEL

7.1. Overview

Polymer concrete (PC) is a commonly used material in construction due to its improved durability and good bond strength to steel substrate. PC has been suggested as a repair and seal material to restore the bond between the cement annulus and the steel casing in wells that penetrate formations under consideration for CO_2 sequestration. Nanoparticles including multiwalled carbon nanotubes (MWCNTs), aluminum nanoparticles (ANPs), and silica nanoparticles (SNPs) were added to an epoxy-based PC to examine how the nanoparticles affect the bond strength of PC to a steel substrate. Slant shear tests were used to determine the bond strength of PC incorporating nanomaterials to steel; results reveal that PC incorporating nanomaterials has an improved bond strength to steel substrate compared with neat PC. In particular, ANPs improve the bond strength by 51% over neat PC. Local shear stresses, extracted from finite element (FE) analysis of the slant shear test, were found to be as much as twice the apparent/average shear/bond strength. These results suggest that the impact of nanomaterials is higher than that shown by the apparent strength. Fourier transform infrared (FTIR) measurements of epoxy with and without nanomaterials showed ANPs to influence curing of epoxy, which might explain the improved bond strength of PC-incorporating ANPs.

7.2. Introduction

PC is a commonly used material in construction and repair work for its high compressive strength, improved durability characteristics, high ductility, resistance to aggressive chemicals and superior bond strength to steel and concrete substrates compared with Portland cement concrete (ACI Committee 548 2009). PC is made by mixing a thermoset polymer, e.g. epoxy, with aggregate as a filler. PC is preferred in bridge deck overlays for its improved abrasion resistance (ACI Committee 548 2009; Ohama 1995). Recently, it was suggested that repair materials are needed to seal the interfacial cracks that often develop between steel casing and the cement annulus in wells in the vicinity of formations identified for CO_2 sequestration Zhang and Bachu 2011) as leaky wells are a critical issue for the implementation of carbon capture and storage. Such application requires PC to have superior bond strength to steel surfaces to accommodate harsh subterrain service conditions. The addition of nanomaterials was shown to improve mechanical properties of PC (Jo et al. 2008; Abdel-Ghaffar et al. 2014) and thus might enable its use to repair of damaged wells.

Polymer cement nanocomposites (PCNs) are a class of PC characterized by the dispersal of nanoparticles in the polymer matrix prior to producing the PC. Inclusion of nanoparticles introduces a significantly large number of particles within the matrix even at very low weight proportions (Tjong 2006). Wetzel et al. (2002) showed that the volume occupied by the addition of 3 microparticles corresponds to 3 million nanoparticles. The very small size and relatively high number of nanoparticles allow significant interaction between nanomaterials and the polymer matrix at the chemical as well as the physical level. Surface functionalized nanoparticles will thus alter the polymer chemistry producing a new type of PCN that may be significantly different than the original polymer matrix (Rider et al. 2015). Surface functionalization of the nanoparticles is an important process for it enabling the nanoparticles to chemically react with the polymer matrix and produce a new polymer nanocomposite. However, in order to effectively disperse the nanoparticles within the matrix, high shear mixing and methods to prevent particle agglomeration such as ultra-sonication are often required (Grossiord et al. 2006).

Carbon nanotubes (CNTs) are made from concentrically rolled single or multiple graphene sheets of nanoscale. CNTs possess exceptional strength, stiffness and failure strain as well as a very high aspect ratio (De et al. 2013). The elastic modulus of CNTs reaches 1 TPa and tensile strength 100 GPa (Musso et al. 2009; Vietri et al. 2014). Uniformly dispersed CNTs improve the bond strength, elastic modulus and ultimate tensile strength of the composite (Wetzel et al. 2006). MWCNTs represent one species of CNTs with similar or little lower mechanical properties and much lower cost compared with CNTs. ANPs are simply aluminum oxide (Al_2O_3) of nanoscale particles. The addition of ANPs was reported to increase the flexural modulus, toughness, glass transition temperature, resistance to fatigue crack propagation (Salemi and Behfarnia 2013), tensile strength and durability (Shekari and Razzaghi 2011). SNPs are among the smallest size nanoparticles available. They are reported to improve the compressive strength, elastic moduli, fatigue strength (Iglesias et al. 2002), adhesion, and scratch and corrosion resistance (Sprenger 2013). The selection of the three nanoparticles (MWCNTs, ANPs, and SNPs) was based on prior efforts to improve adhesion and fracture toughness (Wetzel et al. 2006; Sprenger 2013; Yuan et al. 2005; Momayez et al. 2005).

Bond strength of polymers to substrates is developed due to physical and chemical bonds (Pocius 2011). Chemical bonds are induced by chemical reaction of the polymer to the adhering substrate. Physical bonds are developed through Van Der Waal forces (Zhai et al. 2006). Inclusion of nanoparticles can enable a chemical interaction and/or generate new chemical bonds that would not be activated with the neat polymer. Bond strength tests include pull-off, twist-off (Pocius 2011), flexural (Julio et al. 2004) and slant shear tests (Zhai et al. 2006; Julio et al. 2004). Pull-off test reports the most conservative bond strength among all tests as it provides the lowest bond strength values (Momayez et al. 2005; Zhai et al. 2006; Julio et al. 2004; Saldanha et al. 2013). Momayez et al. (2005) showed that Pull-off in comparison to slant shear, splitting prism and Bi-surface shear tests pull-off not is the most suitable for bond strength tests where tension is the dominant state of stress. Tests like slant shear and Bi-surface shear impose a state of indirect tension by applying compression forces that result in shear stress over the bonded surface in question. However, the slant shear test is more suitable for examining vertical or inclined rather than horizontal bond surface. Two types of failure are associated with slant shear test; cohesive and adhesive failures. Cohesive failure takes place at the polymer side of the interface and correlates to a state of stress where the shear stress in the polymer exceeds the polymer's ultimate shear strength. Adhesive failure takes place at the bond interface between the two materials. Most standards suggest an angle of 60° with the horizontal surface to favor adhesive failure to take place (Julio et al. 2004; Saldanha et al. 2013). Materials that possess significantly high compressive strength tend to experience adhesive failure when surface roughness and interface angle are carefully chosen (Julio et al. 2004). American Society of Testing and Materials (ASTM) standards suggest obtaining the average bond strength by dividing the vertical load by the slanted area of contact leading to what we denote as the apparent bond strength.

The objective of this study is to investigate the influence of incorporating nanomaterials in PC on the apparent bond strength of epoxy PC and steel. We also examine the significance of nanomaterials on the bond strength between PC and steel and the associated effect on the local shear stresses developed at the interface compared with the apparent bond strength. Experimental investigations are conducted to evaluate and explain the significance of nanomaterials on PC-steel bond strength. FE analysis is used to model slant shear tests to estimate local shear stresses that develop along the interface between the two materials

7.3. Experimental Methods

Slant shear tests were carried out for neat PC and PC incorporating MWCNTs, ANPs and SNPs. Compression tests were also performed to extract the stress-strain response of PCs incorporating various nanomaterials.

7.3.1. Materials

Novolac epoxy system was selected for a potential well repair material principally due to its high chemical resistance. Novolac epoxy system (or HCE POLYAMINE) is a low viscosity cycloaliphatic polyamine blend with low viscosity hardener. Three types of nanoparticles were used: MWCNTs, SNPs, and ANPs. The MWCNTs were functionalized with carboxyl (COOH) group with diameter of 20–30 nm and 10–30 μm length. The MWCNTs were produced using Catalyzed Chemical Vapor Deposition Technique by Cheap-Tubes. Functionalization was performed by the manufacturer by means of acid treatment chemistry of H_2SO_4/HNO_3. COOH groups were attached at the ends and side walls of the nanotubes. This process is often performed by adding H_2O_2 to the chemical treatment as reported by Zhu et al. (2003) and Osorio et al. (2008). SNPs were AEREOSIL® 380 chemically prepared silicon dioxide powder produced by Evonik Degussa with an average particle size of 7 nm. ANPs are aluminum oxide (Al_2O_3) with maximum particle size of 50 nm were obtained from Sigma Aldrich Inc. Table 7-1 summarizes mixture proportions of the PCNs. Table 7-2 describes all of PCN mixtures and used denotations. In the table, PC denotes neat PC mixtures, PCNC denotes PCN mixed with MWCNTs, PCNA denotes PCN mixed with ANPs and PCNS denotes PCN mixed with SNPs. The number following the mixture designation reflects the nanomaterial content as percentage of epoxy weight.

Table 7-1. PCN mix proportions

PCN	Proportion (kg/m^3)
Epoxy resin	221
Epoxy hardener	96
Silica particle fillers	1200
Nanomaterial	wt. % of epoxy resin

Table 7-2. Nanoparticles and their % weight of epoxy for the different PCN mixes

PCN	Nanoparticles	% Weight of Epoxy
PC-Neat	None	0%
PCNC-0.5	MWCNTs	0.5%
PCNC-1.0		1.0%
PCNC-2.0		2.0%
PCNA-0.5	ANPs	0.5%

PCN	Nanoparticles	% Weight of Epoxy
PCNA-1.0		1.0%
PCNA-2.0		2.0%
PCNS-0.5	SNPs	0.5%
PCNS-1.0		1.0%
PCNS-2.0		2.0%

NOTE: The number after the PCN mixture designation reflects nanomaterial content as a percentage of epoxy weight.

ANP = aluminum nanoparticle
MWCNT = multiwalled carbon nanotube
PC = polymer concrete
PCN = polymer concrete nanocomposite
PCNA = PCN mixed with ANPs
PCNC = PCN mixed with MWCNTs
PCNS = PCN mixed with SNPs
SNP = silica nanoparticle

7.3.2. Specimen Preparation

The dispersion process of nanoparticles is accomplished by heating the epoxy resin to 110℃ and magnetically stirring at 800 rpm. Nanomaterials were then added to the epoxy and dispersed using magnetic stirring for two hours. Next, the resin incorporating the nanomaterials was placed in a sonicator at 60℃ for two hours. Ultra-sonication improves dispersion by generating microscopic bubbles within the resin that release energy and prevents particle agglomeration, thus leading to a uniform dispersion. Degassing using the sonicator hot bath option was performed to eliminate any air bubbles or voids within the matrix. The resin was then left to cool to room temperature for one hour. The hardener and the resin with dispersed nanoparticles were then mixed together to produce uniform polymer nanocomposite. Crystalline silica (quartz) and ceramic microspheres powder were then added as aggregate fillers to produce PCN mix. Curing was performed in room temperature for seven days. The dispersion technique was kept constant to avoid the difference associated with different processing techniques on the resultant polymer nanocomposite. MWCNTs proved to be more challenging to disperse than ANPs and SNPs due to their high aspect ratio and strong Van der Waals and Coulomb attraction forces. Hence, scanning electron microscope (SEM) images were collected for epoxy samples containing 2.0 wt.% MWCNTs in order to ensure proper dispersion at the highest content applied. Figure 7-1 shows the SEM images at two different locations of epoxy samples confirming no agglomeration achieving uniform dispersion of MWCNTs.

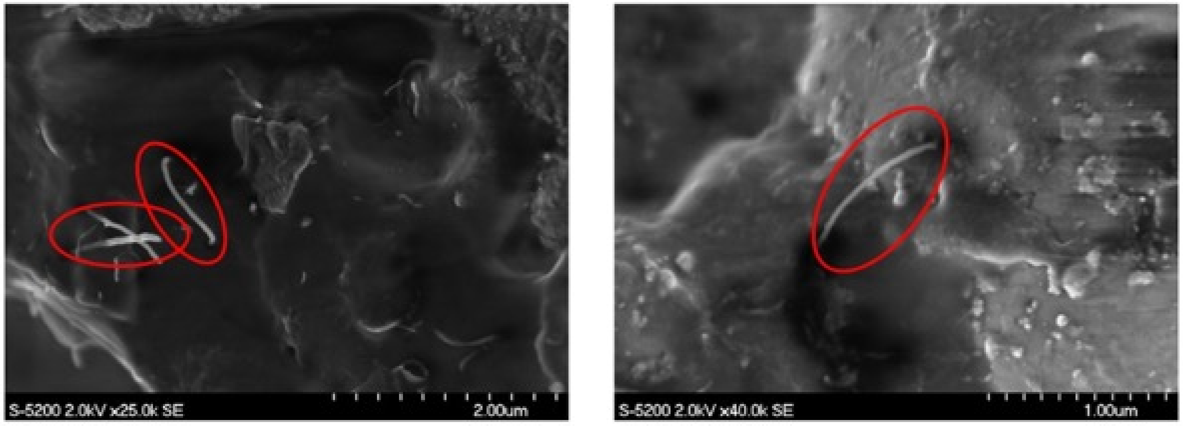

Figure 7-1. SEM images of epoxy samples containing 2.0 wt.% MWCNTs showing proper dispersion of nanotubes

7.3.3. Slant Shear Test

Slant shear tests were used to measure the bond strength of PCN-steel substrates. The steel substrate surface was sandblasted to a minimum of 4.0 mil (0.1016 mm) clean. PCN was cast on the steel part at 60° with the horizontal in two layers each compacted 25 times with the weight of standard concrete compaction rod. Figure 7-2 shows a schematic of the slant shear test as performed according to ASTM C882/C882M (ASTM 2013). Five specimens of each PCN were tested. The alignment of PC to steel was also clarified through high resolution camera to ensure proper alignment and no slippage prior to testing as shown in Figure 7-3. The apparent shear strength is given as

$$\tau = \frac{P\,sin(60)}{A\,/cos(60)} = \frac{P}{A}\sin(60)cos(60) \qquad \textit{Equation 7-1}$$

Where *P* is vertical applied load and *A* is the cross-sectional area of the cylinder.

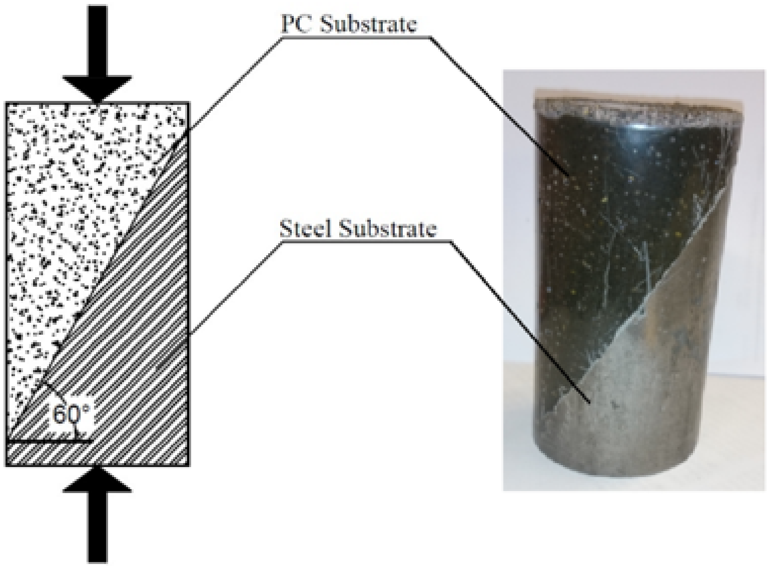

Figure 7-2. Slant shear test (left) schematics showing slant shear angle (right) actual specimen showing steel substrate and PC

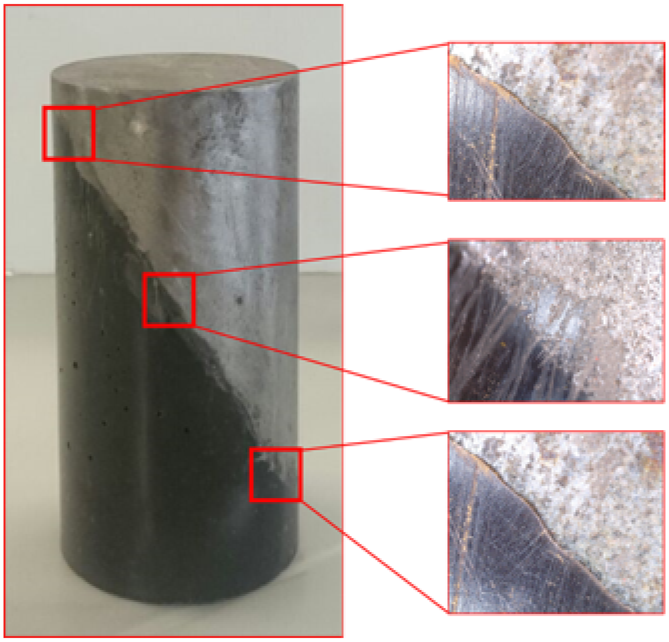

Figure 7-3. Vertical alignment using high resolution camera of PC and steel prior to slant shear testing

7.3.4. *Stress-Strain Behavior of PCN*

Uniaxial compression testing of PCNs were performed using several longitudinal and lateral strains strain gages to extract the constitutive stress-strain relationship conforming with ASTM C469/C469M (ASTM 2014). Five specimens of each PCN mixture were tested. The results of this test allowed determining the compressive strength, modulus of elasticity "*E*" and Poisson's ratio (ν) of the PCN mixes as presented in *Equation 7-1* and *Equation 7-2*, respectively.

$$E = \frac{\Delta\sigma}{\Delta\varepsilon_{VL}} \qquad \text{Equation 7-2}$$

$$\upsilon = \frac{\Delta\varepsilon_{Lat}}{\Delta\varepsilon_{VL}} \qquad \text{Equation 7-3}$$

where $\Delta\sigma$ is the change in vertical stress within linear region of the stress-strain relationship. $\Delta\varepsilon_{VL}$ is the corresponding change in vertical strain and $\Delta\varepsilon_{Lat}$ is the corresponding change in lateral strain within this specific change in stress $\Delta\sigma$.

7.3.5. Fourier Transform Infrared Analysis

To investigate the chemical effect of nanomaterials on PC and the significance of this effect on bond of PC with steel, FTIR spectroscopy analysis was conducted. FTIR analysis was conducted on 25.4 × 25.4 mm epoxy specimen with and without the nanomaterials. Only the ratio of 1% of MWCNTs, SNPs, and ANPs were used for the FTIR analyses. Further FTIR analysis of SNPs incorporating 0.5, 1.0 and 2.0 SNPs was also performed to explain the significance of incorporating SNPs on epoxy. Specimens were prepared using the same method used to prepare PC. A PerkinElmer FTIR with universal attenuated total reflectance (UATR) accessories was used for the analysis. The spectra were recorded with a horizontal ATR accessory and a DiComp crystal (composed of a diamond ATR with a zinc selenide focusing element). 4000 scans were collected at a resolution of 4 cm^{-1}. The spectra were then converted to absorbance using the Kramers-Kronig equation for FTIR analysis (Griffiths and de Hasseth 2007).

7.4. Finite Element Analysis

FE analysis of the slant shear test configuration was conducted using ABAQUS modeling software. PCN was defined as a nonlinear elastic-plastic material using the constitutive stress-strain response measured in the uniaxial compression tests. The steel was assumed to be elastic perfectly plastic material. Convergence studies used two different types of built-in elements: 8-node linear hexagonal and 6-node linear triangular. These element types are capable of producing computationally inexpensive solutions for stress calculations. For each element type, different mesh sizes were used varying from 9,480 to 74,524 elements. Boundary conditions fixed the steel part from the bottom and prevented lateral deformation of the assembly. Figure 7-4(a) shows the boundary conditions as applied on the model. Figure 7-4(c) shows the meshed model using 6-node linear triangular elements. Displacement was applied to the top of PC to simulate slant shear tests. Load-displacement curves were extracted from the simulations and compared to those observed in the slant shear tests.

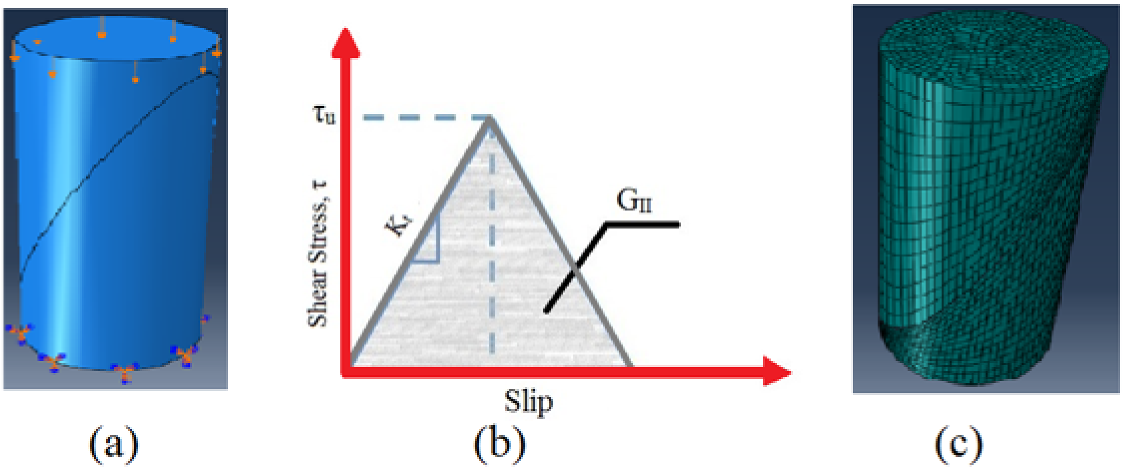

NOTE: In (b), K_t is shear contact stiffness, G_{II} is mode II fracture energy and τ_u is maximum shear stress.

Figure 7-4. FE model using ABAQUS simulation environment: (a) boundary conditions, (b) bilinear shear stress-slip relation, and (c) meshed model using 74,524 elements

In order to define contact between PC and steel, a zero-thickness cohesive contact element was defined. Bilinear shear stress-slippage relationship was used to describe the contact element as shown in Figure 7-4(b) (Meo and Thieulot 2005; Khokhar et al. 2011). This relationship is based on pure in-plane shear fracture mode (mode II) and is defined in ABAQUS using damage and cohesive behavior interaction (Dassault Systèmes 2014). The cohesive element characterizes the initial slope of the stress-slip curve (K_t) which is governed by the interfacial stiffness between the two slant shear test parts. The damage element on the other hand is prescribed using three components; initiation, evolution and stabilization. Firstly, damage initiation represents that maximum nominal stress in shear fracture mode (τ_u) characterized by the peak of the stress-slip curve. Secondly, damage evolution in this model was used based on the critical energy release rate in mode II (G_{II}) which denotes the area under the stress-slip curve. Finally, damage stabilization represents the energy dissipation module and is governed by the viscosity coefficient (V). In general, lower values of V signify rapid energy release and since failure in slant shear test is sudden, a constant low value of 0.001 was selected for all models. The values of τ_u, G_{II}, V and K_t were determined through experimental validation of the FE simulation and back-solving for those parameters Abdel Wahab 2014). This was performed using a trial and error for-loop were the values of the cohesive and damage model were estimated and the resultant load-displacement curve of the simulation was matched with the experimental. Sensitivity analysis of the shear strength, critical energy release rate and interfacial stiffness were performed for the FE model and values reported were proved to match well the experimental observations. Our objective is to use the validated FE model to realize the local shear stresses developed at failure of the slant shear test. Table 7-3 summarizes the contact interaction properties. Figure 7-5 shows load-displacement curves for both FE model and slant shear test for the selected mixes namely PC-Neat, PCNC-0.5, PCNA-0.5, PCNA-2.0, PCNS-0.5 and PCNS-2.0.

Table 7-3. Interface interaction properties as defined in ABAQUS

Contact Property / Mix	Damage			Cohesive Behavior
	Initiation	Evolution	Stabilization	Shear contact stiffness (K_t), MPa/mm
	Maximum shear stress (τ_u), MPa	Fracture energy (G_{II}), N/mm	Viscosity Coefficient (V)	
PC-Neat	43	19	0.001	56
PCNC-0.5	45	29		46
PCNA-0.5	42	17		75
PCNA-2.0	61	24		92
PCNS-0.5	53	21		90
PCNS-2.0	23	37		12

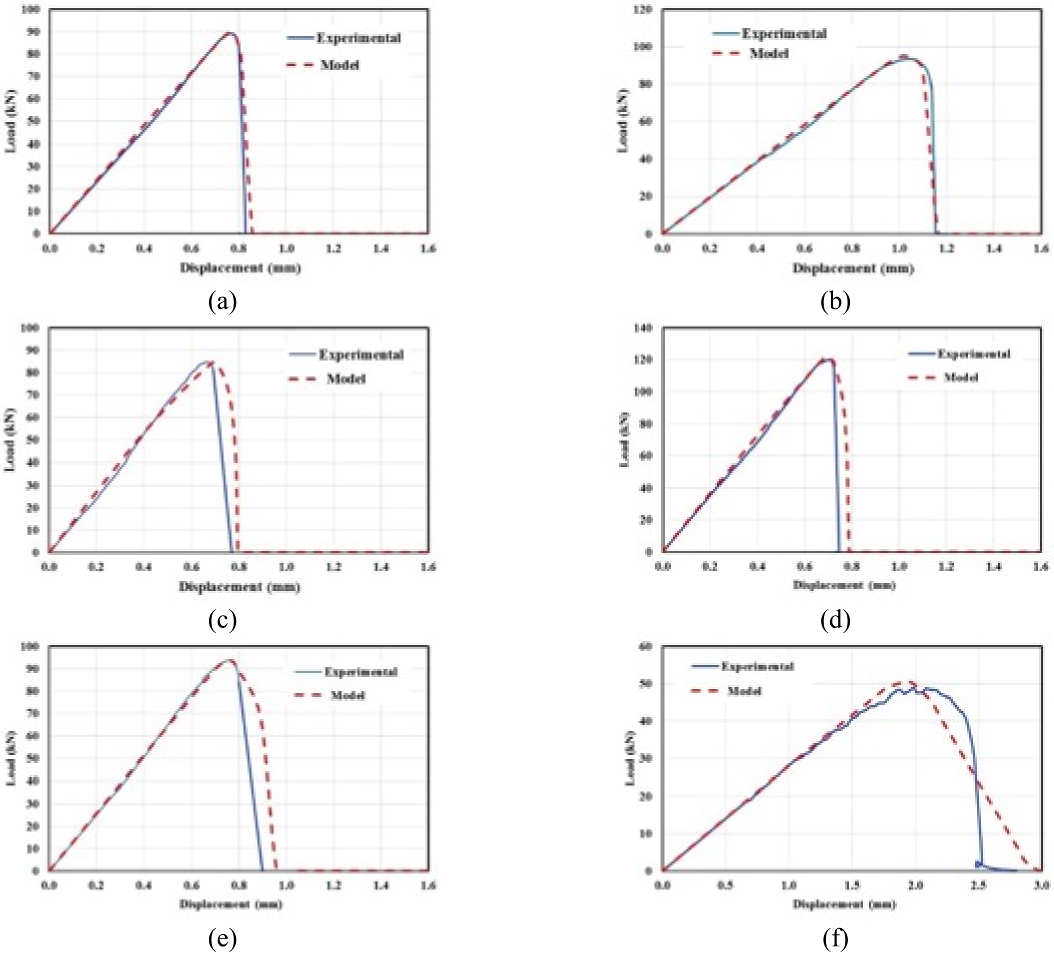

(a) (b)

(c) (d)

(e) (f)

Figure 7-5. Load-displacement curves of PC with different nanomaterials as measured experimentally during slant shear test and extracted using the FE method for (a) PC-Neat, (b) PCNC-0.5, (c) PCNA-0.5, (d) PCNA-2.0, (e) PCNS-0.5, and (f) PCNS-2.0

7.5. Results and Discussion

Apparent shear/bond strength results of slant shear tests of PCN and steel are shown in Figure 7-6. All test specimens failed at the adhesion interface and no cohesive failure was observed as shown in Figure 7-7. As explained later interpreting the results of FE analysis, the samples failed when the fracture energy criteria G_{II} was reached. Hence, sudden failure was observed in the mechanical testing of slant shear where as FE analysis explored the critical location over the shear interface where the fracture criteria was satisfied. PCNs showed a significant increase in apparent bond strength compared with neat PC. Results of mixes incorporating MWCNTs at 0.5, 1.0 and 2.0 wt.% showed a similar increase of 7% in apparent bond strength compared with neat PC. This result suggests no advantage with respect to apparent bond strength by using MWCNTs beyond 0.5 wt.%. An increase in ANPs content corresponded to increase in apparent bond strength: apparent bond strengths of 20, 23 and 51% above neat PC with 0.5, 1.0 and 2.0 wt.% of added ANPs, respectively. This result may be attributed to the possible chemical reactions of ANPs with -OH groups formed on sand blasted steel surface leading to higher bond strength (Zhai et al. 2006). PC specimens incorporating NS showed an increase of 7 and 18% for 0.5 and 1.0 wt.% NS respectively and a significant drop of 41% at 2.0 wt.% content. The decrease in the apparent bond strength at high SNPs contents is attributed to its adverse effect on flowability. Thus, increasing the number of voids onto the PC-steel interface which weakens the bond. Furthermore, since SNPS are unable to interact with either the host matrix or steel. Increasing the content of SNPs hinders the reaction between the polymer matrix and steel as it occupies large unreacted surface area over the interface.

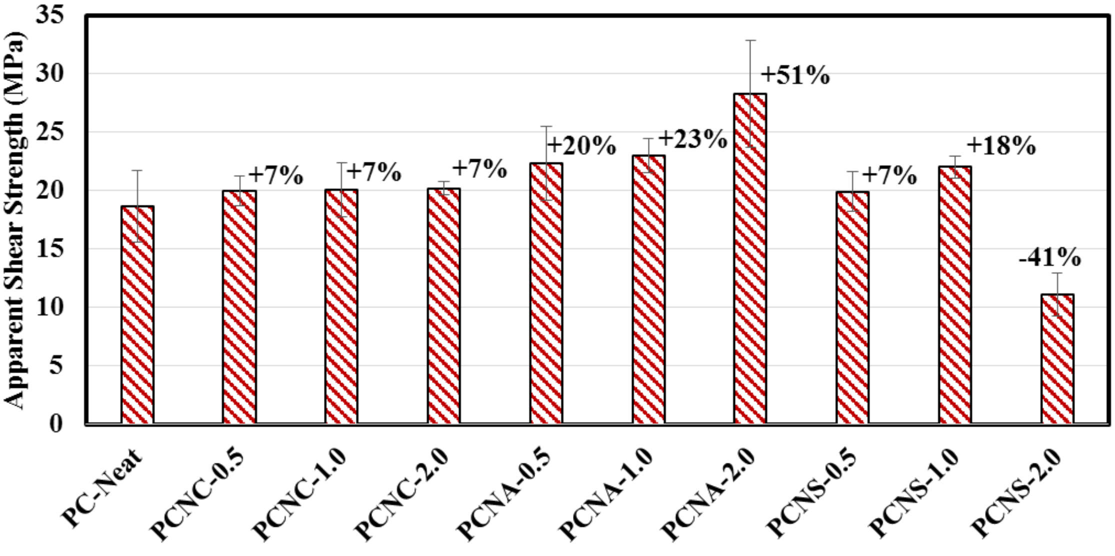

NOTE: % difference shown depicts the difference between the PC with nanomaterials and neat PC shown in first column.

Figure 7-6. Apparent shear strength determined as average stress from slant shear tests for all PCNs

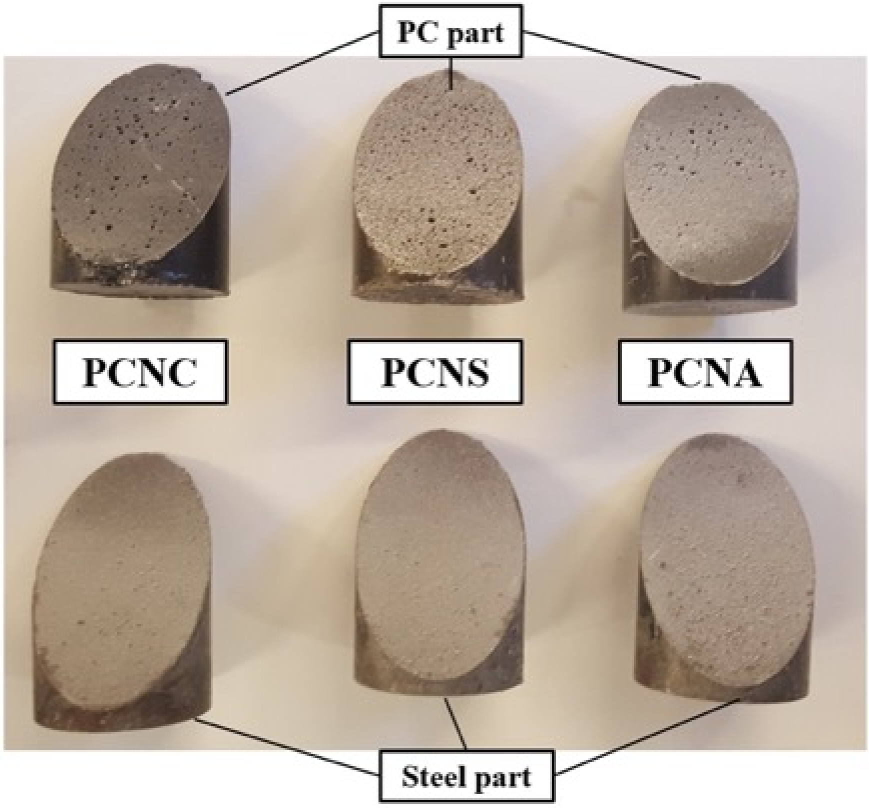

Figure 7-7. Slant shear fracture surface post-failure for PCNC, PCNS and PCNA showing complete adhesion failure

Figure 7-8 shows the stress-strain of the different PC with nanomaterials. In general, the incorporation of nanomaterials into PC resulted in a decrease in stiffness with the exception of PCNA-2.0. PC is highly ductile as proven by the large softening regions established post peak stress. Samples incorporating SNPS reached the strength peak at significantly higher strain in comparison with all other samples. This is attributed to the improvement in shear stress transfer due to the high surface area of nanomaterials and improved packing density of polymeric chains. Table 7-4 presents the calculated elastic modulus and Poisson's ratio for all PC mixes. The change in elastic modulus and Poisson's ratio is greatly affected by the chemical effect of nanoparticles on the host matrix which is further explained with the aid of FTIR observations. It is important to note that, with the proven effect of nanoparticles on the chemistry of epoxy based on the FTIR spectra, application of the rule of mixture to predict the mechanical properties of epoxy nanocomposites and thus PC is not possible. Further research is warranted to suggest alternative methods to classical rule of mixture that can account for the chemical effect of the nanoscale inclusions on the mechanical properties of the matrix.

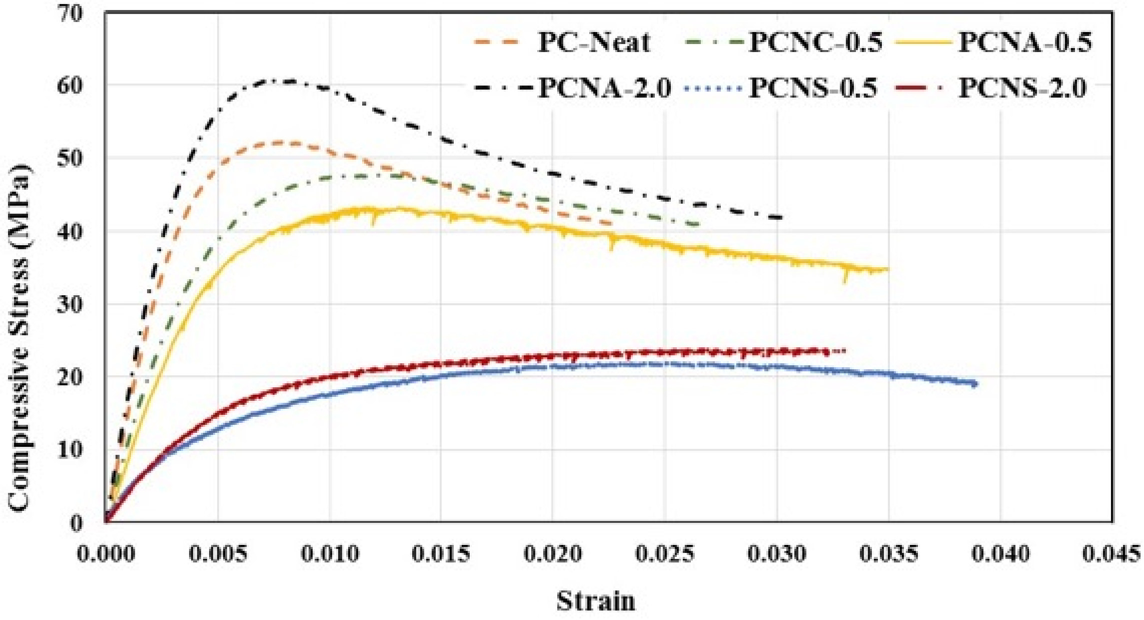

Figure 7-8. Stress-strain relation for different PC incorporating different nanomaterials: PC-Neat, PCNC-0.5, PCNA-0.5, PCNA-2.0, PCNS-0.5, and PCNS-2.0

Table 7-4. Elastic modulus and Poisson's ratio for the different PC incorporating nanomaterials

	PC-Neat	**PCNC-0.5**	**PCNA-0.5**	**PCNA-2.0**	**PCNS-0.5**	**PCNS-2.0**
Elastic modulus (GPa)	14.29 ±2.19	10.30 ±0.44	8.74 ±0.23	15.09 ±1.00	6.23 ±0.25	3.76 ±0.12
Poisson's ratio	0.22 ±0.10	0.36 ±0.02	0.37 ±0.02	0.37 ±0.07	0.36 ±0.01	0.35 ±0.05

NOTE: Values presented are mean ± standard deviation.

All PCs had an increased Poisson's ratio compared with neat PC. FE results showed significantly higher values of maximum local shear stresses compared with the apparent shear strength. Figure 7-9 compares the apparent shear strength and the maximum local shear stresses. An increase in the maximum local shear stress of 88%, 107%, 115%, 125%, 130%, and 166% can be observed for PCNA-0.5, PCNS-2.0, PCNA-2.0, PCNC-0.5, PC-Neat, and PCNS-0.5 respectively. The difference between the apparent/average shear strength and the maximum local shear stress can be attributed to the difference in elastic modulus of PC with and without nanomaterials and steel. Further research is warranted to separate the effect of difference in elastic modulus of PC and steel substrate from the changes in shear strength. Nevertheless, the trend of increasing the shear/bond strength by incorporating nanomaterials can still be observed. There is no obvious relationship between the difference in stiffness between PC incorporating nanomaterials and the difference between apparent shear strength and maximum local shear stress at the interface. This might be attributed to the fact that the apparent shear strength is dependent on the mechanics of the test and the adhesion between PC and steel, which is affected by potential chemical reaction between the nanomaterials and epoxy in PC. Separation of these two effects seems difficult. FTIR analysis described below sheds light on potential chemical reaction of nanoparticles with epoxy and its potential effect of epoxy and PC moduli.

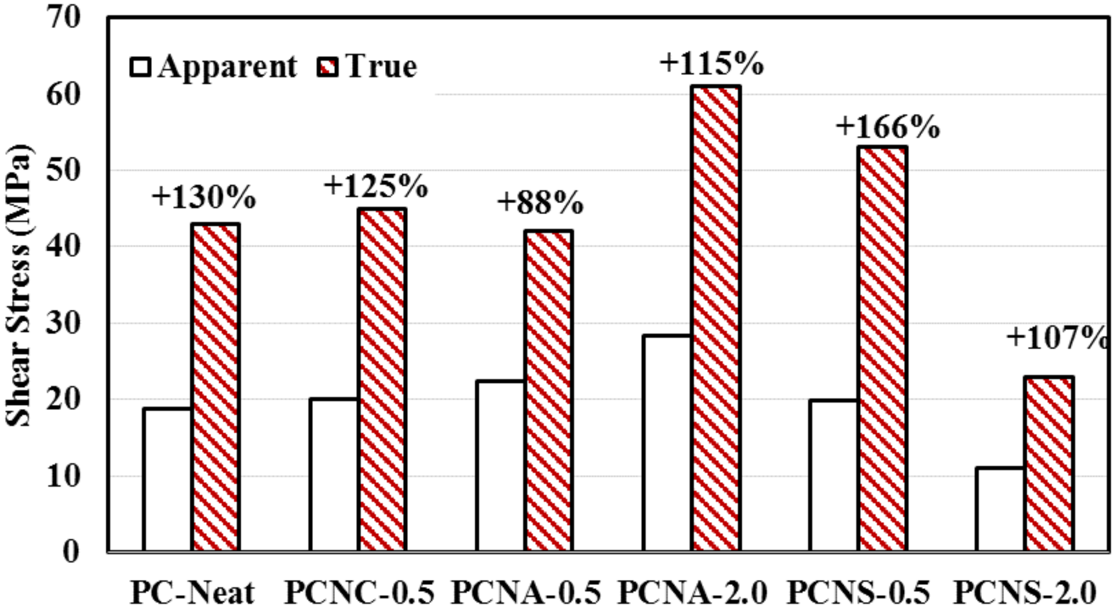

NOTE: The % difference shown is the difference between the two values for different PC mix. The average stress is based on the slant shear standard.

Figure 7-9. Shear strength for different PC incorporating nanomaterials interpreted using apparent shear strength and maximum local shear stress using the FE model

Further analysis of the FE simulation results shows strong correlation between Poisson's ratio and the shear modulus G described as $G = \frac{E}{2(1+\nu)}$ and the maximum local shear stresses at the interface. Since all nanomaterials caused an increase in Poisson's ratio, the maximum local shear stress is decreased by the increase in Poisson's ratio. This analysis supports the results for PCNC-0.5 and PCNA-0.5 in comparison with neat PC. Furthermore, another important factor controlling the maximum local shear stresses is the shear contact stiffness K_t. The shear contact stiffness controls the slippage occurring at the interface (see Figure 7-4) and may correspond to the friction between the contact surfaces. The effect of the shear contact stiffness on local shear stresses is apparent in the case of SNPs. FTIR analysis, discussed below, confirms that SNPs affected epoxy curing but acted as an inert filler. This might explain its ability to increase interface friction compared with MWCNTs or ANPs, which apparently have the ability to chemically react with the epoxy matrix and/or the steel surface.

Finally, FE analysis results were also used to examine the interfacial shear stress contours at the PC-steel interface. Figure 7-9 shows the load-displacement of neat PC extracted from the FE model with magnified slippage in the assembly at vertical displacements of 0.720 mm, 0.802 mm, and 0.837

mm. At each of these points, shear contours on the interface were plotted showing the maximum local shear stress to reach 40 MPa. Locations of maximum local shear stress concentration on the interface are shown in Figure 7-10. Maximum local shear stress only develops at the location of minimum height of PC before reaching ultimate load as shown in Figure 7-10 and Figure 7-11(a). As slippage occurs, the maximum local shear stress moves along the interface. The maximum local shear stress path follows the height of PC from minimum to maximum as shown in transition in Figure 7-11 from (a), (b) and (c). Slant shear tests show that complete slippage occurs after the ultimate load due to release of energy as a result of bond failure.

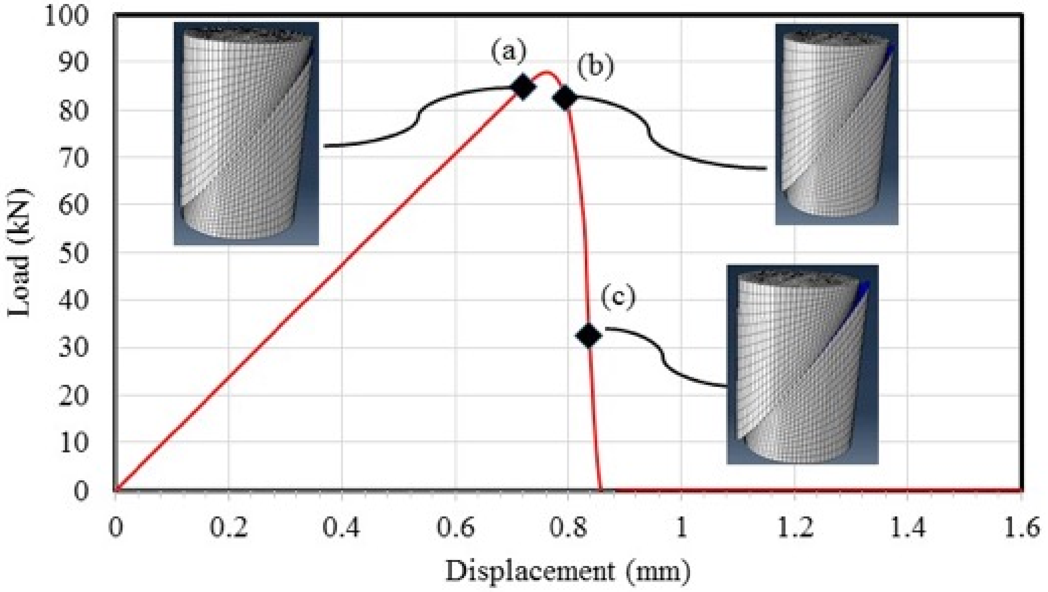

Figure 7-10. Load-displacement extract from FE analysis of neat PC showing magnified slippage at 0.720 mm, 0.802 mm, and 0.837 mm

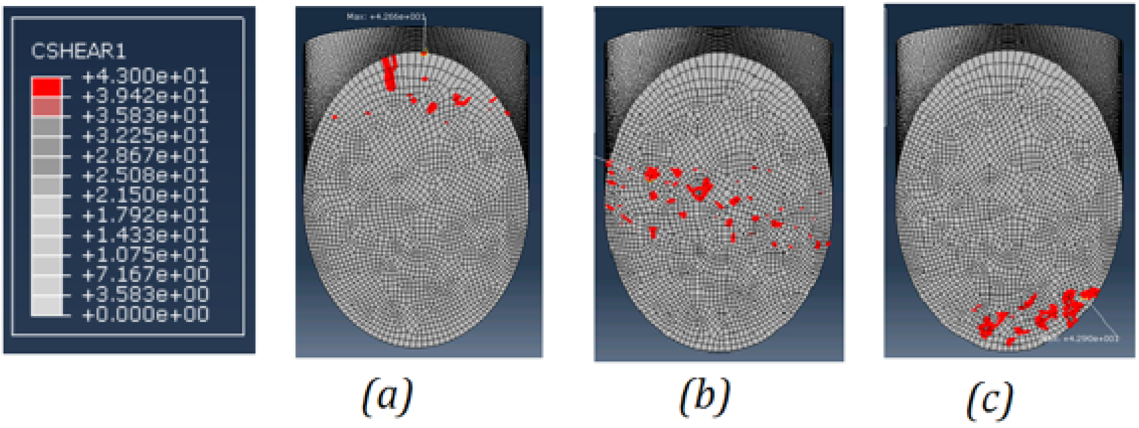

(a) (b) (c)

Figure 7-11. Shear contours showing locations of maximum local shear stress during slippage at vertical slip of (a) 0.720 mm (b) 0.802 mm and (c) 0.837 mm

Nonetheless, incorporating nanoparticles in PC resulted in increasing the bond strength of PC to steel substrates. This improvement in bond strength when measured in terms of maximum local shear stresses is less significant than that measured using the apparent shear strength. FE analysis showed that the increase of bond strength in terms of maximum local shear stress is 5, 23 and 42% for PCNC-0.5, PCNS-0.5, and PCNA-2.0 respectively and a decrease of 2 and 47% for PCNA-0.5 PCNS-2.0 when compared with neat PC. These values are lower than those improvements depicted by the apparent/average shear strength shown in Figure 7-6. The analysis demonstrates that the simplistic approach of averaging the shear stress is insufficient to compare materials with significant different mechanical properties (e.g. elastic modulus and Poisson's ratio). It is obvious that using slant shear test results to compare bond strength of materials with significantly different mechanical properties should be done with care and its results might better be interpreted using the FE method.

FTIR spectrographs for neat epoxy and epoxy incorporating 1% MWCNTs, SNPs, and ANPs are shown in Figure 7-12. FTIR spectra of MWCNTs/epoxy and SNPs/epoxy, show the traditional band of epoxy where absorption bands corresponding to O-H groups appeared at (~3200–3600 cm^{-1}), C-H band (2850–2930 cm^{-1}), N-H band of primary amines (1590– 1615 cm^{-1}), C-N (1030–1115 cm^{-1}), ether (~1230 cm^{-1}) and epoxide ring (~830 cm^{-1}), are all apparent and have similar relative ratios to the neat epoxy. However, the spectra of ANPs/epoxy look very different showing relatively higher ratios of epoxy ring, O-H band and primary N-H band intensities than the neat spectra. This may be attributed to the effect of nanoparticles on the curing behavior of the epoxy matrix. The curing reaction of the epoxy resin proceeds through the amines presented in the polyamide curing agent. The general illustrations of the chemical structures of the epoxy resin (Novolac epoxy-HCR Polyamine) and the possible reactions among its curing process follow Golru et al. (2014). Based on the curing mechanism and the results obtained from FTIR analysis, it can be concluded that the curing reaction was affected by the presence of ANPs. This can be understood from the greater peaks intensities of the epoxy ring (~830 cm^{-1}) and O-H groups (~3350 cm^{-1}) for the epoxy-ANPs nanocomposite compared with the neat sample. This is attributed to the effect of ANPs on epoxy curing reaction producing cured epoxy matrix having un-reacted functional groups; the source of effective bonding with steel surface.

The difference in the epoxy-ANPs nanocomposite can be explained by the fact that ANPs are known as an amphoteric substance meaning it can react with both acids and bases which allows it to act as an acid with a base and a base with an acid. ANPs, thus, reduce the epoxy curing reaction and consequently leave a relatively large amount of the epoxy resin groups (such as the epoxide ring, N-H band of primary amines, O-H groups) unreacted and available. This is represented by the significant increase in the epoxide ring, O-H and primary N-H band intensity in the FTIR spectra. This role of ANPs results in increasing the epoxy's chance to react with the sand blasted steel surface and thus improve the adhesion strength between PC and steel. The ability of ANPs to reduce epoxy curing was reported in the literature by Golru et al. (2014) and Kadar et al. (2008). The increase in ANPs content would be expected to further increase the amount of unreacted epoxy groups and consequently the adhesion strength. This explains the significant increase in bond strength (+51%) observed with 2.0% ANPs compared with neat epoxy. It might be important to note that in addition to the chemical effect, ANPs also worked as solid nanofiller and thus enabled increase of epoxy/PC stiffness at high content of 2.0% compared with neat PC. The final improved bond strength is apparently due to the combined effects of ANPs on the adhesion strength and the stiffness difference between PC and steel.

The above FTIR spectra also show that MWCNTs with its COOH functionalization resulted in esterification reaction with epoxy and produced the ester and amide peaks appearing at 1740 cm^{-1}

and 1665 cm^{-1}, respectively. However, the low content of COOH functionalizing in MWNCTs makes this reaction ineffective due to the fact that curing of Novolac epoxy results in similar chemical groups. This similarity is shown in the inset in Figure 7-12. This explains why the MWCNTs were not able to make significant improvement in adhesion strength between epoxy and steel. Finally, SNPs seem able to broaden the OH-band at 3200-3600 cm^{-1}. To further investigate the effect of SNPs on epoxy curing, FTIR spectra of epoxy incorporating 0.5, 1.0 and 2.0% of SNPs, shown in Figure 7-13, were further investigated.

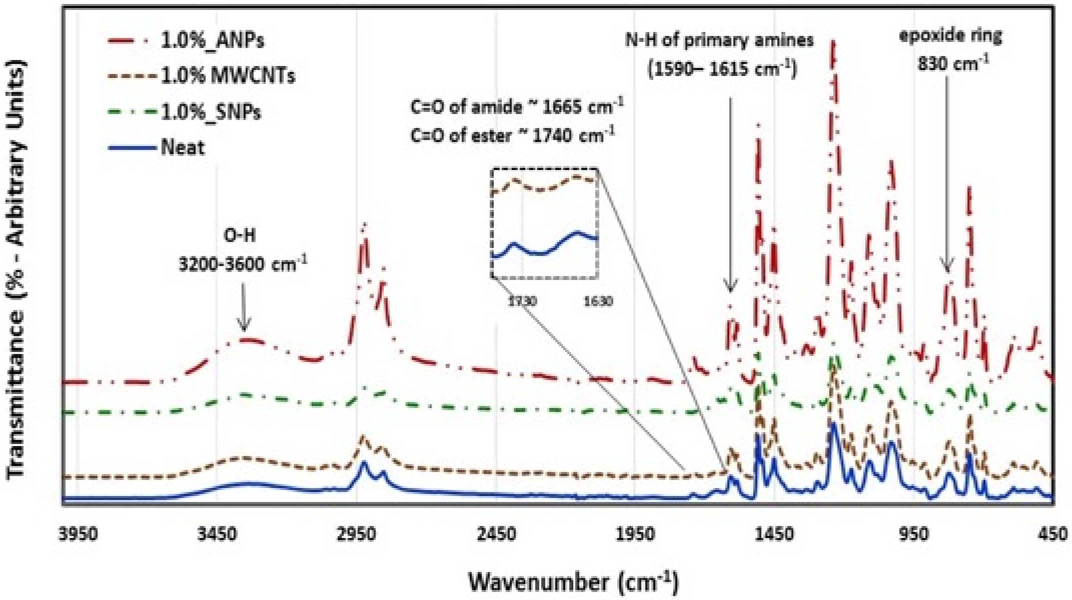

NOTE: Figure shows the main epoxy groups and the significant changes appearing in the spectra using ANPs compared to the other two nanomaterials. The spectra also show a potential broadening of the OH band at 3200-3600 cm^{-1} due to SNPs. The spectra show the significant increase in the epoxy peaks with respect to base spectra in the case of ANPs compared to neat epoxy.

Figure 7-12. FTIR spectra of neat epoxy and epoxy incorporating 1.0% ANPs, MWCNTs and SNPs

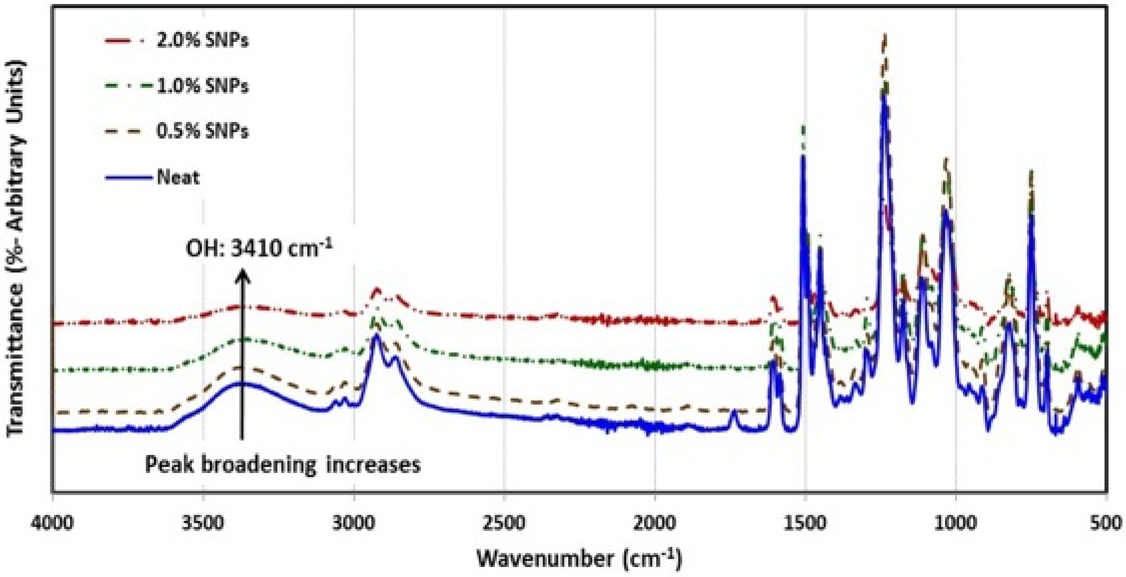

Figure 7-13. FTIR spectra of neat epoxy and epoxy incorporating 0.5, 1.0 and 2.0% SNPs showing the significant band broadening of OH group at 3410 cm^{-1} due to incorporating SNPs

It could be observed in Figure 7-13 that the hydroxyl absorption peak at 3410 cm^{-1} gets further broadening as SNPs content increased. This can be attributed to the effect of SNPs on the curing process of epoxy through phase separation and re-arranging of the hydroxyl groups (Bakhshandeha et al. 2014). The broad band region at about 3200–3600 cm^{-1} reflects the hydroxyl stretching vibration with multimodes of inter- and intramolecular hydrogen bonds and represents combined effects of hydrogen bond in hydroxyl, hydroxyl/carbonyl groups and in water molecules (Mikhaylova et al. 2006; Paterson et al. 2015). The FTIR spectra shows that incorporating SNPs in the epoxy matrix reduced its network formation process via lowering the crosslinking bonds and consequently changed the ratios of hydrogen bond modes which led to different geometry with different force constants and consequently broadening the absorption peak.

It is interesting to note that the effect of SNPs on adhesion was opposite to that of ANPs in spite of the fact that both nanomaterials affected epoxy curing. While both ANPs and SNPs resulted in steric hindrance effect that decreased the reactivity between the epoxy functional groups and the hardener, SNPs did not result in improving adhesion. This can be explained by the fact that the amphoteric and polar nature of ANPs enabled the remaining epoxy and OH groups to bond to steel surface. On the contrary, SNPs caused a shielding barrier in the cured epoxy matrix due to their unreactive nature that prevented utilization of the active epoxy sites and thus did not improve the bond strength of PC and steel. The unreactive nature of fumed silica and SNPs and their need to surface functionalization when used with polymers has been reported in the literature (Massingill et al. 1990; Matehka et al. 1999; Ghanbari and Attar 2015). The above study sheds light on the significance of nanoparticles on changing epoxy curing and the result such changes can make in altering bond of PC made with these epoxy-nanocomposites with steel.

7.6. Conclusions

This paper examines the bond strength of PC incorporating nanomaterials to steel substrates. The slant shear tests revealed that incorporating nanoparticles can improve the apparent bond strength between PCs and steel by up to 51% compared with neat PC. The best improvement in bond strength was achieved by 2.0% wt of ANPs, which was the maximum amount used in this study. MWCNTs showed very limited to no increase in the bond strength with no improvement beyond 0.5 wt.%. SNPs showed a general decrease in bond strength compared to neat PC. The ability of ANPs to improve bond strength of epoxy PC and steel might be attributed to potential chemical reaction of alumina and −OH groups formed on the sand blasted steel surface. The adverse effect of SNPs might be attributed to its inability to chemically react with Novolac epoxy making it to act as an inert filler only increasing friction at the steel interface.

Examining the constitutive stress-strain relation of PC incorporating nanomaterials showed a general decrease in stiffness and increase in Poisson's ratio. The drop in elastic modulus of PC incorporating nanomaterials compared with neat PC, the change in Poisson's ratio along with difference in contact shear stiffness result in a significant difference between the maximum local shear stress occurring at the interface and the apparent/average shear strength. This difference ranged from 88 to 166%. Considering the maximum local shear stresses developed at the interface, the significance of nanomaterials on the bond strength of PC to steel seems lower than that from the apparent bond strength determined from the slant shear test standard. Local shear stresses calculated from the FE method confirmed that maximum local shear stress occurs at the area of minimum PC height and moves towards increasing PC height during the slant shear test. This analysis confirmed that there is a strong correlation between changes in Poisson's ratio and difference between apparent shear strength and the maximum local shear stress. It is concluded that special care should be considered when interpreting slant shear test results to compare bond strength of materials with significantly different mechanical properties. Finally, FTIR analysis showed that ANPs resulted in significant reduction of epoxy curing and thus enabled further epoxy groups to react with the steel surface improving the adhesion strength between PC and steel. FTIR spectra also showed SNPs to alter epoxy curing. However, the unreactive nature of SNPs resulted in shielding barrier and prevented improving bond strength of PC incorporating SNPs with steel. FTIR observations might explain why ANPs were capable to significantly improve the bond strength of PC with steel compared with all other nanoparticles.

7.7. Acknowledgements

This material is based upon work supported by the U.S. Department of Energy (DOE) National Energy Technology Laboratory (NETL) under Grant Number DEFE0009562. This project is managed and administered by the DOE/NETL Storage Division and funded by DOE/NETL and cost-sharing partners. This paper was prepared as an account of work sponsored by an agency of the United States Government. Neither the United States Government nor any agency thereof, nor any of their employees, makes any warranty, express or implied, or assumes any legal liability or responsibility for the accuracy, completeness, or usefulness of any information, apparatus, product, or process disclosed, or represents that its use would not infringe privately owned rights. Reference herein to any specific commercial product, process, or service by trade name, trademark, manufacturer, or otherwise does not necessarily constitute or imply its endorsement, recommendation, or favoring by the United States Government or any agency thereof. The views and opinions of authors expressed herein do not necessarily state or reflect those of the United States Government or any agency thereof. The authors would like to extend their thanks to Epoxy Chemicals Inc. and Transpo Industries Inc. for donating epoxy materials to the project. The authors also extend their thanks to PhD candidate Amina Mannan (University of New Mexico) for her continuous help in conducting and analysis of FTIR.

8. NANOMODIFIED METHYL METHACRYLATE POLYMER FOR SEALING OF MICROSCALE DEFECTS IN WELLBORE SYSTEMS

8.1. Overview

Microscale defects at the steel-cement matrix and rock-cement matrix interfaces (microannuli) are the major reasons to lose the integrity of wellbore systems. Microscale defects/microcracks as small as 30 μm are sufficient to create a significant leakage pathway for fluids. In this paper, the authors propose the use of nanomodified methyl methacrylate (NM-MMA) polymer as a seal material for 30-μm microcracks. Four materials were evaluated for their ability to serve as an effective seal material to seal 30-μm microcracks: microfine cement, epoxy, methyl methacrylate (MMA), and NM-MMA incorporating 0.5% by weight aluminum nanoparticles (ANPs). The seal materials' bond strength with shale were investigated using push-out tests. In addition, the ability to flow fluid through the microcracks was investigated using sagittal microscopic images. Viscosity, surface tension, and contact angle measurements explain the superior ability of MMA seal materials to flow into very thin microcracks, as compared with other materials. Post-test analysis shows MMA seal materials were able to completely fill the microcracks. In addition, incorporating ANPs in MMA resulted in significant improvement in seal material ductility. Dynamic mechanical analysis (DMA) showed that incorporating ANPs in MMA reduced the creep compliance and improved creep recovery of NM-MMA. X-ray diffraction (XRD) analysis shows that incorporating ANPs in MMA resin increases the degree of polymer crystallization resulting in significant improvement in seal material ductility.

8.2. Introduction

Wellbore seal integrity of both production and abandoned oil and gas wells is critical in order to eliminate the possibility of significant leakage along the wellbore system. Recent major incidents that have resulted from the loss of wellbore integrity include the Deepwater Horizon event that released about 6500 million liters of liquid oil in the Gulf of Mexico (Reddy et al. 2012) and the Aliso Canyon event that released about 100,000 metric tons of methane into the atmosphere near Los Angeles, California (Michanowicz et al. 2017). Such incidents result in serious health and environmental hazards in addition to the significant economic burden of containing and remediating the releases. In addition to major seal failures, much smaller seal failures are also of concern to stakeholders as they can result in appreciable leakage. The wellbore seal integrity can be compromised from flaws (fractures, voids) that allow for fluid migration along the axis of the wellbore. A range of factors during the initial well cementing and subsequent well operations can cause wellbore flaws, including incomplete drilling mud removal prior to cementing, cement matrix shrinkage, and changes in pressure and temperature within the casing during operation (Zhang and Bachu 2011). In particular, discrete, fracture-like flaws (micro-scale defects/microcrack) that develop at the steel-cement matrix and rock-cement matrix interfaces, often referred to as microannuli, can serve as a leakage pathway in the wellbore system (Celia et al. 2005; Carey et al. 2007). There have been numerous studies of the behavior and characterization of the steel-cement matrix interface (Nakayama and Beaudoin 1987; Baldan 2004; Zhai et al. 2006; Lacuve 2015; Gomez et al. 2017; Shi and Ming 2017; Stormont et al. 2018). However, much less effort was directed to understand the rock-cement matrix interface or to develop efficient seal materials for microcracks at the cement-rock interface.

Seal of flaws within the wellbore system is usually attempted by forcing the seal material into flaws through perforations in the steel casing or by injection at the bottom of the steel casing shoe. Figure 8-1 shows an example of a wellbore sealing process through perforation in the steel casing.

Wellbore sealing process through metal casing perforation is conducted in three steps; first, the bottom of the well is filled with high density brine up to 2 m below the injection level, second, the metal casing is filled with seal material at the cracking zone, and third, pressure is applied to allow the seal material to flow through the metal casing perforation and fill the microannulus behind the metal casing. Microfine cement paste with water-to-cement (w/c) ratio of 0.7 to 2.0 is the most common seal material used to restore wellbore seal integrity principally due to its much greater flowability compared with regular Type G oil well cement (OWC) (Harris et al. 1992). However, previous research showed that microfine cement was unable to completely fill 800 µm defects, while epoxy polymers (specifically Novolac epoxies) were able to fill defects in the range of 800 µm (Genedy et al. 2017-A). Epoxy polymers have other advantages over cementitious materials as a microcrack seal material, notably superior bond strength with metallic surfaces (Baldan 2004; Genedy et al. 2014). In addition, polymer materials can be engineered by incorporating nanoparticles to alter their mechanical properties and durability (Wetzel et al. 2006; Pocius 2012; Shokrieh et al. 2012; Salemi and Behfarnia 2013). Prior investigations showed that Novolac epoxy incorporating ANPs significantly improved the bond strength at the rock-cement matrix interface compared with microfine cement and neat Novolac epoxy, and it was still able to completely fill 800 µm microcracks (Genedy et al. 2017-A).

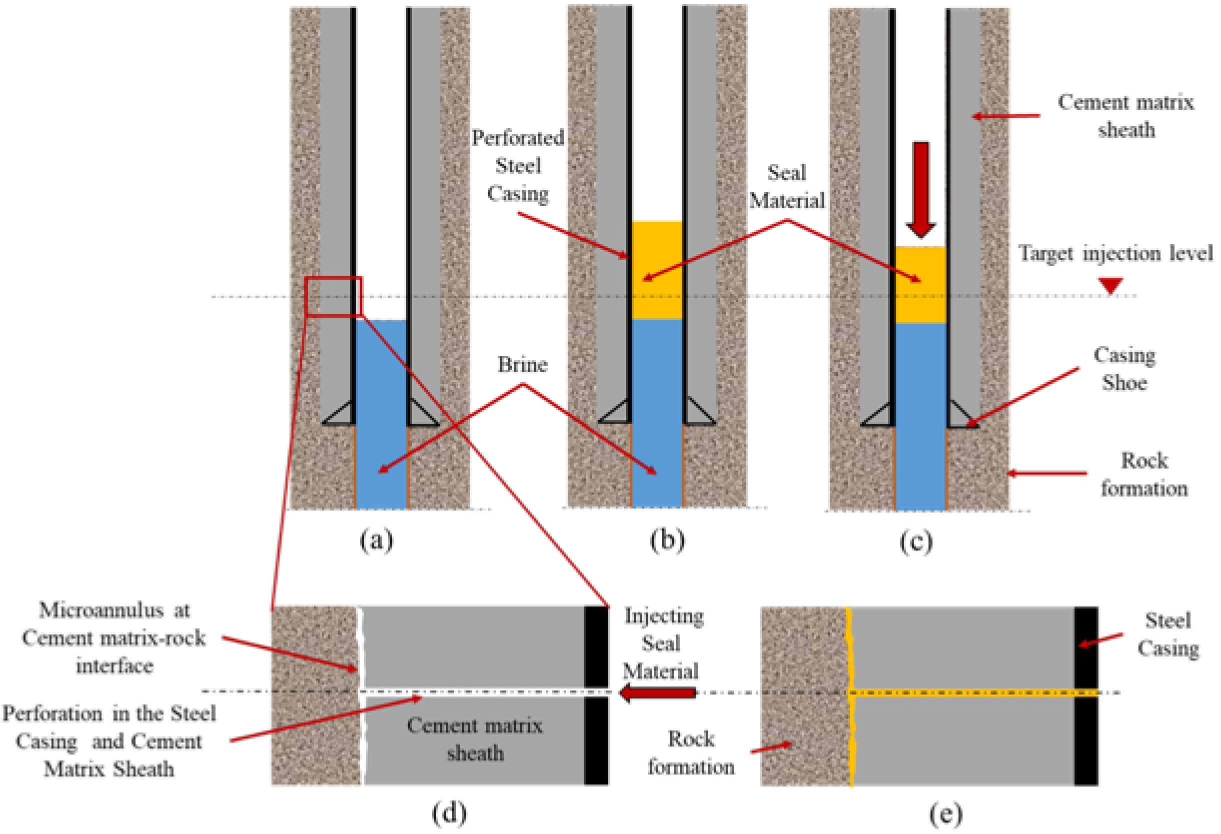

NOTE: Steps are (a) fill bottom hole with high density brine up to 2–3 m below the injection level, (b) fill 5–10 m of casing with seal material, (c) apply pressure to push seal material into the microannulus, (d) microannulus at cement matrix-rock interface before injecting seal material, and (e) sealed microannulus at cement matrix-rock interface.

Figure 8-1. Injection process of seal material

There is a substantial need to seal microcracks smaller than 100 μm. Continuous fracture-like flaws greatly increase the effective permeability of the wellbore system. For example, a 50 μm microcrack at the cement matrix-casing interface in a wellbore with a diameter of 0.23 m and a casing diameter of 0.18 m will increase the effective permeability of a cement matrix by more than 4 orders of magnitude over its intact permeability (Stormont et al. 2018). Seidel and Greene (1985) indicated that a microcrack of 25 μm is large enough to be problematic for gas flow along a well. Checkai et al. (2013) interpreted the size of flaws in cemented wellbore systems from gas leakage and pressure buildup records for 238 wells at 6 different locations. 85% of the flaw sizes, interpreted as continuous smooth-walled fractures, were between 5 and 100 μm.

In this study, the authors examine microcracks as small as 30 μm, which are sufficient to create a leakage pathway for gas within a faulty wellbore system. A seal material is sought with significantly low viscosity, surface tension, and contact angle to be able to penetrate such small microcracks in addition to high bond strength and to prevent debonding and secure seal integrity. Moreover, a ductile seal material would have higher sealing efficiency than a brittle seal material even if the latter has higher strength (Thiercelin et al. 1998). This is because seal materials are exposed to numerous thermal stress cycles during wellbore operation. Ductility is therefore a key material characteristic for seal materials. Previous research showed that Novolac epoxy was able to completely fill 800 μm microcracks (Genedy et al. 2017-A). The authors believe that epoxy surface tension is considerably high enough to allow for complete filling of microcracks as small as 30 μm in width. The authors hypothesize that MMA can be designed as a seal material to seal 30 μm microcracks. MMA is selected due to its significantly very low surface tension and viscosity compared to all other polymers. Moreover, the mechanical and electrical properties of MMA can be engineered by incorporating nanoparticles (Jia et al. 1999; Haggenmueller et al. 2000; Zeng et al. 2004; McClory et al. 2010).

In this paper, the authors investigate the efficiency of MMA incorporating ANPs as a seal material for 30 μm microcracks at the rock-cement matrix interface. The bond strength and the ability to completely fill 30 ± 5 μm microcracks for MMA and NM-MMA incorporating ANPs was measured and compared with microfine cement and Novolac epoxy. Microstructural analysis utilizing XRD and DMA was used to investigate the effect of incorporating ANPs on the properties of MMA resin.

8.3. Experimental Methods

This study required creating specimens of rock-cement matrix interfaces with a 30 μm gap and evaluating the ability of candidate seal materials to penetrate and seal the interface. The bond strength of the sealed interface was measured with push-out tests. Microscopic observations of the sealed interfaces were made. In addition, the surface tension and viscosity were measured for all candidate seal materials. XRD measurements were made to characterize the nanocomposite.

8.3.1. Materials

The rock used in this investigation was Mancos Shale, sourced from TerraTek. Type G (American Petroleum Institute [API] Class G) OWC provided by Grupo Cementos de Chihuahua (GCC) USA and was the reference cement material. Four seal materials were used: microfine cement, Novalac epoxy, MMA, and MMA with ANPs. The microfine cement had a composition comparable to high sulfate-resistant cements and grain size (d_{95}) of 9.5 μm. The microfine cement mix had a w/c ratio of 0.7% and 2.0% of the dry cement weight super plasticizer (as recommended by the manufacturer). Novolac epoxy system is a low viscosity cycloaliphatic polyamine blend with low viscosity hardener. MMA is a low viscosity polymer provided by Transpo Industry, Inc. Benzoyl peroxide powder was used as hardener for the MMA resin. ANPs were used to modify the MMA matrix. ANPs are aluminum oxide (Al_2O_3) with maximum particle size of 50 nm and were obtained from Sigma Aldrich, Inc.

8.3.2. Preparation of Seal Material

Microfine cement seal material was prepared by mixing cement with water for two minutes using a stand mixer. The maximum w/c ratio of 2.0, recommended by the manufacturer, was used to insure maximum flowability can be achieved. Novolac epoxy seal material was prepared by mixing resin and hardener with a resin to hardener ratio of 2:1 as instructed by the manufacturer. The mixture was stirred for at least 1 minute using a stand mixer to achieve uniform mixture. MMA and NM-MMA seal materials were prepared by mixing the resin with 2% hardener by weight using a stand mixer for at least 1 minute until hardener powder is completely dissolved in the resin. To prepare NM-MMA polymer nanocomposite, 0.5% by weight ANPs were added to the MMA resin and manually stirred for 1 min. Afterwards, the mix was sonicated for 1 hour at 40ºC using an ultrasonic homogenizer. The mix was then stirred for 2 additional hours at 80ºC using magnetic stirring at 800 rpm. The polymer resin nanocomposite was left to cool and reach room temperature and then mixed with the required amount of hardener powder for 1 minute until the hardener powder completely dissolved in the resin. The above procedure was used following prior work (Genedy et al. 2015).

8.3.3. Physical Properties of Seal Materials

Viscosity, surface tension, and contact angle with cement matrix surface were measured for all seal materials used in this investigation. Viscosity tests were conducted using a rotational Viscometer following AASHTO T316 (2013). The viscosity was measured for all materials at room temperature (22ºC). SC4-21 needle spindles, rotating at 20 rpm, were used for viscosity measurements. The spindles were allowed to rotate for 1 minute, after which three readings were collected at 15-second intervals.

The surface tension of the seal materials was measured using KRUSS force tensiometer K100 standard plate surface tension test. The test was conducted by submerging a standard platinum plate in the investigated liquid to achieve a wetted depth of 6 mm. The plate was then pulled-out of the liquid with a speed of 10 mm/min. The force required to pull-out the plate was measured and the surface tension of the liquid was calculated using Wilhelmy plate method. Contact angle of seal material with Type G cement matrix surface was measured by allowing a drop of seal material to fall on a hardened cement matrix surface from 1 cm height. A high resolution camera was used to take a photo of the seal material drop before it was absorbed by the cement matrix (Courard 1999). DinoCapture 2.0 angle measurement tool was then used to measure the contact angle of each seal material.

8.3.4. Bond Strength of Seal Material

To measure the bond strength of seal materials, push-out test specimens to simulate sealed cement matrix-rock formations interface shown in Figure 8-1(e) were prepared as shown in Figure 8-2(b). Steel pipes were used to provide confinement to simulate the confinement provided by the infinite rock formation surrounding wellbores. To prepare the push-out specimens, Type G cement matrix hollow cylindrical specimens with height of 50.8 mm, outer diameter of 101.4 mm, and inner diameters of 25.46 ± 0.01 mm. The cement matrix specimens were cast inside steel pipes with thickness of 3.2 mm. The specimens were then cured at controlled environment with 100% humidity and ambient temperature for 28 days. The diameter of the center hole in the hollow cement matrix cylinder was measured after curing using a micrometer and confirmed to meet the desired diameter. After curing, a 25.4 mm shale core was placed in the center of the hole to create a gap between the shale and cement matrix of 30 ± 5 µm. Seal material was then supplied along the top shale-cement matrix contact and allowed to flow by gravity into the microcrack. The seal material was added into the microcrack until the seal material no longer flowed into the microcrack.

Three specimens sealed with each seal material were tested at age 7 days after sealing. Specimens sealed with microfine cement were cured in 100% humidity while specimens sealed with Novolac Epoxy, MMA, or NM-MMA were air cured at room temperature. The push-out test setup and schematic are shown in Figure 8-2. The push-out test was conducted under two-stage displacement control protocol. The test started with a rate of 0. 1 mm/min for the first 5 mm, after which the loading rate was increased to 1.0 mm/min. Test load and displacement were recorded using sampling rate of 1 Hz. The initial lower displacement rate allowed bond failure to take place at low strain rate. The greater displacement rate post-peak reduced the total test time to about 1 hour. The bond strength was calculated using Equation 8-1.

$$\tau = \frac{P}{\pi D L} \qquad \textit{Equation 8-1}$$

where τ is the interfacial bond strength, P is the peak load, D is the diameter of the shale core of 25.4 mm, and L is the embedment length of 25.4 mm (Figure 8-2).

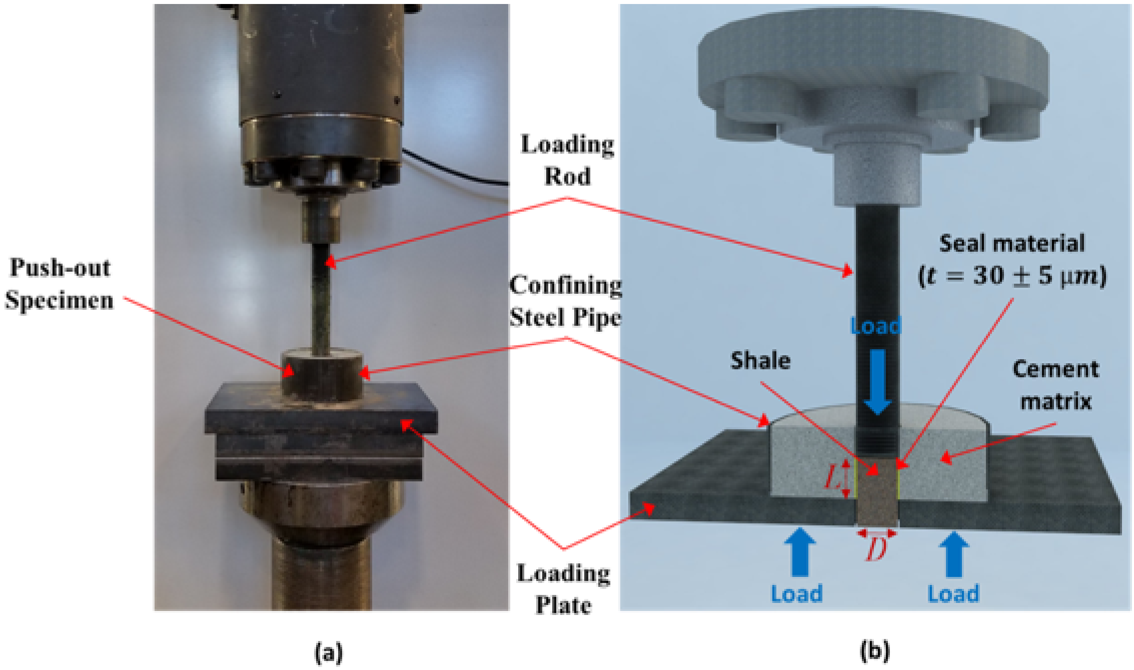

Figure 8-2. (a) Push-out test setup and (b) push-out test schematic

8.3.5. Microscopic Investigation

Sagittal/longitudinal sections of the rock-seal-cement matrix were obtained by vertically sectioning untested specimens. Light microscopes with two different levels of magnification (200× and 500×) were used to observe the shale-cement matrix interface with the different seal materials.

8.3.6. Dynamical Mechanical Analysis

The effect of incorporating ANPs in MMA on the viscoelastic behavior of MMA polymer nanocomposites was investigated using DMA Q800. MMA and NM-MMA specimens were subjected to constant tension stress of 3.5 MPa for 20 minutes. Afterward, the strain was allowed to recover for 40 minutes. The change of strain with time was recorded and the creep compliance was calculated using Equation 8-2.

$$J(t) = \frac{\varepsilon(t)}{\sigma_0} \qquad \text{Equation 8-2}$$

where $J(t)$ is the creep compliance, $\varepsilon(t)$ is the time dependent strain, σ_0 is the applied constant stress.

8.3.7. X-ray Diffraction

Microstructural investigation using XRD was conducted to achieve further understanding of the effect of incorporating ANPs in MMA resin. XRD was conducted using Rigaku, SmartLab XRD machine. The machine is equipped with copper k alpha tube and 1 dimensional silicon strip detectors D/teX. The scan was conducted from 0° to 90° with 0.02° step and scan rate of 6 degrees/min.

8.4. Results and Discussion

The ability to flow through microcracks and the rate of flow in the cracks are significant capabilities of successful seal material to achieve seal integrity. To investigate the ability of the NM-MMA and other seal materials to flow through microcracks, surface tension, viscosity, and contact angle of all seal materials in this study were measured (Figure 8-3, Figure 8-4, and Figure 8-5). Novolac epoxy has 17.7% lower surface tension than microfine cement. This low surface tension allows epoxy to fill smaller microcracks than what microfine cement can fill. However, Novolac epoxy's surface tension is still not low enough to allow epoxy to fill 30 μm microcracks. On the other hand, it was found that MMA and NM-MMA seal materials have 43.2% and 42.7% lower surface tension than microfine cement, respectively, and 31% and 30.5%, respectively, lower than Novolac epoxy. This significantly low surface tension allows MMA to flow through such small microcracks (30 μm) and completely fill the gap and achieve seal integrity. The viscosity of all seal materials is shown in Figure 8-4. It was found that Novolac epoxy has 18.4% lower viscosity than microfine cement while MMA and NM-MMA both have 99.6% lower viscosity than microfine cement. These extremely low viscosities of MMA and NM-MMA result in a higher rate of flow of the seal materials through the microcracks. This high flow rate allows the seal material to penetrate further in the microcrack before hardening and results in an efficient seal of the microcrack. It was also found that incorporating ANPs has no noticeable effect on either viscosity or surface tension of MMA. The contact angle measurements of all seal materials with Type G cement matrix surface are shown in Figure 8-5. The measurements show that the contact angle of Novolac epoxy, MMA, and NM-

MMA are 27%, 62%, and 59% lower than the contact angle of microfine cement with Type G cement matrix surface respectively. The measurements also show that the contact angle of MMA and NM-MMA are 48% and 44% lower than Novolac epoxy. On the other hand, incorporating ANPs in MMA resulted in a very limited increase in the contact angle of MMA with cement matrix by 7% only. The contact angle and surface tension measurements control the ability of seal material to flow into the microcrack (Blunt 2017).

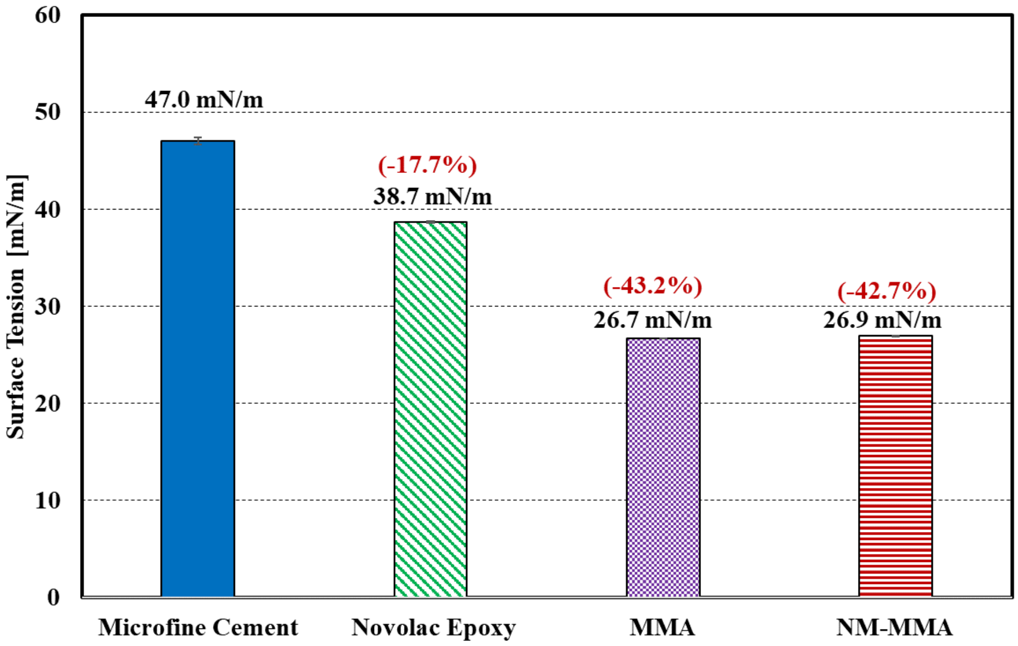

Figure 8-3. Surface tension measurements of all seal materials; % above the bars represents the difference of bond strength of seal material compared with microfine cement

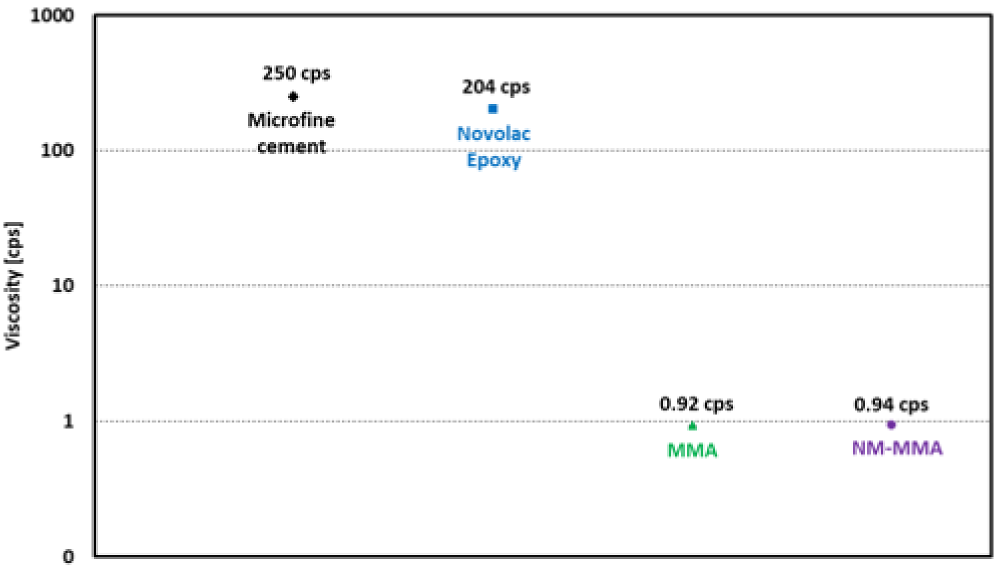

Figure 8-4. Viscosity measurements of all seal materials. Log scale is used to enable display with order of magnitude change in viscosity.

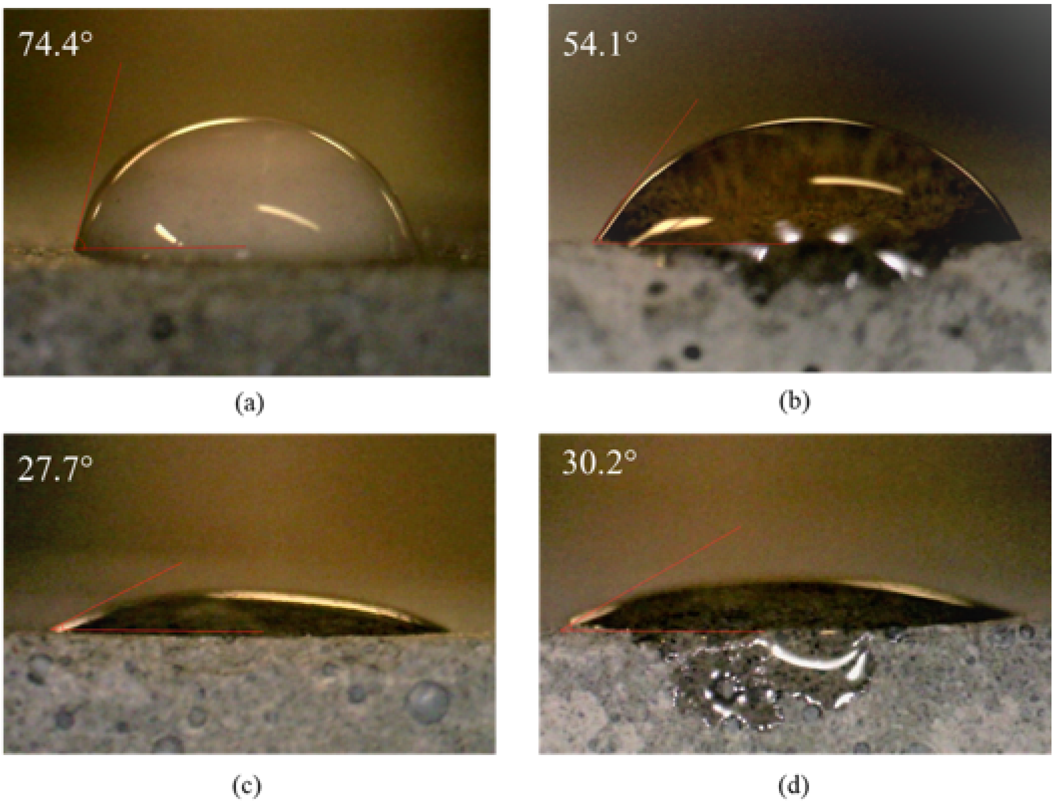

Figure 8-5. Contact angle measurements presenting contact angle value on top left corner of the image for (a) microfine cement, (b) Novolac epoxy, (c) MMA, and (d) NM-MMA with Type G cement matrix surface

The ability of a seal material to replace other fluids (e.g. air or water) is proportional to its surface tension and contact angle (Blunt 2017). To compare the penetrability of seal materials in this study, the authors suggest calculating the Penetrability Index (P_I) as a measure based on Young-Laplace equation as described by Equation 8-3.

$$P_I = \frac{\gamma_w}{\gamma_r \cos \theta_r} \qquad \textit{Equation 8-3}$$

where P_I is the Penetrability Index, γ_r is the seal material surface tension [N/m], θ_r is the seal material contact angle, and γ_w is the water surface tension [N/m].

The calculated Penetrability Index for all seal materials is shown in Figure 8-6. The results show that Novolac epoxy, MMA, and NM-MMA have 8.9%, 44.9%, and 44.5% higher Penetrability Index than microfine cement respectively. Although Novolac epoxy shows increase in the Penetrability Index, this increase was not enough to allow Novolac epoxy to fully penetrate 30 μm microcracks. MMA and NM-MMA were found to have 118% and 112% higher Penetrability Index than Novolac epoxy respectively. These results show that MMA and NM-MMA seal material will be able to penetrate smaller microscale defects than both microfine cement and Novolac epoxy under similar conditions. On the other hand, incorporating ANPs in MMA seal material resulted in a very insignificant reduction in the Penetrability Index of MMA by less than 1.0%.

All push-out specimens were loaded until failure. Failure is defined as the point at which the load dropped below 50% of the maximum load. Median load-displacement curves of specimens sealed with different seal materials are shown in Figure 8-7. All the materials showed similar shear stiffness (represented by slope of load-displacement curves). The load-displacement curves show that microfine cement has very low shear strength compared with polymer seal material. It was also observed that MMA-based seal materials have almost 100% higher bond strength than Novolac epoxy seal material, and about 1000% higher than microfine cement. Incorporating ANPs has no significant effect on the shear capacity of the seal material. However, incorporating ANPs significantly improved the displacement at failure of the seal material indicating significant improvement in ductility.

The apparent bond strength of seal materials was calculated using Equation 8-1. Figure 8-8 shows the bond strength of all seal materials. The results show an increase in the apparent bond strength of Novolac epoxy, MMA, and NM-MMA by 554%, 1088%, and 1061% compared to microfine cement. Statistical analysis using student t-test with 95% level of confidence shows that the increase of bond strength of Novolac epoxy, MMA, and NM-MMA compared to microfine cement was statistically significant. However, the reduction in the bond strength of NM-MMA is statistically insignificant when compared with neat MMA seal material.

Figure 8-9 shows the displacement at failure for all seal materials. Using Novolac epoxy as seal material reduced the displacement at failure by 34.9% compared with microfine cement. However, this reduction was found to be statistically insignificant. On the other hand, the displacement at failure of specimens sealed with MMA and NM-MMA was found to increase the displacement at failure by 156% and 468%, respectively, compared to microfine cement.

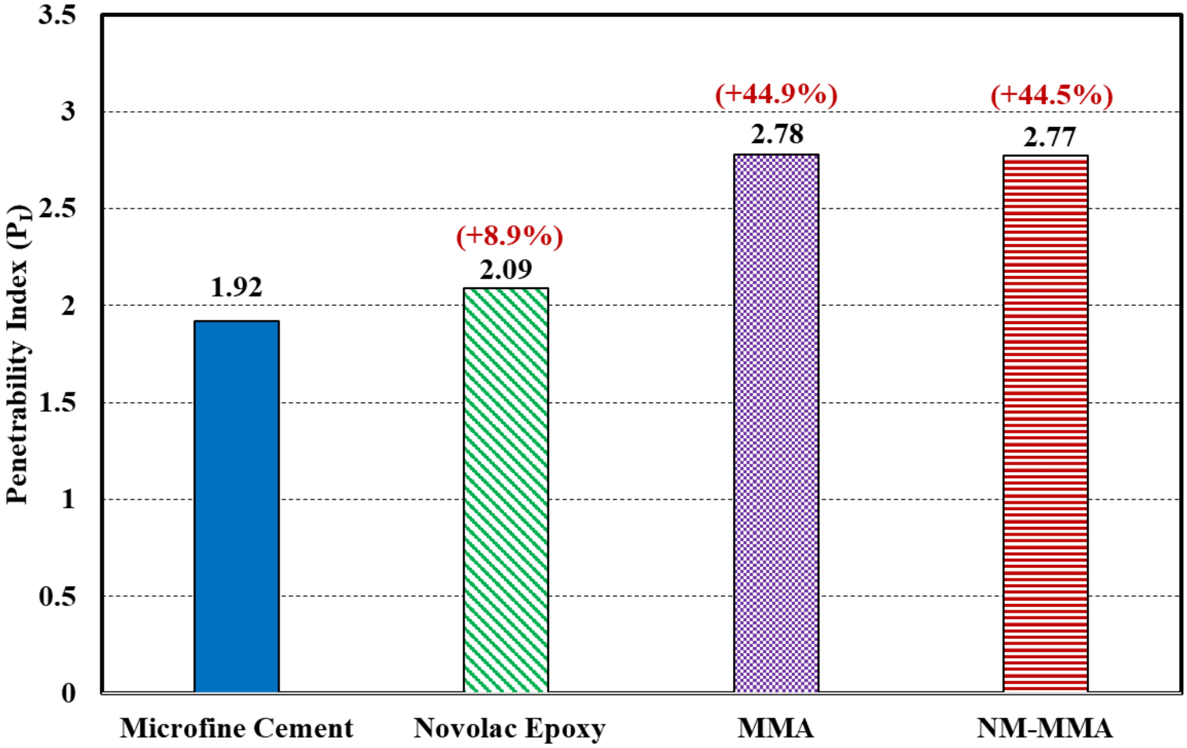

Figure 8-6. Penetrability Index (P_I) of all seal materials; % above the bars represents the difference of Penetrability Index of seal material compared with microfine cement

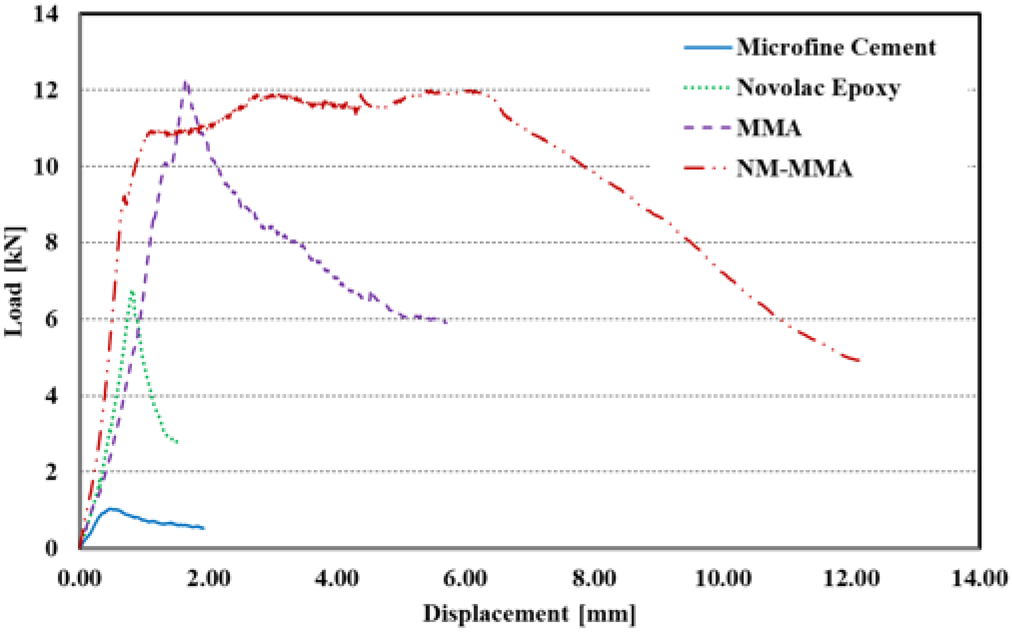

Figure 8-7. Median load-displacement curves of specimens sealed with microfine cement, Novolac epoxy, MMA, and NM-MMA polymer nanocomposite

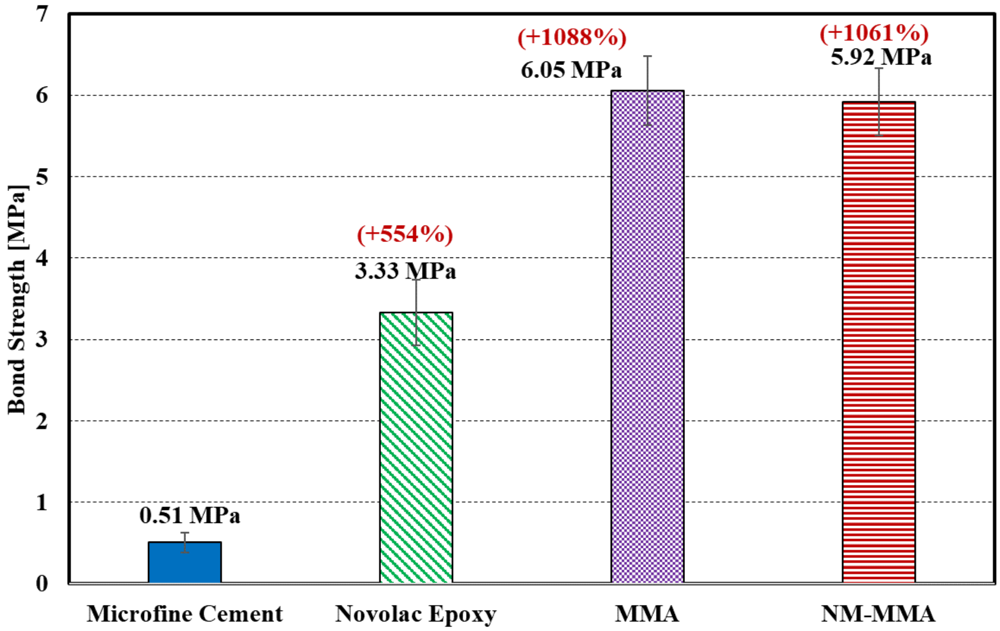

Figure 8-8. The apparent bond strength of all seal materials; % above the bars represents the difference of bond strength of seal material compared with microfine cement currently used in the field

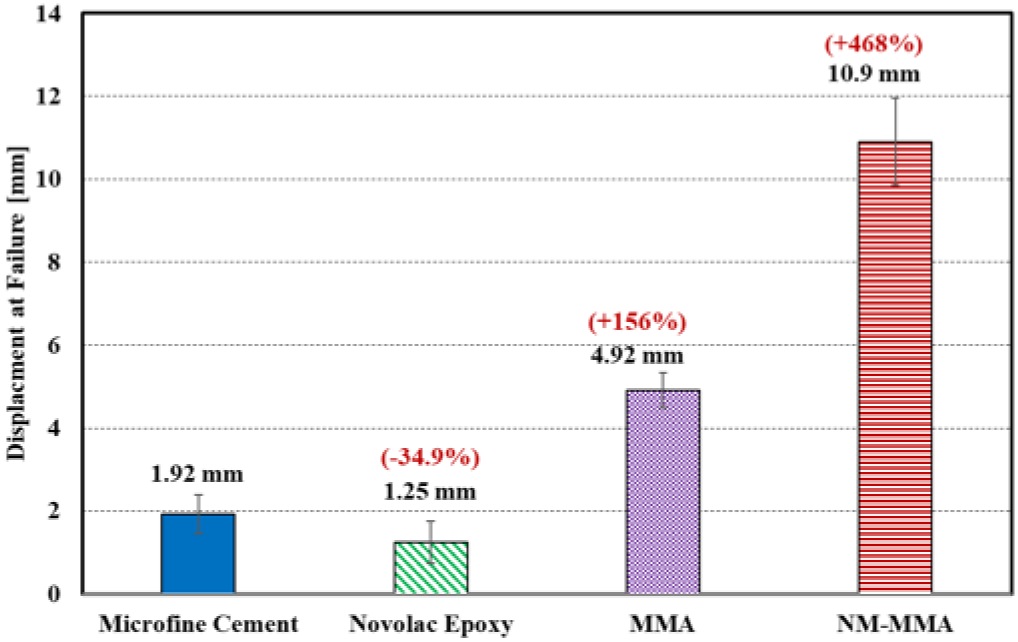

Figure 8-9. Displacement at failure of all seal materials; % above the bars represents the difference of bond strength of seal material compared with microfine cement

The toughness of push-out specimens was calculated as the area under the load-displacement curve until failure (Figure 8-10). It was found that the toughness was increase by 223%, 2638%, and 8135% for Novolac epoxy, MMA, and NM-MMA, respectively, compared to microfine cement. These results show that incorporating 0.5% ANPs in MMA was able to increase the displacement at failure and toughness of push-out specimens by 122% and 201% respectively. It is important to note that such increase in ductility and toughness of seal material will have a significant effect on seal efficiency. A seal material with relatively high strength and very high failure displacement and ability to absorb energy will show much improved efficiency compared to current seal technology.

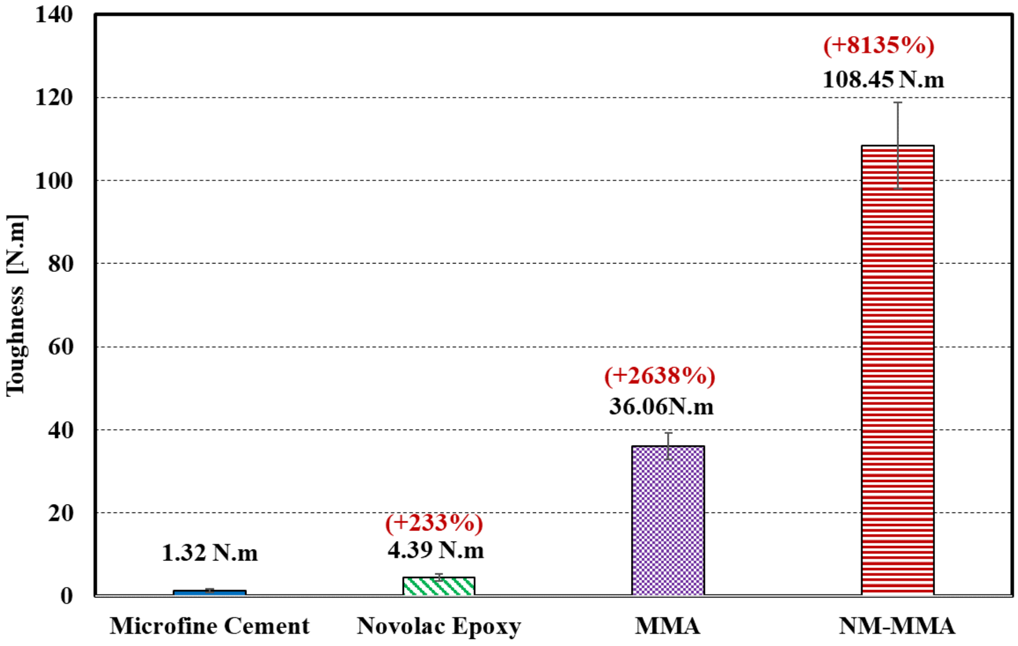

Figure 8-10. Toughness of all seal materials; % above the bars represents the difference of bond strength of seal material compared with microfine cement

Microscopic investigation of the cement matrix-shale interface was conducted to explain the bond strength. Figure 8-11 and Figure 8-12 show photomicrographs of cement matrix-shale interfaces sealed with microfine cement and Novolac epoxy respectively. Figure 8-11 shows that microfine cement has a very limited penetration in the cement matrix-shale interface. Moreover, Novolac epoxy was found to discreetly fill the cement matrix-shale interface as shown in Figure 8-12. This shows that both microfine cement and Novolac epoxy were not able to fill the 30 μm microcracks. This explains the relatively low bond strength of both materials. This also explains the reduction in the values of the bond strength measured compared with those reported before for seal of 800 μm microcracks (Genedy et al. 2017-A). On the other hand, NM-MMA was able to completely fill 30 μm microcracks as shown in Figure 8-13.

The viscoelastic behavior of MMA and NM-MMA obtained from creep test is shown in Figure 8-14. The initial creep compliance was calculated using Equation 8-2. For consistency, the initial creep compliance was calculated at time of 2 seconds for all specimens and it was found to be 2394 ± 135.7 μm/N and 1988.2 ± 159.9 μm/N for MMA and NM-MMA respectively. This represents a decrease of 17% in creep compliance due to incorporating 0.5 wt.% ANPs in MMA resin. Furthermore, the strain recovery was found to be 77.3 ± 2.4% and 83.0 ± 2.1% for MMA and NM-

MMA respectively. Moreover, the elastic modulus of MMA and NM-MMA was found to be 418.6 ± 23.4 MPa and 505.2 ± 41.9 MPa respectively.

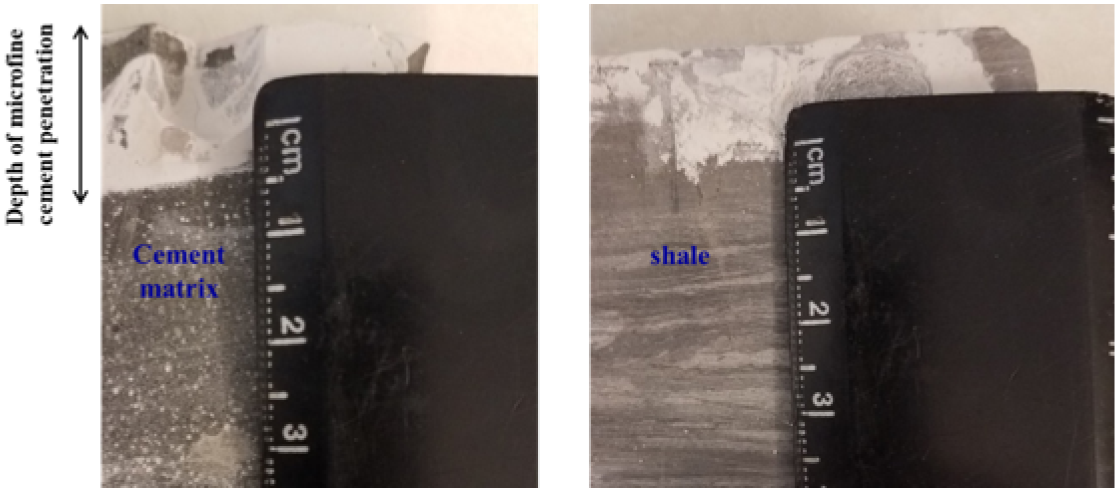

Figure 8-11. Microscopic images of cement matrix-shale interface sealed with microfine cement with two different sides showing depth of microfine cement penetration of cement matrix and shale sides

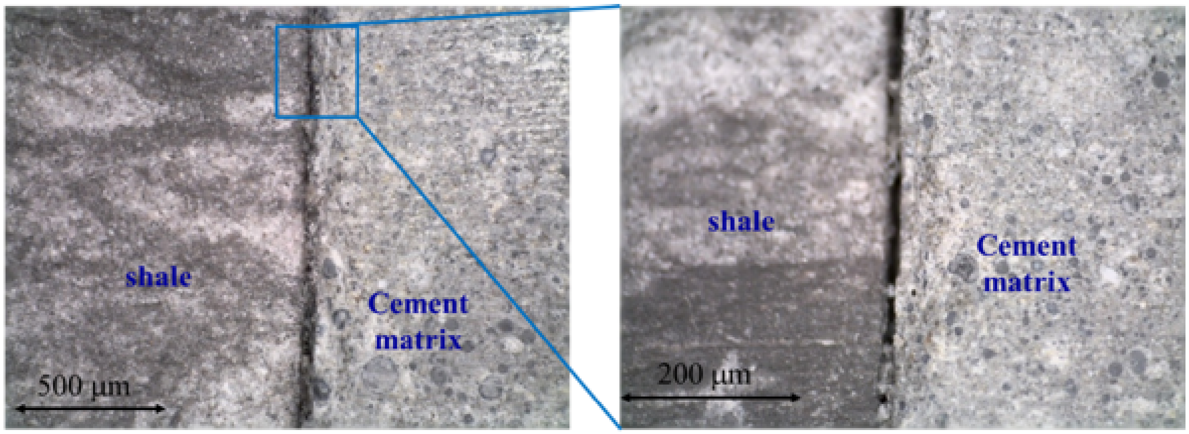

NOTE: Right photo at high magnification shows the inability of epoxy to penetrate 30 μm microcracks.

Figure 8-12. Microscopic images of cement matrix-shale interface sealed with Novolac epoxy with two different levels of magnification showing gabs in sealed interface.

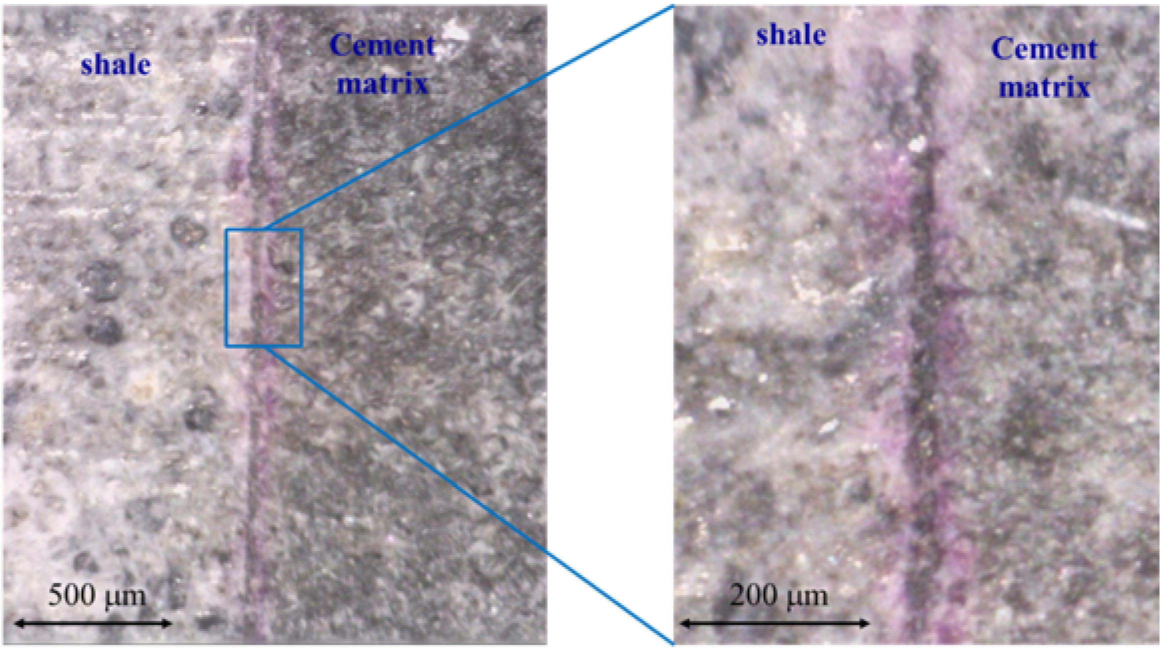

NOTE: Right photo proves the ability of NM-MMA to fill the microcracks and infiltrate both shale and cement matrix sides.

Figure 8-13. Microscopic images of cement matrix-shale interface sealed with NM-MMA with two different levels of magnification showing the ability of the NM-MMA seal material to completely fill the gap at the shale-cement matrix interface

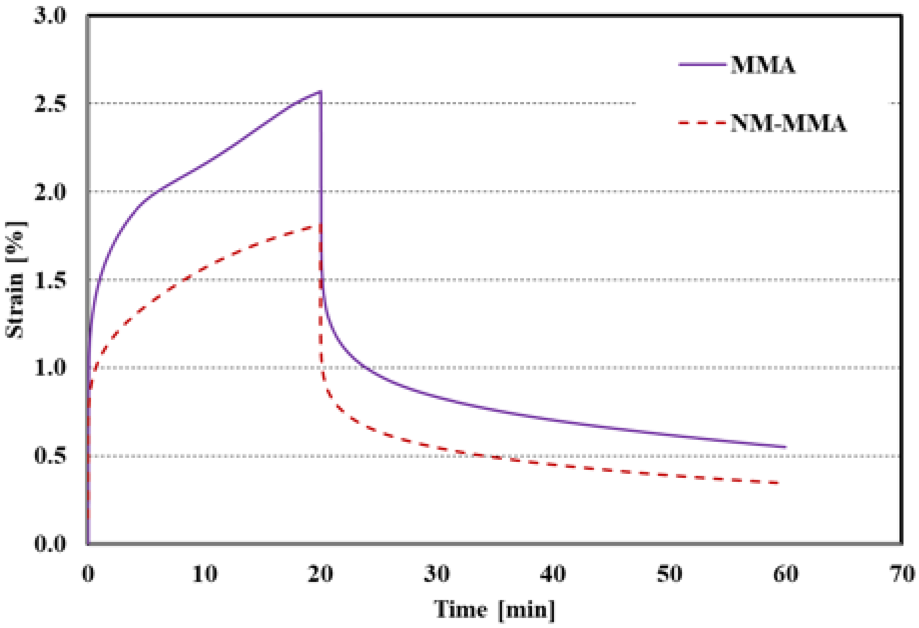

Figure 8-14. The viscoelastic behavior of MMA and NM-MMA obtained from creep test

To investigate the reinforcement effect of nanoparticles on the mechanical behavior of polymer nanocomposites, several models were developed to estimate the mechanical properties of the composite. The ability of two models to estimate the mechanical properties of the MMA/ANPs polymer nanocomposite was investigated. The elastic modulus of the NM-MMA was estimated using the modified rule of mixture presented by Equation 8-4 after Kuo et al. (2005).

$$E_c = \eta E_p V_p + E_m V_m \qquad \textit{Equation 8-4}$$

where E_c is the composite modulus of elasticity [MPa], E_p is the particles modulus of elasticity [MPa], E_m is the matrix modulus of elasticity [MPa], V_p is the particles volume fraction, V_m is the matrix volume fraction, and η is strengthening coefficient.

The modulus of elasticity of ANPs is assumed to be 393 GPa after Naous et al. (2006). The matrix modulus of elasticity was measured using DMA and the strengthening coefficient for ANPs was assumed to be ≈ 0.1 for particles with aspect ratio ≈ 1 (Kuo et al. 2005). Moreover, the Halpin–Tsai equation presented in Equation 8-5 and Equation 8-6 was also examined to estimate the modulus of elasticity of NM-MMA polymer nanocomposite (Naous et al. 2006).

$$E_c = E_m\left(\frac{1 + \xi\eta V_p}{1 - \eta V_p}\right) \qquad \textit{Equation 8-5}$$

$$\eta = \frac{\frac{E_p}{E_m} - 1}{\frac{E_p}{E_m} + \xi} \qquad \textit{Equation 8-6}$$

The constant ξ was assumed to be 2 for spherical particles like ANPs (Naous et al. 2006). The estimated modulus of elasticity of NM-MMA using the modified rule of mixture and the Halpin–Tsai method compared with the measured value are shown in Figure 8-15. The calculations show that the modified rule of mixture overestimated the polymer nanocomposite modulus of elasticity by more than 29% while he Halpin–Tsai underestimated the modulus by more than 15%. Failure of both models to estimate the modulus of MMA-ANPs polymer nanocomposite can be explained by the fact that these models are micromechanics models that do not take into account the potential chemical reaction between the nanoparticles and the polymer matrix. Such chemical reaction can alter the microstructure and the mechanical properties of the matrix and thus would result in change in the polymer nanocomposite properties.

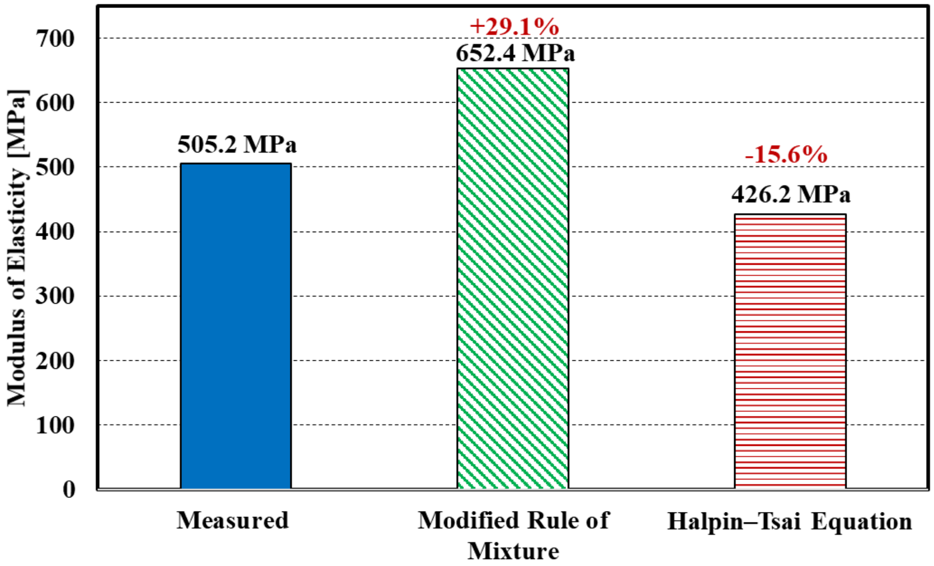

NOTE: The % above the bars represents the difference of estimated modulus of elasticity compared with measured value.

Figure 8-15. The estimated modulus of elasticity of NM-MMA using modified rule of mixture and Halpin–Tsai method compared to the measured value

Polymers with semicrystalline microstructure are well known to have higher plastic deformation than aligned cross-linked polymers (Parks and Ahzi 1990; Bartczak et al. 1992; G'sell 1994). In addition, it was also reported that the increase in degree of crystallinity in polymeric matrix would result in increase in the elastic modulus (Ferry 1980). XRD scans for both MMA and NM-MMA specimens were measured to investigate the effect of incorporating ANPs on the degree of crystallization of MMA (Figure 8-16). It can be observed from the XRD scans that two peaks (at 2θ of 24° and 68°) were detected in the NM-MMA spectroscopy that are not observable in the neat MMA profile. These peaks can be associated to 3-Methyl-1,5-diphenyl-4,5,9, 13b-tetrahydro, which is considered a crystallized organic structure. The new peaks can be associated with the increase in the degree of polymer crystallization (Bai et al. 1998). This explains the significant increase in the failure displacement/ductility in the case of NM-MMA seal material compared with standard MMA.

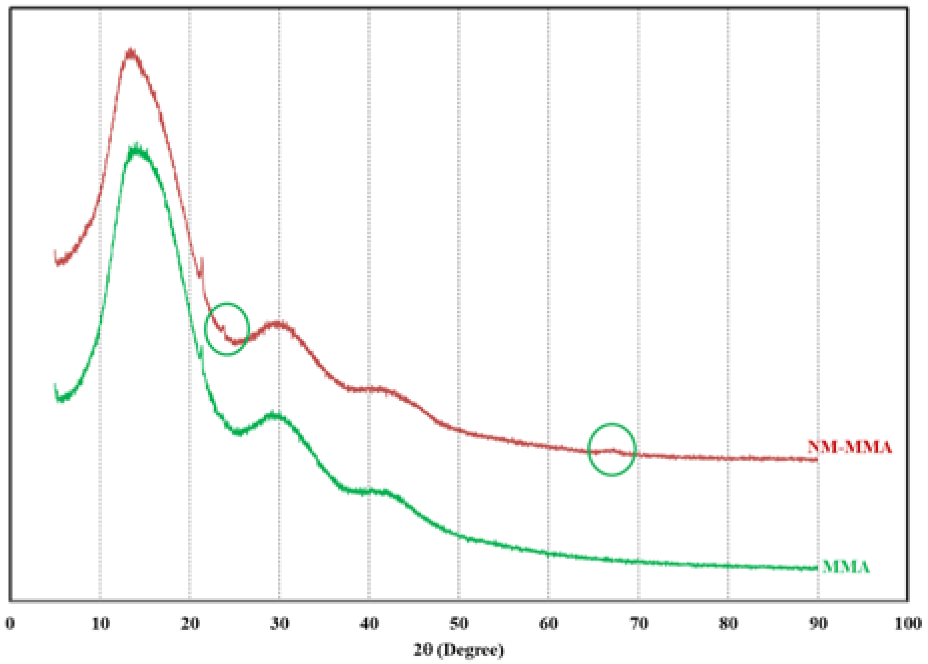

Figure 8-16. XRD scans for both MMA and NM-MMA specimens

We note that the mechanical properties of MMA make it suitable for seal of microcannulas cracks. Adding and dispersing ANPs in MMA to produce NM-MMA will increase the cost associated with nanomaterials cost and cost of processing. Nevertheless, we suggest that the significant improvement of seal ductility, reduction in creep compliance and improved in creep recovery of NM-MMA compared with MMA makes NM-MMA a more attractive micro annulus seal material than MMA due to the significant importance of ductility and creep characteristics in resisting debonding of sealed cracks when subjected to cyclic stresses during well operation. The mechanical properties of the NM-MMA nanocomposite prove its superior capabilities for use as a seal material (Genedy et al. 2017-B). Limitations of the above study include the fact that the above testing was conducted only at ambient temperature and pressure while seal materials will often be exposed to much greater pressures and temperatures. In addition, the long-term durability of the new seal material to operate in brine environment shall also be investigated. Moreover, time-dependent behavior (e.g. creep) of the new NM-MMA nanocomposite at high temperature and in brine environment shall also be examined. Finally, more research is warranted to measure permeability of the sealed interface under confining pressure and cyclic stresses simulating operational conditions of wellbores.

8.5. Conclusions

A new NM-MMA seal material for sealing 30 μm microcracks in wellbores was developed and examined. MMA and NM-MMA incorporating 0.5% ANPs by weight of the MMA resin proved to provide performance as a seal material capable of sealing 30 μm cement matrix-shale interface microcracks. The polymer nanocomposite showed improved bond strength (1061% higher than microfine cement), excellent ductility (468% higher displacement at failure than microfine cement), and superior toughness (8135% higher than microfine cement). The improved mechanical properties of NM-MMA show that it would have superior performance as a seal material compared with microfine cement currently used as the standard technology to seal wellbore microcracks.

Microscopic investigations of the shale-cement matrix interface showed that microfine cement did not flow through 30 μm microcracks and has a very limited penetration depth. Moreover, Novolac epoxy was also unable to completely fill the gap between the shale and the cement matrix. In contrast, MMA-based seal materials were able to completely fill the wellbore microcracks. Contact angle and surface tension measurements showed that MMA and NM-MMA have a much higher penetrability in cement matrix than microfine cement and Novolac epoxy. This helps MMA to flow in microscale defects and cracks. Moreover, it was found that incorporating 0.5% ANPs by weight in MMA was able to increase the displacement at failure and toughness by 122% and 201% respectively. Viscoelastic investigation using DMA showed that incorporating ANPs in MMA matrix reduced creep compliance of NM-MMA by 17% and improve creep recovery by 7.3%. XRD analysis shows that incorporating ANPs in MMA increased the degree of polymer crystallization enabling significant increase in polymer ductility and toughness and reduction of polymer creep compliance.

8.6. Acknowledgements

The authors greatly acknowledge this support. The authors would also like to thank Dr. Kateryna Artyushkova for facilitating the use of the force tensiometer and Dr. Eric Peterson for his help in conducting and analyzing the XRD test.

9. ENGINEERING A LOW MODULUS POLYMER-MODIFIED CALCIUM-SILICATE-HYDRATE (C-S-H) BINDER FOR WELLBORE APPLICATIONS

9.1. Overview

The continued rise of hydrocarbon exploration and CO_2 sequestration efforts necessitates ensuring wellbore integrity as a top priority in the oil and gas industry. Interfacial debonding of typical oil well cement (OWC) with steel casing can result in potentially gas leakage to surface or hydrocarbon contamination of water-bearing formations affecting wellbore integrity. This paper describes a new polymer-modified synthetic calcium-silicate-hydrate/styrene-butadiene rubber (SBR) binder. The new C-S-H/SBR binder is produced by calcining calcium carbonate and mixing this with fumed silica (SiO_2), deionized water and SBR. Mechanical, physical, chemical and microstructural characterization was conducted to describe the new C-S-H binder. Results from the experimental investigation demonstrate the ability to engineer a new C-S-H binder with low elastic modulus and improved toughness by controlling the SBR content and method of C-S-H synthesis. The new binder suggests the development of a new family of low-modulus silica-polymer binders that might be useful for other engineering applications.

9.2. Introduction

Shrinkage of OWC and the formation of weak calcium hydroxide (CH) crystals significantly decreases the bond strength at the cement-steel and cement-rock interfacial zones and thus are well-known reasons for forming microannulus pathways for gas leakage in oil and gas wellbores (Genedy et al. 2017; Nakayama and Beaudoin 1987; Mehta and Monteiro 2013). Furthermore, a high swell coefficient and roughness of the surrounding rock can also weaken interfacial bonds that inevitably create leakage pathways (Ladva et al. 2004). The conditions described above favor debonding of the cement interfaces over an extended time period of years of service creating critical wellbore integrity concerns where gas leakage to surface or hydrocarbon contamination of water-bearing formations can take place (Carey et al. 2007; Stormont et al. 2018). Interfacial debonding and wellbore seal integrity directly contributed to the massive blowout in the Aliso Canyon subsurface reservoir, in Los Angeles, California, that released an estimated 97,000 metric tons of methane gas into the atmosphere over an approximate period of 6 months (Conley et al. 2016). Furthermore, impacts from the Deepwater Horizon oil spill in 2010 and the recently discovered Taylor oil spill, which has been leaking for more than 14 years, can still be felt in the gulf coast region today (Kastler et al. 2019; Fears 2018).

Cement hydration results in one key material responsible for strength, bond and durability of cement; that is, calcium-silicate-hydrate (C-S-H). Many investigators have conducted extensive studies to characterize C-S-H and have synthesized C-S-H with various procedures and conditions. Beaudoin and Feldman (1986) produced synthetic C-S-H by mixing aqueous solutions of calcium oxide (CaO) and sodium metasilicate at various CaO/SiO_2 weight ratios (C/S ratios) while drying of the samples was accomplished by bathing the specimens in acetone and ether. The dried C-S-H powder was then compacted into small discs with compacting pressures ranging from 510–1360 MPa. Alizadeh et al. (2011) synthesized C-S-H at C/S ratios between 0.7 and 1.5 to chemically and mechanically simulate C-S-H products found in cement paste. Foley et al. (2012) and Kim et al. (2013), synthesized C-S-H at various C/S ratios using calcium oxide, fumed silica, and deionized water employing different drying techniques to characterize the nanoscale mechanical properties through nanoindentation and thermogravimetric analysis (TGA). Aboubakr et al. (2015), used similar synthesis techniques to establish correlation between the microstructural and viscoelastic properties of C-S-H.

The mechanical and chemical characteristics of synthetic C-S-H have been identified by numerous research and the formation of an absorbed interlayer of water plays a critical role in the dynamic mechanical properties of C-S-H as described by Alizada et al. (2011). Silicates make up approximately 75% of hydrated Portland cement paste (Mehta and Monteiro 2013), and manipulation of the microstructural phases and nano-structure of C-S-H is crucial for controlling the properties of concrete on a macro-scale. Fully understanding each phase of C-S-H formation and how each phase contributes to the mechanical and chemical properties of cement is critical for controlling specified properties that are needed for wellbore applications.

Studies have demonstrated that the addition of SBR creates a polymer network within setting cement that significantly reduces the ultimate compressive strength while increasing the strain at failure (Shirshova et al. 2011; Ohama 1995; Van Gemert and Beeldens 2013; Yue and Wang 2013). Ohama (1995) showed the typical composition of industrial SBR latex, which is nearly 50% water by weight with small amounts of surfactant and a vinyl carboxylic acid present. Previous researchers revealed that the addition of polymers to cement creates a film and fills voids within the microstructure (Ohama 1995; Van Gemert and Beeldens 2013). This creates an unfavorable interaction between water absorption and polymer hardening of the hydrated and un-hydrated cement particles. The addition of SBR latex to cement based concrete inhibits and strengthens certain mechanical and chemical properties which makes way for the concept of optimizing targeted properties for wellbore applications. SBR latex has shown to have an adverse effect on the formation of C-S-H and C_3S. The addition of SBR can hinder the hydration process which limits the formation of key components of hydrated cement (Yue and Wang 2013).

We hypothesize that a new binder of polymer-modified C-S-H can be synthesized and developed for wellbore applications. The new binder can be engineered to achieve a set of desired characteristics that are not attainable using current cement technology. Such characteristics include low elastic modulus, high bond strength, high strain at failure and low shrinkage. The new binder will significantly reduce the chance of microcracking, due to shrinkage and operation stresses, at the cement-steel and cement-rock formation interfaces improving overall wellbore integrity.

9.3. Experimental Methods

9.3.1. Synthesis of C-S-H/SBR Composite

Calcium oxide (CaO), also known as quicklime, was produced by calcining reagent grade calcium carbonate ($CaCO_3$), from Mallinckrodt Chemicals, at 900°C. The purity of the lime was greater than 99.5% and was confirmed by weight loss in TGA. Fumed silica (SiO_2) from Sigma Aldrich, with a purity of greater than 99.8% was used as the silicate part in the synthetic C-S-H. Prior investigations showed that the mechanical properties of C-S-H are dependent on C/S ratio and that at C/S ratio of 1.5 the mechanical properties of C-S-H is similar to that produced by hydrating commercial cement. Therefore, C/S ratio of 1.5 was used herein. Deionized water was added to the calcium oxide and silica at a C/S ratio of 1.5 to produce a low viscosity slurry that can be easily mixed. Various amounts of commercial grade SBR latex, ranging from 0% to 15%, by weight of the CaO plus SiO_2 contents, was added to the slurry before mixing. The slurry was placed in a continuous rotary mixer (Figure 9-1: Step 1) for seven days to allow the C-S-H reaction to fully transpire. The excess water was then extracted by placing the slurry under a vacuum filtering system for 24 hours (Figure 9-1: Step 2). The material was then subjected to a standard drying method until the powder achieved

11% relative humidity (RH). All preparation of the materials during synthesis and prior to testing was performed in a nitrogen environment to prevent CO_2 contamination.

The standard method for drying the material to 11% RH used a saturated lithium chloride solution, which allowed reaching a water content that is comparable to cement paste when evaporative water has been removed. The lithium chloride solution was prepared in accordance with the American Society of Testing and Materials (ASTM) Standard E 104-02 (ASTM 2007). The drying system consisted of a 3-beaker set up in series as seen in Figure 9-1: Step 3. The beaker containing the saturated lithium chloride was maintained on a hot plate at a constant 50°C ambient temperature. The beaker containing the vacuumed C-S-H, equilibrated to 11% RH for an average of 1 week or until the change in mass was less than 0.1% per day. The last beaker was directly hooked up to the vacuum source with drierite (calcium sulfate and cobalt chloride) to prevent any excess water from entering the vacuum line. This standard drying method was used for all C-S-H preparations due to the relatively quick drying times. Researchers have used this method of drying to equilibrate C-S-H to 11% previously (Feldman and Ramachandran 1971; Young and Hansen 1986; Thomas et al. 1998).

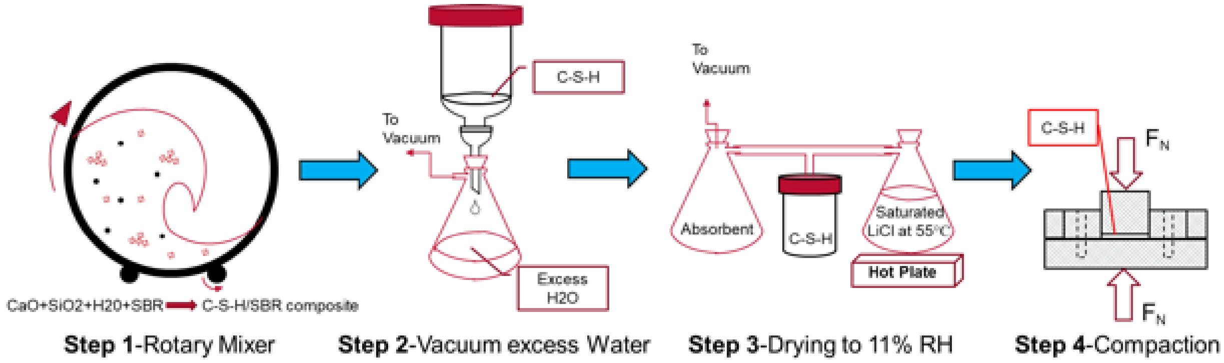

Figure 9-1. Synthesis schematic

Compaction was performed by a square, high strength steel mold measuring 200 × 200 mm with a small 10 × 30 mm insert where the powder to be compacted was placed (Figure 9-1: Step 4). The dried C-S-H powder was placed in the insert where the raised inset will apply pressure. Instron Universal Testing Machine was used to induce a compaction pressure of 400 MPa on the C-S-H powder to achieve a level of porosity and density, 30% and 2000 kg/m^3 respectively, similar to C-S-H produced by hydrating cement (Alizadeh et al. 2011; Alizadeh 2009). A nitrogen environment was not maintained during the compaction, but specimens were immediately moved to the controlled environment once compaction was completed. The compaction loading rate was applied at 1 kN/second and held at the ultimate load for 4 minutes, before unloading completely. A total of 40 specimens 30 × 10 × 1.8 mm of C-S-H with various amounts of SBR latex were produced using the above procedure prior to conducting mechanical, physical, and chemical characterization.

9.3.2. Mechanical Characterization of C–S–H

9.3.2.1. Dynamic mechanical analysis

Dynamic mechanical analysis (DMA) tests were conducted using a TA Instruments, Q800 DMA. DMA was used to characterize the compacted specimens at 25°C and an RH of 11%. The single cantilever setup was used for force controlled bending testing. The span to thickness aspect ratio of 1:10 was maintained for accurate data acquisition during testing. The test started with an initial static force of 0.002 N and the load was ramped up linearly with a loading rate of 0.5 N/min until failure. Due to the brittle nature of the material, a 0.113 N·m torque was applied with a torque wrench to secure the specimen in the cantilever clamp.

9.3.2.2. Direct Shear Test

An ELE International digital shear apparatus was used for the direct shear test. A direct shear test was implemented to examine the bond strength of C-S-H to a steel interface. The compacted C-S-H was carefully removed and placed into the direct shear testing machine (Figure 9-2(a)). After securing the mold into the shearing apparatus and applying the normal force starting at 80 kg, six screws, that held the mold in place during compaction, were removed. A shear force was applied to the top portion of the mold, which contained the confined C-S-H powder as seen in Figure 9-2(b). A constant displacement rate of 0.90 mm/min was applied while the normal force was held constant for the entirety of the test. Subsequent tests were conducted with the normal force increased in increments of 40 kg ranging from 80 kg to 160 kg. Three replicas for each SBR content were tested.

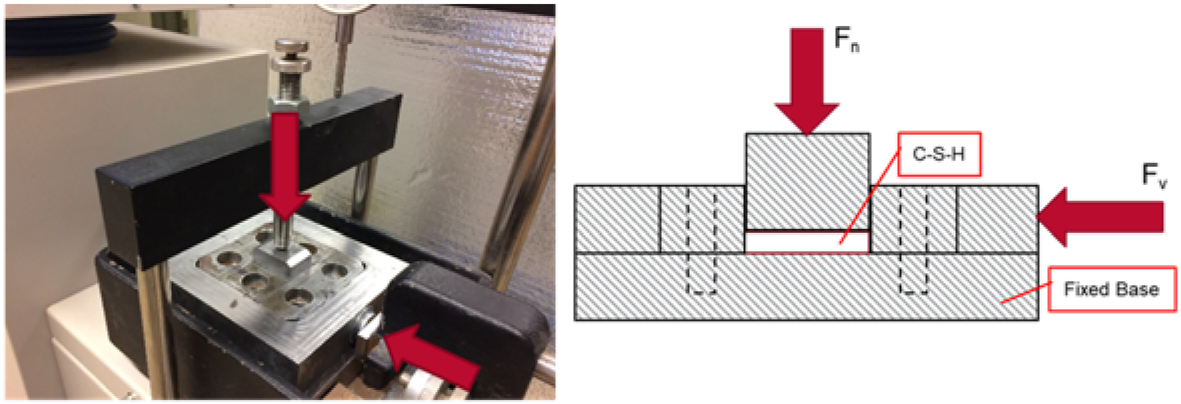

a) Compaction mold in shear apparatus b) Diagram of shear apparatus

Figure 9-2. Direct shear test apparatus and schematic showing load application during test

9.3.3. Physical Characterization of C-S-H

9.3.3.1. Density

Density measurements following ASTM C914-95 (ASTM 2004) were used to determine the difference between neat (0% SBR) samples and samples with SBR latex, by calculating the specific modulus and specific strength of the material. Specimens of standard dried C-S-H were compacted at 400 MPa and broken into smaller pieces. The specimens were then weighed using a Mettler

Toledo XS-64 and then immediately dipped into paraffin wax until each specimen was entirely coated with wax. The specimens were weighed while submerged in ethyl alcohol. The density was recorded and statistically analyzed.

9.3.4. *Chemical Characterization of C-S-H*

9.3.4.1. Thermogravimetric Analysis

TGA was performed on the standard dried C-S-H powder from 25°C to 1000°C with a temperature ramp of 10°C/min. The objective was to compare and confirm the formation of C-S-H and CH with the addition of SBR latex and examine whether SBR was interfering with the chemical formation of the microstructural phases. Mass loss was used to estimate the percent content of water, CH, and CO_2. TGA tests were employed to estimate CH and $CaCO_3$ contents as well as stoichiometric formulas of C-S-H, following Equation 9-1 and Equation 9-2 (Kim et al. 2012). In these Equations C-S-H is described as $(CaO)_{C/S} \cdot (SiO_2) \cdot (H_2O)_x$ where x is the amount of water in synthetic C-S-H. The notation $\%mL_1$ represents the mass loss from 145°C to 350°C, $\%mL_2$ represents mass loss from 350°C to 500°C, and $\%mL_3$ represents mass loss from 600°C to 825°C. The mass remaining at 1000°C is considered to be C-S-H. To exclude any chance of nonabsorbed water being calculated into the stoichiometric mass balance, initial weights were not recorded until a temperature of 145°C was reached. The equations were developed from a mass balance assuming the slurry is composed of enough water and a mole of C-S-H and CH will be synthesized in the process. Previous researchers used similar temperature ranges as those reported herein (Kim et al. 2013; Alizadeh 2009). Confirmation was obtained by using the stoichiometric formulas to calculate the percent of calcium and hydrate formations in the given material with silicate held at 1 mole.

$$C/S = \frac{\overline{C/S}\left(100 - \%mL_1 - 4.113\%mL_2 - 2.274\%mL_3\right) - 3.36\%mL_2}{100 - \%mL_1 - \%mL_2 - 2.274\%mL_3} \qquad \textit{Equation 9-1}$$

$$x = \frac{\%mL_1(3.115\overline{C/S} + 3.337)}{100 - \%mL_1 - \%mL_2 - 2.274\%mL_3} \qquad \textit{Equation 9-2}$$

9.3.5. *Microstructural Characterization of C-S-H*

9.3.5.1. X-ray Diffraction Analysis

X-ray diffraction (XRD) analysis is widely used to detect various chemicals and to investigate the crystalline structures present in a given compound. XRD analysis was conducted on standard dried C-S-H/SBR specimens and examined to determine how the addition of SBR affects the formation of different microstructural phases of the C-S-H crystalline structure reported by past investigators (Foley et al. 2012). C-S-H has a weak crystalline structure due to its amorphous nature and does not produce many strong XRD peaks. The XRD peaks acquired were compared with published results and characterized accordingly. Previous work has shown that CH and C-S-H peaks are shown to dominate the XRD profile for cement pastes. This work also showed a notable phase change with impact on the basal-spacing of C/S mixtures above 1.0 (Alizadeh 2009; Jain and Neithalath 2009).

9.3.5.2. ^{29}Si Magic Angle Spinning Nuclear Magnetic Resonance

^{29}Si magic angle spinning (MAS) nuclear magnetic resonance (NMR) spectroscopy was performed on standard dried C-S-H powder in 7 mm cylinders spun at 3.6 kHz. An excess of 10,000 scans were performed on each sample resulting in an average testing time of 24 hours. An ASX 300 spectrometer at 59.6 MHz, 7.05 T magnetic field, was used for single pulse analysis without proton decoupling or cross polarization. The ^{29}Si chemical shifts are referenced to $Si(CH_3)_4$ at 0 ppm and with a secondary reference using $Si[(CH_3)_3]_8Si_8O_{20}$ at 11.8 ppm relative to $Si(CH_3)_4$. Hydrated cement exhibits commonly observed chains of Q^1, Q_b^2 and Q^2 typically seen at -79.5, 84.6 and -85.3 ppm respectively. ^{29}Si MAS NMR spectroscopy can determine the polymerization of silicates and describes the mean length (L) of silicate chains calculated by the Q^2/Q^1 ratio (Equation 9-3) (Young and Hansen 1986). The average degree of silicate connectivity, n_c, uses the calculated fractions of Q^n to represent the polymerization of C-S-H (Equation 9-4) (LeSaout et al. 2004). A high n_c value indicates a high degree of polymerization of C-S-H.

$$L = 2(1 + \frac{Q^2}{Q^1}) \qquad \textit{Equation 9-3}$$

$$n_c = \frac{Q^1 + 2Q^2 + 3Q^3}{Q^1 + Q^2 + Q^3} \qquad \textit{Equation 9-4}$$

9.3.5.3. Scanning Electron Microscope Imaging

Scanning electron microscope (SEM) imaging was conducted on the fractured surface of C-S-H specimens tested by the DMA instrument. The Vega3 Tescan SEM was used to characterize the microstructure of the fractured surface. A secondary electron transmission was used to inspect the surface topography with minimal interference. The specimens were coated with 3-5 nm of carbon as an insulator to enhance the resolution of the microcracks. An accelerating voltage of 15 kV was also used in an effort to optimize the resolution. Careful attention was focused on the microcracks formed on the fractured surface during fracture of the specimens under flexural stresses.

9.4. Results and Discussion

The flexural stress versus strain curve for C-S-H with various SBR contents are shown in Figure 9-3, and the flexural strength are displayed in Figure 9-4. The results of control specimens of neat C-S-H ensured the validity of the DMA test, as it matched within ±11% previously reported elastic modulus (E) values obtained for C-S-H using nanoindentation (Kim et al. 2013). With the addition of SBR, the E gets reduced, stress at failure and strain at failure is increased along with the toughness (a material's ability to absorb energy to failure). These results demonstrate a common trend as the SBR content increases. The standard C-S-H compacted to 400 MPa without SBR had an E of 6.6 GPa ± 0.4 GPa. Similar values of E have been stated for Type G OWCs cured in simulated wellbore conditions (Guner and Ozturk 2015). In comparison, the elastic modulus of C-S-

H incorporating 15% SBR was reduced by nearly 200% to 2.3.0 ± 0.3 GPa, as shown in Figure 9-4. The specimens also experienced a slightly higher ultimate strength compared with neat C-S-H as the SBR content increases. With the addition of 15% SBR, the flexural strength was 12.3 MPa compared with a flexural strength of 9.7 MPa for neat C-S-H. Specimens of C-S-H with higher contents of SBR displayed early nonlinearity behavior as toughness also increased by approximately 330%, as the content of SBR rose to 15%. T-tests comparing neat C-S-H and C-S-H incorporating 15% SBR produced statistically significant difference when comparing *E*, ultimate strength, strain at failure, and toughness to samples without SBR. No statistical difference was observed between C-S-H specimens incorporating 10% and 15% SBR. Significantly reducing the *E* and increasing the strain at failure by 190% and 180% respectively, will limit the propagation of microannulus cracks, thereby limiting potential leakage pathways under wellbore operating conditions.

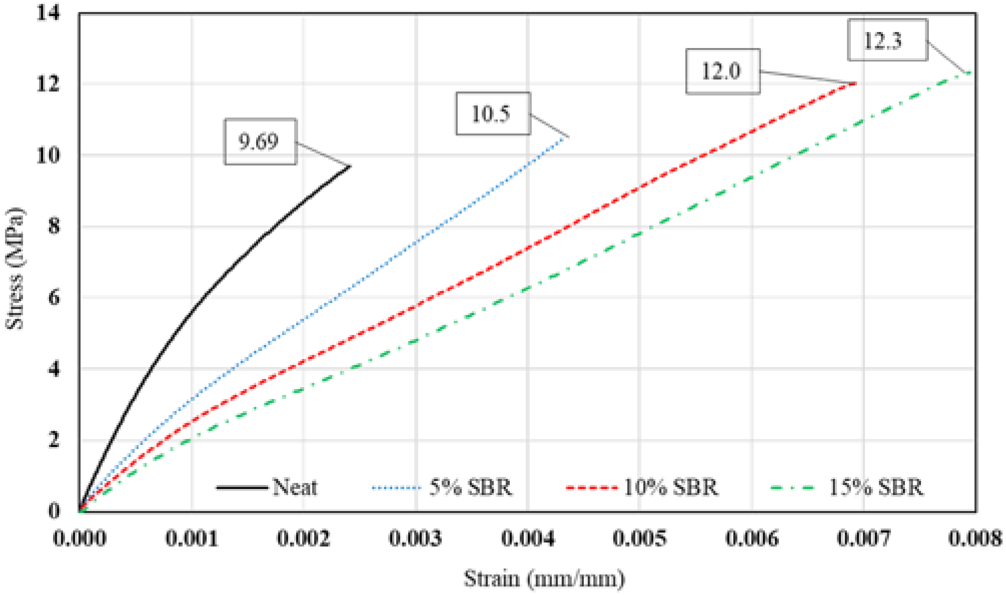

NOTE: Boxed numbers represent flexural strength.

Figure 9-3. Stress versus strain curves of C-S-H incorporating SBR obtained using DMA

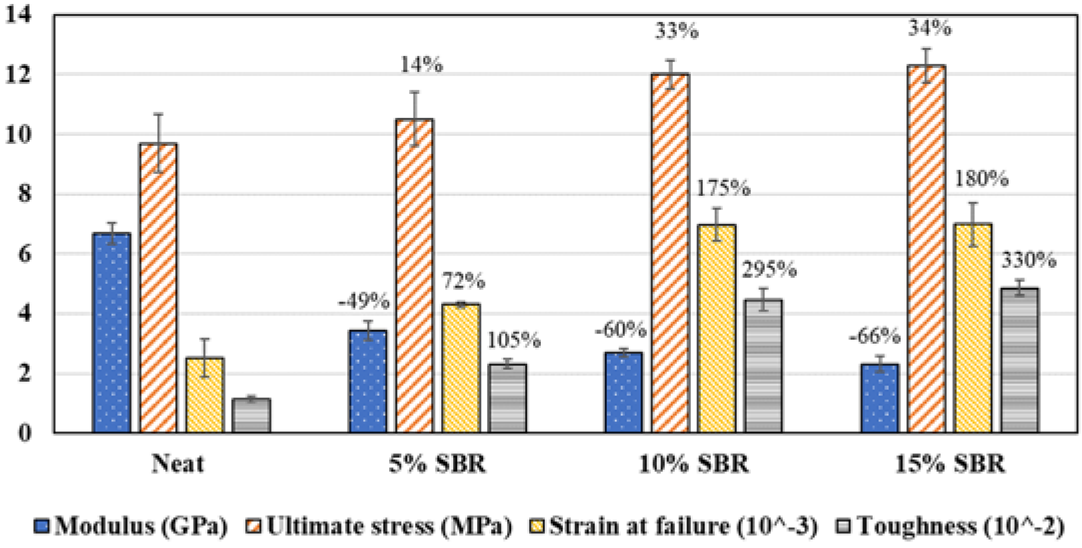

NOTE: The % above the bars represent the change when compared with neat C-S-H characteristics

Figure 9-4. Mechanical properties of C-S-H/SBR composite obtained using DMA

Direct shear tests showed that the bond strength of C-S-H incorporating SBR, to a smooth steel interface, increased by 221% when compared with neat C-S-H. This result also shows a common trend with the incremental increase of SBR. Figure 9-5 shows the progressive increase of the bond strength of C-S-H with steel as the SBR content increases. This demonstrates the significant effect of adding SBR for improving bond of synthetic C-S-H to various interfaces. Good bond between the binder and both steel and rock is essential for wellbore integrity. Reducing the probability of microannulus cracks created by shrinkage and temperature fluctuation during operation, will significantly improve wellbore integrity.

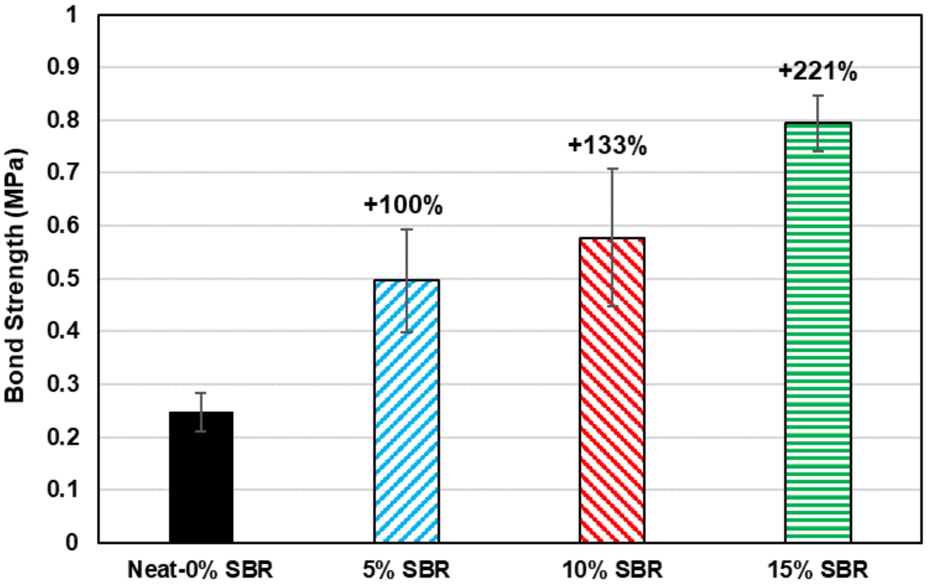

NOTE: The % above the bars represent improvement of bond strength when compared with neat C-S-H.

Figure 9-5. Bond strength between new binder and steel

Figure 9-6 shows the decrease in density of C-S-H with the incorporation of SBR. The density of neat C-S-H is in the same range reported by other researchers (Alizadeh et al. 2011; Foley et al. 2012). Material property charts allow C-S-H to be categorized and compared with other materials in the material performance chart. Material property charts for C-S-H with various SBR contents are established using elastic modulus and density as shown in Figure 9-7. Figure 9-7 also shows the C-S-H neat samples located in a different region than a cluster of C-S-H incorporating. The neat C-S-H falls in the nontechnical ceramic classification which includes concrete, ceramics, and clay bricks. The samples incorporating SBR fall in between the concrete and polymers material classification (Ashby 2017). This is indicative of a material performance deviation and directly correlates to the low modulus and high ultimate strength of C-S-H incorporating SBR. These observations demonstrate the ability to engineer new species of polymer-silica binders with physical and mechanical characteristics that is desired for wellbore applications and might be of interest to other engineering applications.

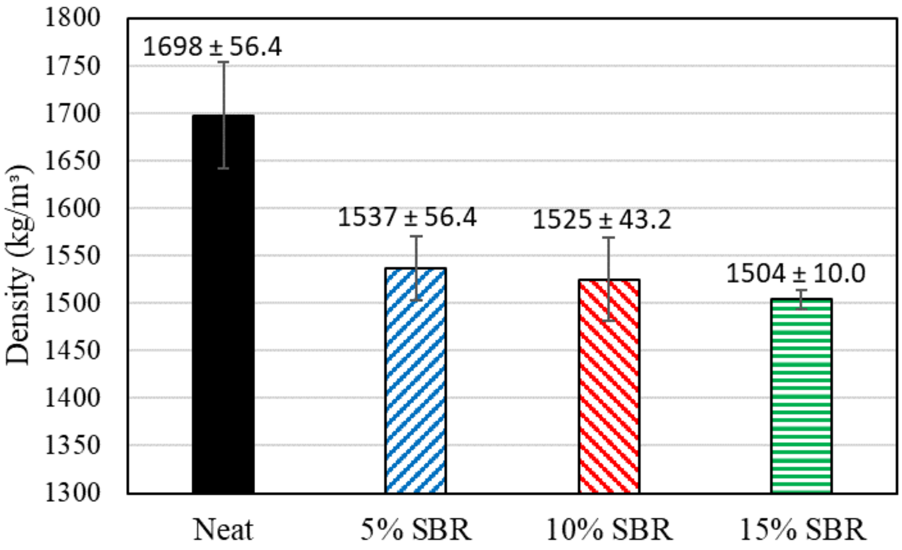

Figure 9-6. Density measurements of C-S-H with standard deviation

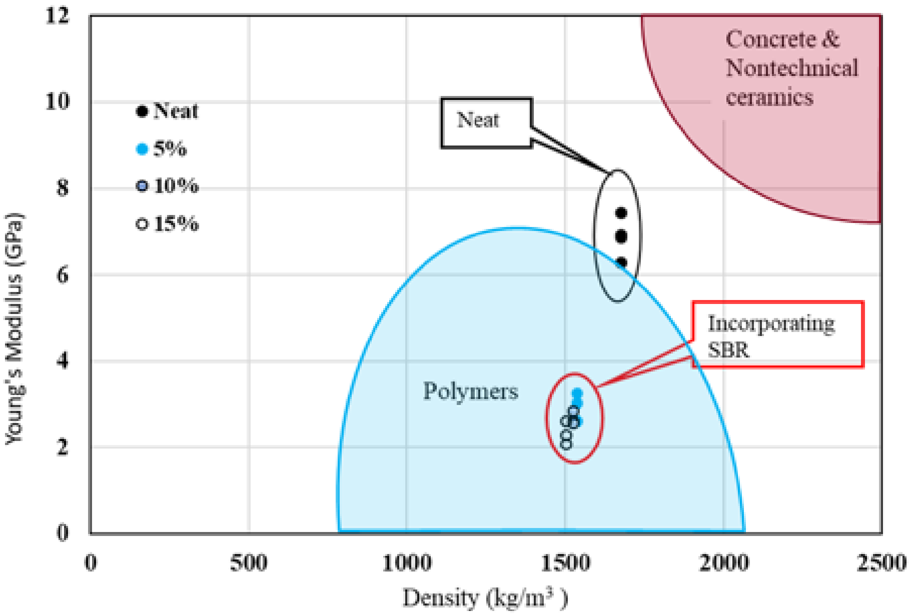

Figure 9-7. Material performance indices for C-S-H/ SBR composite with various SBR contents compared with neat C-S-H

TGA curves shown in Figure 8 for synthetic C-S-H incorporating SBR show a suppressed chemical reaction with high SBR content, resulting in less C-S-H product after the 7 days of mixing. Figure 9-8 shows the formation of C-S-H to be hindered by the addition of SBR. This observation agrees with previous models of cement modification with SBR reported by other researchers (Ohama 1995). On the other hand, the water content continues to increase as the SBR content increases. This observation is apparent in Table 9-1. This would appear to show that the SBR latex assists the C-S-H in retaining the inner water layer that is chemically bonded to the crystalline structure. The polymer film slows the overall calcium-silica reaction, lessens the C/S quantity, and increases the absorbed inner layer of water. TGA analysis shows the 20% reduction of the C/S stoichiometric quantities as SBR content increases. This observation can be attributed to a well documented phenomenon that happens in latex modified cements, as polymer particles inhibit the hydration of the cement particles by creating a polymer film (Van Gemert and Beeldens 2013). It is thought to be a similar effect on the formation of C-S-H inhibited by the physical attachment of SBR particles to the crystalline structure of C-S-H. Furthermore, CH contents had a modest rise with the increase of SBR and $CaCO_3$ contents remained steady throughout the samples.

Table 9-1. Standard dried C-S-H composition from TGA and estimated stoichiometric formula

SBR Content	Mass Loss (145°C–350°C)(%)	C/S	x	Mass Loss (350°C–500°C)(%)	CH Content %	Mass Loss (600°C–825°C)(%)	$CaCO_3$ Content %
Neat	7.26	1.23	0.690	2.89	10.6	2.45	2.2
5%	6.31	1.12	0.590	4.10	12.9	1.54	1.9
10%	8.52	1.01	0.850	4.95	13.6	2.81	2.7
15%	8.44	0.94	0.829	5.66	14.4	1.89	2.2

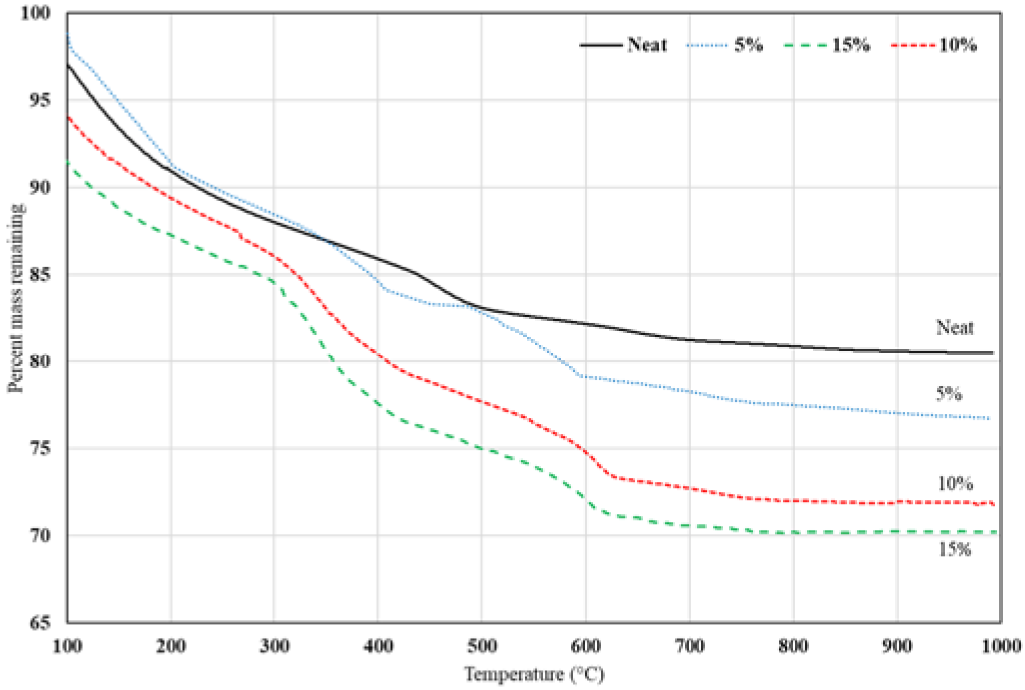

Figure 9-8. TGA curves for C-S-H incorporating SBR with varying amounts of SBR

XRD measurements as demonstrated in Figure 9-9 showed typical peaks representing C-S-H phases along with CH. Outcomes were confirmed by comparison with published results (Kim et al. 2013).

The formation of the crystalline structure of C-S-H have negligible change as the SBR content increases. Peaks at 29°, 32°, and 48° represent the formation of C-S-H and coincide with previous investigations (Kim et al. 2013; Jain and Neithalath 2009). The presence of CH is represented by slim spikes at 18° and 34°. Due to the peaks for $CaCO_3$ occurring at 29.5°, XRD analysis typically does not pick up indications of $CaCO_3$. Other signals of $CaCO_3$ are lost in background noise. Peaks obtained from the XRD spectra for C/S=1.5 matched well with published results (Kim et al. 2013).

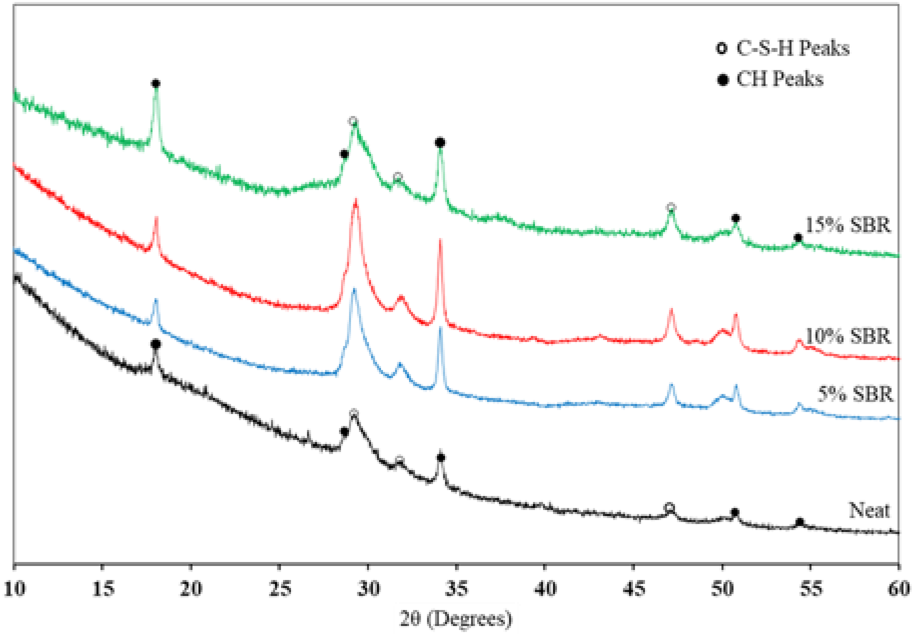

NOTE: Slim peaks at 18° and 34° represent CH and the peaks at 29° and 32° represent C-S-H.

Figure 9-9. XRD analysis spectrum of neat C-S-H and C-S-H incorporating varying amounts of SBR

NMR spectra of C-S-H neat and with varying amounts of SBR depicted in Figure 9-10. The vertical lines at -78.9, -82.6, and -85 ppm represent crystalline connectivity at correlating to Q^1, Q^2_b, and Q^2 silicate connections respectively (Kim et al. 2013). Deconvolution analysis was performed to determine the approximate fractions of each crystalline phase and can also be seen in Figure 9-10.

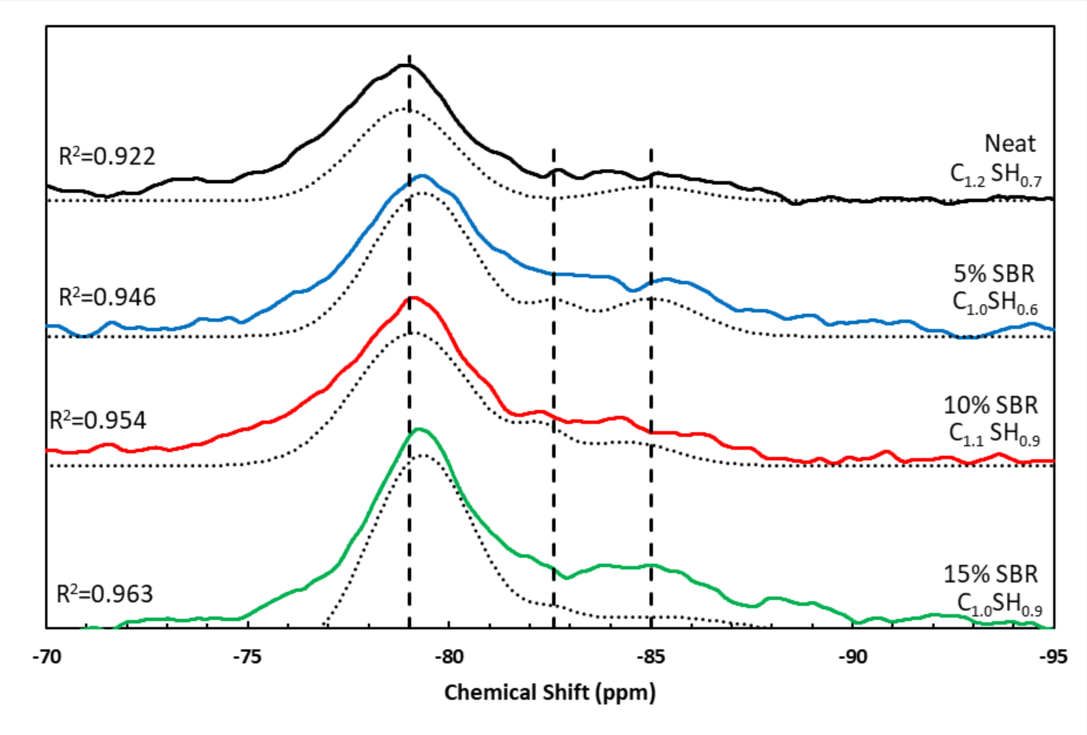

Figure 9-10. ^{29}Si solid state NMR Spectra with deconvolution curves (dotted line)

The negative chemical shifts at Q^1 and Q^2 sites, associated with the SBR content increases, may indicate an increase in the degree of silicate tetrahedra polymerization (Alizadeh 2009). The results of deconvolution analysis of ^{29}Si MAS NMR spectra are presented in Table 9-2. Values of silicate end chains, represented by Q^1, also increased along with Q^2_b signals as SBR content increased. This is thought to happen as the interlayer of water assists in forming new Q^2 and Q^2_b chains. Q^2_b represents a single bridging site creating a middle tetrahedron in the C-S-H chain that links the Q^2 species and chain-end Q^1 (Le Saout et al. 2004; Li et al. 2019). As the inner layer of water becomes trapped, due to the polymer film, the dissipation of the inner water layer creates shielding and crosslinking mechanisms between the C-S-H layers, resulting in more Q^2 formations (Alizadeh 2009). Mean chain lengths (L) remained constant at 2.81±0.07 while values of n_c, representing a high degree of C-S-H polymerization, decreased from 1.97 to 1.28 with the increase of SBR content and coincides with published results (Kim et al. 2013).

Table 9-2. Q^n intensities extracted from deconvolution of ^{29}Si MAS NMR spectra

C-S-H Formula	SBR %	Q^1	Q^2_b	Q^2	Q^2/Q^1	n_c	L
$C_{1.2}\ SH_{0.7}$	0%	0.695	--	0.305	0.439	1.97	2.88
$C_{1.0}SH_{0.6}$	5%	0.706	0.178	0.115	0.163	1.29	2.83
$C_{1.1}\ SH_{0.9}$	10%	0.714	0.178	0.107	0.150	1.29	2.80

C-S-H Formula	SBR %	Q^1	Q^2_b	Q^2	Q^2/Q^1	n_c	L
$C_{1.0}SH_{0.9}$	15%	0.730	0.090	0.180	0.246	1.27	2.74

To further explain the improvement in mechanical properties, SEM images of the fractured surface was investigated. SEM images for neat C-S-H and C-S-H incorporating 15% SBR are shown in Figure 9-11. SEM imagery provided some visual insight for the physical effects of SBR on the fracture characteristics of C-S-H incorporating SBR. Microcracks were observed on the fracture surface of the specimens after DMA testing. When comparing the fractured surface of neat C-S-H with C-S-H incorporating 15% SBR (Figure 9-11(b) to Figure 9-11(c)), it is noted that SBR films are bridging the microcracks, leading to improvements in ductility and strength. Figure 9-11(c) provides a close-up of a micro-fracture, giving a perspective on how effective SBR is at limiting the propagation of the micro-cracks enabling the composite C-S-H-SBR to continue carrying loads and provide a relatively high strain at failure.

The above work introduces a new binder for wellbore applications that has never been used before. The above investigation showed that the new C-S-H/SBR composite has numerous favorable characteristics for wellbore applications including low elastic modulus and thus low stresses during cyclic and thermal operations, improved bond strength, improved tensile strength and significantly improved failure strain and toughness. All the above improvements suggest that the new low modulus C-S-H/SBR binder might be an excellent candidate for wellbore applications. The new binder might also be useful for other engineering applications with similar operational conditions. Further research is warranted to examine methods to create chemically bonded SBR to C-S-H to further improve the mechanical behavior of the material. It is important to note that the limited content of the SBR in the mix will limit the cost of the new binder. Considering the combined weight of CaO, SiO_2 with the recommended use of 10-15% SBR, a 15% increase in cost can be anticipated. In view of the significant reduction of probability of cracking of the new binder compared with current cementing technology, one can show such cost increase to be very marginal in wellbore applications.

Finally, a hypothesis to explain the chemical and mechanical response of C-S-H incorporating SBR is depicted in Figure 9-12. The proposed hypothesis is an adapted model from Ohama's 3-stage model for polymer concrete (PC; Ohama 1995). Figure 9-12 shows the nonuniform distribution of SBR particles on the initial mix of water, lime and silica that interact to form a crystalline structure (Phase 0). As the silica tetrahedra form and interact with the SBR particles, the propagation of the silicate chains is slowed as the polymer particles become attached to the crystalline structure described by Phase 1 and 2. Phase 3 describes the condition of a fully developed polymer film coating C-S-H, reducing the reaction and resulting in limiting C-S-H production. This results in the new C-S-H/SBR composite with low elastic modulus and improved properties including improved bond, reduced elastic modulus and high failure strain. The new proposed synthesis method and binder might open the door for a new family of silica/polymer binders for other engineering applications that would benefit from low modulus binder with improved mechanical behavior.

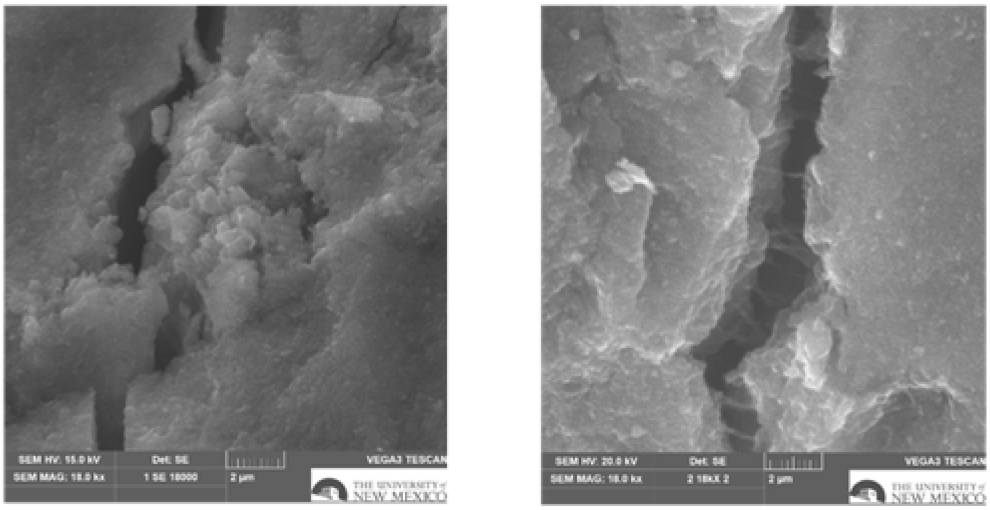

a) C-S-H neat **b)** C-S-H w/ 15% SBR

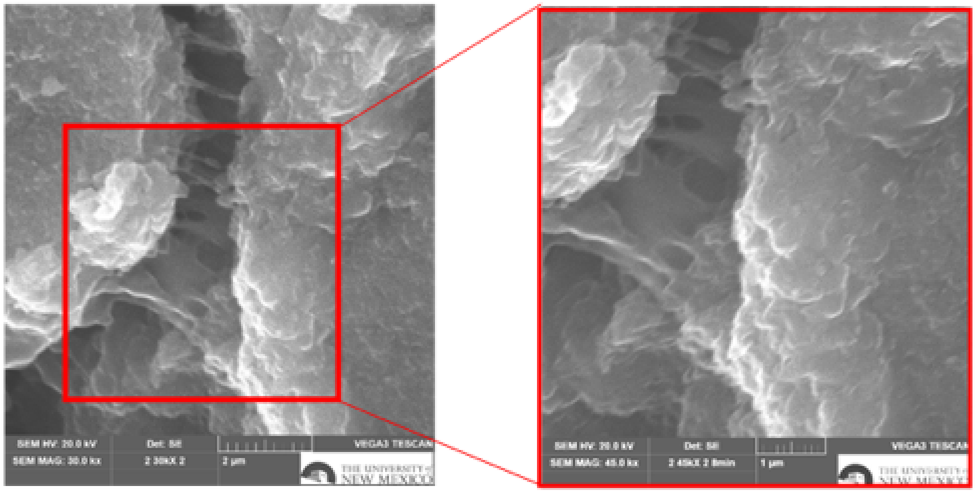

c). SBR latex bridging microcracks with close up

Figure 9-11. (a)–(c) SEM micrographs of fractured surface of C-S-H incorporating SBR

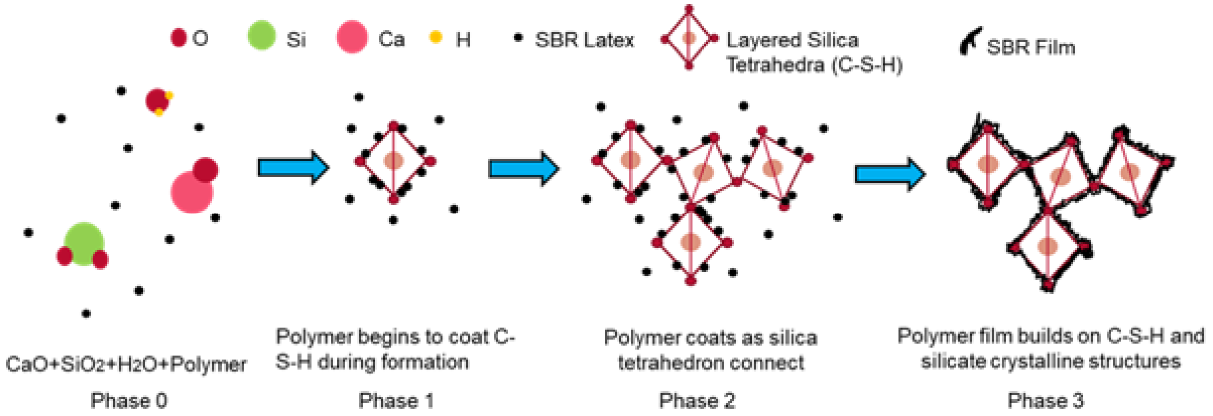

Figure 9-12. Schematic representation of SBR film inhibiting the formation of C-S-H

9.5. Conclusions

C-S-H was synthesized from a C/S ratio of 1.5 to mimic C-S-H formed in OWC applications. The synthetic C-S-H was dried to 11% RH, compacted to 400 MPa and characterized by various methods. Mechanical properties acquired from DMA and direct shear testing, along with chemical properties from TGA and microstructural characteristics with XRD analysis, ^{29}Si MAS NMR and SEM were acquired to characterize the effect due to incorporating SBR latex. DMA results showed the ability to control Young's modulus of elasticity while increasing the ultimate tensile strength capacity and toughness of C-S-H. The material performance indices of specimens containing SBR showed a clear deviation from the neat specimens. Neat C-S-H lies in the concrete classification and the C-S-H/SBR composite lies between the concrete and polymer regions on the material classification index. Chemical analysis confirmed the formation of C-S-H occurred and was inhibited by the addition of SBR. TGA curves also revealed the inhibited formation of the C-S-H structure had an increase of attached inner water layers. XRD analysis did not display any adverse effect on the C-S-H formation due to the addition of SBR. NMR spectra displayed a negative shift for C-S-H with SBR indicating a higher degree of silicate polymerization. Furthermore, SEM imagery shows SBR particles spanning the microcracks on the fracture surface, providing insight on the enhanced mechanical properties of the new C-S-H/SBR binder. The above work demonstrates the ability to engineer a new low-modulus binder for wellbore applications with improved mechanical properties with the addition of various amounts SBR during C-S-H synthesis. The new binder has a lower probability of cracking and debonding from the steel casing in wellbores compared with current cements used in wellbore applications.

9.6. Acknowledgments

The authors would also like to thank Dr. Hien, Dr. Eric Peterson, Mike Spidle and Dr. Karen Ann Smith from the University of New Mexico and Dr. Usama Kandil from Egyptian Petroleum Research Institute with their help in conducting the microstructural analysis. The authors greatly acknowledge this support. We thank David Sassani for providing a technical review of this work.

REFERENCES

Section 1

Berner, U. R. (1992). Evolution of pore water chemistry during degradation of cement in a radioactive waste repository environment. Waste Management, 12, p. 201-219.

Pabalan, R. T., F. P. Glasser, D. A. Pickett, G. R. Walter, S. Biswas, M. R. Juckett, L. M. Sabido, and J. L. Myers (2009). Review of Literature and Assessment of Factors Relevant to Performance of Grouted Systems for Radioactive Waste. CNWRA 2009-001. Center for Nuclear Waste Regulatory Analyses, San Antonio, TX.

Kutchko, B.G., Strazisar, B.R., Dzombak, D.A., Lowry, G.V., and N. Thaulow (2007). Degradation of well cement by CO_2 under geologic sequestration conditions. Environmental Science & Technology 41.13, pp. 4787–4792.

Matteo, E.N. and G. W. Scherer (2012). Experimental study of the diffusion controlled acid degradation of Class H Portland cement. International Journal of Greenhouse Gas Control 7, pp. 181–191.

Carey, J.W., K. Lewis, S. Kelkar, and G. A. Zyvoloski (2013). Geomechanical Behavior of Wells in Geologic Sequestration. In: Energy Procedia 37, pp. 5642–5652.

Hansen, F. D. and M. K. Knowles (2000). Design and analysis of a shaft seal system for the Waste Isolation Pilot Plant. Reliability Engineering and System Safety, 69, 87-98.

Blanco-Martín, L., R. Wolters, J. Rutqvist, K-H. Lux, and J. T. Birkholzer (2016). Thermal-hydraulic-mechanical modeling of a large-scale heater test to investigate rock salt and crushed salt behavior under repository conditions for heat-generating waste. Computers and Geotechnics, 77, 120-133.

Sobolik, S. R., S. P. Gomez, E. N. Matteo, T. A. Dewers, P. Newell, M. Reda Taha, J. C. Stormont (2015). Geomechanical Modeling to Predict Wellbore Stresses and Strains for the Design of Wellbore Seal Repair Materials for Use at a CO2 Injection Site. *Proceedings of the 49th US Rock Mechanics / Geomechanics Symposium held in San Francisco*, CA, USA, 28 June – 1 July 2015.

Gajo, A., F. Cecinato, and T. Hueckel (2015). A micro-scale inspired chemo-mechanical model of bonded geomaterials. International journal of Rock Mechanics and Mining Sciences, 80, 425-438

Hu, L. B. and T. Hueckel (2007). Coupled chemo-mechanics of intergranular contact: Toward a three-scale model. Computers and Geotechnics, 34, 306-327.

Dewers, T., Newell, P, Broome, S, Heath, J, and Bauer, S, (2014), Geomechanical Behavior of Cambrian Mount Simon Sandstone Lithofacies, Iowa Shelf, USA. International Journal of Greenhouse Gas Control, 21, 33-48.

Genedy, M, Kandil, U, Stormont, J, Matteo, E, Reda Taha, MM (2016), A new polymer nanocomposite repair material for restoring wellbore seal integrity. International Journal of Greenhouse Gas, Submitted for review.

Stormont, J.C., Ahamd, R., Ellison, J., Reda Taha, M., and Matteo, E.N., 2015. Laboratory measurements of flow through wellbore cement-casing microannuli. In: ARMA 15-294, Proceedings of the 49th US Rock Mechanics-Geomechanics Symposium, San Francisco, CA, USA. American Rock Mechanics Association.

Section 2

J.W. Carey, M. Wigand, S.J. Chipera, G. WoldeGabriel, R. Pawar, P.C. Lichtner, S.C. Wehner, M.A. Raines, G.D. Guthrie, Int. J. Greenh. Gas Control 1 (2007) 75

H.B. Shao, J.R. Ray, Y.S. Jun, Environ. Sci. Technol. 44 (2010) 5999.

A. Allahverdi, F. Skvara, Ceram.-Silik. 44 (2000) 114.

W. Crow, J.W. Carey, S. Gasda, D.B. Williams, M. Celia, Int. J. Greenh. Gas Control 4 (2010) 186.

Y.S. Jun, D.E. Giammar, C.J. Werth, Environ. Sci. Technol. 47 (2013) 3.

B.G. Kutchko, B.R. Strazisar, D.A. Dzombak, G.V. Lowry, N. Thaulow, Environ. Sci. Technol. 41 (2007) 4787.

Matteo, E.N. and G.W. Scherer. 2012. "Experimental study of the diffusion-controlled acid degradation of Class H Portland cement," *International Journal of Greenhouse Gas Control* 7 (March): 181–191.

B.G. Kutchko, B.R. Strazisar, S.B. Hawthorne, C.L. Lopano, D.J. Miller, J.A. Hakala, G.D. Guthrie, Int. J. Greenh. Gas Control 5 (2011) 880.

J.W. Bullard, H.M. Jennings, R.A. Livingston, A. Nonat, G.W. Scherer, J.S. Schweitzer, K.L. Scrivener, J.J. Thomas, Cem. Concr. Res. 41 (2011) 1208.

George W. Scherer, Michael A. Celia, Jean-Herve Prevost, Stefan Bachu, Robert Bruant, Andrew Duguid, Richard Fuller, Sarah E. Gasda, Mileva Radonjic and Wilasa Vichit-Vadakan
Carbon Dioxide Capture for Storage in Deep Geologic Formations – Results from the CO2 Capture Project Geologic Storage of Carbon Dioxide with Monitoring and Verification - Volume 2
Edited by: Sally M. Benson, Lawrence Berkeley Laboratory, Berkeley, CA, USA

A. Duguid, Energy Procedia (2009) 8.

Q.Y. Li, Y.M. Lim, K.M. Flores, K. Kranjc, Y.S. Jun, Environ. Sci. Technol. 49 (2015) 6335.

Xiao Zhen, You Yong, Xu Chun Guang, Robotics and Computer-Integrated Manufacturing (2017)

Walsh, S. D., Mason, H. E., Frane, W. L., & Carroll, S. A. (2014). Mechanical and hydraulic coupling in cement–caprock interfaces exposed to carbonated brine. *International Journal of Greenhouse Gas Control, 25*

Zhang, J., & Scherer, G. W. (2011). Comparison of methods for arresting hydration of cement. *Cement and Concrete Research,41*(10)

Fetter, C. W. (2014). Applied hydrogeology: Pearson new international edition. Edinburgh: Pearson education.

Section 3

ASTM A. 305-14 Standard practice for mechanical mixing of hydraulic cement pastes and mortars of plastic consistency ASTM C305-14. ASTM Int West Conshohocken PA. 2014. www.astm.org.

Axelsson, M., G. Gustafson, and Å Fransson. 2009. Stop mechanism for cementitious grouts at different water-to-cement ratios. Tunn Undergr Space Technol. 2009;24(4):390-397. doi:10.1016/j.tust.2008.11.001.

Bachu, S., and D. B. Bennion. 2009. Experimental assessment of brine and/or CO2 leakage through well cements at reservoir conditions. Int J Greenh Gas Control. 2009;3(4):494-501. doi:10.1016/j.ijggc.2008.11.002.

Baghbanan, A., and L. Jing. 2008. Stress effects on permeability in a fractured rock mass with correlated fracture length and aperture. Int J Rock Mech Min Sci. 2008;45(8):1320-1334. doi:10.1016/j.ijrmms.2008.01.015.

Bandis, S. C., A. C. Lumsden, and N. R. Barton. 1983. Fundamentals of rock joint deformation. Int J Rock Mech Min Sci Geomech Abstr. 1983;20(6):249-268. doi:10.1016/0148-9062(83)90595-8.

Bellabarba, M., H. Bulte-Loyer, B. Froelich, S. Le Roy-Delage, R. van Kuijk, S. Zeroug, D. Guillot, N. Moroni, S. Pastor, and A. Zanchi. 2008. Ensuring zonal isolation beyond the life of the well. Oilfield Rev. 2008;20(1):18–31.

Berkowitz, B. 2002. Characterizing flow and transport in fractured geological media: A review. Adv Water Resour. 2002;25(8):861-884. doi:10.1016/S0309-1708(02)00042-8.

Bois, A.-P., A. Garnier, F. Rodot, J. Sain-Marc, and N. Aimard. 2011. How to prevent loss of zonal isolation through a comprehensive analysis of microannulus formation. SPE Drill Complet. 2011;26(01):13-31. doi:10.2118/124719-PA.

Bonett, A., and D. Pafitis. 1996. Getting to the root of gas migration. Oilfield Rev. 1996;8(1):36–49.

Boukhelifa, L., N. Moroni, S. G. James, S. Le Roy-Delage, M. J. Thiercelin, and G. Lemaire. 2004. Evaluation of cement systems for oil and gas well zonal isolation in a full-scale annular geometry. SPE Paper 87195; 2004. doi:10.2118/87195-MS.

Bourgoyne, A. T., S. L. Scott, and J. B. Regg. 1999. Sustained casing pressure in offshore producing wells. In: Offshore Technology Conference; 1999. doi:10.4043/11029-MS.

Brufatto, C., J. Cochran, L. Conn, D. Power, S. Z. A. A. El-Zeghaty, B. Fraboulet, T. Griffin, S. James, T. Munk, and F. Justus. 2003. From mud to cement—building gas wells. Oilfield Rev. 2003;15(3):62–76.

Carroll, S. A., J. Iyer, and S. D. C. Walsh. 2017. Influence of chemical, mechanical, and transport processes on wellbore leakage from geologic CO2 storage reservoirs. Acc Chem Res. 2017;50(8):1829-1837. doi:10.1021/acs.accounts.7b00094.

Celia, M. A., J. M. Nordbotten, B. Court, M. Dobossy, and S. Bachu. 2011. Field-scale application of a semi-analytical model for estimation of CO2 and brine leakage along old wells. Int J Greenh Gas Control. 2011;5(2):257-269. doi:10.1016/j.ijggc.2010.10.005.

Checkai, D., S. Bryant, and Q. Tao. 2013. Towards a frequency distribution of effective permeabilities of leaky wellbores. Energy Procedia. 2013;37:5653-5660. doi:10.1016/j.egypro.2013.06.487.

Crow, W., J. W. Carey, S, Gasda, D. Brian Williams, and M. A. Celia. 2010. Wellbore integrity analysis of a natural CO2producer. Int J Greenh Gas Control. 2010;4(2):186-197. doi:10.1016/j.ijggc.2009.10.010.

Davies, R. J., S. Almond, R. S. Ward, R. B. Jackson, C. Adams, F. Worrall, L. G. Herringshaw, J. G. Gluyas, and M. A. Whitehead. 2014. Oil and gas wells and their integrity: Implications for shale and unconventional resource exploitation. Mar Pet Geol. 2014;56:239-254. doi:10.1016/j.marpetgeo.2014.03.001.

DeBruijn, G. G., A. Garnier, R. Brignoli, D. C. Bexte, and D. Reinheimer. 2009. Flexible Cement Improves Wellbore Integrity in SAGD Wells. SPE Paper 119960; 2009. doi:10.2118/119960-MS.

Duguid, A., R. Butsch, J. W. Carey, M. A. Celia, N. Chugunov, S. Gasda, T. S. Ramakrishnan, V. Stamp, and J. Wang. 2013. Pre-injection baseline data collection to establish existing wellbore leakage properties. Energy Procedia. 2013;37(Supplement C):5661-5672. doi:10.1016/j.egypro.2013.06.488.

Dusseault, M. B., M. N. Gray, and P. A. Nawrocki. 2000. Why oilwells leak: cement behavior and long-term consequences. SPE Paper 64733; 2000. doi:10.2118/64733-MS.

Dusseault, M. B., R. E. Jackson, and D. Macdonald. 2015. Towards a road map for mitigating the rates and occurrences of long-term wellbore leakage. Univ Waterloo Geofirma Eng LTD. 2014. http://geofirma.com/wp-content/uploads/2015/05/lwp-final-report_compressed.pdf.

Eklund, D., and H. Stille. 2008. Penetrability due to filtration tendency of cement-based grouts. Tunn Undergr Space Technol. 2008;23(4):389-398. doi:10.1016/j.tust.2007.06.011.

Feng, Y., X. Li, and K. E. Gray. 2017. Development of a 3D numerical model for quantifying fluid-driven interface debonding of an injector well. Int J Greenh Gas Control. 2017;62:76-90. doi:10.1016/j.ijggc.2017.04.008.

Forchheimer, P. H. 1901. Wasserbewegung durch boden. Zeitz Ver Duetch Ing. 1901;45:1782–1788.

Gasda, S. E., S. Bachu, M. A. and Celia. 2004. Spatial characterization of the location of potentially leaky wells penetrating a deep saline aquifer in a mature sedimentary basin. Environ Geol. 2004;46(6-7):707-720. doi:10.1007/s00254-004-1073-5.

Gasda, S. E., M. A. Celia, J. Z. Wang, and A. Duguid. 2013. Wellbore permeability estimates from vertical interference testing of existing wells. Energy Procedia. 2013;37(Supplement C):5673-5680. doi:10.1016/j.egypro.2013.06.489.

Gatlin, C. 1960. Petroleum engineering, drilling and well completions. ENGLEWOOD CLIFFS N J PRENTICE-HALL INC 1960 341 P. 1960.

Goodwin, K. J., and R. J. Crook. 1992. Cement sheath stress failure. SPE Drill Eng. 1992;7(04):291-296. doi:10.2118/20453-PA.

Gray, K. E., E. Podnos, and E. Becker. 2009. Finite-element studies of near-wellbore region during cementing operations: part I. SPE Drill Complet. 2009;24(01):127-136. doi:10.2118/106998-PA.

Hansen, T.-S., S. Roald, T. Nomeland, and B. Grant. 2003. Predictable and successful rock injection-the first time around A new improved system for cost-effective control of water in-leakage during tunnel excavation may reduce the need for expensive sandwich lining systems. Mater GEOENVIRONMENT. 2003;50:137–140.

Hawkes, C. D., P. J. McLellan, and S. Bachu. 2005. Geomechanical factors affecting geological storage of CO2 in depleted oil and gas reservoirs. J Can Pet Technol. 2005; 44(10). doi:10.2118/05-10-05.

Ingraffea, A. R., M. T. Wells, R. L. Santoro, and S. B. C. Shonkoff. 2014. Assessment and risk analysis of casing and cement impairment in oil and gas wells in Pennsylvania, 2000–2012. Proc Natl Acad Sci. 2014;111(30):10955-10960. doi:10.1073/pnas.1323422111.

Jackson, P. B., and C. E. Murphey. 1993. Effect of casing pressure on gas flow through a sheath of set cement. SPE Paper 25698; 1993. doi:10.2118/25698-MS.

Jackson, R. B. 2014. The integrity of oil and gas wells. Proc Natl Acad Sci. 2014;111(30):10902-10903. doi:10.1073/pnas.1410786111.

Jannot, Y., and D. Lasseux. 2012. A new quasi-steady method to measure gas permeability of weakly permeable porous media. Rev Sci Instrum. 2012;83(1):015113. doi:10.1063/1.3677846.

Javadi, M., M. Sharifzadeh, K. Shahriar, and Y. Mitani. 2014. Critical Reynolds number for nonlinear flow through rough-walled fractures: The role of shear processes. Water Resour Res. 2014;50(2):1789–1804.

Jorne, F., and F. M. A. Henriques. 2016. Evaluation of the grout injectability and types of resistance to grout flow. Constr Build Mater. 2016;122:171-183. doi:10.1016/j.conbuildmat.2016.06.032.

Kang, M., E. Baik, A. R. Miller, K. W. Bandilla, and M. A. Celia. 2015. Effective permeabilities of abandoned oil and gas wells: analysis of data from Pennsylvania. Environ Sci Technol. 2015;49(7):4757-4764. doi:10.1021/acs.est.5b00132.

King, G. E., and D. E. King. 2013. Environmental risk arising from well-construction failure--differences between barrier and well failure, and estimates of failure frequency across common well types, locations, and well age. SPE Prod Oper. 2013;28(04):323-344. doi:10.2118/166142-PA.

Kjøller, C., M. Torsæter, A. Lavrov, and P. Frykman. 2016. Novel experimental/numerical approach to evaluate the permeability of cement-caprock systems. Int J Greenh Gas Control. 2016;45(Supplement C):86-93. doi:10.1016/j.ijggc.2015.12.017.

Lange, D. A., H. M. Jennings, and S. P. Shah. 1993. Relationship between fracture surface roughness and fracture behavior of cement paste and mortar. J Am Ceram Soc. 1993;76(3):589-597. doi:10.1111/j.1151-2916.1993.tb03646.x.

Lavasani, S. M., N. Ramzali, F. Sabzalipour, and E. Akyuz. 2015. Utilisation of fuzzy fault tree analysis (FFTA) for quantified risk analysis of leakage in abandoned oil and natural-gas wells. Ocean Eng. 2015;108:729-737. doi:10.1016/j.oceaneng.2015.09.008.

Lavrov, A., Todorovic J, Torsæter M. Numerical study of tensile thermal stresses in a casing-cement-rock system with heterogeneities. In: American Rock Mechanics Association; 2015. https://www.onepetro.org/conference-paper/ARMA-2015-110. Accessed September 10, 2017.

Lecampion B, Bunger A, Kear J, Quesada D. Interface debonding driven by fluid injection in a cased and cemented wellbore: Modeling and experiments. Int J Greenh Gas Control. 2013;18:208-223. doi:10.1016/j.ijggc.2013.07.012.

LeNeveu DM. Analysis of potential acid gas leakage from wellbores in Alberta, Canada. Int J Greenh Gas Control. 2011;5(4):862-879. doi:10.1016/j.ijggc.2011.01.009.

Manceau JC, Tremosa J, Audigane P, Lerouge C, Claret F, Lettry Y, Fierz T, Nussbaum C. Well integrity assessment under temperature and pressure stresses by a 1:1 scale wellbore experiment. Water Resour Res. 2015;51(8):6093-6109. doi:10.1002/2014WR016786.

Mirza J, Saleh K, Langevin M-A, Mirza S, Bhutta MAR, Tahir MM. Properties of microfine cement grouts at 4°C, 10°C and 20°C. Constr Build Mater. 2013;47:1145-1153. doi:10.1016/j.conbuildmat.2013.05.026.

Miyazaki B. Well integrity: an overlooked source of risk and liability for underground natural gas storage. Lessons learned from incidents in the USA. Geol Soc Lond Spec Publ. 2009;313(1):163-172. doi:10.1144/SP313.11.

National Academies of Sciences E. Characterization, Modeling, Monitoring, and Remediation of Fractured Rock.; 2015. doi:10.17226/21742.

Nogues JP, Court B, Dobossy M, Nordbotten JM, Celia MA. A methodology to estimate maximum probable leakage along old wells in a geological sequestration operation. Int J Greenh Gas Control. 2012;7:39-47. doi:10.1016/j.ijggc.2011.12.003.

Nowamooz A, Radilla G, Fourar M. Non-Darcian two-phase flow in a transparent replica of a rough-walled rock fracture. Water Resour Res. 2009;45(7):W07406. doi:10.1029/2008WR007315.

Orlic B. Some geomechanical aspects of geological CO2 sequestration. KSCE J Civ Eng. 2009;13(4):225-232. doi:10.1007/s12205-009-0225-2.

Rocha-Valadez T, Hasan AR, Mannan S, Kabir CS. Assessing wellbore integrity in sustained-casing-pressure annulus. SPE Drill Complet. 2014;29(01):131–138.

Roy P, Walsh SDC, Morris JP, Iyer J, Hao Y, Carroll S, Gawel K, Todorovic J, Torsæter M. Studying the impact of thermal cycling on wellbore integrity during CO2 injection. In: American Rock Mechanics Association; 2016. https://www.onepetro.org/conference-paper/ARMA-2016-668. Accessed September 20, 2017.

Rusch DW, Sabins F, Aslakson J. Microannulus Leaks Repaired with Pressure-Activated Sealant. SPE Paper 91399; 2004. doi:10.2118/91399-MS.

Saponja J. Surface casing vent flow and gas migration remedial elimination-new technique proves economic and highly successful. J Can Pet Technol. 1999;38(13). doi:10.2118/99-13-06.

Schreppers G. A framework for wellbore cement integrity analysis. In: 49th US Rock Mechanics/Geomechanics Symposium. American Rock Mechanics Association; 2015. https://www.onepetro.org/conference-paper/ARMA-2015-349.

Seidel FA, Greene TG. Use of expanding cement improves bonding and aids in eliminating annular gas migration in Hobbs Grayburg-San Andres wells. SPE Paper 14434; 1985. doi:10.2118/14434-MS.

Shadravan A, Ghasemi M, Alfi M. Zonal isolation in geothermal wells. In: Fortieth Workshop on Geothermal Reservoir Engineering. ; 2015:26–28. https://www.researchgate.net/profile/Mohammadreza_Ghasemi4/publication/281050519_Zonal_Isolation_in_Geothermal_Wells/links/55d2b33408aec1b0429ef1fa.pdf.

Southon JN. Geothermal well design, construction and failures. In: Proceedings World Geothermal Congress. ; 2005:24–29.

Tipler PA, Mosca G. Physics for Scientists and Engineers. Macmillan; 2007.

van Thienen-Visser K, Hendriks D, Marsman A, Nepveu M, Groenenberg R, Wildenborg T, van Duijne H, den Hartogh M, Pinkse T. Bow-tie risk assessment combining causes and effects applied to gas oil storage in an abandoned salt cavern. Eng Geol. 2014;168:149-166. doi:10.1016/j.enggeo.2013.11.002.

Vidic RD, Brantley SL, Vandenbossche JM, Yoxtheimer D, Abad JD. Impact of shale gas development on regional water quality. Science. 2013;340(6134):1235009. doi:10.1126/science.1235009.

Viswanathan HS, Pawar RJ, Stauffer PH, Kaszuba JP, Carey JW, Olsen SC, Keating GN, Kavetski D, Guthrie GD. Development of a hybrid process and system model for the assessment of wellbore leakage at a geologic CO2 sequestration site. Environ Sci Technol. 2008;42(19):7280-7286. doi:10.1021/es800417x.

Vrålstad T, Skorpa R, Opedal N, De Andrade J. Effect of thermal cycling on cement sheath integrity: realistic experimental tests and simulation of resulting leakages. SPE Paper 178467; 2015. doi:10.2118/178467-MS.

Wang H, Tao G, Shang X. Understanding acoustic methods for cement bond logging. J Acoust Soc Am. 2016;139(5):2407-2416. doi:10.1121/1.4947511.

Watson TL, Bachu S. Identification of wells with high CO2-leakage potential in mature oil fields developed for CO2-enhanced oil recovery. SPE Paper 112924; 2008. doi:10.2118/112924-MS.

Witherspoon PA, Wang JSY, Iwai K, Gale JE. Validity of Cubic Law for fluid flow in a deformable rock fracture. Water Resour Res. 1980;16(6):1016-1024. doi:10.1029/WR016i006p01016.

Zhang M, Bachu S. Review of integrity of existing wells in relation to CO2 geological storage: What do we know? Int J Greenh Gas Control. 2011;5(4):826-840. doi:10.1016/j.ijggc.2010.11.006.

Zhang W, Eckert A, Liu X. Numerical simulation of micro-annuli generation by thermal cycling. In: American Rock Mechanics Association; 2017. https://www.onepetro.org/conference-paper/ARMA-2017-0354.

Zhang Z, Nemcik J. Fluid flow regimes and nonlinear flow characteristics in deformable rock fractures. J Hydrol. 2013;477:139-151. doi:10.1016/j.jhydrol.2012.11.024.

Zimmerman RW, Bodvarsson GS. Hydraulic conductivity of rock fractures. Transp Porous Media. 1996;23(1):1-30. doi:10.1007/BF00145263.

Section 4

Akhavan, A., S.-M.-H. Shafaatian, F. Rajabipour, Quantifying the effects of crack width, tortuosity, and roughness on water permeability of cracked mortars, Cement and Concrete Research 42 (2) (2012) 313–320. doi:10.1016/j.cemconres.2011.10.002.

API, Specification for Cements and Materials for Well Cementing. API Specification 10a: American Petroleum Institute, Washington, DC (2009).

Asadollahi, P. Stability analysis of a single three dimensional rock block: effect of dilatancy and high- velocity water jet impact, Ph.D. thesis, University of Texas at Austin (2009).

ASTM. 2014. ASTM, 305-14 Standard practice for mechanical mixing of hydraulic cement pastes and mortars of plastic consistency ASTM C305-14, ASTM International, West Conshohocken, PA (2014).

Axelsson, M., G. Gustafson, A. Fransson, Stop mechanism for cementitious grouts at different water-to-cement ratios, Tunnelling and Underground Space Technology 24 (4) (2009) 390–397. doi:10.1016/j.tust.2008.11.001.

Bachu, S., D. B. Bennion, Experimental assessment of brine and/or CO_2 leakage through well cements at reservoir conditions, International Journal of Greenhouse Gas Control 3 (4) (2009) 494–501. doi:10.1016/j.ijggc.2008.11.002.

Barton, C. C., P. A. Hsieh, Physical and hydrologic-flow properties of fractures, in: 28th International Geological Congress Field Trip Guidebook, Vol. 385, 1989, p. 36.

Bellabarba, M., H. Bulte-Loyer, B. Froelich, S. Le Roy-Delage, R. van Kuijk, S. Zeroug, D. Guillot, N. Moroni, S. Pastor, A. Zanchi, Ensuring zonal isolation beyond the life of the well, Oilfield Review 20 (1) (2008) 18–31.

Berest, P., B. Brouard, M. Karimi-Jafari, L. Van Sambeek, Transient behavior of salt caverns-interpretation of mechanical integrity tests, International Journal of Rock Mechanics and Mining Sciences 44 (5) (2007) 767–786. doi:10.1016/j.ijrmms.2006.11.007.

Bianch, L. Permeability of crystalline rock interpreted from measured orientations and apertures of fractures, Analysis of Acid Zone 8 (2) (1968) 231–245.

Bielicki, J. M., M. F. Pollak, J. P. Fitts, C. A. Peters, E. J. Wilson, Causes and financial consequences of geologic CO_2 storage reservoir leakage and interference with other subsurface resources, International Journal of Greenhouse Gas Control 20 (2014) 272–284. doi:10.1016/j.ijggc.2013.10.024.

Bois, A.-P., A. Garnier, F. Rodot, J. Sain-Marc, N. Aimard, How to prevent loss of zonal isolation through a comprehensive analysis of microannulus formation, SPE Drilling & Completion 26 (01) (2011) 13–31. doi:10.2118/124719-PA.

Boukhelifa, L., N. Moroni, S. G. James, S. Le Roy-Delage, M. J. Thiercelin, G. Lemaire, Evaluation of cement systems for oil and gas well zonal isolation in a full-scale annular geometry, Society of Petroleum Engineers, 2004. doi:10.2118/87195-MS.

Brufatto, C., J. Cochran, L. Conn, D. Power, S. Z. A. A. El-Zeghaty, B. Fraboulet, T. Griffin, S. James, T. Munk, F. Justus, From mud to cementbuilding gas wells, Oilfield Review 15 (3) (2003) 62–76.

Carey, J. W., M. Wigand, S. J. Chipera, G. Wolde Gabriel, R. Pawar, P. C. Lichtner, S. C. Wehner, M. A. Raines, G. D. Guthrie Jr., Analysis and performance of oil well cement with 30 years of CO_2 exposure from the SACROC Unit, West Texas, USA, International Journal of Greenhouse Gas Control 1 (1) (2007) 75–85. doi:10.1016/S1750-5836(06)00004-1.

Checkai, D., S. Bryant, Q. Tao, Towards a frequency distribution of effective permeabilities of leaky wellbores, Energy Procedia 37 (2013) 5653–5660. doi:10.1016/j.egypro.2013.06.487.

Chilingar, G. V., B. Endres, Environmental hazards posed by the Los Angeles Basin urban oil-fields: an historical perspective of lessons learned, Environmental Geology 47 (2) (2005) 302–317. doi:10.1007/s00254-004-1159-0.

Crandall, D., G. Bromhal, Z. T. Karpyn, Numerical simulations examining the relationship between wall-roughness and fluid flow in rock fractures, International Journal of Rock Mechanics and Mining Sciences 47 (5) (2010) 784–796. doi:10.1016/j.ijrmms.2010.03.015.

Dagan, G. Higher-order correction of effective permeability of heterogeneous isotropic formations of lognormal conductivity distribution, Transport in Porous Media 12 (3) (1993) 279–290. doi:10.1007/BF00624462.

Davies, R. J., S. Almond, R. S. Ward, R. B. Jackson, C. Adams, F. Worrall, L. G. Herring- Shaw, J. G. Gluyas, M. A. Whitehead, Oil and gas wells and their integrity: Implications for shale and unconventional resource exploitation, Marine and Petroleum Geology 56 (2014) 239–254. doi:10.1016/j.marpetgeo.2014.03.001.

De Andrade, J., S. Sangesland, J. Todorovic, T. Vralstad, Cement sheath integrity during thermal cycling: A novel approach for experimental tests of cement systems, Society of Petroleum Engineers, 2015. doi:10.2118/173871-MS.

Duguid, A., J. W. Carey, R. Butsch, Well Integrity Assessment of a 68 year old well at a CO_2 injection project, Energy Procedia 63 (2014) 5691–5706. doi:10.1016/j.egypro.2014.11.602.

Dusseault, M. B., R. E. Jackson, D. Macdonald, Towards a road map for mitigating the rates and occurrences of long-term wellbore leakage, University of Waterloo Waterloo, ON, Canada, 2014.

Eklund, D. and H. Stille, Penetrability due to filtration tendency of cement-based grouts, Tunnelling andFeng, Y., X. Li, K. E. Gray, Development of a 3d numerical model for quantifying fluid-driven interface debonding of an injector well, International Journal of Greenhouse Gas Control 62 (2017) 76–90. doi:10.1016/j.ijggc.2017.04.008.

Forchheimer, P. H. Wasserbewegung durch boden, Zeitz. Ver. Duetch Ing. 45 (1901) 1782–1788.

Gale, J. E. Comparison of coupled fracture deformation and fluid flow models with direct measurements of fracture pore structure and stress-flow properties, American Rock Mechanics Association, 1987.

Gale, J. F., R. M. Reed, J. Holder, Natural fractures in the Barnett Shale and their importance for hydraulic fracture treatments, AAPG bulletin 91 (4) (2007) 603–622.

Gasda, S. E., S. Bachu, M. A. Celia, Spatial characterization of the location of potentially leaky wells penetrating a deep saline aquifer in a mature sedimentary basin, Environmental Geology 46 (6-7) (2004) 707–720. doi:10.1007/s00254-004-1073-5.

Gatlin, C. Petroleum engineering: drilling and well completions, Prentice-Hall Englewood Cliffs, NJ, USA, 1960.

Gentier, S. Morphologie et comportement hydromcanique d''une fracture naturelle dans le granite sous conrainte normale, BRGM, 1987.

Goodwin, K. J., R. J. Crook, Cement sheath stress failure, SPE Drilling Engineering 7 (04) (1992) 291–296. doi:10.2118/20453-PA.

Gray, K. E., E. Podnos, E. Becker, Finite-element studies of near-wellbore region during cementing operations: part I, SPE Drilling & Completion 24 (01) (2009) 127–136. doi:10.2118/106998-PA.

Hakami, E., E. Larsson, Aperture measurements and flow experiments on a single natural fracture, International Journal of Rock Mechanics and Mining Sciences & Geomechanics Abstracts 33 (4) (1996) 395–404. doi:10.1016/0148-9062(95)00070-4.

Huerta, N. J., S. L. Bryant, B. R. Strazisar, B. G. Kutchko, L. C. Conrad, The influence of confining stress and chemical alteration on conductive pathways within wellbore cement, Energy Procedia 1 (1) (2009) 3571–3578. doi:10.1016/j.egypro.2009.02.151.

Jackson, R. B., A. Vengosh, T. H. Darrah, N. R. Warner, A. Down, R. J. Poreda, S. G. Osborn, K. Zhao, J. D. Karr, Increased stray gas abundance in a subset of drinking water wells near Marcellus shale gas extraction, Proceedings of the National Academy of Sciences 110 (28) (2013) 11250–11255. doi:10.1073/pnas.1221635110.

Johns, R. A., J. S. Steude, L. M. Castanier, P. V. Roberts, Nondestructive measurements of fracture aperture in crystalline rock cores using X ray computed tomography, Journal of Geophysical Research: Solid Earth 98 (B2) (1993) 1889–1900. doi:10.1029/92JB02298.

Jorne, F., F. M. A. Henriques, Evaluation of the grout injectability and types of resistance to grout flow, Construction and Building Materials 122 (2016) 171–183. doi:10.1016/j.conbuildmat.2016.06.032.

Khishvand, M., A. H. Alizadeh, M. Piri, In-situ characterization of wettability and pore-scale displacements during two- and three-phase flow in natural porous media, Advances in Water Resources 97 (2016) 279–298. doi:10.1016/j.advwatres.2016.10.009.

Kjller, C., M. Torster, A. Lavrov, P. Frykman, Novel experimental/numerical approach to evaluate the permeability of cement-caprock systems, International Journal of Greenhouse Gas Control 45 (Supplement C) (2016) 86–93. doi:10.1016/j.ijggc.2015.12.017.

Lavrov, A., J. Todorovic, M. Torster, Numerical study of tensile thermal stresses in a casing-cement-rock system with heterogeneities, American Rock Mechanics Association, 2015.

Lecampion, B., A. Bunger, J. Kear, D. Quesada, Interface debonding driven by fluid injection in a cased and cemented wellbore: Modeling and experiments, International Journal of Greenhouse Gas Control 18 (2013) 208–223. doi:10.1016/j.ijggc.2013.07.012.

LeNeveu, D. M. Analysis of potential acid gas leakage from wellbores in Alberta, Canada, International Journal of Greenhouse Gas Control 5 (4) (2011) 862–879. doi:10.1016/j.ijggc.2011.01.009.

Mirza, J., K. Saleh, M.-A. Langevin, S. Mirza, M. A. R. Bhutta, M. M. Tahir, Properties of microfine cement grouts at 4 °C, 10 °C and 20 °C, Construction and Building Materials 47 (2013) 1145–1153. doi:10.1016/j.conbuildmat.2013.05.026.

Mitchell, J. K. Soil improvement-state of the art report, Proceedings, 11th International conference on SMFE (1981) 509–565.

Osborn, S. G., A. Vengosh, N. R. Warner, R. B. Jackson, Methane contamination of drinking water accompanying gas-well drilling and hydraulic fracturing, Proceedings of the National Academy of Sciences 108 (20) (2011) 8172–8176. doi:10.1073/pnas.1100682108.

Peng, S., J. Fu, J. Zhang, Borehole casing failure analysis in unconsolidated formations: A case study, Journal of Petroleum Science and Engineering 59 (3) (2007) 226–238. doi:10.1016/j.petrol.2007.04.010.

Piggott, Andrew R., Elsworth Derek, Laboratory assessment of the equivalent apertures of a rock fracture, Geophysical Research Letters 20 (13) (1993) 1387–1390. doi:10.1029/93GL01384.

Pruess, K., Y. W. Tsang, On two-phase relative permeability and capillary pressure of rough-walled rock fractures, Water Resources Research 26 (9) (1990) 1915–1926. doi:10.1029/WR026i009p01915

Renshaw, C. E. On the relationship between mechanical and hydraulic apertures in rough-walled fractures, Journal of Geophysical Research: Solid Earth 100 (B12) (1995) 24629–24636. doi:10.1029/95JB02159.

Sanei, M., L. Faramarzi, A. Fahimifar, S. Goli, A. Mehinrad, A. Rahmati, Shear strength of discontinuities in sedimentary rock masses based on direct shear tests, International Journal of Rock Mechanics and Mining Sciences 75 (2015) 119–131. doi:10.1016/j.ijrmms.2014.11.009.

Southon, J. N. Geothermal well design, construction and failures, Proceedings World geothermal congress (2005) 24–29.

Stormont, J. C., S. Garcia Fernandez, M. R. Taha, E. N. Matteo, Gas flow through cement-casing microannuli under varying stress conditions, Geomechanics for Energy and the Environment 13 (2018) 1–13. doi:10.1016/j.gete.2017.12.001.

Tolppanen, P., P. Syrjanen, Hard Rock Tunnel Grouting Practice in Finland, Sweden, and Norway-Literature Study, Finnish Tunnelling Association, 2003.

Tsang, Y. W., C. F. Tsang, Channel model of flow through fractured media, Water Resources Research 23 (3) (1987) 467–479. doi:10.1029/WR023i003p00467.

Underground Space Technology 23 (4) (2008) 389–398. doi:10.1016/j.tust.2007.06.011.

Vignes, B. Contribution to well integrity and increased focus on well barriers in a lifecycle aspect, Ph.D. thesis, Faculty of Science and Technology, University of Stavanger, Stavanger (2011).

Viswanathan, H. S., R. J. Pawar, P. H. Stauffer, J. P. Kaszuba, J. W. Carey, S. C. Olsen, G. N. Keating, D. Kavetski, G. D. Guthrie, Development of a hybrid process and system model for the assessment of wellbore leakage at a geologic CO_2 sequestration site, Environmental Science & Technology 42 (19) (2008) 7280–7286. doi:10.1021/es800417x.

Vralstad, T., R. Skorpa, N. Opedal, J. De Andrade, Effect of thermal cycling on cement sheath integrity: realistic experimental tests and simulation of resulting leakages, Society of Petroleum Engineers, 2015. doi:10.2118/178467-MS.

Wang, M., Y.-F. Chen, G.-W. Ma, J.-Q. Zhou, C.-B. Zhou, Influence of surface roughness on nonlinear flow behaviors in 3d self-affine rough fractures: Lattice Boltzmann simulations, Advances in Water Resources 96 (2016) 373–388. doi:10.1016/j.advwatres.2016.08.006.

Wang, W., A. Dahi Taleghani, Impact of hydraulic fracturing on cement sheath integrity; A modelling approach, Journal of Natural Gas Science and Engineering 44 (2017) 265–277. doi:10.1016/j.jngse.2017.03.036

Witherspoon, P. A., J. S. Y. Wang, K. Iwai, J. E. Gale, Validity of Cubic Law for fluid flow in a deformable rock fracture, Water Resources Research 16 (6) (1980) 1016–1024. doi:10.1029/WR016i006p01016.

Yuan, Z., J. Schubert, U. C. Esteban, P. Chantose, C. Teodoriu, Casing Failure Mechanism and Characterization under HPHT Conditions in South Texas, International Petroleum Technology Conference, 2013. doi:10.2523/IPTC-16704-MS.

Zeng, Z., R. Grigg, A Criterion for Non-Darcy Flow in Porous Media, Transport in Porous Media 63 (1) (2006) 57–69. doi:10.1007/s11242-005-2720-3.

Zhang, M., S. Bachu, Review of integrity of existing wells in relation to CO_2 geological storage: What do we know?, International Journal of Greenhouse Gas Control 5 (4) (2011) 826–840. doi:10.1016/j.ijggc.2010.11.006.

Zhang, W., A. Eckert, X. Liu, Numerical simulation of micro-annuli generation by thermal cycling, American Rock Mechanics Association, 2017.

Section 5

Alonso, E. and Olivella, S. (2006) Unsaturated soil mechanics applied to geotechnical problems, Unsaturated Soils 2006, pp. 1-35.

Alonso, E.E., Gens, A. and Josa, A. (1990) A Constitutive Model for Partially Saturated Soils. Geotechnique 40, 405-430.

Bartlett, R. A. and Gay, D. M. and Phipps, E. T.(2006). Automatic Differentiation of C++ Codes for Large-Scale Scientific Computing in International Conference on Computational Science 2006. Springer Berlin Heidelberg, edited by Alexandrov, V.N. and van Albada, G.D. and Sloot, P.M.A. amd Dongarra, J., p. 525-532.

Collin, F., Chambon, R. and Charlier, R. (2006) A finite element method for poro mechanical modelling of geotechnical problems using local second gradient models. International journal for numerical methods in engineering 65, 1749-1772.

Guimarães, L.d.N., Gens, A., Sanchez, M. and Olivella, S. (2006) THM and reactive transport analysis of expansive clay barrier in radioactive waste isolation. Communications in numerical methods in engineering 22, 849-859.

Hammond, G.E., Lichtner, P.C. and Mills, R.T. (2014) Evaluating the performance of parallel subsurface simulators: An illustrative example with PFLOTRAN. Water Resources Research 50, 208-228.

Heroux, M.A., Bartlett, R.A., Howle, V.E., Hoekstra, R.J., Hu, J.J., Kolda, T.G., Lehoucq, R.B., Long, K.R., Pawlowski, R.P. and Phipps, E.T. (2005) An overview of the Trilinos project. ACM Transactions on Mathematical Software (TOMS) 31, 397-423.

Karrech, A. (2013) Non-equilibrium thermodynamics for fully coupled thermal hydraulic mechanical chemical processes. Journal of the Mechanics and Physics of Solids 61, 819-837.

Kim, J. (2010) Sequential Methods for Coupled Geomechanics and Multiphase Flow. Stanford University.

Lichtner, P.C. (1996) Continuum formulation of multicomponent-multiphase reactive transport. Reviews in mineralogy 34, 1-82.

Lichtner, P.C., Steefel, C.I. and Oelkers, E.H. (2018) Reactive transport in porous media. Walter de Gruyter GmbH & Co KG.

Mikelić, A., Wang, B. and Wheeler, M.F. (2014) Numerical Convergence study of iterative coupling for coupled flow and geomechanics. COMP_GEOSCI 18, 325-341.

Olivella, S., Gens, A., Carrera, J. and Alonso, E. (1996) Numerical formulation for a simulator (CODE_BRIGHT) for the coupled analysis of saline media. Engineering computations 13, 87-112.

Rutqvist, J., Ijiri, Y. and Yamamoto, H. (2011) Implementation of the Barcelona Basic Model into TOUGH-FLAC for simulations of the geomechanical behavior of unsaturated soils. Comput Geosci 37, 751-762.

Salinger, A., Bartlett, R., Bradley, A., Chen, Q., Demeshko, I., Gao, X., Hanson, G., Mota, A., Muller, R., Nielsen, E., Ostien, J.T., Pawlowski, R.P., Perego, M., Phipps, E.T., Sun, W. and Tezaur, I.K. (2016) Albany: Using component-based design to develop a flexible, generic multiphysics analysis code. International Journal for Multiscale Computational Engineering.

Sanchez, M., Gens, A. and Olivella, S. (2010) Effect of thermo-coupled processes on the behaviour of a clay barrier submitted to heating and hydration. An Acad Bras Cienc 82, 153-168.

Slattery, S.R., Wilson, P.P.H. and Pawlowski, R.P. (2013) The Data Transfer Kit: A geometric rendezvous-based tool for multiphysics data transfer, Internationial Conference on Mathematics and Computational Methods Applied to Nuclear Science and Engineerying (M&C 2013).

Sun, W.-C., Ostien, J. and Salinger, A.G. (2013a) A stabilized assumed deformation gradient finite element formulation for strongly coupled poromechanical simulations at finite strain. Int. J. Numer. Anal. Meth. Geomech.

Sun, W. (2015) A stabilized finite element formulation for monolithic thermo-hydro-mechanical simulations at finite strain. INT_J_NUM_METH_ENG.

Sun, W., Ostien, J.T. and Salinger, A.G. (2013b) A stabilized assumed deformation gradient finite element formulation for strongly coupled poromechanical simulations at finite strain. INT_J_NUM_ANA_METH_GEO.

Terzaghi, K., Peck, R.B. and Mesri, G. (1996) Soil Mechanics in Engineering Practice. Wiley-Interscience.

Section 6

AASHTO, T316. (2013). Viscosity determination of asphalt binder using rotational viscometer. Washington, DC: AASHTO Standards.

Atta, A. M., Abdou, M. I., El-Sayed, A. A.. Ragab, M. E., (2008), New bisphenol novolac epoxy resins for marine primer steel coating applications, Progress in Organic Coatings, 63, 372-376

Baldan, A. (2004). Adhesively-bonded joints and repairs in metallic alloys, polymers and composite materials: Adhesives, adhesion theories and surface pretreatment. *J. of Mater. Sci., 39*(1), 1–49. doi:10.1023/b:jmsc.0000007726.58758.e4

Brand, J. Van der (2004). On the adhesion between aluminium and polymers, Ph.D. Thesis, Netherlands

Carey, J. W., Wigand, M., Chipera, S. J., WoldeGabriel, G., Pawar, R., Lichtner, P. C., and Guthrie, G. D. (2007). Analysis and performance of oil well cement with 30 years of CO2 exposure from the SACROC Unit, West Texas, USA. Int. J. of Greenhouse Gas Control. 1(1), 75–85. doi:10.1016/s1750-5836(06)00004-1

Celia, M., Bachu, S., Nordbotten, J., Gasda, S., and Dahle, H. (2005). Quantitative estimation of CO2 leakage from geological storageAnalytical models, numerical models, and data needs. Greenhouse Gas Control Technologies. 7, 663–671. doi:10.1016/b978-008044704-9/50067-7

Duguid, A., & Scherer, G. W. (2010). Degradation of oilwell cement due to exposure to carbonated brine. *International Journal of Greenhouse Gas Control, 4*(3), 546-560. doi:10.1016/j.ijggc.2009.11.001

Genedy, M., Stormont, J., Matteo, E., and Taha, M. R. (2014). Examining epoxy-based nanocomposites in wellbore seal repair for effective CO2 sequestration. *Energy Procedia*. *63*, 5798–5807. doi:10.1016/j.egypro.2014.11.612

Golru, S. S., Attar, M.M., Ramezanzadeh, B. (2014). Studying the influence of nano-Al2O3particles on the corrosion performance and hydrolytic degradation resistance of an epoxy/polyamide coating on AA-1050. Progress in Organic Coatings 77, 1391–1399. doi:10.1016/j.porgcoat.2014.04.017

Griffiths, P., and De Hasseth, J. A. (2007). Fourier Transform Infrared Spectrometry, second ed. Hoboken, NJ: Wiley-Blackwell.

Hill, L. W. (1997). Calculation of crosslink density in short chain networks. Progress in Organic Coatings. 31(3), 235–243. doi:10.1016/s0300-9440(97)00081-7

Huet, B. M., Prevost, J. H., & Scherer, G. W. (2010). Quantitative reactive transport modeling of Portland cement in CO2-saturated water. *International Journal of Greenhouse Gas Control, 4*(3), 561-574. doi:10.1016/j.ijggc.2009.11.003

Kardar, P., Ebrahimi, M., and Bastani, S. (2008). Study the effect of nano-alumina particles on physical–mechanical properties of UV cured epoxy acrylate via nano-indentation. Progress in Organic Coatings. 62(3), 321–325. doi:10.1016/j.porgcoat.2008.01.015

Kutchko, B. G., Strazisar, B. R., Dzombak, D. A., Lowry, G. V., & Thaulow, N. (2007). Degradation of Well Cement by CO 2 under Geologic Sequestration Conditions. *Environmental Science & Technology, 41*(13), 4787-4792. doi:10.1021/es062828c

Kutchko, B. G., Strazisar, B. R., Lowry, G. V., Dzombak, D. A., & Thaulow, N. (2008). Rate of CO 2 Attack on Hydrated Class H Well Cement under Geologic Sequestration Conditions. *Environmental Science & Technology, 42*(16), 6237-6242. doi:10.1021/es800049r

Ladva, H. K., Craster, B., Jones, T. G., Goldsmith, G., and Scott, D. (2005). The cement-to-formation interface in zonal isolation. SPE Drilling & Completion. 20(03), 186–197. doi:10.2118/88016-pa

Lee, J., and Yee, A. (2000). Inorganic particle toughening I: micro-mechanical deformations in the fracture of glass bead filled epoxies. Polymer. 42(2), 577–588. doi:10.1016/s0032-3861(00)00397-9

Liang, Y., and Pearson, R. (2009). Toughening mechanisms in epoxy–silica nanocomposites (ESNs). Polymer. 50(20), 4895–4905. doi:10.1016/j.polymer.2009.08.014

Liteanu, E., Spiers, C. J., and Peach, C. J. (2009). Failure behaviour wellbore cement in the presence of water and supercritical CO2. *Energy Procedi., 1*(1), 3553–3560. doi:10.1016/j.egypro.2009.02.149

Matteo, E. N., & Scherer, G. W. (2012). Experimental study of the diffusion-controlled acid degradation of Class H Portland cement. *International Journal of Greenhouse Gas Control, 7*, 181-191. doi:10.1016/j.ijggc.2011.07.012

Mehta, P. K. and Monteiro, P. J.M. (2013), Concrete: Microstructure, Properties, and Materials, fourth ed. McGraw-Hill Education, USA.

Nakayama, M., and Beaudoin, J. (1987). A novel technique for determining bond strength development between cement paste and steel. Cement Conc. Res., 17(3), 478–488. doi:10.1016/0008-8846(87)90011-1

Nasir, O., and Fall, M. (2008). Shear behaviour of cemented pastefill-rock interfaces. Engineering Geology. 101(3-4), 146–153. doi:10.1016/j.enggeo.2008.04.010

Pocius, A. V. (2012). *Adhesion and adhesives technology: An introduction,* second ed.*).* Cincinnati, OH: Hanser Publications.

Ramezanzadeh B., Attar M.M., Farzam M. (2011). Effect of ZnO nanoparticles on the thermal and mechanical properties of epoxy-based nanocomposite. J. Therm. Anal. Calorim., 103, 731–739. doi:10.1007/s10973-010-0996-1

Rimmelé, G., Barlet-Gouédard, V., Porcherie, O., Goffé, B., & Brunet, F. (2008). Heterogeneous porosity distribution in Portland cement exposed to CO2-rich fluids. *Cement and Concrete Research, 38*(8-9), 1038-1048. doi:10.1016/j.cemconres.2008.03.022

Salemi, N., and Behfarnia, K. (2013). Effect of nano-particles on durability of fiber-reinforced concrete pavement. *Cons. Bldg. Mater.. 48*, 934–941. doi:10.1016/j.conbuildmat.2013.07.037

Sharifi Golru, S., Attar, M., and Ramezanzadeh, B. (2014). Studying the influence of nano-Al2O3 particles on the corrosion performance and hydrolytic degradation resistance of an epoxy/polyamide coating on AA-1050. Progress in Organic Coatings. 77(9), 1391–1399. doi:10.1016/j.porgcoat.2014.04.017

Shokrieh, M. M., Kefayati, A. R., and Chitsazzadeh, M. (2012). Fabrication and mechanical properties of clay/epoxy nanocomposite and its polymer concrete. *Mater. and Design. 40,* 443–452. doi:10.1016/j.matdes.2012.03.008

Soares-Pozzi, A. C., Dibbern-Brunelli, D., (2016), Study of the influence of saline solutions in carbon/epoxy composite by luminescence, Raman and UATR/FT-IR spectroscopy. J. Materials Science, 51, 9342-9355.

Tchoquessi Doidjo, M. R., Belec, L. Aragon, E., Joliff, Y., Lanarde, L., Meyer, M., Bonnaudet, M., Perrin, F.X., (2013) Influence of silane-based treatment on adherence and wet durability of fusion bonded expoxy-steel joints, Progress in Organic Coatings, 73, 1765-1772.

Wetzel, B., Rosso, P., Haupert, F., and Friedrich, K. (2006). Epoxy nanocomposites – fracture and toughening mechanisms. *Eng. Frac. Mech. 73*(16), 2375–2398. doi:10.1016/j.engfracmech.2006.05.018

Zhai, L., Ling, G., Li, J., and Wang, Y. (2006). The effect of nanoparticles on the adhesion of epoxy adhesive. *Mater. Lett. 60*(25-26), 3031–3033. doi:10.1016/j.matlet.2006.02.038

Zhang, M., and Bachu, S. (2011). Review of integrity of existing wells in relation to CO2 geological storage: What do we know? Int. J. of Greenhouse Gas Control. 5(4), 826–840. doi:10.1016/j.ijggc.2010.11.006

Section 7

Dassault Systèmes. 2014. "Abaqus Theory Guide." *SIMULIA Abaqus 6.14 Documentation*. http://wufengyun.com:888/books/stm/default.htm?startat=book01.html#stm

Abdel Wahab, M. *The Mechanics of Adhesives in Composite and Metal Joints: Finite Element Analysis with ANSYS*, DEStech Publications Inc., Lancaster, PA, USA, 2014

Abdel-Ghaffar, F., U. F. Kandil & A. A. Abdel-Khalek. Nano-modified polymer concrete for infrastructure applications. *International Journal of Academic Research*. 2014; 6, 1.

ACI Committee 548, Polymers and Adhesives in Concrete, State of the Art Report, 2009.

ASTM C469/C469M. Standard test method for static modulus of elasticity and Poisson's ratio of concrete in compression. *ASTM International*, West Conshohocken, PA. 2014.

ASTM C882/C882M-13a. Standard test method for bond strength of epoxy-resin systems used with concrete by slant shear. *ASTM International*, West Conshohocken, PA. 2013.

Bakhshandeha, E., A. Jannesari; Z. Ranjbar; S. Sobhani; M. Reza Saeb. Anti-corrosion hybrid coatings based on epoxy–silicanano-composites: Toward relationship between the morphologyand EIS data; Progress in Organic Coatings 77 (2014) 1169–1183.

De, V. M. F., S. H. Tawfick, R. H. Baughman & A. J. Hart. Carbon nanotubes: present and future commercial applications. *Science (New York, N.Y.)*. 2013; 339, 6119, 535-9.

Ghanbari, A. and M.M. Attar. A study on the anticorrosion performance of epoxy nanocomposite coatings containing epoxy-silane treated nano-silica on mild steel substrate. Journal of Industrial and Engineering Chemistry, 23 (2015) 145–153.

Golru, S. S., M. M. Attar; B. Ramezanzadeh. Studying the influence of nano-Al2O3 particles on the corrosion performance and hydrolytic degredation resistance of an epoxy/polyamide coating of AA-1050, Progress in Organic Coatings, 77 (2014), 1391-1399.

Griffiths, P., J.A. de Hasseth. *Fourier Transform Infrared Spectrometry*, 2nd ed.; Wiley-Blackwell: Hoboken, NJ, USA, 2007.

Grossiord, N., J. Loos, O. Regev, C. E. Koning. Toolbox for dispersing carbon nanotubes into polymers to get conductive nanocomposites. *Chemistry of Materials*, 2006; 18: 1089-1099.

Iglesias, J. G., J. González-Benito, A. J. Aznar, J. Bravo & J. Baselga. Effect of Glass Fiber Surface Treatments on Mechanical Strength of Epoxy Based Composite Materials. *J. of Colloid and Interface Science*. 2002; 250, 1, 251-260.

Jo, B. W., S. K. Park & D. K. Kim. Mechanical properties of nano-MMT reinforced polymer composite and polymer concrete. *Construction and Building Materials*. 2008; 22, 1, 14-20.

Julio, E., F. Branco & V. Silva. Concrete-to-concrete bond strength. Influence of the roughness of the substrate surface. *Construction and Building Materials*. 2004; 18, 9, 675-681.

Kadar, P., M. Ebrahimi; S. Bastani. Study the effect of nano-alumina particles on physical-mechanical properties of UV cured epoxy acrylate via nano-indentation. Progress in Organic Coatings, 62 (2008), 321-325.

Khokhar, Z. R., I. A. Ashcroft, and V. S. Silberschmidt. Interaction of matrix cracking and delamination in cross-ply laminates: Simulations with stochastic cohesive zone elements. *Applied Composite Materials* 18.1 (2011);3-16.

Massingill, J.L., P.S. Sheih; R.C. Whiteside; D.E. Benton; D.K. Morissearnold; Fundamental studies of epoxy resins for can and coil. II. Flexibility and adhesion, Journal of Coating Technology, 62 (1990) 31–39.

Matejka; L., K. Dusek; J. Plestil; J. Kriz; F. Lednicky. Formation and structure of the epoxy–silica hybrids, Polymer, 40 (1999) 171–181.

Meo, M. and E. Thieulot. Delamination modeling in a double cantilever beam. *Composite Structures* 71 (2005); 429-434.

Mikhaylova, Y., G. Adam; L. Haussler; K. J. Eichhorn; B. Voit. Temperature-dependent FTIR spectroscopic and thermoanalytic studies of hydrogen bonding of hydroxyl (phenolic group) terminated hyperbranched aromatic polyesters. Journal of Molecular Structure, 788 (2006), 80–88.

Momayez, A., M. R. Ehsani, A. A. Ramezanianpour & H. Rajaie. Comparison of methods for evaluating bond strength between concrete substrate and repair materials. *Cem. & Conc. Res.* 2005; 35, 4, 748.

Musso, S., J. M. Tulliani, G. Ferro & A. Tagliaferro. Influence of carbon nanotubes structure on the mechanical behavior of cement composites. *Composites Science and Technology*. 2009; 69, 1985-1990.

Ohama, Y. Handbook of polymer-modified concrete and mortars: properties and process Technology. William Andrew, USA, 1995.

Osorio, A.G.; Silveira, I.C.L.; Bueno, V.L.; Bergmann, C.P. H2SO4/HNO3/HCl—Functionalization and its effect on dispersion of carbon nanotubes in aqueous media. *Appl. Surf. Sci*. 2008, 255, 2485–2489.

Paterson, D. A., A. Martinez-Felipe; S. M. Jansze; A. TM. Marcelis, K. MD. Storey, C. T. Imrie. New insights into the liquid crystal behavior of hydrogen-bonded mixtures provided by temperature-dependent FTIR spectroscopy. 42 (2015), 928-939.

Pocius, A. V. *Adhesion and Adhesives Technology: An Introduction*. 2nd ed. Hanser; 2011.

Rider, A. N., Q. An, N. Brack & E. T. Thostenson. Polymer nanocomposite - fiber model interphases: Influence of processing and interface chemistry on mechanical performance. *Chemical Engineering Journal*. 2015; 269, 121-134.

Saldanha, R., E. Julio, D. Dias-da-Costa & P. Santos. A modified slant shear test designed to enforce adhesive failure. *Construction and Building Materials*. 2013; 41, 673-680.

Salemi, N. and K. Behfarnia. Effect of nano-particles on durability of fiber-reinforced concrete pavement. *Construction and Building Materials*. 2013; 48, 1, 934-941.

Shekari, AH, Razzaghi MS. Influence of nanoparticles on durability and mechanical properties of high performance concrete. Procedia Eng 2011;14:3036–41.

Sprenger, Stephan. Epoxy resin composites with surface-modified silicon dioxide nanoparticles: A review. *Journal of Applied Polymer Science* 130.3 (2013): 1421-1428

Tjong, S. C. Structural and mechanical properties of polymer nanocomposites. *Materials Science & Engineering R*. 2006; 53, 73-197.

Vietri, U., L. Guadagno, M. Raimondo, L. Vertuccio & K. Lafdi. Nanofilled epoxy adhesive for structural aeronautic materials. *Composites Part B: Engineering*. 2014; 61, 4, 73-83.

Wetzel, B., F. Haupert, K. Friedrich, M. Q. Zhang & M. A. Rong. Impact and wear resistance of polymer nanocomposites at low filler content. *Polymer Engineering & Science*. 2002; 42, 9, 1919-1927.

Wetzel, B., P. Rosso, F. Haupert, and K. Friedrich. Epoxy nanocomposites - fracture and toughening mechanisms. *Engineering Fracture Mechanics*. 2006; 73, 16, 2375-2398.

Yuan, J., S. Zhou, G. Gu, and L. Wu. Effect of the particle size of nanosilica on the performance of epoxy/silica composite coatings. *Journal Of Materials Science* 40.15 (2005): 3927-3932.

Zhai, L., G. Ling, J. Li, and Y. Wang. The effect of nanoparticles on the adhesion of epoxy adhesive. *Materials Letters*. 2006; 60, 3031-3033.

Zhang, M. and S. Bachu. Review of integrity of existing wells in relation to CO2 geological storage: What do we know? International Journal of Greenhouse Gas Control. 2011; 5, 4, 826-840.

Zhu, J.; Kim, J.; Peng, H.; Margrave, J.L.; Khabashesku, V.N.; Barrera, E.V. Improving the dispersion and integration of single-walled carbon nanotubes in epoxy composites through functionalization. *Nano Lett.* 2003, 3, 1107–1113.

Section 8

AASHTO (2013). “Viscosity determination of asphalt binder using rotational viscometer.” *T316,* AASHTO Standards, Washington, DC.

Bai, S., Hu, J.Z., Pugmire, R.J., Grant, D.M., Taylor, C.M., Rubin, J.B., Peterson, E. J. (1998). “Solid state NMR and wide angle X-ray diffraction studies of supercritical fluid CO2-treated poly (ethylene terephthalate)” *Macromol,* 31(26), 9238–9246.Bartczak, Z., Cohen, R.E., Argon, A.S. (1992). “Evolution of the crystalline texture of high-density polyethylene during uniaxial compression.” *Macromol*, 25(18), 4692–4704.

Baldan, A. (2004) “Adhesively-bonded joints and repairs in metallic alloys, polymers and composite materials: Adhesives, adhesion theories and surface pretreatment.” *J. Mater. Sci.*, 39 (1), 1–49.

Blunt, M.J. (2017). *Multiphase Flow in Permeable Media: A Pore-scale Perspective*. Cambridge University Press, Cambridge, United Kingdom.

Carey, J.W., Wigand, M., Chipera, S.J., WoldeGabriel, G., Pawar, R., Lichtner, P. C., Guthrie, G.D. (2007). “Analysis and performance of oil well cement with 30 years of CO2 exposure from the SACROC Unit, West Texas, USA.” *Int. J. Greenhouse Gas Control*, 1(1), 75–85.

Celia, M. A., Bachu, S., Nordbotten, J. M., Gasda, S. E., Dahle, H. K. (2005). “Quantitative estimation of CO2 leakage from geological storage Analytical models, numerical models, and data needs.” *Greenhouse Gas Control Technologies*, 7, 663–671.

Checkai, D., Bryant, S., Tao, Q. (2013). “Towards a frequency distribution of effective permeabilities of leaky wellbores.” *Energy Procedia*, 37, 5653–5660.

Courard, L. (1999). “How to analyse thermodynamic properties of solids and liquids in relation with adhesion?” *In Proceedings of the 2nd International RILEM Symposium ISAP 99*, RILEM Publications, 9-20.

Ferry, J. D. (1980). *Viscoelastic properties of polymers*. John Wiley & Sons.

Genedy, M., Stormont, J., Matteo, E., Reda Taha, M. (2014). “Examining epoxy-based nanocomposites in wellbore seal repair for effective CO2 sequestration.” *Energy Procedia*, 63, 5798–5807.

Genedy, M., Daghash, S., Soliman, E., Reda Taha, M.M. (2015). “Improving fatigue performance of GFRP composite using carbon nanotubes.” *Fibers*, 3(1), 13–29.

Genedy, M., Kandil, U.F., Matteo, E.N., Stormont, J., Reda Taha, M.M. (2017-A). “A new polymer nanocomposite repair material for restoring wellbore seal integrity.” *Int. J. Greenhouse Gas Control,* 58, 290–298.

Genedy, M., Stenko, M., Stormont, J., Matteo, E.N., Dewers, T., Reda Taha, M.M. (2017-B). “Methyl Methacrylate Nanocomposite (MMNC) for Sealing Ultra-Thin Wellbore Microcracks and Methods for Making.” *U.S. Provisional Patent*, April 2017.

Gomez, S.P., Sobolik, S.R., Matteo, E.N., Reda Taha, M., Stormont, J.C. (2017). “Investigation of wellbore microannulus permeability under stress via experimental wellbore mock-up and finite element modeling.” *Comput. Geotech*, 83, 168–177.

G'sell, C., Dahoun, A. (1994). “Evolution of microstructure in semi-crystalline polymers under large plastic deformation.” *Mater. Sci. Eng. A.*, 175(1-2), 183–199.

Haggenmueller, R., Gommans, H.H., Rinzler, A.G., Fischer, J.E., Winey, K.I. (2000). “Aligned single-wall carbon nanotubes in composites by melt processing methods.” *Chem. Phys. Lett.*, 330(3-4), 219–225.

Harris, K. L., Vinson, E. F., Bour, D. L., Ewert, D. P., & Gerke, R. R. (1992). “Repair of microannuli and cement sheath.” *U.S. Patent No. 5,127,473*. Washington, DC: U.S. Patent and Trademark Office.

Jia, Z., Wang, Z., Xu, C., Liang, J., Wei, B., Wu, D., Zhu, S. (1999). “Study on poly (methyl methacrylate)/carbon nanotube composites.” *Mater. Sci. Eng. A.*, 271(1-2), 395–400.

Kuo, M. C., Tsai, C. M., Huang, J. C., & Chen, M. (2005). PEEK composites reinforced by nano-sized SiO2 and Al2O3 particulates. *Materials Chemistry and Physics*, *90*(1), 185-195.

Lacuve, M., Chougnet, A., Allouche, M., Mazard, C. (2015). “A method to improve adhesion strength at the cement/steel-casing interface and its effect on cement evaluation log response.” *Offshore Mediterranean Conference and Exhibition*, Ravenna, Italy.

McClory, C., McNally, T., Baxendale, M., Pötschke, P., Blau, W., Ruether, M. (2010). “Electrical and rheological percolation of PMMA/MWCNT nanocomposites as a function of CNT geometry and functionality.” *Eur. Polym. J.,* 46(5), 854–868.

Michanowicz, D.R., Buonocore, J.J., Rowland, S.T., Konschnik, K.E., Goho, S. A., Bernstein, A.S. (2017). “A national assessment of underground natural gas storage: Identifying wells with designs likely vulnerable to a single-point-of-failure” *Environ. Res. Lett.*, 12(6), 064004.

Nakayama, M. and Beaudoin, J. (1987). “A novel technique for determining bond strength development between cement paste and steel.” *Cem. Concr. Res*, 17(3), 478–488.

Naous, W., Yu, X. Y., Zhang, Q. X., Naito, K., & Kagawa, Y. (2006). Morphology, tensile properties, and fracture toughness of epoxy/Al2O3 nanocomposites. *Journal of Polymer Science Part B: Polymer Physics*, *44*(10), 1466-1473.

Parks, D.M., Ahzi, S. (1990). "Polycrystalline plastic deformation and texture evolution for crystals lacking five independent slip systems." *J. Mech. Phy. Solids*, 38(5), 701–724.

Pocius A.V. (2012). *Adhesion and Adhesives Technology: An Introduction.* second ed., Hanser Publications, Ohio.

Reddy, C.M., Arey, J.S., Seewald, J.S., Sylva, S.P., Lemkau, K.L., Nelson, R.K., Carmichael, C.A., McIntyre, C.P., Fenwick, J., Todd Ventura, G., Van Mooy, B.A., Camilli, R. (2012). "Composition and fate of gas and oil released to the water column during the Deepwater Horizon oil spill." *Proceedings of the National Academy of Sciences,* 109(50). 20229–20234.

Salemi, N. and Behfarnia, K. (2013). "Effect of nano-particles on durability of fiber-reinforced concrete pavement." *Const. Bldg. Mater.*, 48, 934–94.

Seidel, F.A. and Greene, T.G. (1985). "Use of expanding cement improves bonding and aids in eliminating annular gas migration in Hobbs Grayburg-San Andres wells." *In Proc. SPE Annual Technical Conference and Exhibition*, Society of Petroleum Engineers.

Shi, J. and Ming, J. (2017). "Influence of defects at the steel-mortar interface on the corrosion behavior of steel." *Constr. Build. Mater*, 136, 118–125.

Shokrieh, M.M., Kefayati, A.R., Chitsazzadeh, M. (2012). "Fabrication and mechanical properties of clay/epoxy nanocomposite and its polymer concrete." *Mater. Des., 40*, (2012) 443–452.

Stormont, J.C., Fernandez, S.G., Reda Taha, M., Matteo, E.N. (2018). "Gas flow through cement-casing microannuli under varying stress conditions." *Geomech. Energy Environ*, 18, 1–13.

Thiercelin, M. J., Dargaud, B., Baret, J. F., & Rodriquez, W. J. (1998). Cement design based on cement mechanical response. *SPE drilling & completion*, *13*(04), 266-273.

Wetzel, B., Rosso, P., Haupert, F., Friedrich, K. (2006). "Epoxy nanocomposites–fracture and toughening mechanisms." *Eng. Frac. Mech,* 73(16), 2375–2398.

Zeng, J., Saltysiak, B., Johnson, W.S., Schiraldi, D.A., Kumar, S. (2004). "Processing and properties of poly (methyl methacrylate)/carbon nano fiber composites" *Compos. Part B: Eng.*, 35(3), 173–178.

Zhai, L., Ling, G., Li, J., Wang, Y. (2006). "The effect of nanoparticles on the adhesion of epoxy adhesive." *Mater. Lett.*, 60(25-26), 3031–3033.

Zhang, M. and Bachu, S. (2011). "Review of integrity of existing wells in relation to CO2 geological storage: What do we know?" *International Journal of Greenhouse Gas Control*, 5(4), 826-840.

Section 9

Aboubakr, S.H., M.L. Begaye, U.F. Kandil, M.R. Taha, Multi-scale Viscoelastic Characterization of Synthetic C-S-H, 5th Int. Symp. Nanotechnol. Constr. (2015).

Alizadeh, R.A. Nanostructure and Engineering Properties of Basic and Modified Calcium-Silicate-Hydrate Systems, (2009) 250. doi:10.13140/RG.2.1.3892.8089.

Alizadeh, R., J.J. Beaudoin, L. Raki, Mechanical properties of calcium silicate hydrates, Mater. Struct. Constr. 44 (2011) 13–28. doi:10.1617/s11527-010-9605-9.

Ashby, M. Materials selection in mechanical design, 5th Edition, Butterworth-Heinemann, Elsevier, (2017).

ASTM. 2004. 914-95 ASTM Standard C, Standard test method for Bulk Density and Volume of Solid Refractories by Wax Immersion, ASTM Int., PA, 2004: pp. 187–189.

ASTM. 2007. 104-02 ASTM Standard E, Standard Practice for maintaining Constant Relative Humidity by Means of Aqueous Solution., ASTM Int., West Conshohocken, PA, 2007.

Beaudoin, J. J., R. F., Feldman, Dependence of degree of silica polymerization and intrinsic mechanical properties of C-S-H- on C / S ratio, Int. Congr. Chem. Cem. 6 (1986) 1–6.

Carey, J.W., M. Wigand, S.J. Chipera, G. WoldeGabriel, R. Pawar, P.C. Lichtner, S.C. Wehner, M.A. Raines, G.D. Guthrie, Analysis and performance of oil well cement with 30 years of CO2 exposure from the SACROC Unit, West Texas, USA, Int. J. Greenh. Gas Control. 1 (2007) 75–85. doi:10.1016/S1750-5836(06)00004-1.

Conley, S., G. Franco, I. Faloona, D.R. Blake, J. Peischl, T.B. Ryerson, Methane emissions from the 2015 Aliso Canyon blowout in Los Angeles, CA, Science. 2348 (2016) 2–7. doi:10.1126/science.aaf2348.

Fears, D. A 14-year-long oil spill in the Gulf of Mexico verges on becoming one of the worst in U.S. history, Washington Post. (2018) 1–7.

Feldman, V.S., R. F., & Ramachandran, Differentiation of interlayer and adsorbed water in hydrated Portland cement by thermal analysis, Cem. Concr. Res. 1 (1971) 607–620.

Foley, E.M., J.J. Kim, M.M. Reda Taha, Synthesis and nano-mechanical characterization of calcium-silicate-hydrate (C-S-H) made with 1.5 CaO/SiO_2 mixture, Cem. Concr. Res. 42 (2012) 1225–1232. doi:10.1016/j.cemconres.2012.05.014.

Genedy, M., U.F. Kandil, E.N. Matteo, J. Stormont, M.M. Reda Taha, A new polymer nanocomposite repair material for restoring wellbore seal integrity, Int. J. Greenh. Gas Control. (2017). doi:10.1016/j.ijggc.2016.10.006.

Guner, O., D., Ozturk, Comparison of Mechanical Behaviour of G Class Cements for different Curing Time, (2015) 445–451.

Jain, J., N. Neithalath, Physico-chemical changes in nano-silica and silica fume modified cement pastes in response to leaching, Int. J. Mater. Struct. Integr. 3 (2009) 114–133. doi:10.1504/IJMSI.2009.028608.

Kastler, J., D. Ph, K. Fillingham, S. Beresford, T. Greely, I. Editors, V. Virginia, S. Grant, E. Day-miller, P. Keener, D. Bader, S. Richards, K. Morris-zarneke, K. Leavitt, K. Fuller, S. Ryack-bell, J. Philippoff, A. Lebeau, M. Timmons, Special Issue Featuring the Gulf of Mexico Research Initiative; Research Resulting from the 2010 Deepwater Horizon Oil Spill NMEA Chapter Representatives :, 33 (2019).

Kim, J.J., E.M. Foley, M.M. Reda Taha, Nano-mechanical characterization of synthetic calcium-silicate-hydrate (C-S-H) with varying CaO/SiO_2 mixture ratios, Cem. Concr. Compos. 36 (2013) 65–70. doi:10.1016/j.cemconcomp.2012.10.001.

Ladva, H.K.J., B. Craster, T.G.J. Jones, G. Goldsmith, D. Scott, The Cement-to-Formation Interface in Zonal Isolation, in: 2004. doi:10.2523/88016-MS.

Le Saout, G., E. Lécolier, A. Rivereau, H. Zanni, Chemical structure of cement aged at normal and elevated temperatures and pressures, Cem. Concr. Res. 36 (2004) 71–78. doi:10.1016/j.cemconres.2004.09.018.

Li, Q., A. P. Hurt, N. J. Coleman, The Application of ^{29}Si NMR Spectroscopy to the Analysis of Calcium Silicate-Based Cement Using Biodentine^{TM} as an Example, Journal of Functional Biomaterials, (2019) 10, 25, doi:10.3390/jfb10020025

Mehta, P.J.M., P. K. Monteiro, Concrete Microstructure, Properties, and Materials, 4th ed., McGraw Hill, USA, 2013.

Nakayama, M., J.J. Beaudoin, A novel technique for determining bond strength development between cement paste and steel, Cem. Concr. Res. (1987). doi:10.1016/0008-8846(87)90011-1.

Ohama, Y. Handbook of polymer-modified concrete and mortars: properties and process technology, William Andrew, 1995.

Shirshova, N., A. Menner, G.P. Funkhouser, A. Bismarck, Polymerised high internal phase emulsion cement hybrids: Macroporous polymer scaffolds for setting cements, Cem. Concr. Res. 41 (2011) 443–450. doi:10.1016/j.cemconres.2011.01.017.

Stormont, J. C., S. G. Fernandez, M. M. Reda Taha, E. N., Matteo, Gas flow through cement-casing microannuli under varying stress conditions," J. of Geom. for Energy and the Env. 13 (2018) 1-13, doi.org/10.1016/j.gete.2017.12.001.

Thomas, J. J., H. M. Jennings, H. M., & A. J. Allen, The surface area of cement paste as measured by neutron scattering: Evidence for two C-S-H morphologies, Cem. Concr. Res. 28 (1998) 897–905.

Van Gemert, D., A. Beeldens, Evolution in modeling cement hydration and polymer hardening in polymer-cement concrete, Adv. Mater. Res. 687 (2013) 291–297. doi:10.4028/www.scientific.net/AMR.687.291.

Young, W., J. F., & Hansen, Volume relationships for CSH formation based on hydration stoichiometries, MRS Online Proc. Libr. Arch. 85 (1986).

Yue, X.B., R. Wang, Influence of SBR latex on the formation of C-S-H in C3S paste, Adv. Mater. Res. 687 (2013) 329–334. doi:10.4028/www.scientific.net/amr.687.329.

DISTRIBUTION

Email—Internal

Name	Org.	Sandia Email Address
Technical Library	01177	libref@sandia.gov

This page left blank

This page left blank